



DIFFRACTIVE PHOTON DISSOCIATION  
IN A HIGH PRESSURE HYDROGEN TIME PROJECTION CHAMBER

A thesis  
submitted to the Faculty of The Rockefeller University  
in partial fulfillment of the requirements  
for the degree of Doctor of Philosophy

by

Gregory R. Snow

3 November 1983  
The Rockefeller University  
New York, New York

c Copyright by Gregory R. Snow, 1983



"Die ganzen 50 Jahre bewusster Grübelei haben mich der Antwort der Frage 'Was sind Lichtquanten' nicht näher gebract. Heute glaubt zwar jeder Lump, er wisse es, aber er täuscht sich."

--Albert Einstein writing to  
Michele Besso, 12 December 1951  
Correspondance 1903-1955,  
Paris, France: Hermann (1972)

"After 50 years of brooding, the answer to the question 'What are light quanta?' still eludes me. Today many people think they know the answer, but they are mistaken."

-- my translation

## ACKNOWLEDGMENTS

A student in experimental high energy physics acquires the detailed skills of his profession through a combination of guidance from and imitation of his collaborators.

I had the good fortune to work with and learn from Konstantin Goulianos, my research advisor, whose mechanical ingenuity and aesthetic view resulted in the very elegant detector, TREAD. I thank him for leading me through the experiment from the earliest stages of prototype, proposal, and negotiations with Fermilab. It has been an additional bonus to have Dino as a good friend.

The efforts and ideas of Rodney Cool, Harry Sticker, Sebastian White, Tom Chapin, and Jerry Silverman are inadequately reflected in this thesis. I learned a great deal from them, and I would jump at the opportunity to work with them on future research projects.

I shared an office with Keith Jenkins during the period of analysis and thesis writing. His advice was valuable and his presence made for an enjoyable and comfortable work environment.

I had the great honor of working with Professor Yue Hua Chou, who joined the group for two years from the Institute for High Energy Physics in Beijing. I value highly the scientific, cultural, and human exchange which her visit allowed and remember with fondness the interactions with Yue Hua and the other Chinese physicists at Fermilab.

Superb technical, electronic, and engineering support was provided by Richard Heidecker and Donald Humbert. They are true experts. I am very much indebted to Arlene van de Rijn for her logistic help during my time away at Fermilab, to Rose Settembrino for her conscientious and efficient help in preparing this manuscript, and especially to

Ruth Snyder for innumerable favors and heartfelt care during my entire graduate school career.

The enormous assistance we received at Fermilab is gratefully acknowledged. In particular, I wish to thank Peter Garbincius, our liason physicist, for his help in bringing the experiment into operation; Ron Currier, the proton laboratory engineer, for supervising the design, construction, and installation of many important elements of the TREAD set-up; Bill Strickland for his help in mechanical design; Del Hoffman and the proton laboratory machine shop personnel for the speedy and flawless construction of numerous needed parts; and Jesse Guerra and Henry Schram for their help in mounting and maintaining the experiment on the floor of the Tagged Photon Facility.

I also wish to thank the Magnet Facility for building our magnet; Henry Koecher for use of the Lab 6 facilities during the assembly and initial testing of TREAD; and the Fermilab ad hoc safety committee which, under chairman George Biallas, helped us develop a safe system.

I would like to thank Leon Lederman for the freedom to ride his horse, Rondo, who provided me with many hours for thinking and daydreaming while roaming the Illinois prairie.

I mention my special friends, Donna Macri, John Greenhalgh, Bruce Collick, and Randy Furlong, for their support and good humor throughout this thesis project.

# ABSTRACT

We have performed an experiment at the Tagged Photon Facility of Fermilab to study the diffraction dissociation of high energy photons on hydrogen

$$\gamma + p \rightarrow X + p$$

in the region  $0.02 < |t| < 0.1 \text{ (GeV/c)}^2$ ,  $M_X^2/s < 0.1$ . In this process, incident photons whose energies range from 70 to 140 GeV transform coherently to massive hadronic states in the mass range  $M_X < 5 \text{ GeV/c}^2$ . We measure the inclusive differential cross section

$$\frac{d^2\sigma}{dt dM_X^2} \quad (1)$$

The behavior of this cross section, especially when compared to the corresponding cross sections for the diffraction dissociation of incident hadrons (pions, kaons, and protons), reveals some fundamental characteristics of photon hadronic interactions.

We use the Recoil Technique to determine the missing mass,  $M_X$ , and the square of the 4-momentum transfer,  $t$ . The recoil detector, TREAD, is a cylindrical time projection chamber filled with high pressure hydrogen gas which serves both as the target and as the drift medium for the ionization track created by recoil protons. The ionization drifts up to 75 cm in a high axial electric field. Concentric sense wires mounted on endplates sample different parts of the track, yielding the polar angle of the recoil. The energy of the recoil is determined by stopping the proton in scintillation counters located inside the high pressure vessel.

We have found that, as in the case of hadron dissociation, the photon dissociation cross section (1) exhibits exponential  $t$  dependence, falls as  $1/M_x^2$  with  $M_x^2$  for high masses,  $M_x^2 > 4 \text{ (GeV/c}^2\text{)}^2$ , and obeys a Factorization Rule. If one views diffraction dissociation as mediated by Regge exchanges, this behavior is consistent with that predicted by triple-Pomeron dominance. Furthermore, the application of a Finite Mass Sum Rule to the data indicates that the photon may have a "direct" hadronic interaction in addition to that described by the Vector Dominance Model of photon hadronic interactions.

## TABLE OF CONTENTS

Acknowledgments.....	i
Abstract.....	iii
Table of Contents.....	v
List of Figures.....	viii
List of Tables.....	xiii
 CHAPTER I.     Introduction and Motivation.....	1
A.   The Hadronic Character of the Photon.....	1
B.   The Experiment -- Photon Diffraction Dissociation.....	3
C.   Hadron Diffraction Dissociation.....	5
D.   The Comparison of Photon and Hadron Diffraction Dissociation.....	11
 CHAPTER II.    Experimental Technique.....	19
A.   Introduction:   The Recoil Technique.....	19
B.   Kinematics of the Recoil Measurement.....	20
C.   The Experimental Arrangement.....	21
D.   Precision of the Recoil Technique for Diffractive Physics.....	22
E.   Previous Applications of the Recoil Technique.....	25
 CHAPTER III.   The Recoil Spectrometer, TREAD.....	30
A.   Overview.....	30
B.   TREAD -- The TPC and its Performance Characteristics....	36
1.   Sense Wire Gain.....	39
2.   Drift Velocity.....	41
3.   Spatial Resolution and Angular Resolution.....	44



C. TREAD -- Apparatus Details.....	49
1. High Pressure Vessel.....	49
2. Heating Jacket.....	49
3. Solenoidal Magnet.....	51
4. Correction Coils.....	54
5. External parts to Main Vessel.....	55
6. Endcap Details.....	56
7. Gas Circulation and Purification System.....	61
8. TREAD Safety.....	62
9. Front anticounter and Multiplicity Counters.....	70
10. Material TREAD Presents to Beam.....	70
 CHAPTER IV. The Tagged Photon Beam.....	 97
A. The Electron Beam.....	97
B. Tagging System and C-Counter.....	99
C. Tagging System Calibration.....	102
D. The Pion Beam.....	103
E. Running Conditions.....	104
 CHAPTER V. Data Acquisition.....	 111
A. Photon Trigger Logic.....	111
B. Some Hardware Details.....	114
C. Other Triggers.....	116
D. Summary of March-April 1982 Data.....	118
 CHAPTER VI. Data Analysis.....	 122
A. Overview.....	122
B. Calibration of Pulse Height Counters.....	125
1. Conversion of Pulse Height to Kinetic Energy.....	125
2. Light Attenuation in Pulse Height Counters.....	129
3. Calibration Using Longitudinal Muons.....	131
4. Calibration Using NaI Light Pulsers.....	133

C.	Determination of the Recoil Polar Angle.....	134
1.	Track Finding.....	134
2.	Track Fitting.....	135
3.	Calibration of Drift Velocity.....	136
D.	dE/dx Calibration.....	138
E.	Anticounter Calibration.....	139
F.	Multiplicity Counter Calibration.....	140
G.	Recoil Time-of-Flight Calibration.....	142
H.	Essential Cuts for First Round Event Selection.....	142
I.	Cross Calibration of T AND $\theta$ Algorithms Using Pion Elastic Events.....	145
J.	Final Event Selection.....	146
K.	Corrections.....	147
L.	Mass Resolution.....	147
1.	Pion Elastic Mass Resolution.....	148
2.	$\rho^0$ Mass Resolution.....	151
CHAPTER VII. Results.....		164
A.	The Mass Distributions.....	164
B.	The t Distributions.....	165
C.	The Factorization Rule.....	166
D.	The Finite Mass Sum Rule.....	168
CHAPTER VIII. Appendix: Cross Sections and Results for Publication.....		180
A.	Extraction of Elastic Events.....	180
B.	Normalization.....	181
C.	Elastic Cross Sections.....	182
D.	Inelastic Cross Sections.....	183
E.	Resonance Structures.....	187
F.	Conclusion.....	188
References.....		201

## LIST OF FIGURES

Figures appear at the end of each chapter.

### CHAPTER I

- I.1 Comparison of photon and pion total hadronic cross sections
- I.2 Expected missing mass distribution for photon diffraction dissociation
- I.3 Hadron diffraction dissociation diagram
- I.4 Differential cross section for  $pd \rightarrow Xd$  as a function of  $M_X^2$  at 275 GeV/c
- I.5 Diffractive to total cross section ratios vs.  $\sigma_T$  for  $K_p^\pm$ ,  $\pi_p^\pm$ , and  $p_p^\pm$  at 100 GeV/c
- I.6 Regge diagrams for total cross section and diffraction dissociation
- I.7 Test of the first-moment Finite Mass Sum Rule at 275 GeV/c and  $|t| = 0.035 \text{ (GeV/c)}^2$

### CHAPTER II

- II.1 Diagram before and after photon-proton collision
- II.2 Experimental arrangement
- II.3 Contributions to the mass resolution vs.  $M_X^2$
- II.4 Contributions to the fractional mass resolution vs.  $M_X^2/s$

### CHAPTER III

- III.1 Cutaway diagram of upstream TPC: photon impinging on proton
- III.2 Cutaway diagram of upstream TPC: sequence of events after collision
- III.3 Recoil proton ionization trail arriving at the sense wire plate

- III.4 TREAD schematic diagram -- side view
- III.5 TREAD schematic diagram -- end view
- III.6 The drift field in the vicinity of a sense wire
- III.7 Sense wire voltage vs. pressure for different wire diameters at fixed gain
- III.8 Sense wire breakdown voltage vs. pressure
- III.9 Drift velocity vs. E/p in hydrogen gas
- III.10 Sense wire pulse height spectrum for cosmic ray tracks distributed through the entire drift space
- III.11 Wire 3A (upstream) residuals from cosmic ray tracks distributed through the entire drift distance
- III.12 Spatial resolution vs. drift distance, averaged over all wires
- III.13 Measured angular resolution vs. drift distance, with the prediction from spatial resolution in Figure III.12
- III.14 Kink angle  $\Delta\theta = \theta_1 - \theta_2$  between cosmic ray half tracks as a function of drift distance
- III.15 Axial component of central field viewed along central axis of TREAD
- III.16 Axial component of fringe field viewed at anticounter position
- III.17 Downstream endcap and TPC assembly extracted from TREAD
- III.18 Aluminum exit window
- III.19 Pulse height counter light pipe with O-ring clamp
- III.20 Signal and high voltage feedthrough plug
- III.21 Alpha source feedthrough and assembly
- III.22 -130 kV high voltage feedthrough
- III.23 Schematic diagram of the gas circulation and purification system
- III.24 Detailed gas system diagram
- III.25 Beryllium window mount and the flapper valve

## CHAPTER IV

- IV.1 Electron beam line schematic
- IV.2 Primary proton beam profile
- IV.3 Electron beam profile after horizontal dispersion
- IV.4 Electron beam profile after horizontal focussing
- IV.5 Photon beam profile just upstream of TREAD
- IV.6 Tagging system schematic
- IV.7 Top view of tagging counters
- IV.8 Tagged photon energy spectrum

## CHAPTER V

- V.1 Data acquisition system
- V.2 Online event picture of wire hits in typical event (side view)
- V.3 Online event picture (end view)

## CHAPTER VI

- VI.1 Cosmic ray pulse height spectrum in counter 32U
- VI.2 Light attenuation in pulse height counter; pulse height vs.  $z$
- VI.3 Longitudinal muon pulse height spectrum with fits
- VI.4 NaI calibration source pulse height spectrum
- VI.5 Tracking of NaI calibration with longitudinal muons
- VI.6 Charged particle multiplicity of the diffractive state  $X$  for  $\pi^- (\gamma) + p \rightarrow X + p$  in the mass range  $4 < M_X^2 < 10 \text{ GeV}^2$
- VI.7 Recoil ionization energy loss,  $dE/dx$ , versus kinetic energy,  $T$
- VI.8  $T \cdot dE/dx$  with and without anticounter cut

- VI.9 The effect of the truncated mean algorithm for  $dE/dx$  on the product  $T \cdot dE/dx$
- VI.10 The  $t$  dependence of the over-the-sense-wire contribution to the angular resolution from Monte Carlo simulation
- VI.11 Contributions to the angular resolution versus  $|t|$
- VI.12  $M_x^2$  resolution versus  $|t|$  for  $\pi^- p$  elastic events -- measured and predicted

## CHAPTER VII

- VII.1 Missing mass distribution for  $\gamma p \rightarrow Xp$  with  $70 < p_\gamma < 140$  GeV/c
- VII.2 Missing mass distribution for  $\gamma p \rightarrow Xp$  with  $1/M_x^2$  fit in high mass region
- VII.3 Missing mass distribution for  $\gamma p \rightarrow Xp$  showing higher masses
- VII.4 Missing mass distribution for  $\pi^- p \rightarrow Xp$  with 100 GeV/c incident pions
- VII.5 The  $t$  distributions for  $\rho^0$  events and high mass events
- VII.6 The slope parameter  $b$  versus  $M_x^2$  for  $\gamma p \rightarrow Xp$  and  $\pi^- p \rightarrow Xp$
- VII.7 Distributions of the  $\pi^+ \pi^-$  mass for different  $t$  intervals in  $\gamma p \rightarrow p \pi^+ \pi^-$  at 9.3 GeV
- VII.8 Differential cross sections  $d^2\sigma/dtdM_x^2$  at  $t = -0.05$  (GeV/c) $^2$  for  $\pi^- p$  at 100 GeV/c and  $\gamma p \rightarrow Xp$  at 75-148 GeV/c normalized by the corresponding total cross sections
- VII.9 Test of the FMSR for pion and photon data

## CHAPTER VIII

- VIII.1 Photon missing mass distributions showing "elastic"  $\rho$  events and inelastic diffraction dissociation events separately
- VIII.2 Differential cross sections for pion elastic scattering and  $\rho$  photoproduction as a function of  $t$
- VIII.3 The slope parameter  $b$  in the region  $0.02 < |t| < 0.1$  (GeV/c) $^2$  as a function of  $M_x^2$  for  $\pi^- p \rightarrow Xp$  at 100 GeV/c and  $\gamma p \rightarrow Xp$  at 75-148 GeV/c

- VIII.4 Differential cross sections  $(d^2\sigma/dt dx)/\sigma_T$  at  $t = -0.05 \text{ (GeV/c)}^2$  for  $\pi^- p \rightarrow Xp$  at 100 GeV/c and  $\gamma p \rightarrow Xp$  at 75-148 GeV/c
- VIII.5 Test of the Finite Mass Sum Rule for incident pions and photons
- VIII.6 The resonance structures  $A_1(1270)$  and  $A_3(1680)$  for the pion and  $\rho'(1600)$  for the photon

## LIST OF TABLES

Tables appear at the end of the chapters

### CHAPTER III

III.1      Summary of TREAD dimensions and performance parameters

### CHAPTER VIII

- VIII.1      Differential cross sections  $d\sigma/dt$  and fits to the form  $Ae^{bt}$
- VIII.2a      Inelastic differential cross sections  $d^2\sigma/dtdM_x^2$  for pions and photons
- VIII.2b      Differential cross sections including  $\pi^-p$  elastic and  $\rho$  signals
- VIII.3      Differential cross sections  $d^2\sigma/dtdx$  scaled to  $\sigma_T$  for pions and photons with fits in  $(1-x)$
- VIII.4      Parameters of resonance structures obtained by fits to the pion ( $A_1$  and  $A_3$ ) and photon ( $\rho'$ ) data



## CHAPTER I. INTRODUCTION AND MOTIVATION

### I.A. THE HADRONIC CHARACTER OF THE PHOTON

During the past 20 years, experiments have shown that high energy photons initiate hadronic interactions in a manner similar to the more "conventional" hadrons. The striking correspondence between the behavior of the photon and pion total cross sections on protons is shown in Figure I.1 (from Genz and Schmidt, 1973). The points represent the data from various photon total cross section measurements, and the solid line is the average of the  $\pi^+ - p$  and  $\pi^- - p$  cross sections divided by 220. Both the photon and the pion cross sections go through prominent resonances at low energies and become smoother as the energy increases. Beyond the scale of this plot, both cross sections continue to fall up to about  $\sqrt{s} = 10$  GeV. Above 10 GeV, both show a logarithmic rise.

Photon-hadron similarities are generally understood (Bauer et al., 1978) in the context of the Vector Dominance Model (VDM) which, in its simplest form, views a high-energy, physical photon as a superposition of two types of states: a bare photon, which does not interact strongly, and a hadronic photon, which has as its constituents the three lowest-mass, neutral vector mesons, the  $\rho^0(770)$ , the  $\omega(783)$ , and the  $\phi(1020)$ . In the VDM, a photon hadronic interaction is pictured as a two-step process. The photon first transforms to a vector meson,  $V$ , with a coupling parameter  $eM_V^2/f_V^2$ , and then the vector meson independently interacts with the target with a typical hadronic cross section. An uncertainty principle argument relates the energy fluctuation required for the photon-vector meson transition to the lifetime,  $\tau$ , of this virtual hadronic state:

$$\Delta E \cdot \Delta t \cong 1, \quad \Delta E \cong \frac{M_V^2}{2E_\gamma}, \quad \tau \cong \frac{1}{\Delta E} = \frac{2E_\gamma}{M_V^2} \quad (\text{I.1})$$

Thus, 100 GeV photons can travel 70f as virtual  $\rho^0$  mesons.

The VDM and its related formalism provide a good intuitive picture of photon hadronic interactions and make predictions in qualitative agreement with most experimentally-observed features. However, there are discrepancies between quantitative predictions and experimental data. Quantitative agreement requires additional input to the model.

For example, the VDM contribution to the total photon-nucleon cross section can be written in terms of the individual vector meson-nucleon cross sections:

$$\sigma_{\gamma N} = \sum_V \left( \frac{e^2}{f_V^2} \right) \sigma_{VN} \quad (\text{I.2})$$

High energy experiments studying the reactions  $e^+e^- \rightarrow \rho^0, \omega, \phi$  disclose the coupling parameters, and photoproduction experiments on nuclear targets determine the  $\sigma_{VN}$ . Equation (I.2) yields a value about 20% smaller than the 120 $\mu\text{b}$  total cross section observed at high energies, the  $\rho^0$ ,  $\omega$ , and  $\phi$  contributing 85 $\mu\text{b}$ , 10 $\mu\text{b}$ , and 7 $\mu\text{b}$ , respectively. Generalized Vector Dominance Models incorporate higher-mass vector mesons, the  $J/\psi$  for example, and Regge recurrences of the lower-mass mesons into the photon's hadronic part to supply the missing contributions, but the added constituents are required to interact with smaller-than-expected hadronic cross sections. An alternative is to suppose that the bare, non-VDM part of the photon interacts hadronically, but with a small cross section.

Other discrepancies indicate the need for a more complete description of the photon's hadronic content. In high energy hadronic collisions with heavy nuclei, photon shadowing occurs. That is, the hadronic cross section per target nucleon decreases with increasing  $A$ ,

and for a given A, the degree of shadowing grows with photon energy. This is consistent with the VDM view that the photon interacts through constituents whose mean free path in nuclear matter is short. The energy dependence is a consequence of Equation (I.1) in that, as the photon energy increases, the virtual lifetimes of the vector mesons grow linearly while their attenuation distances in nuclei remain approximately constant. However, the simple VDM predicts the shadowing effect to be roughly 50% more severe than what is observed. Higher-mass vector mesons, whose lifetimes are shorter, or the bare photon itself, could serve as less-strongly shadowed constituents of the hadronic photon and account for the discrepancy.

#### I.B. THE EXPERIMENT -- PHOTON DIFFRACTION DISSOCIATION

This dissertation describes an experiment to measure the inclusive diffraction dissociation (DD) of photons on protons

$$\gamma + p \rightarrow X + p$$

at high energies and low momentum transfer. Photon DD provides a new way to study the hadronic constituents of the photon, test the validity of the simple VDM view of photon hadronic interactions, and examine the appropriateness of the various schemes to generalize or embellish it. The experiment was performed in the Tagged Photon Facility at the Fermi National Accelerator Laboratory. The experiment number was E-612.

In DD, the photon transforms coherently, without the exchange of quantum numbers, to a massive hadronic state while the proton recoils away intact. Figure I.2 is a plot from the Proposal of the experiment showing the distribution of masses expected to appear in photon DD for 50 GeV/c incident photons. In addition to the VDM-associated low-mass resonances and the  $J/\psi$ , new resonances might be produced, along with a

continuum of masses like that found in the DD of pions, kaons, and protons.

We measure the inclusive differential cross section

$$\frac{d^2\sigma}{dt dM_x^2} \quad (I.3)$$

in the kinematic range  $0.02 < |t| < 0.1 \text{ (GeV/c)}^2$  and  $M_x^2/s < 0.1$  using incident photons whose energies range from 70 to 140 GeV.

The measurement of the photon dissociation cross section (I.3) contributes to our knowledge of the photon's hadronic content on two levels. First, we compare the behavior of our measured cross section to those previously measured for the DD of incident hadrons. Physicists from The Rockefeller University have been involved in the study of hadron DD and elastic scattering at Fermilab since 1972. One series of experiments (Bartenev et al., 1973a, 1973b, 1974; Akimov et al., 1975a, 1975b, 1975c, 1976) used the primary protons in the Main Ring to study pp and pd diffraction dissociation from 50 to 400 GeV, and an experiment in the Meson Lab (Cool et al., 1981a, 1981b, 1982; Goulianos et al., 1982) measured DD for  $\pi^\pm p$ ,  $K^\pm p$ , and  $p^\pm p$  at 100 and 200 GeV. Results on hadron DD will be summarized in Section I.C. As a control experiment for our study of photon DD, we measured the cross section (I.3) for  $\pi^- p$  with a 100 GeV pion beam in the same apparatus. Our result is that, to a large extent, the photon behaves like a hadron in DD.

Second, small discrepancies between photon and pion DD lead us to comment on the constituents of the photon's hadronic part and the validity of the simple VDM. The Finite Mass Sum Rule and a Factorization Rule, both described in the next section, are sensitive to the mass  $M_0$  of the incident particle at the time of the hadronic interaction. The two rules are satisfied by the pion data with  $M_0^2 = M_\pi^2$ . Applied to the photon data, the two rules are satisfied

simultaneously only when  $M_0^2 \approx 0.5 \text{ (GeV/c}^2\text{)}^2$ . We interpret the non-zero value as an average over the masses of the photon's hadronic constituents and conclude that the photon may interact hadronically in its bare, massless state with a probability of approximately 20%.

### I.C. HADRON DIFFRACTION DISSOCIATION

A one-sentence definition of diffraction dissociation, also referred to as inclusive inelastic diffraction, is given in a 1981 review article (Alberi and Goggi, 1981) on the diffraction of hadronic waves: In the process of single diffraction dissociation, one of the initial state hadrons emerges from the interaction with a momentum close to the kinematic limit having excited the other hadron, whose original mass is  $M_0$ , to a system of effective mass,  $M_x > M_0$ . The word "single" is used to distinguish the process from "double" diffraction dissociation in which both hadrons are excited to states of greater mass. The word "diffraction" is used because scattering at high energies and small momentum transfer resembles the diffraction of light in many ways. "Dissociation" refers to the strong decay of the massive  $M_x$  to known hadrons.

DD is characterized by momentum transfers  $\sqrt{|t|} \ll M_p$ ; hence the process is outside the regime of present QCD predictions. Low  $|t|$  is required to excite the internal degrees of freedom of the dissociating hadron without fragmenting the target/recoil hadron. The target hadron is said to recoil coherently. Naming the dissociating hadron  $h$  and the target hadron  $a$ , we can picture the reaction  $h + a \rightarrow X + a$  as in Figure I.3. The quantity  $t$  is carried between independent vertices, but no quantum numbers are exchanged.

At low  $|t|$ , the diffractively produced mass  $M_x$  is related to the Feynman scaling variable  $x = p_{||}/p_{||}^{\text{(max)}}$  in the center of mass according to

$$1-x \equiv \frac{M_x^2 - M_h^2}{s} \quad (I.4)$$

The quantity  $q_{||} = M_a (1-x)$  is the forward momentum transfer, and hence the minimum momentum transfer  $\sqrt{|t|}_{\min}$  required to produce a mass  $M_x$ . One expects that the target,  $a$ , will recoil coherently if the wavelength associated with  $q_{||}$  is larger than the target radius, taken to be about  $1f$ . This leads to the coherence condition for DD :

$$1-x \equiv \frac{M_x^2 - M_h^2}{s} < 0.1 \quad (I.5)$$

The coherence condition gives the range of masses which can be diffractively produced at a given  $s$ . It simply states that in DD only a small fraction of the available energy can go into the production of  $M_x$ .

Figure I.4 (from Akimov et al., 1975b) shows the  $M_x^2$  dependence of the inclusive differential cross section  $d^2\sigma/dtdM_x^2$  for  $p + d \rightarrow X + d$  at  $s = 1032 \text{ GeV}^2$ . At two different  $|t|$  values, the elastic peaks, reduced by a factor of 50, and the inelastic diffractive peaks are shown. Above the one-pion threshold for inelastic production, the mass spectrum consists of resonance-like structures superposed on a continuum. Resonance production is usually called diffractive excitation while the continuum is referred to as diffraction dissociation.

For high masses above the resonance region,  $M_x^2 > 4 (\text{GeV}/c^2)^2$ , the cross section falls approximately as  $1/M_x^2$  with  $M_x^2$ , as shown by the smooth curve through the data points. At a given value of  $M_x^2$ , the cross section falls exponentially with  $t$  as expected for diffractive processes. The exponential  $t$  dependence is usually expressed in terms of a slope parameter  $b$ ; that is,  $d\sigma/dt \sim \exp(bt)$ . In the high mass region, the slope parameter is independent of  $M_x^2$  and has a value about half that for elastic scattering. Furthermore, the cross sections for

hadron DD exhibit a slow logarithmic rise with  $s$  at high energies, similar to the rise of hadronic total cross sections.

We anticipate the absence of a prominent elastic peak for photon DD at  $M_X^2 = M_Y^2 = 0$ . Whereas the total elastic cross section in hadronic collisions is typically 15-20% of the total cross section in the region of  $s=1000 \text{ GeV}^2$ , the elastic  $\gamma$ -p cross section is only about 0.075% of the total photon cross section at these energies (Breakstone et al., 1981). As we shall see, this absence is compensated by a prominent peak at the  $\rho^0$  mass,  $M_X^2 = M_p^2 = 0.6 (\text{GeV}/c^2)^2$ , which can be viewed as the elastic scattering of the dominant hadronic constituent of the photon.

Using the relation (I.4), differential cross sections for DD are often expressed in terms of the scaling variable  $x$  instead of  $M_X^2$ . In the region  $|t| < 0.1 (\text{GeV}/c)^2$  and  $M_X^2 > 4 (\text{GeV}/c^2)^2$ , the measured cross sections for the DD of various hadrons,  $h + a \rightarrow X + a$ , are well described by

$$\frac{d^2\sigma}{dt dx} = \frac{A}{1-x} e^{bt} + A' (1-x) e^{b't} \quad (\text{I.6})$$

where the constants  $A$ ,  $A'$ ,  $b$ , and  $b'$  depend on  $h$  and  $a$ . The first term is identified with single DD and contains the observed exponential  $t$  dependence and  $1/M_X^2$  dependence. An  $s$ -dependent factor is sometimes included in the numerator of this term. The second term is mostly due to non-diffractive contributions with  $b' \approx b$ . The diffractive and non-diffractive terms are approximately equal at  $(1-x) = 0.1$ , while at  $(1-x) = 0.03$ , the diffractive term is about 90% of the inclusive cross section.

The Factorization Rule referred to in this chapter states that the ratio of the diffractive term in (I.6) to the total cross section is a constant, depending on  $s$ ,  $x$ , and  $t$ , but not on the incident hadron  $h$ .

Figure I.5 (from Cool et al., 1981a) shows the ratio  $R=A/\sigma_T$  versus  $\sigma_T$  for six different incident hadrons at 100 GeV/c. The Factorization Rule holds for these hadrons within the experimental accuracy of <10%.

The global properties of DD, in particular the  $1/M_x^2$  behavior and the Factorization Rule, are predicted by Regge formalism, suitably generalized to the case of inelastic particle production. Figure I.6 illustrates how expressions for total cross sections and DD cross sections arise from the exchange of Regge trajectories,  $\alpha(t)$ . A particular trajectory, the Pomeron (P), carries the quantum numbers of the vacuum and dominates both cross sections.

The total cross section, through the optical theorem, is related to the forward ( $t=0$ ) elastic scattering amplitude and is written as

$$\sigma_T^{ha}(s) = \beta_{hP}(0) \beta_{aP}(0) \quad (I.7)$$

where  $\beta_{hP}(t)$  is the coupling of the mediating Pomeron to the hadron  $h$  at the top vertex. The expression for the DD cross section is derived similarly. The target hadron,  $a$ , emits a Pomeron  $\alpha_P(t)$ , and the excitation of the hadron  $h$  arises from the total P-h cross section,  $\sigma_T^{Ph}$ . The optical theorem applied to  $\sigma_T^{Ph}$  relates  $\sigma_T^{Ph}$  to elastic P-h scattering, which calls for another Pomeron exchanged at  $t=0$ . The DD cross section is written as

$$\frac{d^2 \sigma^{ha}}{dt dx} = \frac{\beta_{aP}^2(t) \beta_{hP}(0) G_{PPP}(t)}{16\pi (1-x)} \quad (I.8)$$

where  $G_{PPP}(t)$  is the triple-Pomeron coupling.

The  $1/M_x^2$  dependence is apparent in (I.8). Dividing (I.8) by (I.7), the  $\beta_{hP}(0)$  terms cancel, which is equivalent to the Factorization Rule. The Factorization Rule is often referred to in the literature as



"factorization of the diffractive vertex", which is appropriate in view of this discussion and the diagrams in Figure I.6. Indeed, observing a  $1/M_x^2$  dependence and a positive test of factorization are taken as evidence for triple-Pomeron dominance of diffraction dissociation.

The Regge picture is expected to apply only to the high mass part of the DD spectrum. The first-moment Finite Mass Sum Rule (FMSR) relates the high mass continuum to the low mass resonance region (also referred to as the low mass enhancement) and elastic scattering. The FMSR derives from duality, which proposes that the diffractive cross sections can be described equivalently by an infinite series of s channel resonances or by t channel Reggeon exchanges. The resonances and Reggeons are dual to each other. The consequence is that the high  $M_x^2$  data appropriately extrapolated to low  $M_x^2$  should average over the structure observed at low  $M_x^2$ , including the elastic peak. Quantitatively, the FMSR predicts the equality

$$|t| \frac{d\sigma_{el}}{dt} + \int_{\uparrow}^{v_0} v \frac{d^2\sigma}{dt dv} dv = \int_{\uparrow}^{v_0} v \frac{d^2\sigma}{dt dv} dv \quad (I.9)$$

integral of data                      function obtained  
over resonance region                  from  $v > v_0$

where  $v = M_x^2 - M_h^2 + |t|$  is the cross symmetric variable. The value of  $v_0$  must lie beyond the resonance region but is otherwise arbitrary.

The FMSR is a non-trivial constraint. Because the elastic cross section for hadrons is large compared to the inelastic cross section, equation (I.9) can be satisfied only through an interplay of the two terms on the left side. As  $|t|$  increases from zero, the resonance contribution must fall faster than the high mass contribution and, as a result, the exponential slope of the low mass region must be larger than the slope of the high mass region. The FMSR was first shown to be

satisfied for proton dissociation in  $pd \rightarrow Xd$  (Akimov et al., 1976). It also holds (Cool et al., 1980) for  $pp \rightarrow Xp$  and  $\pi^{\pm}p \rightarrow Xp$ .

Figure I.7 (from Akimov et al., 1976) shows (i) the values of  $v \cdot d^2\sigma/dtdM_x^2$  versus  $M_x^2$  derived from the pd experiment at 275 GeV/c and  $|t|=0.035$  (GeV/c)<sup>2</sup>, (ii) the experimental value of  $|t|d\sigma_{el}/dt$  derived from (Akimov et al., 1975c) represented as a Gaussian-shaped area for illustrative purposes, and (iii) the fit to the data in the high mass region of  $v \cdot d^2\sigma/dtdM_x^2$  represented by the solid curve at the constant value of  $3.1 \text{ mb}(\text{GeV}/c)^{-2}$ . The straight-line fit demonstrates the  $1/M_x^2$  behavior of the cross section. The sum of the areas under the two dotted lines, representing the left-hand side of (I.9), equals the area under the solid curve, representing the right-hand side of (I.9). The FMSR is satisfied to a high degree of accuracy.

In the  $\pi^-p$  control experiment which we performed along with the photon experiment, elastic  $\pi^-p$  and inelastic DD mass distributions were accumulated simultaneously. Due to resolution in the measurement of  $M_x^2$ , elastic scattering appears as a peak of finite width which extends above the inelastic threshold and overlaps low mass DD events. In applying the FMSR, the elastic events can be treated just as the inelastic ones; namely, by multiplying the apparent cross section  $d^2\sigma/dtdv$  by  $v = M_x^2 - M_h^2 + |t|$  and integrating over  $v$  down to values which are low enough to include all events. For a resolution broadened peak which is symmetric around  $M_x = M_h$ , the elastic events in this procedure are, in effect, multiplied by  $|t|$ , as required by the FMSR. The procedure is illustrated in the FMSR analysis presented in Chapter VII.

#### I.D. THE COMPARISON OF PHOTON AND HADRON DIFFRACTION DISSOCIATION

The claim that photon DD is very similar to hadron DD is based on our observation that the corresponding cross sections exhibit the same general features. We observe a continuous spectrum of photon-induced, diffractively excited masses and a  $1/M_x^2$  dependence for the high mass region. The  $t$  distributions are exponential, with a slope in the high mass region about half as steep as that for the "elastic scattering" of the  $\rho^0$ . Furthermore, the Factorization Rule is satisfied within our experimental accuracy.

Through Equations (I.7), (I.8), and (I.9), we see how the Factorization Rule and FMSR depend on the incident mass  $M_0$  of the dissociating hadron (or photon). Due to our experimental uncertainty, the test of factorization does not favor a particular value for  $M_0$  for the photon. However, under the assumption that the FMSR should hold, we must introduce a nonzero value for  $M_0$ . As mentioned previously, this value turns out to lie somewhere between the mass of a bare photon and the mass of the  $\rho^0$ . Our interpretation of this result is that the photon interacts primarily as a vector meson but may also have a direct, non-VDM hadronic interaction. Naively speaking, we say that our study of photon DD allows us to weigh the photon at the time of its hadronic interaction.

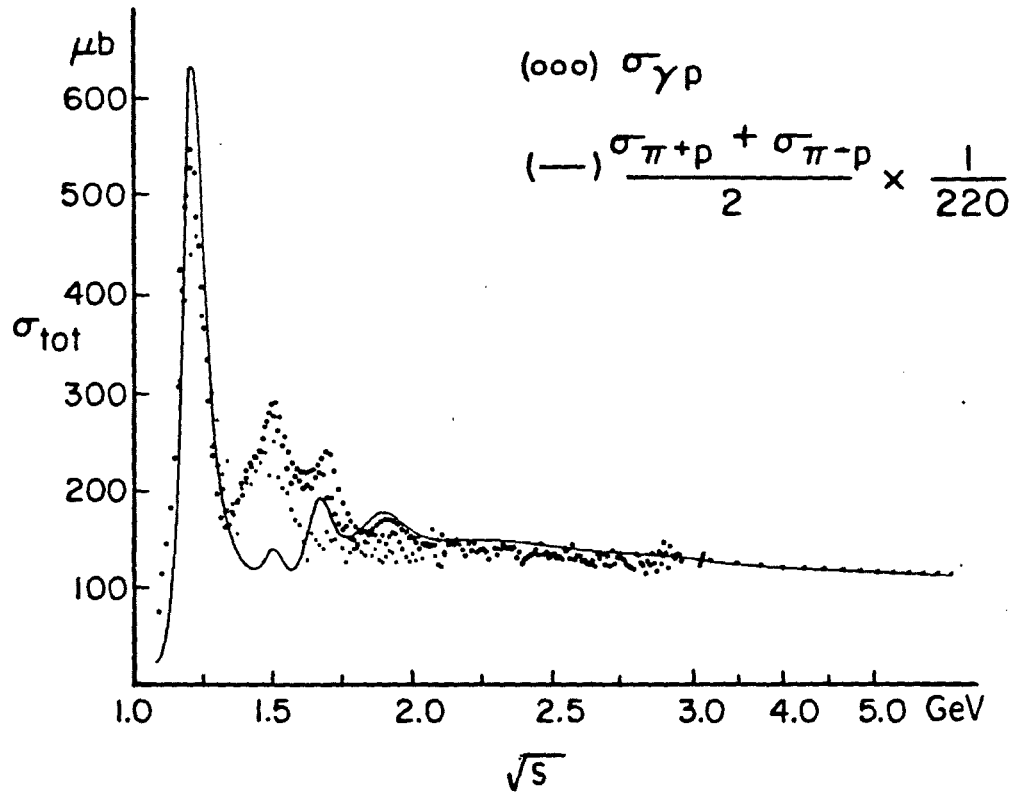


FIG. I.1 - Comparison of photon and pion total hadronic cross sections

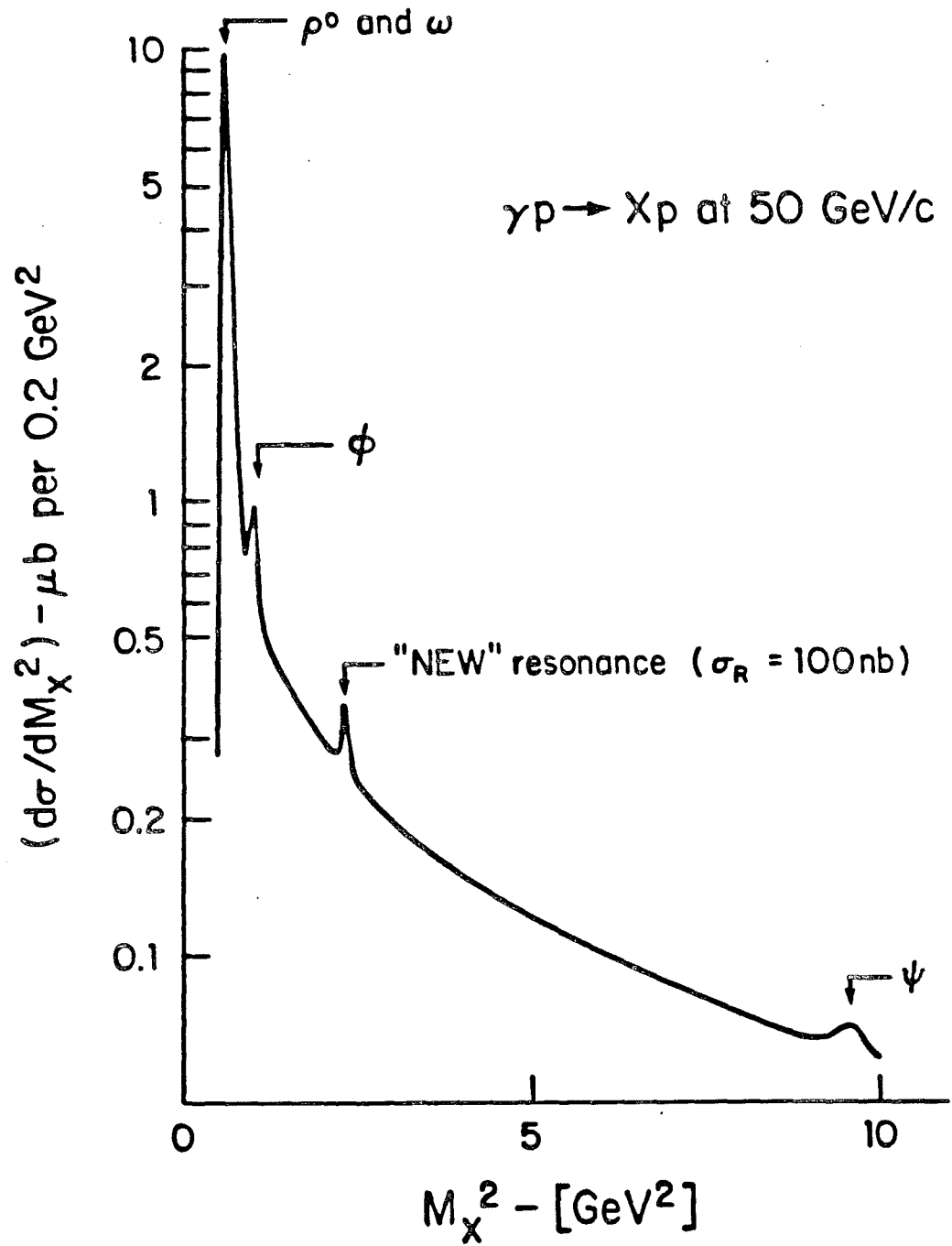


FIG. I.2 - Expected missing mass distribution for photon diffraction dissociation

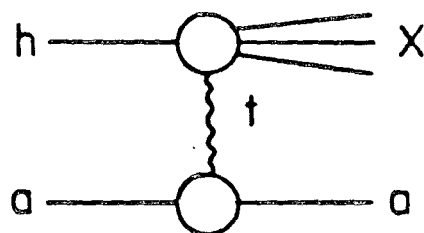


FIG. 1.3 - Hadron diffraction dissociation diagram

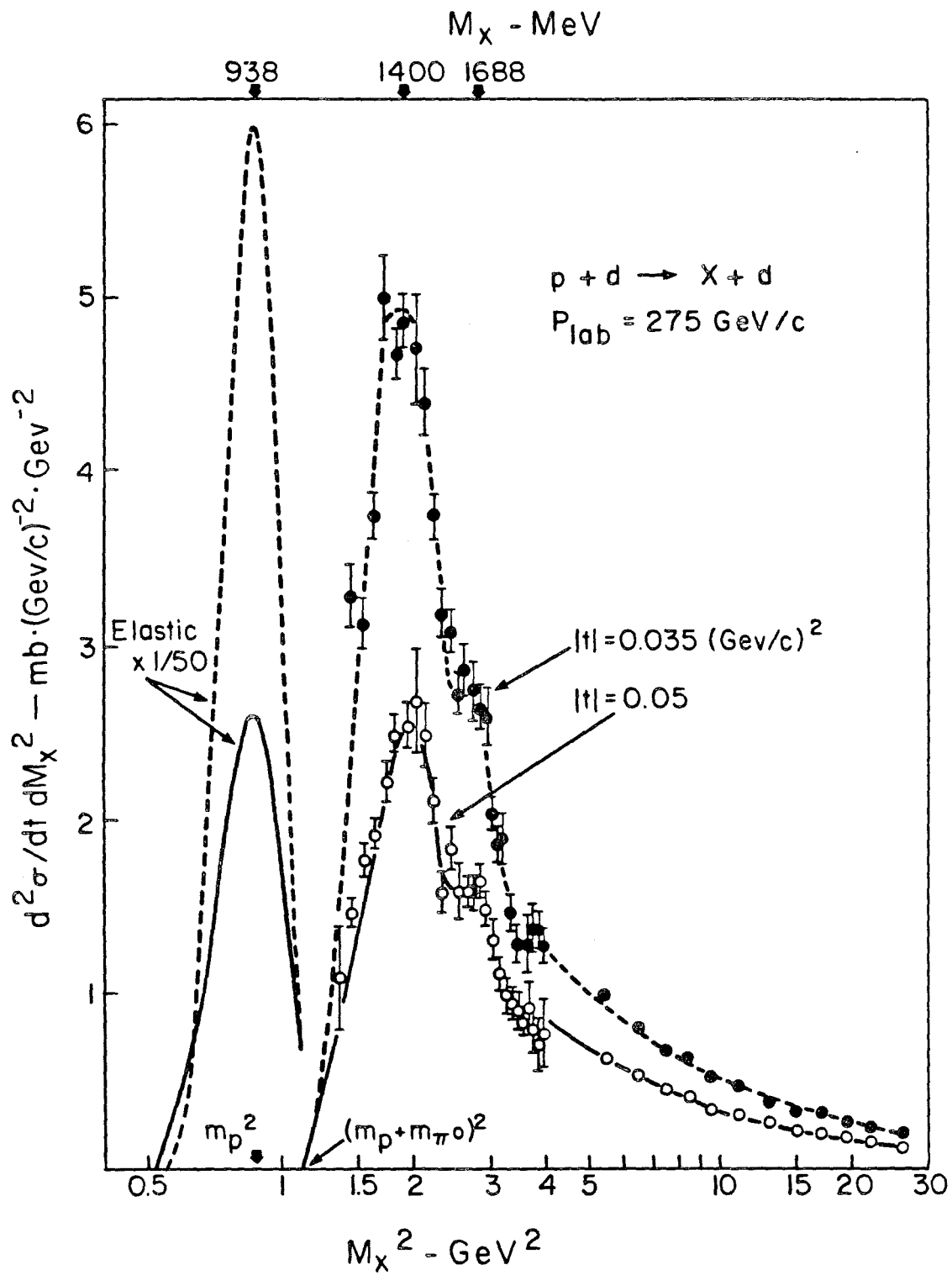


FIG. I.4

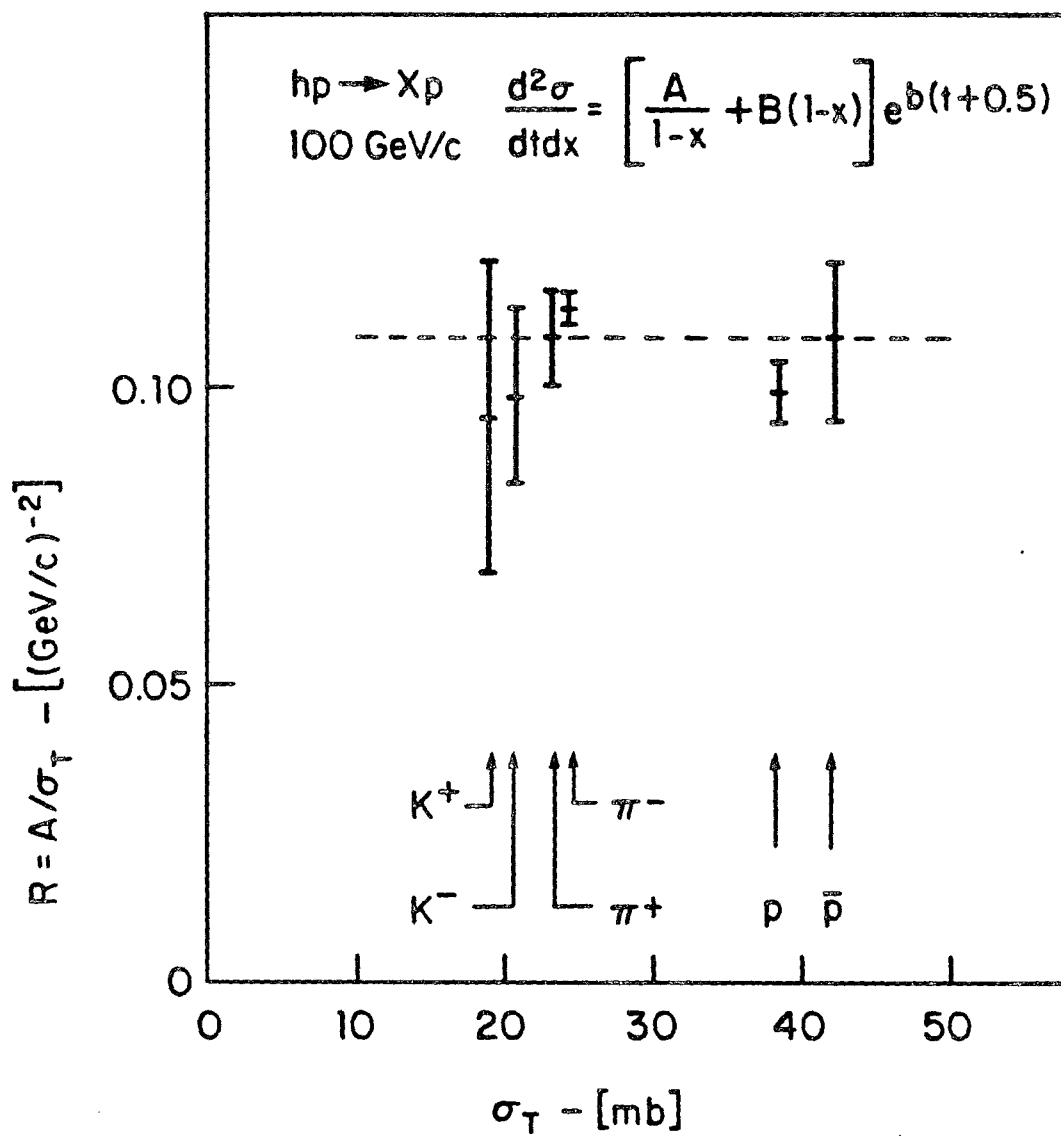


FIG. 1.5 - Diffractive to total cross section ratios vs.  $\sigma_T$  for  $K^\pm p$ ,  $\pi^\pm p$ , and  $p^\pm p$  at 100 GeV/c



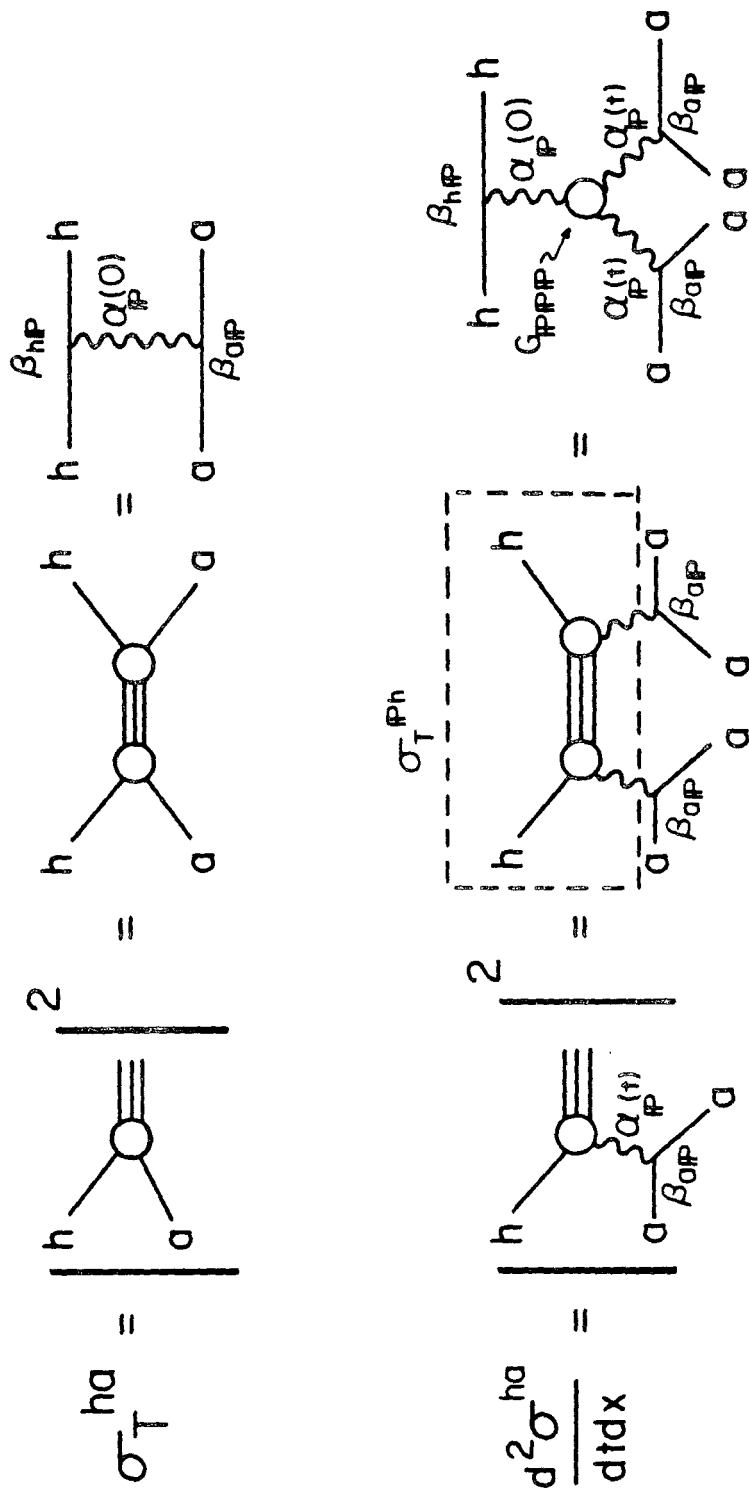


FIG. 1.6 - Regge diagrams for total cross section and diffraction dissociation

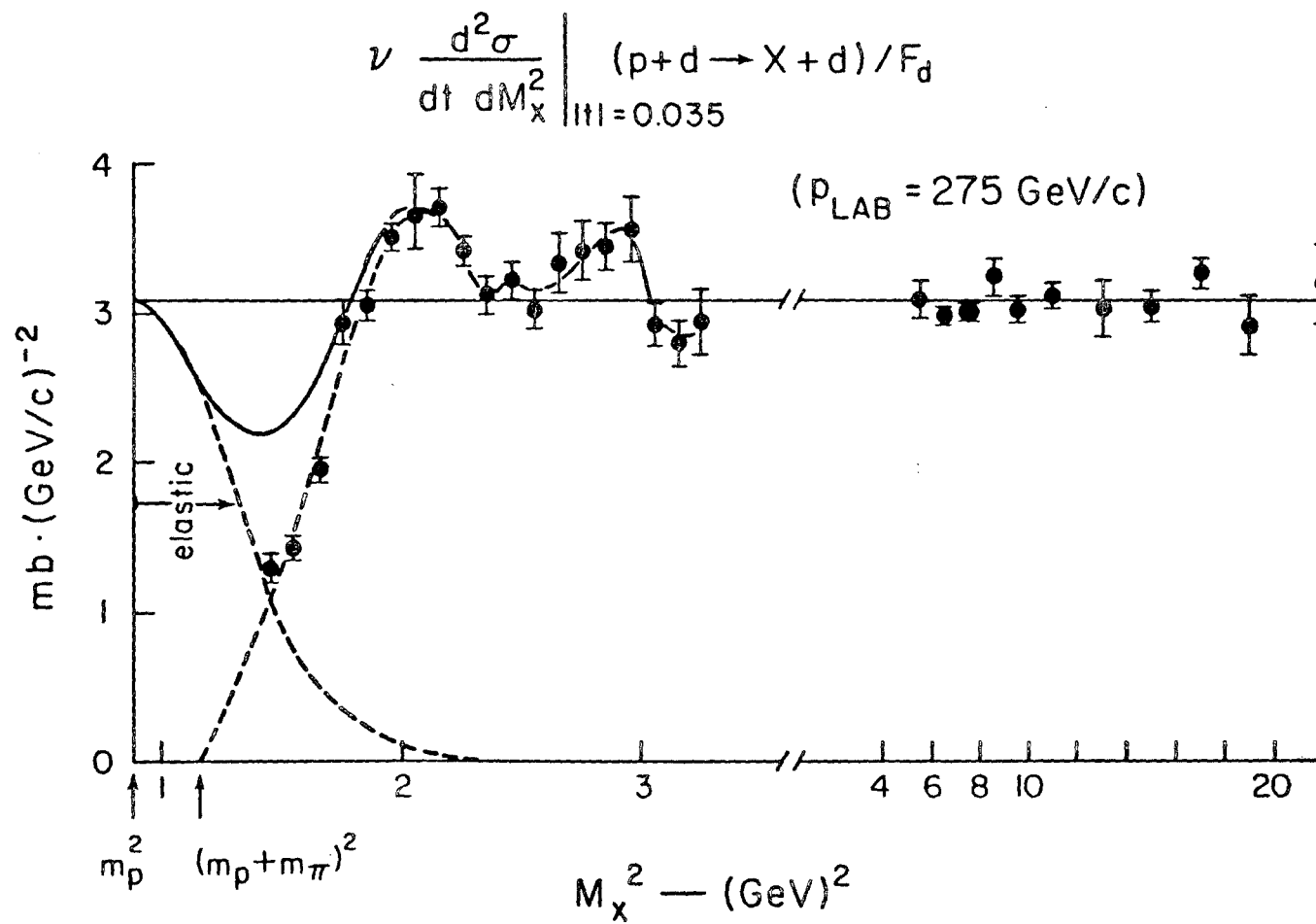


FIG. I.7 - Test of the first-moment Finite Mass Sum Rule

## CHAPTER II. EXPERIMENTAL TECHNIQUE

### II.A. INTRODUCTION: THE RECOIL TECHNIQUE

The massive state,  $X$ , of interest in the inclusive reaction

$$\gamma + p \rightarrow X + p$$

exists for such a short time that it travels a distance on the order of a few proton radii in the laboratory frame before decaying. One may reconstruct the mass of this excited photon and determine the square of the 4-momentum transfer,  $t$ , in a "direct" manner by observing the decay products of  $X$  or in an "indirect" manner by observing the recoil proton. The direct route requires one to

- 1.) measure the energies and relative production angles of all decay products of  $X$  and the energy of the incident photon.

The indirect route relies on conservation of total 4-momentum and requires one to

- 2.) measure the energy of the incident photon, and the kinetic energy and polar angle of the recoil proton.

The desire to study large diffractive masses with a modestly-sized apparatus made the latter option more appealing. The largest allowable diffractively-produced mass increases with increasing incident energy, making high incident energies favorable. In choice 1.), the error in the determination of  $t$  grows with incident energy, and a large, expensive apparatus is required to detect and sort out the tracks of the

fast forward particles. In choice 2.), determination of  $t$  is independent of incident energy, and recoil protons in the MeV energy range call for a smaller detection apparatus. The method of observing the recoiling target particle to determine the missing mass of the excited incident particle constitutes the Recoil Technique.

## II.B. KINEMATICS OF THE RECOIL MEASUREMENT

Figure II.1 is a diagram before and after a photon-proton collision illustrating our application of the Recoil Technique to the study of photon diffraction dissociation. Photons, whose energy is measured by the tagging system of Fermilab's Tagged Photon Facility, impinge on protons in a sample of high-pressure hydrogen gas. With an energy ranging from 70 to 140 GeV, the photon carries so much momentum compared to the thermal motion of the proton in the gas that the target proton can be considered stationary in the laboratory frame. The collision area is surrounded by the recoil spectrometer, TREAD (The Recoil Energy and Angle Detector), which was conceived, designed, and constructed by the Experimental Physics Group of Rockefeller University. TREAD, with its associated electronic data acquisition system, is designed to

1. select the diffractive events in which the target proton recoils at a large angle ( $45-90^\circ$  with respect to the photon's direction) with kinetic energy in the range 10-59 MeV and
2. measure these quantities with good resolution.

The kinetic energy that the recoil proton gains in the collision is only a very small fraction of the photon's total energy, but it is very large compared to the binding energy of a few eV which holds the proton in the hydrogen atom. That is, the "work function" associated with the proton in the gaseous target is entirely negligible.

From the measured incident photon momentum,  $p_\gamma$ , the recoil proton's kinetic energy,  $T$ , and polar angle,  $\theta$ , one determines the invariant four-momentum transfer squared,  $t$ , and the missing mass,  $M_x$ , using the following equations:

$$t = -2M_p T \quad (\text{II.1})$$

$$M_x^2 \approx 2p_\gamma \sqrt{|t|} (\cos \theta - \sqrt{|t|} / 2M_p) \quad (\text{II.2})$$

where the polar axis from which  $\theta$  is measured is the incident direction of the photon, and  $M_p$  is the proton mass. The first relation follows easily from the definition of 4-momentum transfer and the definition,  $T = E_{\text{tot}} - M_p$ , of recoil kinetic energy. It is relativistically exact and valid for any incident momentum. The second relation follows from 4-momentum conservation and is a good approximation when  $T \ll M_p \ll p_\gamma$ .

### II.C. THE EXPERIMENTAL ARRANGEMENT

Figure II.2 shows the physical layout of the experiment. A collimated beam of bremsstrahlung photons is created by passing a beam of monoenergetic electrons through a thin tungsten radiator. The electrons are bent into an array of lead-glass and lead-scintillator shower counters where their final energy is measured. The neutral photons, whose momentum is thereby tagged to  $\pm 2\%$ , pass through a hole in a wall of shielding blocks and then through a thin entrance window into TREAD. TREAD consists of two independent cylindrical time projection chambers (TPC's) filled with high pressure hydrogen gas. The hydrogen serves both as the target and as the drift medium for the ionization tracks created by recoil protons. The ionization drifts up to 75 cm in a high axial electric field. Concentric sense wires mounted on endplates sample different parts of the track, yielding the polar angle,  $\theta$ , of the recoil. The kinetic energy,  $T$ , of the recoil is determined by stopping the proton in scintillation counters located

inside the high pressure vessel. The multiplicity of the charged particles amongst the decay products of the massive state,  $X$ , is measured with two thin scintillation counters located outside the vessel; this is the only quantity associated with  $X$  that we measure directly.

In order to eliminate background, it is important to identify the recoil particle as a proton. For low energy recoils, the product of  $T$  and  $dE/dx$ , the ionization energy loss per unit path length in the hydrogen gas, is proportional to the recoil mass. A measurement of  $dE/dx$  from the sense wire pulse heights, accurate to about 13%, allows bona fide recoil protons to be selected by a cut on recoil mass.

#### II.D. PRECISION OF THE RECOIL TECHNIQUE FOR DIFFRACTIVE PHYSICS

This section describes the uncertainties in the determination of  $t$  and  $M_X^2$  due to uncertainties in the measurements of  $T$ ,  $\theta$ , and  $p_Y$ . I describe the resolution in  $t$  first.

Equation (II.1) illustrates that, assuming the recoil particle has been identified as a proton with mass  $M_p$ ,  $t$  depends only on the measurement of  $T$  by the scintillation counters. The error in  $t$  is

$$|\Delta t| = 2 M_p \Delta T \quad (\text{II.3})$$

A fractional uncertainty of a few percent in  $T$  leads to the same fractional uncertainty in  $t$ . The situation would be very different if one were to rely on the observation of the decay products of  $X$  to determine  $t$ . For in that case,  $t$  is approximated by (Ekelof, 1976)

$$t = - \left( \frac{M_X^2}{2p_Y} \right)^2 - (p_Y \theta_X)^2 \quad (\text{II.4})$$

where  $\theta_x$  is the polar angle of the center-of-mass motion of the X decay products. The error in the determination of  $t$  is dominated by the uncertainty in the calculation of  $\theta_x$  from the measured directions and momenta of the several forward tracks. The error is approximately

$$|\Delta t| \approx 2p_\gamma \sqrt{|t|} \Delta\theta_x \quad (\text{II.5})$$

which grows linearly with the incident photon momentum. A 10% determination of  $t$  for  $|t| = 0.05 \text{ (GeV/c)}^2$  and  $p_\gamma = 100 \text{ GeV/c}$  would require a resolution of 0.1 mrad in  $\theta_x$ . Such precision in the determination of  $\theta_x$  would be difficult, if not impossible, to achieve with a downstream calorimeter/spectrometer measuring both neutral and charged tracks. It is clear that determining  $t$  from the recoil kinetic energy,  $T$ , is both more precise and more economical.

The contributions to the resolution in  $M_x^2$  due to the uncertainties in  $p_\gamma$ ,  $t$ , and  $\theta$  are obtained by differentiating Equation (II.2) with respect to these parameters. The contributions are:

$$\left. \frac{\Delta M_x^2}{M_x^2} \right|_{p_\gamma} = \frac{\Delta p_\gamma}{p_\gamma} \quad (\text{II.6})$$

$$\left. \frac{\Delta M_x^2}{M_x^2} \right|_t = \frac{1}{2} \left| \frac{M_x^2}{|t|} - \frac{p_\gamma}{M_p} \right| \Delta t \quad (\text{II.7})$$

$$\left. \Delta M_X^2 \right|_{\theta} = 2 p_Y \sqrt{|t|} \left[ 1 - \left( \frac{M_X^2}{2 p_Y \sqrt{|t|}} + \frac{\sqrt{|t|}}{2 M_P} \right)^2 \right]^{\frac{1}{2}} \Delta \theta \quad (\text{II.8})$$

The total resolution in  $M_X^2$  is obtained by combining these contributions in quadrature. Furthermore, the resolution in  $M_X$  follows from

$$\Delta M_X^2 = 2 M_X \Delta M_X \quad (\text{II.9})$$

Figure II.3 shows the separate contributions to  $\Delta M_X^2$ , the total  $\Delta M_X^2$ , and  $\Delta M_X$  plotted against  $M_X^2$  for  $|t| = 0.05 \text{ (GeV/c)}^2$ , and  $p_Y = 100 \text{ GeV/c}^2$ . For this plot, I assume  $\Delta p_Y/p_Y = 0.02$ ,  $\Delta t = 0.002 \text{ (GeV/c)}^2$ , and  $\Delta \theta = 6 \text{ mrad}$ ; these are our estimated uncertainties (1 standard deviation). The measured mass resolution for pion elastic events and  $\rho^0$  photoproduction events is compared with that expected from Equations (II.6) to (II.8) in Chapter VI.L.

It is useful to express the mass resolution given in Equations (II.6), (II.7), and (II.8) in terms of the parameter,  $M_X^2/s$ , which is a measure of the diffractive character of dissociation processes. Recall from Chapter I the coherence condition,  $M_X^2/s < 0.1$ . In Figure II.4, I plot the FRACTIONAL resolution in  $M_X^2$ , as a function of  $M_X^2/s$  using the same values for  $p_Y$ ,  $t$ ,  $\Delta p_Y$ ,  $\Delta t$ , and  $\Delta \theta$  as in Figure II.3.

In the region  $0.05 < M_X^2/s < 0.1$ , the total fractional  $M_X^2$  resolution has the approximately constant value 0.03, which leads to a  $M_X$  resolution of 1.5%. For photon momenta in the interval 70 to 140 GeV/c, this region in  $M_X^2/s$  corresponds to the mass range  $2.6 < M_X < 5.1 \text{ GeV/c}^2$ . For smaller values of  $M_X^2/s$ , however, the mass resolution becomes worse because of the contribution from the angle,  $\theta$ . Hence, good angular resolution is most important for small diffractive masses. The mass resolution for our observation of the  $\rho^0$  meson is a



case in point. The  $\rho^0$  mass of  $0.770 \text{ GeV}/c^2$  is produced with  $M_x^2/s$  in the interval from 0.002 to 0.004, and the total  $M_x$  resolution curve is off the scale of Figure II.4 for this interval.

## II.E. PREVIOUS APPLICATIONS OF THE RECOIL TECHNIQUE

In this section, I describe a sample of experiments in both primary and secondary beams which have used the Recoil Technique to study various processes. The premium of good  $t$  resolution at high energies was awarded in each case. An added, and essential, attraction of the Recoil Technique in primary or "main ring" beams is that there is no need for a downstream detector which would interfere with the primary beam.

During the years 1972-1974, a group from Clermont-Ferrand and Lyon studied (Ekelof 1976, and refs. therein) elastic and inelastic scattering of protons on  $^4\text{He}$  using the primary beam of the CERN Proton Synchrotron and a target box of gaseous He with thin windows. The  $24 \text{ GeV}/c$  proton beam traversed the target essentially unperturbed. The recoil arm was a movable telescope which measured the kinetic energy ( $4 - 100 \text{ MeV}$ ) of recoil He nuclei stopping in a 4-layer bank of semiconductor detectors. The kinetic energy measurement led to a resolution in  $t$  of  $0.0015 (\text{GeV}/c)^2$ . The polar angle was determined by the position of the telescope arm. The angular resolution of  $9 \text{ mrad}$  arose from the angular acceptance of the semiconductor bank and the multiple scattering of the recoil on its  $\sim 0.5$  meter path into the telescope. The resulting missing mass resolution was about  $100 \text{ MeV}/c^2$  over the  $0.938$  to  $2.6 \text{ GeV}/c^2$  mass range covered by the experiment.

The  $t$ -distribution of elastic scattering data showed a clear diffraction minimum at  $|t| = 0.2 (\text{GeV}/c)^2$ ; the  $N^*$  isobar data, at a missing mass of  $1.4 \text{ GeV}/c^2$ , showed a maximum at the same  $|t|$  value. Both of these features are explained by the Glauber model of multiple

scattering in nuclei, and this experiment provided the highest-energy data available at that time for comparison with calculations (Auger et al., 1976).

From 1972-1974, a group of physicists from Rockefeller University, University of Rochester, Fermilab, and the U.S.S.R. performed a series of experiments using the Recoil Technique to reveal many important features of proton-proton and proton-deuteron elastic scattering and diffraction dissociation at Fermilab energies (see refs. in Chapter I.B). An internal gas jet target of hydrogen or deuterium intercepted the circulating protons in Fermilab's Main Ring at different times in the acceleration cycle, allowing incident proton energies from 8 to 400 GeV to be selected. A set of ten small solid-state detectors, mounted on a movable carriage at a distance of 2.5 meters from the beam-jet interaction point, measured the kinetic energy and angle of low-momentum recoil particles. Recoil protons or deuterons travelled to the detectors through vacuum to eliminate multiple Coulomb scattering along the way.

When the deuterium jet was used, each recoil detector was a two-layer stack of silicon or lithium counters. A thin front counter measured  $dE/dx$ , and a thicker back counter measured the remaining kinetic energy; the combination of the two counters served to distinguish deuterons from protons. Proton-deuteron interactions in the range  $0.013 < |t| < 0.14 \text{ (GeV/c)}^2$  were measured with this arrangement. When pure hydrogen was used in the jet, only a single counter layer was required to detect the elastic recoils, so the accessible  $|t|$  range for p-p interactions could be extended down to  $0.001 \text{ (GeV/c)}^2$ , which is well inside the Coulomb interference region. The uncertainties in the recoil measurements, and hence in the missing mass measurements, were dominated by the recoil angular resolution of a few milliradians, primarily due to the size of the solid-state detectors and the jet target.

Many of the diffraction dissociation results from this series of experiments are referred to in Chapter I.C. In addition, the group parameterized the slopes of the  $t$ -distributions for  $p$ - $p$  and  $p$ - $d$  elastic scattering over the wide range of available energies, finding greater shrinkage of the forward peak in the  $p$ - $d$  case (Bartenev et al., 1973a and Akimov et al., 1975c). They also deduced the behavior of the ratio of the real to the imaginary part of the  $p$ - $p$  elastic scattering amplitude from the very low  $|t|$  data, with the important result that the ratio crosses zero (from negative to positive) around an incident beam energy of 280 GeV (Bartenev et al., 1973b). In 1973, this timely result was consistent with the then exciting and somewhat controversial measurement of a rising  $p$ - $p$  total cross section at the CERN ISR.

Rockefeller University's Experiment 396 in the Meson Lab at Fermilab (see refs. in Chapter I.B) is an example of an experiment in a secondary beam which used the Recoil Technique. E-396 traded the wide range of proton energies and high intensity offered by the Main Ring for a variety of incident projectiles: positive and negative protons, kaons, and pions at 100 and 200 GeV/c. The physics goals of E-396 were similar to those at the internal target, i.e., study elastic scattering and diffractive dissociation at very low  $|t|$ , this time with a target of 1 atm hydrogen gas and a small recoil detector designed with emphasis on good angular resolution at low  $|t|$ .

On either side of the mylar target cylinder, two rectangular drift chambers with very thin mylar windows measured the polar angle of  $45$ - $90^\circ$  recoil protons. An angular uncertainty of 3 mrad arose chiefly from multiple Coulomb scattering in the gas and mylar windows in the recoil's path. One of eight 1" thick plastic scintillation counters, viewed by phototubes at each end, stopped 5-50 MeV recoils and measured their energy with a resolution of about 1 MeV. Two thin scintillation counters just downstream of the hydrogen target recorded the charged multiplicity of forward final states. The presence of the E-396 recoil

detector caused very little disturbance to the incident beam, so the beam could be used by another experiment mounted downstream.

Taken together with the p-p and p-d data from the internal target experiments, the  $p^{\pm}p$ ,  $K^{\pm}p$ , and  $\pi^{\pm}p$  diffraction dissociation data from E-396 give a rather complete picture of the phenomenology of inclusive hadron dissociation at high energies and low  $|t|$ . Also, the elastic data from E-396 showed that there is no unitarity-violating break in the slopes of elastic t-distributions, in contrast to what had been suggested by an interpretation of other experiments (Cool et al., 1981b, and refs. therein).

The design of TREAD grew from the design of the E-396 recoil detector; the changes were required to make TREAD more suitable for photon dissociation. Because the  $\gamma - p$  total cross section is ~200 times smaller than the p-p total cross section, event rate considerations led to a denser hydrogen target (factor of 15), a longer target (factor of 3), and greater solid angle coverage (factor of 3) for detection of recoil protons in TREAD.

The last recoil detector I discuss, located downstream of TREAD, is the most prominent inhabitant of Fermilab's Tagged Photon Lab - Experiment 516. It was able to take data with TREAD in place in the beam during the E-612 test run in 1981. The experiment combines a low-momentum recoil spectrometer with a large-scale, momentum-analyzing, downstream calorimeter to yield a more complete picture of many exclusive photoproduction processes. The collaborators in E-516 include physicists from Fermilab, University of Colorado, University of California at Santa Barbara, University of Toronto, and Carleton University. The E-516 spectrometer is intended to become available for use by other groups as a laboratory facility.

In the recoil spectrometer, three layers of cylindrical MWPC cells surround a liquid hydrogen target and measure the angle of low-momentum

recoil particles. The kinetic energy is measured by stopping the recoils in two layers of plastic scintillator followed by two layers of liquid scintillator. Time-of-flight and  $dE/dx$  measurements yield good separation of recoil protons from pions up to 600 MeV. A  $t$  resolution of 5% is achieved throughout the range  $0.06 < |t| < 1.2 \text{ (GeV/c)}^2$ . An on-line trigger processor allows the recoil measurement to be integrated into the trigger with various downstream criteria to select particular high-mass inclusive or exclusive channels to be recorded. Using the measured photon energy from the tagging system, and the energy and angle of the recoil proton, the trigger processor calculates the missing mass of candidate events, and, typically, a minimum missing mass of  $2 \text{ GeV/c}^2$  is required to record an event.

The recoil information is essential for analyzing the data on inclusive  $J/\psi$  meson and charmed D meson photoproduction. The procedure in both cases is to compare the missing mass calculated from the recoil proton with the  $J/\psi$  or D mass reconstructed from decay products detected downstream.  $J/\psi$  mesons are identified by their decay to two muons, and the task is to classify each event as "elastic" (missing mass equals reconstructed  $J/\psi$  mass), "quasi-elastic" (missing mass equals  $J/\psi$  mass, but recoil is an excited  $N^*$  isobar), or "inelastic" (missing mass indicates that the  $J/\psi$  is accompanied by other downstream hadrons). Single D mesons are identified downstream by their  $K\pi$  or  $K\pi\pi^0$  decay modes; an additional accompanying pion indicates that the D is actually the product of a  $D^*$  decay. The recoil 4-momentum is used to determine whether the missing 4-momentum opposite the detected D is just that of its associated partner, or whether the D pair is accompanied by other hadrons. A preliminary result (Sliwa, 1983) is that only  $14 \pm 11\%$  of the photoproduced D pairs are created with no accompanying hadrons.

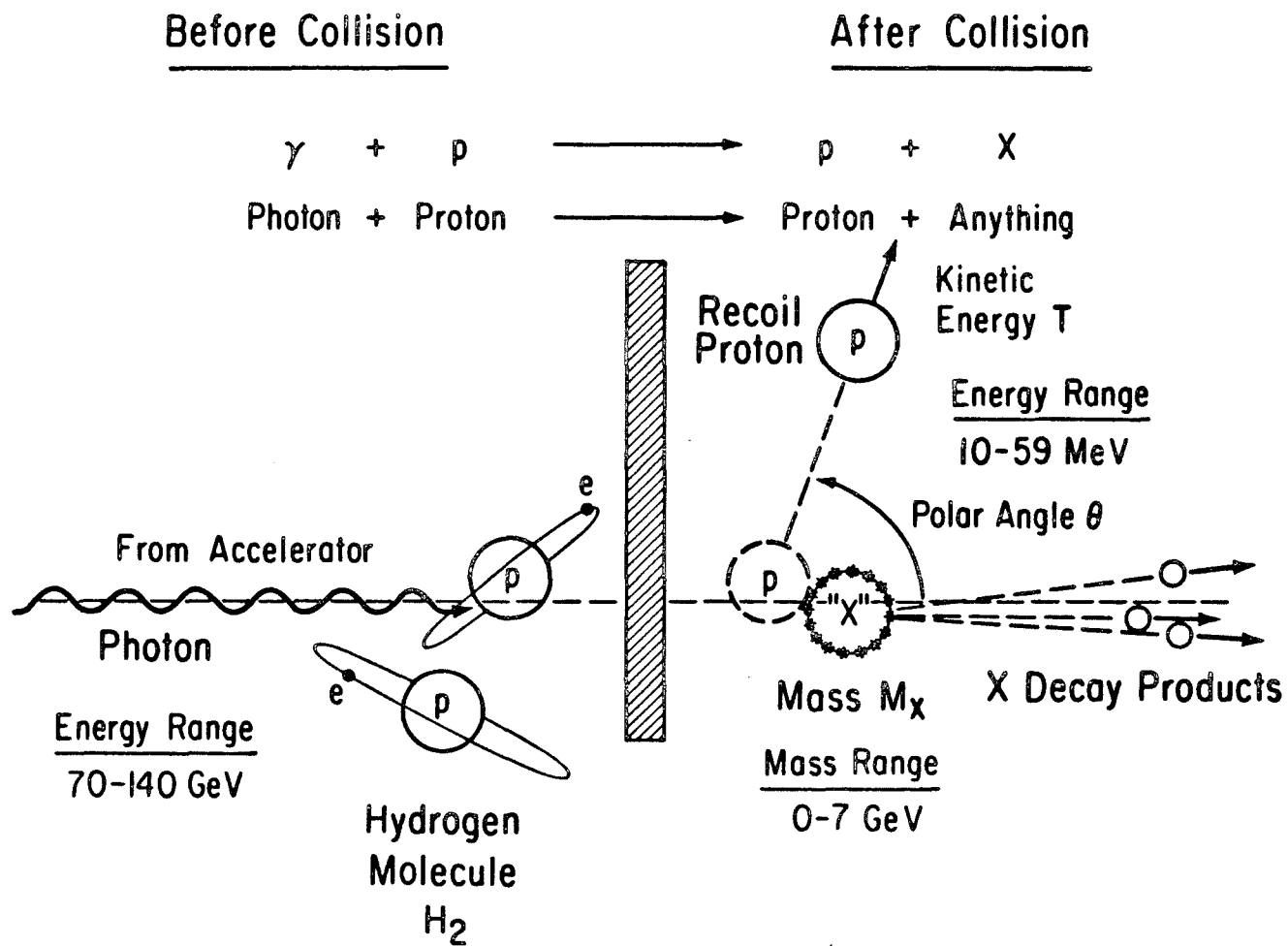


FIG. II.1

## EXPERIMENTAL ARRANGEMENT

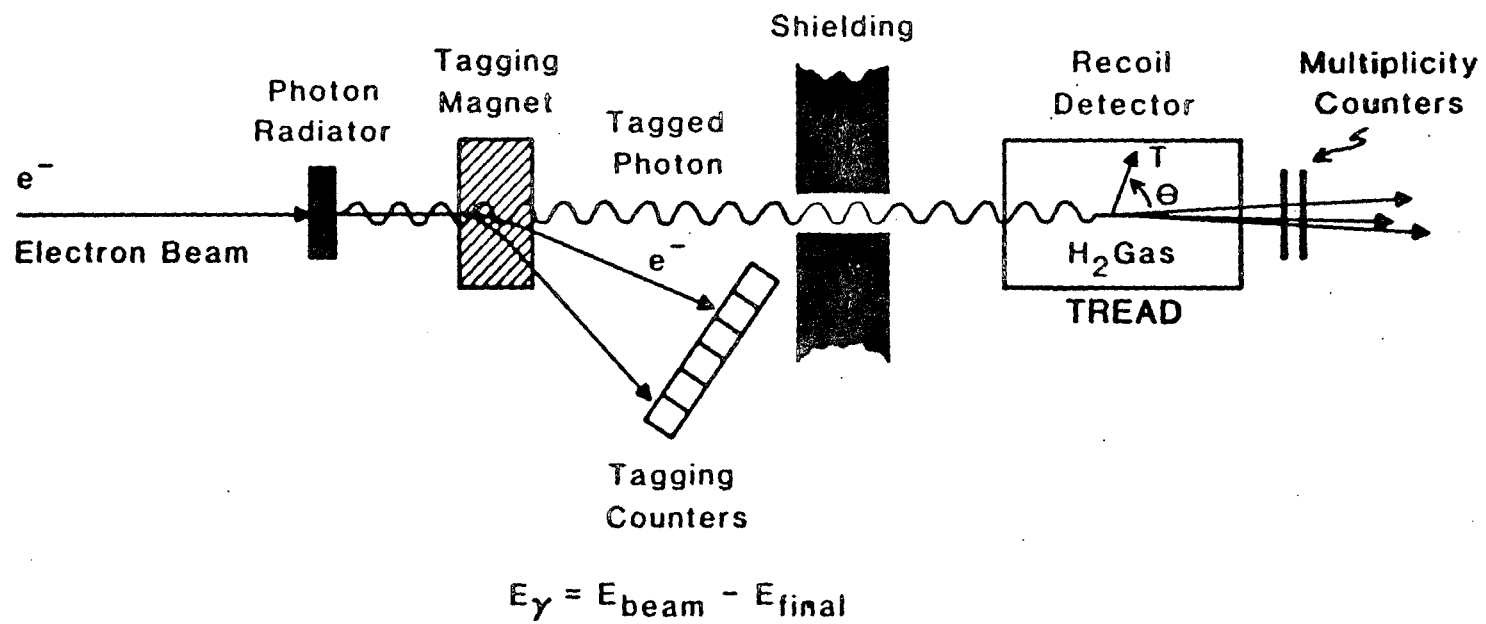


FIG. II.2

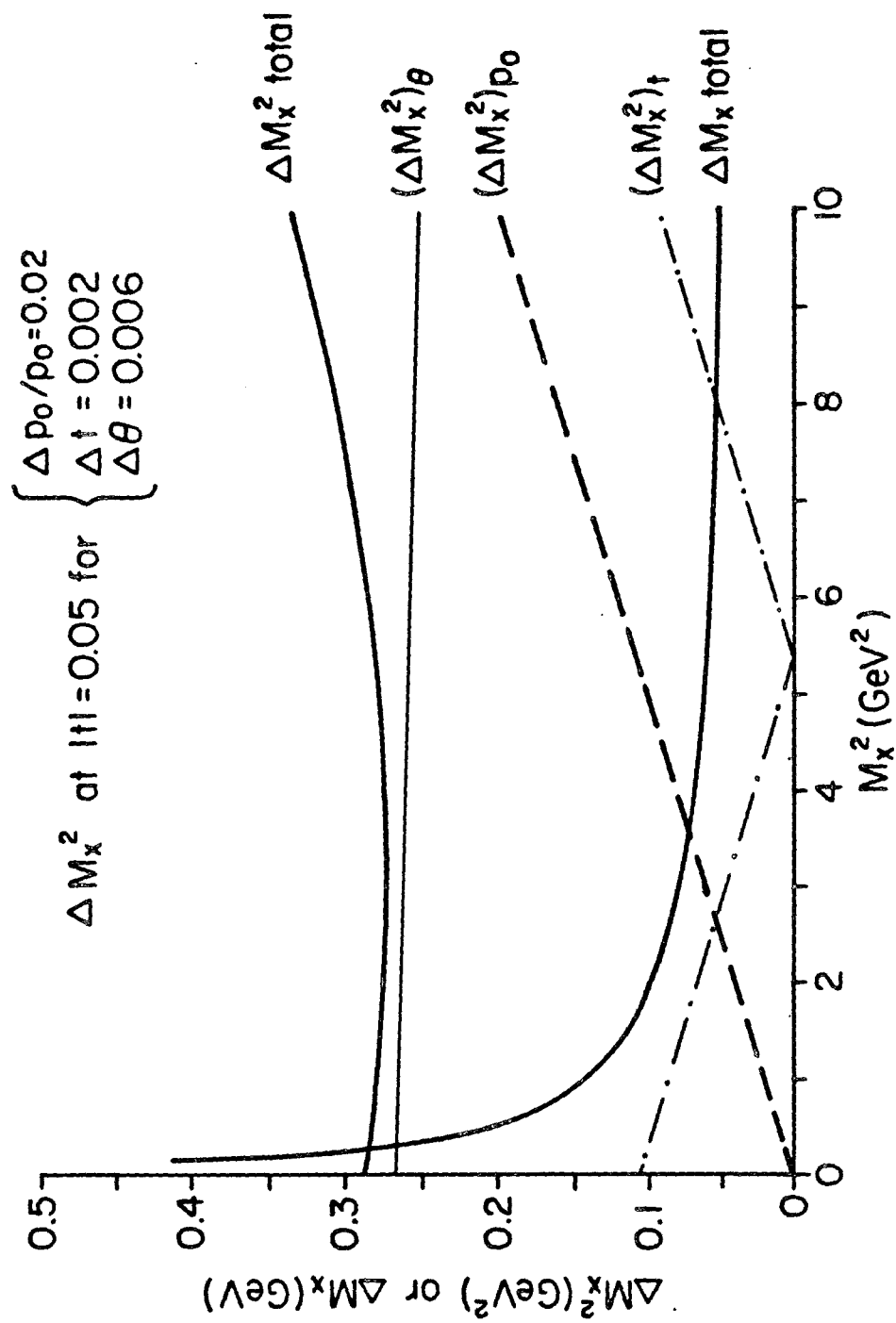


FIG. II.3 - Contributions to the mass resolution vs.  $M_x^2$



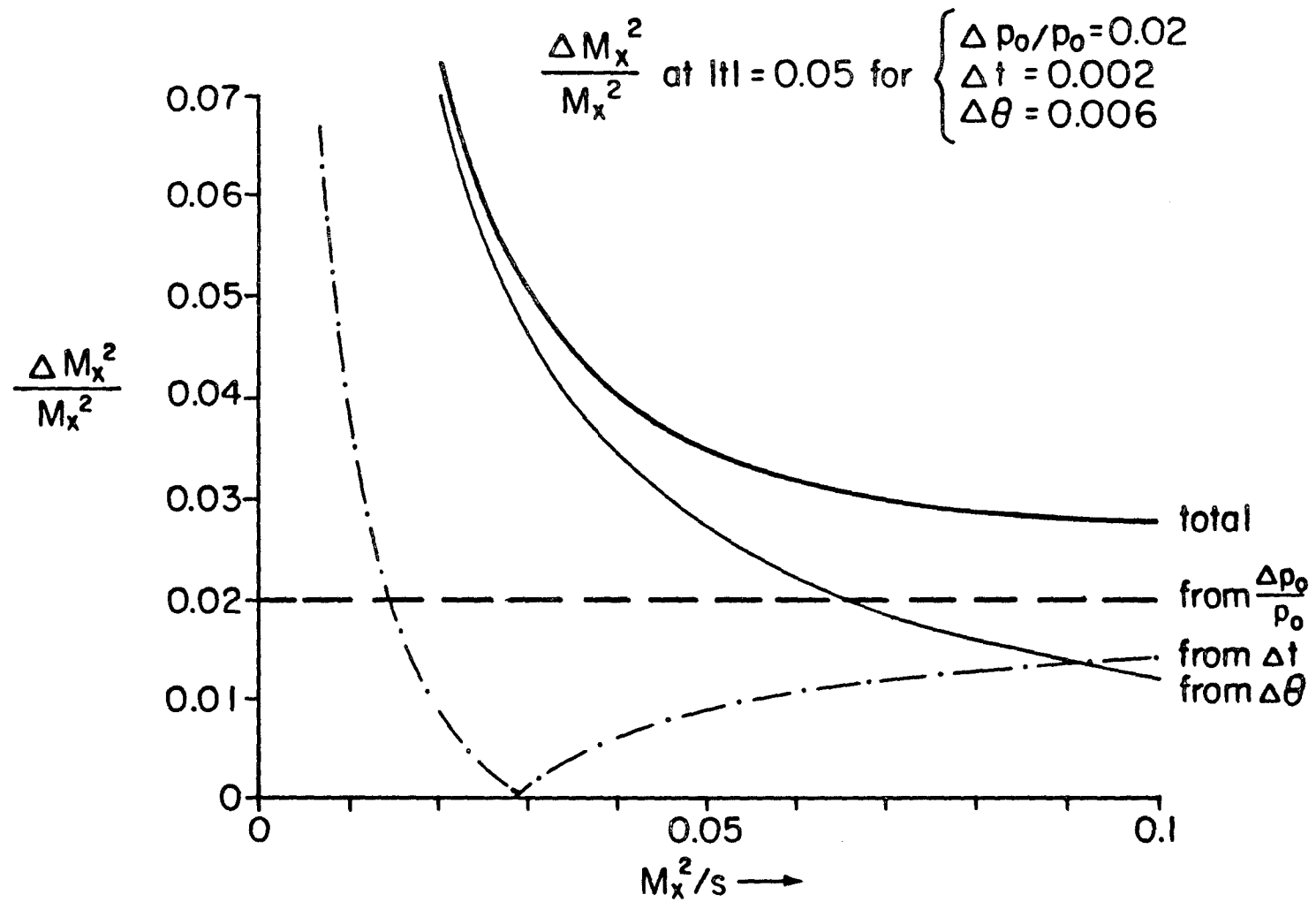


FIG. II.4 - Contributions to the fractional mass resolution vs.  $M_x^2/s$

### CHAPTER III. THE RECOIL SPECTROMETER, TREAD

In Chapter II, it was stated that the recoil spectrometer, TREAD (The Recoil Energy and Angle Detector), is used to measure the polar angle and kinetic energy of the recoil proton in the inclusive reaction

$$\gamma + p \rightarrow X + p$$

The aim of this chapter is to explain how the detector works and to present detailed documentation of its performance and its technical components. I proceed through three stages. Section III.A outlines the sequence of physical events in the observation and measurement of a typical photon-proton collision. Section III.B is devoted to the operational characteristics of the measurement techniques employed in TREAD, with particular emphasis on the TPC's. Section III.C focuses on the mechanical and electrical components of the TREAD vessel, their assembly, and engineering details.

#### III.A. OVERVIEW

Figure III.1 is a cutaway schematic diagram of the upstream cylindrical time projection chamber in the interior of the TREAD high pressure vessel. We see a tagged photon travelling along the axis of the cylinder, impinging on a molecule of hydrogen gas in the interaction region. It takes about 5 nanoseconds for a non-interacting photon to traverse the total 150 cm length of hydrogen target of both TPC's. We select for study collisions between the photon and a single proton in which the proton recoils and stops in one of the 1 1/8" thick plastic

scintillation counters in the surrounding counter bank. The light generated by the stopping proton in the counter is transmitted through a lucite light guide, not shown here, to a photomultiplier tube located outside the vessel, and the kinetic energy of the proton is inferred from the phototube output signal.

Behind each of the 16 pulse height counters in the counter bank is a 1/4" thick scintillation counter, called an anticounter or veto counter, separated optically from the pulse height counter by a thin sheet of black bakelite. The detection of a signal in an anticounter indicates that the proton has passed through the corresponding pulse height counter. As explained in Chapter VI, the calculation of the recoil kinetic energy from the light generated in the pulse height counter assumes that all the energy is deposited in the counter. We reject "punch through" events because the kinetic energy cannot be determined properly from this procedure.

The  $t$  range we measure in the experiment,  $0.02 < |t| < 0.11 \text{ (GeV/c)}^2$ , is determined by the counters. Taking into account the energy the proton loses by ionizing hydrogen atoms as it travels to the pulse height counter, the lower limit corresponds to a 10 MeV proton which has just enough energy to make it to the counter and generate a signal over the discriminator threshold in the fast logic system. Such a proton requires about 5 nanoseconds to cover the 22.9 cm distance from the interaction point to the counter surface. The upper limit in  $|t|$  corresponds to a 59 MeV proton which just ranges out in the pulse height counter before penetrating the anticounter. The time of flight for the highest energy proton in our  $|t|$  range is about 2.2 nanoseconds.

Figure III.2 depicts the events in the chamber after a collision and the measurement of the polar angle,  $\theta$ , of the recoil proton. Along its path from the collision point to the counter face, the proton creates a trail of electron-ion pairs. The total ionization consists of

pairs created in primary ionizing collisions and secondary pairs produced by energetic primary electrons. The number of pairs created per centimeter of track length varies, roughly, as the inverse of the proton's kinetic energy. Recoil protons in the middle of the  $t$  range create about 1500 ion pairs/cm in 15 atm of hydrogen gas. The ionized electrons then drift toward the aluminum ground plate in a 1.73 kV/cm electric field formed between the aluminum high voltage plate, elevated to a negative potential of -130 kV, and the ground plate. Not shown in the figure are two "cages" of coaxial field shaping rings, one located inside the counter bank and one located outside, which shape the electric field within the drift region to a uniformity of about 0.1%. In this uniform field, all parts of the ionized electron track drift with the same velocity, preserving the polar angle of the recoil proton with respect to the photon's incident direction.

The drift velocity of electrons in hydrogen is a function of  $E/N$ , the ratio of the electric field to the density of the gas. In 15 atm of hydrogen at room temperature, the 1.73 kV/cm field leads to a drift velocity of 0.39 cm/microsecond, giving a maximum drift time of 193 microseconds for tracks created near the high voltage plate. As the track reaches the ground plate, it projects itself on a set of concentric, octagonal, positive high voltage sense wires mounted on the plate.

Figure III.3 is a close-up view of the ionized electron track projecting itself on the ground plate and the sense wires. To orient the reader, imagine that a quadrant has been sliced from the circular plate and that it lies perpendicular to the page. The wavy line at right represents the photon direction with respect to which the recoil polar angle,  $\theta$ , is referred. Each sense wire is suspended at the center of a 1/4" groove machined on the face of the 1/2" thick aluminum plate. As the track of ionized electrons arrives, different segments are directed toward different sense wires along the electric field lines shown in the figure. Each sense wire attracts a segment whose length is

approximately equal to the 1/4" width of the groove. As electrons are accelerated in the extremely high field very near a given sense wire, avalanche multiplication occurs and a detectable signal is induced on the wire. The sense wires are AC coupled to preamplifiers located outside the high pressure vessel. The arrival times of the signals on each wire are recorded by a system of time-to-digital converters, and the polar angle is deduced from the wire time differences and a knowledge of the drift velocity. As shown in Chapter II, combining the measurement of  $\theta$  with measurements of the recoil kinetic energy and the incident photon's momentum, the mass,  $M_x$ , of the excited photon can be calculated.

In addition to the arrival times, the pulse heights of the signals on six of the eight sense wires are recorded by separate peak-detect/sample-and-hold circuits. The pulse height of the signal generated on a given wire is proportional to the number of electrons in the cluster focussed on the wire, and hence reflects the  $dE/dx$  of the original recoil proton. This information is combined with the measured recoil kinetic energy,  $T$ , to identify recoil particles as protons.

If the original photon does not collide with a proton in the upstream TPC, it has a chance to interact with a proton in the downstream TPC. The downstream chamber is an exact copy of the upstream chamber -- it has its own high voltage plate, scintillator bank, and sense wire/ground plate -- but it is mirror-reflected with respect to the upstream chamber. The two high voltage plates are back-to-back in the center of the TREAD vessel, so ionization tracks from recoil protons in the two chambers drift in opposite directions. Each 1/4" thick high voltage plate has rounded edges and a 6" diameter hole in the center to allow the photon beam and dissociation products created in the upstream chamber to pass into the downstream chamber. Each hole is covered with thin household aluminum foil for continuity of the high voltage potential, as shown in Figure III.2. The beam hole in the center of

each of the sense wire plates is similarly covered with aluminum foil to preserve the continuity of the ground potential.

Table III.1 summarizes the important performance parameters and physical dimensions of the TREAD apparatus.

Table III.1

Summary of TREAD Dimensions and Performance parameters

Length of H <sub>2</sub> Target	152.4 cm
Radial Distance to PH Counters	22.9 cm
Number of PH counters	16/half of TREAD
PH Counter Thickness	2.86 cm
Kinetic Energy Resolution	$\Delta T = 1 \text{ MeV}$
Anticounter Thickness	0.64 cm
Solid Angle Coverage	85% in azimuth
Maximum Drift Distance	76.2 cm
Drift Field High Voltage	-130 kV
Drift Field	1.73 kV/cm
Drift Velocity	0.39 cm/ $\mu$ sec
H <sub>2</sub> Pressure	15 atm
E/p	$0.79 \text{ kV m}^{-1} \text{ psia}^{-1}$
Number of Sense Wire Octagons	8 (16 halves)
Sense Wire Spacing	1.91 cm
Sense Wire Diameter	35 $\mu$ m
Sense Wire Voltage	6.7 kV for proton recoils 7.7 kV for cosmic rays
Sense Wire Gain at 6.7 kV	$\sim 150$
Typical Spatial Resolution in z	228 $\mu$ m
Polar Angle Resolution for Recoil Protons	$\sigma_{\theta} = 5.5 \text{ mrad}$
dE/dx Resolution	13.5%
Recoil Mass Resolution, $\Delta(M_r/M_p)$	15%
Time of Flight Resolution	1.5 nsec
Axial Magnetic Field	1 kGauss

### III.B. TREAD - THE TPC AND ITS PERFORMANCE CHARACTERISTICS

The remainder of this chapter, Sections III.B and III.C, will parallel the reference (Chapin et al., 1982) which is an instrumentation paper published in Nuclear Instruments and Methods by the physicists who participated in the design, construction, and initial testing of TREAD. The TPC performance characteristics depend critically on many design parameters, so Section III.B calls for more detailed description of mechanical components. Section III.C elaborates on mechanical assemblies and can be regarded as technical documentation of TREAD design.

Figure III.4 is a schematic diagram of TREAD's upstream TPC drawn to scale. Clearly visible are the inner and outer field shaping cages and, completely enclosed by the cage rings, the cylindrical drift region between the high voltage plate and the ground/sense wire plate. The cage rings and the high voltage plates are insulated from the wall of the steel vessel by a 1/2" thick  $\times$  72" long polyethylene tube. Two pulse height counters and two anticounters are shown with the lightpipes that feed through the upstream endcap. The two identical endcap assemblies are mounted on the flanges of a 26" i.d.  $\times$  84" long stainless steel tube. The scintillation counters and TPC's are supported mechanically from the endcaps. Structural supports are made of G-10 or aluminum. The vessel can be pressurized up to 240 psi with hydrogen. The photon beam enters through a 2" diam.  $\times$  0.030" thick hemispherical beryllium window. Non-interacting photons and decay products from interacting photons exit from TREAD through a 8" diam.  $\times$  0.080" thick hemispherical aluminum window mounted at the center of the downstream endcap.

A two-layer, water-cooled solenoidal magnet coil surrounds the vessel. This was designed to produce a 1 kG longitudinal magnetic field to confine Compton electrons of energy  $< 1$  MeV within the beam region and away from the sense wires. The flux lines are returned through the



endcaps and through a set of 16 iron bars that run the length of the vessel and are screwed to the vessel flanges. The phototubes on each endcap are protected from the fringe field of the magnet by a small correction coil located around the phototube region and by individual magnetic shields. Between the magnet and the vessel is an automatically controlled heating jacket which maintains a constant vessel temperature just above the ambient temperature of the magnet. A thermal insulation layer separates the heating jacket from the magnet coils. Details of the magnet's design, its performance, and the heating jacket appear in Section III.C.

A cross section of TREAD is shown in Figure III.5 . Each of the eight sense wire octagons is segmented into two independent halves, and the wire halves are arranged in a way that naturally partitions the chamber into eight azimuthal sectors. Associated with each wire sector is a pair of adjacent pulse height counters. A proton recoil that stops in one of the two counters in a given sector will deposit ionization over a combination of wire halves unique to that sector. This information is incorporated in the trigger in order to reduce background. The trigger and data acquisition system will be described in Chapter V.

The sense wires are stainless steel or nichrome of 35  $\mu\text{m}$  diameter. Gold-plated tungsten wires of the same diameter did not work as well. They usually broke down before reaching a useful operating voltage, presumably due to poor surface characteristics. The wires are supported in the grooves of the plate on 1/8" o.d. glass tubes that go through holes drilled in the plate. The ends of the pieces of glass tubing were flame polished to eliminate sharp points. The ends of the wire halves are brought through the glass posts to solder terminals on the other side of the plate. At those posts which are not terminals, the wires are guided around the corners under the heads of common straight pins which are inserted into the glass tubes and epoxied on the back. Each sense wire is strung with a tension of ~30 grams. Figure III.6 shows the

position of a sense wire in a groove and the electric field lines which result in a drift field of 1.75 kV/cm with 7 kV on the sense wire.

Electronegative impurities in the hydrogen gas, the most abundant of which is oxygen, absorb electrons and decrease their number as they drift toward the sense wires. Uniform efficiency for detecting tracks throughout the chamber requires the oxygen impurity level to be below 0.1 ppm. Other impurities from outgassing of the various materials inside the vessel must also be removed. For this reason, a closed loop system was built that circulates the hydrogen through a purifier. Details of the TREAD gas circulation and purification system appear in Section III.C .

The drift velocity and gain stability of the TPC's are monitored by  $^{244}\text{Cm}$   $\alpha$ -sources which create ionized electrons that drift onto the outer wire, 4A', of each sense wire plate. The ionization produced by the emitted 5.8 MeV  $\alpha$ -particles, which in 15 atm of  $\text{H}_2$  have a range of 1.2 cm, is about 1000 times that of minimum ionizing particles. This facilitates monitoring the TPC's even during start-up when the hydrogen may not yet be purified.

The sources are deposited on the tips of 0.020" diameter wires which are mounted on lucite holders. In each TPC, one such assembly is positioned 2" above the sense wire while another is placed 30" away, directly under the high voltage plate. The latter is viewed by a 1/8" diameter ZnS scintillation counter which serves to produce a zero-time reference for the measurement of the drift time. The details of this alpha source assembly are shown in Figure III.21 . The ratio of the pulse height on wire 4A' from the "far" source to that of the "near" source monitors the attenuation due to electron attachment. A quantitative measurement of pulse height attenuation was performed using the signals generated by cosmic rays passing through different parts of the chamber. We estimate that the pulse height attenuation as a function of drift time is characterized by a time constant of 1.8

milliseconds. This implies an attenuation of about 10% for a recoil track drifting the entire 30" drift region.

Figure III.5 also shows a cross sectional view of the pulse height counters and anticounters. The pulse height counters are 30" long  $\times$  1 1/8" thick and have a trapezoidal cross section with parallel sides of 3" and 3 3/8". The anticounters are 30.5" long  $\times$  3.5" wide  $\times$  1/4" thick. All counters are made of NE110 plastic scintillator. An encapsulated 1/2" diameter  $\times$  1/4" long  $\alpha$ -source of  $^{241}\text{Am}$  adjacent to a NaI crystal (Model LP-241, Isotope Products Laboratories, Berkeley, CA) is glued at the far end of each pulse height counter facing the phototube. These sources are used as constant output light pulsers for monitoring the gain stability of the counters. Counter calibration is discussed in Chapter VI.B.

#### III.B.1 Sense Wire Gain

The sense wire gain in hydrogen was measured, prior to building TREAD, in a simple proportional counter consisting of an anode wire stretched along the axis of an 0.5" i.d. aluminum cylinder. Two parallel "flats" milled on the cylinder wall provided thin windows to allow triggering on minimum ionizing electrons from a  $\beta$ -source. Measurements were carried out with 20  $\mu\text{m}$  and 50  $\mu\text{m}$  diameter sense wires at pressures from 5 to 15 atm.

The sense wire gain,  $G$ , can be calculated from the expression (Townsend, 1902)

$$\ln G = \int_{r_1}^{r_2} \alpha(r) dr \quad (\text{III.1})$$

where  $\alpha$ , the inverse of the electron mean free path for ionization (first Townsend coefficient), is a function of the pressure  $p$  and of the reduced electric field strength,  $E(r)/p$ . The integral is evaluated along the path of the electric field lines from the surface of the anode to that of the cathode.

Hydrogen ionization coefficients,  $\alpha/p$ , have been measured (Rose, 1956) in the region  $0.5 < p < 45$  Torr and  $15 < E/p < 1000$   $\text{V}\cdot\text{cm}^{-1}\cdot\text{Torr}^{-1}$ . Rose's data are represented well by the simple formula

$$\alpha/p = a \exp(-bp/E) \quad (\text{III.2})$$

where  $a = 5.1 \text{ cm}^{-1}\cdot\text{Torr}^{-1}$  and  $b = 138.8 \pm 0.4 \text{ V}\cdot\text{cm}^{-1}\cdot\text{Torr}^{-1}$ . Our measurements of gain in the region  $5 < p < 15$  atm and  $E/p < 90$   $\text{V}\cdot\text{cm}^{-1}\cdot\text{Torr}^{-1}$  are in good agreement with values calculated from Equation (III.1) using  $\alpha/p$  given by Equation (III.2). This is shown in Figure III.7 where our data on sense wire voltage versus pressure at fixed gain are compared with the calculated curves.

The maximum gain just before electrical breakdown was found to be in the range  $(2-5) \times 10^4$ , approximately independent of pressure or sense wire diameter. In Figure III.8, breakdown voltages at various pressures measured with the 35  $\mu\text{m}$  diameter wires of TREAD are compared with constant gain curves calculated from Equations (III.1) and (III.2). These results show that, for our configuration and within our pressure range, the maximum obtainable gain is approximately constant and equal to a few  $\times 10^4$ .

While recording recoil proton data with 15 atm of hydrogen, the sense wire voltage was 6.7 kV yielding a gain of about 150. At this gain, the sense wire signals from minimum ionizing recoils were below the thresholds of triggering discriminators. This helped to reduce

background triggers. Triggers from minimum ionizing cosmic rays were used in calibration runs during which the sense wire voltages were increased to 7.7 kV.

### III.B.2 Drift Velocity

The drift velocity of electrons in hydrogen gas does not saturate as it does in other drift chamber gas mixtures; that is, no plateau appears in a plot of the drift velocity versus the ratio  $E/N$ . Using the time projection technique with hydrogen in TREAD requires that  $E/N$  be both uniform throughout the drift region and stable over time. Uniformity of about 0.01% and stability of about 0.1% are required to obtain a resolution in the measurement of the recoil polar angle of a few milliradians.

The uniformity of the electric field between the high voltage plate and the sense wire plate is established by the two cages of field shaping metal rings. The outer cage, located outside the scintillation counters, consists of 48 rings made of 1/8" diameter copper wire connected by a chain of 100 megaohm metal film resistors. The thickness of the wire was chosen to prevent corona discharge. The 1% resistors were specially made by Victoreen, Inc., Cleveland, Ohio, with a solid core and 1/8" diameter tinned copper leads, also to prevent corona. The spacing between the centers of the rings is 5/8" , and they are held in place by resting in slots machined in the G-10 supports that form the "stalls" for the scintillation counters, as shown in Figure III.5 .

The rings were shaped into circles on a special jig. The ends of each ring slip into a 3" piece of 1/8" i.d. and 1/4" o.d. copper tubing and are soldered in place. The leads on the resistors fit into holes drilled in these pieces of tubing and are cemented in place with conducting epoxy. The 1/4" thick high voltage plate screws onto a G-10 ring that fixes the positions of the G-10 support stalls. Calculations

show that this configuration yields an electric field over the region of the sense wires such that the percentage longitudinal modulation and the percentage radial component are many orders of magnitude smaller than our 0.01% goal for uniformity.

During the testing of TREAD at high drift voltages, we found that the electric field between the outer cage and the vessel wall (about 50 kV/cm) permanently altered the values of the 100 megaohm resistors by as much as 13% . Special conducting guards connected to one of the leads of each resistor were installed to reduce the electric field at the resistor. This problem and the concern that an electrostatic charge buildup on the scintillation counters could distort the drift field led to the addition of the inner field-shaping cage.

Since the inner cage sits in the uniform field formed by the outer rings, corona discharge was not a problem, and therefore thin wire could be used for its construction. Each inner cage consists of 96 rings of 0.002" diameter Cu-Be wire connected to a bleeder chain made of  $2 \times 22$  megaohm 1 W carbon resistors per stage. Each cage was hand-wound using the tension from a hanging weight. The rings are positioned in slots cut in the G-10 rods that support the cage. The ends of each ring are soldered to brass pins embedded in one of the G-10 rods. These pins also serve as sockets for the resistors between adjacent rings.

The stability of the electric field over time is governed by the high voltage power supply which creates the field. We use a commercial 200 kV, 0.5 milliamp power supply, Model RHR-200N100, manufactured by Spellman High Voltage Electronics Corporation, Plainview, New York. This supply has 0.01% voltage regulation, 0.05% stability over eight hours, and 0.02% ripple at 40 kHz. A 60 megaohm resistor in series with the 60 foot long RG19 high voltage cable provides a filter for the ripple. The power supply, the feedthrough of the RG19 cable into the vessel, and the connection to the high voltage plates are described in detail in Section III.C.

The uniformity and stability of the gas density,  $N$ , depends on the gas temperature and pressure. The temperature is held constant and uniform by the heating jacket around the vessel. The heating jacket controller responds to six thermocouples in contact with the surface of the vessel and compensates for room temperature changes and temperature fluctuations in the magnet cooling water. An internal thermometer monitors the gas temperature, and the temperature is recorded after every spill during data taking. The temperature stability can be estimated by histogramming the average recorded temperature for all of the photon and pion runs during 1982. The result is a symmetric distribution with a mean of  $298.8^\circ\text{K}$  ( $78.2^\circ\text{F}$ ) and an rms deviation of  $1.8^\circ\text{K}$  ( $3.2^\circ\text{F}$ ), so the temperature is stable to 0.6%.

A pressure transducer continuously monitors the gas pressure and automatically activates input and exhaust valves to keep the pressure within preset limits. In practice, the pressure is kept within 0.01 psi of the low preset limit by allowing the gas to leak at a slow constant rate.

The drift velocity in hydrogen was measured in TREAD using the  $\alpha$ -source monitors. Our data at pressures from 24 to 220 psi are shown in Figure III.9 along with other measurements (Lowke, 1963) performed at lower pressures. The drift velocity is plotted as a function of  $E/p$ , the ratio of the drift field to the hydrogen gas pressure. The line through the data points in the region  $0.3 < E/p < 3$   $\text{kV} \cdot \text{m}^{-1} \cdot \text{psia}^{-1}$  represents a fit to the form

$$v_D = v_0 (E/p)^{b + c \ln(E/p)} \quad (\text{III.3})$$

which parameterizes the drift velocity around  $E/p = 1 \text{ kV} \cdot \text{m}^{-1} \cdot \text{psia}^{-1}$ , close to our normal operating conditions. We find  $v_0 = (4.82 \pm 0.10) \text{ mm}/\mu\text{s}$ ,  $b = 0.6$ , and  $c = -0.1$ . The error in  $v_0$  is

the variance obtained among data sets at different pressures. Our results show that density corrections to the drift velocity (Huxley and Crompton, 1974) in the pressure range  $24 < p < 220$  psi are  $\leq 2\%$ .

### III.B.3 Spatial Resolution and Angular Resolution

The spatial resolution in  $z$  was measured using tracks from cosmic rays passing through diagonally opposite pulse height counters. As can be seen from Figure III.5, such cosmic ray tracks deposit ionization on all 16 sense wire halves. In order to simulate the fits to proton recoil tracks, cosmic ray tracks were treated as back-to-back recoil tracks, and the sense wire times from each cosmic ray half-track were fit independently to a straight line. The spatial resolution for a particular wire was obtained by measuring the difference of the  $z$  position recorded by the wire from the position predicted by the fit to the other wires.

As described in Chapter V, cosmic ray events were collected in special calibration runs. In order to make the sense wires efficient for minimum ionizing signals, the cosmic ray runs were taken with high voltage of 7.7 kV on the wires, in contrast to the 6.7 kV used for recoil proton data. The resulting large signals on the outer wire 4A' from the alpha source monitors required wires 4A' and 4B' to be disconnected during the cosmic ray runs. Therefore, only seven wires could be used in the fit for each half of a cosmic ray track. The track-fitting routine is described in Chapter VI.C. The spatial resolution results presented in this section are derived from cosmic ray tracks which passed through the TPC approximately perpendicular to the  $z$  axis. This minimizes (small) resolution effects which arise for tracks at larger angles.

Figure III.10 shows a pulse height spectrum from wire 3A (upstream) for cosmic ray tracks distributed through the entire 75 cm long drift space. The curve is a Landau distribution fit to the data.



Figure III.11 shows the residuals,  $z(\text{meas}) - z(\text{fit})$ , of wire 3A (upstream), also obtained for tracks distributed through the entire drift distance. The fitting routine used to determine the  $z(\text{fit})$  value does not include the  $z(\text{meas})$  value for wire 3A in the fit. A Gaussian fit to the distribution has a width of  $\pm 213 \mu\text{m}$ . Variations in the spatial resolution exist from wire to wire. Averaging the measured widths of the residual distributions obtained for the 14 wires (28 halves) used for cosmic rays yields  $228 \pm 40 \mu\text{m}$ ; this is the average spatial resolution in the chamber. Similar variations in spatial resolution also exist along the length of a particular wire. This variation can be seen by preparing histograms similar to Figure III.11 according to which azimuthal counter sector had the cosmic ray trigger.

Figure III.12 shows the spatial resolution as a function of drift distance, averaging over all wires. Each point represents the width of a Gaussian fit to the residual distribution for all wires for cosmic ray tracks originating from a particular bin in  $z$ . The left hand ordinate is  $\sigma_z^2$  and the right hand ordinate is  $\sigma_z$ . Comparing Figures III.11 and III.12, the width in Figure III.11 is consistent with what one expects for tracks drifting on the average through one half of the 75 cm long drift space.

The line in Figure III.12 is a fit to the form

$$\sigma_z^2 = \sigma_0^2 + \sigma_1^2 (z/1\text{cm}) \quad (\text{III.4})$$

We find  $\sigma_0 = (128 \pm 7) \mu\text{m}$  and  $\sigma_1 = (33 \pm 1) \mu\text{m}$ . The term proportional to  $z$  is due to the diffusion of the electron clusters as they drift toward the sense wire plate. The value we obtain for  $\sigma_1$  is of the order we expect from known transport coefficients in hydrogen (Wagner et al., 1967). The diffusion width along the drift direction is  $\sigma_D^2 = (68 \mu\text{m})^2 (z/1\text{cm})$ . Our effective sense wire discriminator threshold for cosmic ray data is 12 drift electrons, and the statistical fluctuations in the arrival time of this number of electrons relative to the mean should lead to

$\sigma_1 = 30\% \times \sigma_D = 21\mu\text{m}$ . The intercept  $\sigma_0$  reflects the ultimate spatial resolution obtainable with the TPC. This intrinsic resolution is limited, among other factors, by the original spatial size of the ionization trail which is focussed on the sense wires (this is a small effect) and systematic distortions of the electric field near the sense wires due to the octagonal geometry.

The expected angular resolution for each half of a cosmic ray track can be calculated from the measured spatial resolution in the following manner. If the spatial coordinates determined by the arrival times at the sense wires are fit to a straight line, the angle of the track is the slope of that line. The uncertainty in the slope parameter depends on the uncertainty in the individual spatial points. Assuming for simplicity the same uncertainty,  $\sigma_z$ , for each of  $n$  points, the resulting angular uncertainty is given by

$$\sigma_{\theta\text{pred}} = \frac{2\sqrt{3} \sigma_z}{w} \sqrt{\frac{1}{n(n^2-1)}} \quad (\text{III.5})$$

where  $w$  is the  $3/4"$  spacing between the sense wires. A convenient rule of thumb is that, for seven wire fits to cosmic ray half tracks, a  $100 \mu\text{m}$  spatial resolution gives rise to a  $100 \text{ mrad}$  angular resolution. Taking the value for  $\sigma_z$  at  $z = 37.5 \text{ cm}$  in Figure III.12, we expect an angular resolution  $\sigma_{\theta\text{pred}} = 2.35 \text{ mrad}$  for tracks originating in the center of the chamber. We measure the angular resolution,  $\sigma_{\theta\text{meas}}$ , directly by comparing the angle,  $\theta_1$ , of the fit on one half of each cosmic ray track to the angle,  $\theta_2$ , of the fit on the other half. The width of the difference distribution,  $\Delta\theta = \theta_1 - \theta_2$ , has equal contributions from  $\theta_1$  and  $\theta_2$  :

$$\sigma_{\Delta\theta}^2 = \sigma_{\theta_1}^2 + \sigma_{\theta_2}^2 = 2\sigma_{\theta\text{meas}}^2 \quad (\text{III.6})$$

So  $\sigma_{\theta\text{meas}}$  is derived from the measured width  $\sigma_{\Delta\theta}$  of the difference distribution. Figure III.13 shows the angular resolution  $\sigma_{\theta\text{meas}}$  and

$\sigma_{\Theta\text{meas}}^2$ , determined in this manner, as a function of drift distance. For a track drifting from the middle of the chamber, the measured resolution is 3.35 mrad. The figure also shows the angular resolution  $\sigma_{\Theta\text{pred}}$  predicted from the spatial resolution shown in Figure III.12. The discrepancy between the measured and predicted angular resolutions stems from distortions of the tracks as they drift toward the sense wire plate. A measure of these distortions can be obtained by defining a systematic error contribution to the angular resolution of a half cosmic track in terms of the measured angular resolution and that predicted from residuals:

$$\sigma_{\Theta\text{syst}}^2 = \sigma_{\Theta\text{meas}}^2 - \sigma_{\Theta\text{pred}}^2 \quad (\text{III.7})$$

At the center of the chamber, a systematic angular uncertainty  $\sigma_{\Theta\text{syst}} = 2.39$  mrad must be added in quadrature to the  $\sigma_{\Theta\text{pred}} = 2.35$  mrad predicted from residuals to account for the 3.35 mrad measured resolution.

One can visualize the track distortions through Figure III.14 which displays the centers of the  $\Delta\theta = \theta_1 - \theta_2$  distributions as a function of the drift distance. The farther a cosmic ray is from the sense wire plate the more the fits to the two half tracks are "kinked" with respect to each other. Before fitting the tracks which enter into the distributions for this figure, as well as Figures III.11 to III.13, zero-time offsets were subtracted from the measured wire times which optimized the results only for the first bin in  $z$ .

Adjusting zero-time offsets for tracks originating in a given  $z$  bin or counter sector permits flexibility in track fitting and optimization of results in the following two senses. First, the offsets for wires in half tracks can be adjusted relative to one another so that the residual distributions for straight line fits are centered on zero. This procedure artificially removes systematic distortions from half tracks, or rather, absorbs the curvature into the offsets. Second, the

offsets can be adjusted to tilt a "straightened" half track to match the angle of the other half and remove the kink.

One could, in principle, map the track distortions in the TPC's by studying cosmic rays divided in many z bins and according to azimuthal sector. One could then improve the recoiled proton angular resolution by applying corrections to measured tracks with z-dependent and counter-dependent wire offsets. Our limited cosmic ray statistics does not permit a fine segmentation of the chamber for this purpose, but a course segmentation allowed by the existing cosmic ray data indicates that such mapping of the distortions in the chamber is possible.

Specifically, the cosmic ray data in each half of TREAD was divided into five bins in z, and counter-by-counter offset optimization was performed for the three bins closest to the sense wire plates. When plots corresponding to Figures III.12 to III.14 are prepared using these offsets, the following improvements result. First, the slope of  $\sigma^2$  vs. z becomes less steep ( $\sigma_1 = 28\mu\text{m}$  in Equation III.4) in closer agreement with the calculation from electron diffusion. Second, measured and predicted angular resolutions of 2.70 and 2.18 mrad, respectively, in the center of the chamber agree more closely with each other, and this calls for a  $\sigma_{\text{syst}}$  of only 1.58 mrad. Third, the kink angle  $\Delta\theta$  throughout the chamber is less than 1 mrad.

The most important conclusion from these studies is that by using chamber calibrations which depend on the z position, the angular resolution can be improved by at least 0.81 mrad ( $\sigma_{\text{syst}} = 1.58$  mrad instead of 2.39 mrad) for tracks originating in the center of the chamber.

### III.C. TREAD - APPARATUS DETAILS

The presentation of the mechanical details of the TREAD apparatus in this section starts with the high pressure vessel and proceeds outward.

#### III.C.1 High Pressure Vessel

The vessel was designed to withstand a pressure of 20 atm with a safety factor of at least four. Its 84" long by 26" i.d. cylindrical shell was cold-rolled from 1/2" thick Type 304 stainless steel. The 3" thick flanges were welded on the cylinder and are also made of 304 stainless steel. The 36" diameter by 2 1/2" thick endcaps are made of Type A515 carbon steel - a magnetic steel which provides a return path for the solenoidal magnetic field. The endcaps were plated with a 0.002" thick layer of nickel to prevent rusting. After the nickel plating, the endcaps were heated to 375°F for four hours to bake out trapped hydrogen which could cause "hydrogen embrittlement" (see TREAD Safety, III.C.8). The polyethylene insulator was cast inside the vessel and shrank upon cooling to an outer diameter about 3/8" less than the 26" i.d. of the vessel. The insulator is centered inside the vessel by resting on a 1/4" thick strip of aluminum which runs the length of the vessel.

#### III.C.2 Heating Jacket for Stable Vessel Temperature

Between the high pressure vessel and the solenoidal magnet coils is the automatically-controlled heating jacket. The heating jacket maintains the vessel, and hence the gas inside, at a constant, uniform temperature by compensating for fluctuations in the surrounding magnet's temperature. It was known that the cooling water supplied to the coils could vary in temperature by as much as 30°F depending on season and

usage. Actual variations in the magnet's temperature were much less than this. In practice, maintaining the vessel temperature about 5°F above the nominal temperature of the magnet made the vessel immune to shorter-term fluctuations.

The heating jacket consists of 12 separate resistive heating strips placed parallel to the axis of the cylinder. The strips are positioned between 1" wide  $\times$  3/4" high  $\times$  78" long G-10 spacer bars that form a cage around which the magnet coils are wound. In each heating strip, two resistive lines dissipate heat across a 6" wide aluminum fin. The heating strip material is manufactured by the Chemelex Division of the Raychem Corporation. Its output capacity is 60 Watts/ft at room temperature, which yields a total capacity of about 5 kWatts for the heating jacket. The high pressure vessel is wrapped with a layer of 3M Brand 1312 glass tape to isolate it electrically from the heating jacket. Six thermocouples, placed in a symmetric configuration between the vessel and the heating jacket, allow the vessel temperature to be read locally by the heating jacket controller. Thermal insulating strips made of non-flammable ceramic fiber lie between the heating strips and the surrounding magnet coils.

The power supply (208 VAC 3 $\phi$  , 10A per phase) and controls for the heating jacket are located in a unit which sits behind the gas circulation system on top of the frame for TREAD. The six thermocouples are connected to a scanner manufactured by the Gil Instruments Company. The scanner transmits the value of the lowest-reading thermocouple to a proportional power controller, Payne Model 18E-4-70, where it is compared to a preset reference temperature. The power controller regulates the output voltage of the power supply to all the heating strips to maintain equilibrium. The heating strips are connected in parallel, so the power supply can deliver up to 208 VAC to each strip.

During the experiment, the heating jacket was set to 80°F . Over three months, the internal thermometer measured the gas temperature to have a mean of 78.2°F with an rms deviation of 3.2°F .

### III.C.3 Solenoidal Magnet

The purpose of the solenoidal magnet is to confine low energy Compton electrons within the beam region and away from the active area of the TPC. A photon beam with intensity  $10^6/\text{sec}$  produces about  $3 \times 10^4$  Compton electrons/sec in the energy range 1/2 to 1 MeV in TREAD. The 1 kG longitudinal field curls these electrons into spirals of radii  $< 1/2"$ . The effect of this field on the path of recoil protons is negligible.

The solenoidal magnet consists of two layers of coils with 150 turns of conductor each. The conductor is 0.46"  $\times$  0.46" copper with a 0.25" diameter circular hole for the cooling water. The bottom coil has an inner diameter of 28.5", the top coil 29.5". The coils cover the 78" length of the vessel between the 3" thick end flanges. The coils can be seen in the TREAD schematic, Figure III.4 .

The magnet coils were wound around the TREAD vessel at Fermilab's Magnet Facility. The heating jacket and the G-10 support cage were placed on the vessel first. Then, rotating on a horizontal winding machine, the vessel wound the conductor around itself while a tensioner pulled the conductor taut. Electrical insulating tape (3M Type 1312) was wrapped around the conductor strand as it went onto the vessel. The bottom coil was wound from the downstream end of TREAD to the upstream end, then the top coil continued from upstream back to downstream. This allows the coils to be powered in series with the power connections at one end of the vessel. At the TPL, an adjustable 240 kWatt power supply delivers 500 amps to the magnet, yielding a voltage drop of 60 V and a central magnetic field of about 1 kGauss. The magnet dissipates 30 kWatts at 500 amps.

Sixteen iron bars return the magnetic flux lines between the endcaps. Each bar is 1.25" thick  $\times$  2.5" wide  $\times$  89" long. The bars are fastened to the flanges of the main vessel with a screw at each end and are placed symmetrically around the cylinder.

The cooling water circuitry was configured to minimize temperature gradients along the length of the vessel. Each coil is divided into 10 separate water circuits of 15 turns each, and the water flows in parallel through these circuits. Specially designed tees provide electrical continuity but allow for water connections. In a given coil (top or bottom), the direction of the water flow alternates from one circuit to the next, and if the flow is in one direction in a bottom circuit, it is in the opposite direction in the corresponding top circuit. Near the bottom of the vessel, two 1.5" i.d. brass pipes serve as input and output manifolds for the cooling water. Rubber hose segments carry the water from the manifolds to the magnet coils. Under steady-state conditions, a magnet current of 500 amps and a cooling water flow rate of 17 gallons/minute ( = 2.27 cubic ft/minute) yield a cooling water temperature rise of 14°F and, hence, an overall magnet temperature rise of about 7°F. An input pressure of 60 psi gives rise to the 17 gal/min flow rate and a pressure drop of about 25 psi between the manifolds.

As a safety precaution, Klixon Thermal Switches were placed in contact with the magnet coils and the power connections at various points. Klixons are normally-closed below 175°F and open when exposed to temperatures above that value. They are interlocked to the magnet's power supply and disable the power in the event the magnet overheats due to loss of cooling water flow.

Measurements of the magnetic field characteristics were made at an early stage in the assembly of the TREAD vessel. A Bell Model 620 Portable Gaussmeter with a calibrated SAK4-1808 Axial Hall Probe was used to measure the axial field inside the vessel and the fringe field



outside the endcaps, and to determine the effectiveness of the phototube magnetic shields. Some of the results are presented here. Figure III.15 shows the axial component of the field measured along the central axis of TREAD for two values of the field current: 500 Amps and 750 Amps. Both sets of measurements were taken at the downstream end of TREAD. The measurements at 500 Amps were made with an 11" diameter  $\times$  18" long iron tube mounted on the endcap and the 8" diameter endcap hole open. The measurements at 750 Amps were made without the tube, but with the 8" endcap hole covered by a 11" diameter A516 steel plate with a 3" diameter central hole. The field is approximately constant and almost entirely longitudinal throughout the TPC drift regions, although a 4-5% radial component exists near the sense wire plates. This is due to the fact that the 3" thick vessel flanges prohibit the magnet coils from extending all the way to the endcaps.

Figure III.16 shows the axial component of the fringe field which leaks through an anticounter hole, at a radius of 12.125" on the endcap, into the vicinity of the corresponding phototube. The measurements were made with the axial Hall probe pointing at the center of a 1.125" diameter anticounter hole, with and without a 2" diameter  $\times$  6" long phototube magnetic shield in place. As indicated by the "shield-off" dotted curve, about 15 Gauss, or 1.5% of the 1 kGauss central field, is present in the anticounter phototube region. Other measurements show that this fringe field is approximately uniform across the entire face of the endcap. In fact, the return path for the field lines provided by the endcaps and return bars saturates at about 1 kGauss, as the leakage field increases more rapidly than the central field above 1 kGauss. This can be seen, for example, by comparing the 1 kG and 1.5 kG "shield-on" measurements in Figure III.16 .

Figure III.16 also shows that the 15 Gauss fringe field can be reduced to 0.3 Gauss at the center of a 6" long magnetic shield or to 0.2 Gauss at the center of an 8" shield. 8" long shields were chosen to protect the phototubes of both the pulse height counters and

anticounters. The light pipes extend into the phototube shields so that the light pipe/photocathode interfaces are positioned in the minimum axial field within the shields. The effect of the leakage field on phototube pulse heights was measured by comparing magnet-on and magnet-off calibration runs using longitudinal muons. The magnetic shields were in place. A 1 kG central field causes gain shifts of up to about 5%, although the effect is not in the same direction for every counter.

To provide the flexibility of zeroing the field inside the shields independently from the magnet, the correction coils, described below, were introduced.

#### III.C.4 Correction Coils

The measurements of the field characteristics described in the preceeding section, in particular the saturation of the return path above 1 kGauss and the large leakage field, called for the introduction of the correction coils. Two correction coils were made to enclose phototubes in an adjustable field to cancel the leakage field from the main solenoid. The coils are entirely enclosed by the inerting hoods. Each coil is wound on a 28" diameter  $\times$  8" long aluminum spool which is supported on legs that screw into the endcap. Each coil has 90 turns of AWG 12 (0.081" dia.) copper magnet wire with a 0.004" thick insulating film of polyurethane nylon. Hall probe measurements show that an axial correction field of about 25 Gauss is created in the vicinity of the phototubes when 9.5 amps flow in a given coil, in which case the coil dissipates 95 watts of power with a voltage drop of 10 V across the coil. At the TPL, the two correction coils are powered in parallel by a Hewlett Packard 12 VDC supply. With a 1 kGauss central field, the leakage field inside the phototube magnetic shields can be zeroed to within 0.1 Gauss by running the correction coils at 10.8 volts (11.8 volts at the supply). These were the magnet running conditions for the all of the data collected in 1982.

### III.C.5 External Parts to the Main Vessel

The structural support for the TREAD vessel was designed for ease and flexibility of movement and positioning. TREAD can be rotated about a vertical axis as well as rolled along or transverse to the beam direction. As shown in Figure III.17, the cylindrical vessel is mounted in a rectangular iron frame. The gas circulation system and heating jacket power controller rest on top of this frame. The iron return bars for the magnetic field are clearly visible in the Figure. The frame sits on a large track bearing, which allows the vessel to rotate. The track bearing is secured to a double cart assembly which permits motion in two directions. The top cart rolls transverse to the beam direction, and the bottom cart rolls parallel to the beam direction on rails on the TPL floor.

Also shown in Figure III.17 is the "mini-crane" which is used to extract the endcaps and the TPC's from the vessel. The mini-crane can be mounted on top of either end of the rectangular frame. The endcap is then attached to a wheeled trolley that rolls in a Unistrut track on the bottom of the crane.

Should a window rupture while TREAD is filled with gas at high pressure, the vessel would recoil against the explosion. To guard against the damage this could cause, the rectangular frame of TREAD is secured to the TPL floor with four steel "tie-down" rods. They are required to be attached whenever TREAD is pressurized.

### III.C.6 Endcap Details

#### a) Beryllium Entrance Window

Beryllium was chosen for the entrance window because of its strength and its long radiation length compared to other metals. The window is a hemisphere, 2" diameter  $\times$  0.030" thick, with a 1/2" thick flange to facilitate mounting. A cross section of the window is shown in the mounting diagram, Figure III.25, which is discussed later. The hemispherical design allows a given structural safety factor to be achieved with minimum thickness. The window allows photons to pass into the interaction region with relative ease. The 0.030" thickness of Be is 0.2% of a radiation length. The hydrogen target itself (150 cm at 15 atm) represents 0.32% of a radiation length. The mounting of the beryllium window on the vessel is described in Section III.C.8.

The window was progressively machined from a single block of Type S-65 beryllium alloy at the Speedring Corporation in Cullman, Alabama. Because of the brittleness of beryllium, any tool bit creates 0.001-0.002" deep microcracks which could propagate under stress. To avoid this problem, the window was "etched" in a room temperature solution of sulphuric acid, chromic acid, and water. In this process, the piece is submerged in the solution until a desired thickness is dissolved from the surface. In our case, approximately 0.004" was removed from the window surface after the final tooling. Two beryllium windows were manufactured, one to serve as a spare.

#### b) Aluminum Exit Window

A thin rear window allows the decay products of interacting photons to pass out of TREAD to the multiplicity counters and, perhaps in a future experiment, to a downstream momentum-analyzing spectrometer. A thin window also allows non-interacting photons to pass to the target

of any experiment mounted downstream of TREAD. A diameter larger than that of the Be entrance window is required to allow for the transverse momentum of the decay products.

Similar to the Be entrance window, the exit window is a hemisphere, 8" diameter  $\times$  0.080" thick, with a 1.5" thick flange for mounting, as shown in Figure III.18. It is made of Alcad 2024-T3 aluminum and was progressively machined from a single block of material at the Walco Tool and Engineering Co., Lockport, Ill. One spare window was also made. The window covers an 8" diameter hole in the center of the downstream endcap and is fastened directly to the endcap with 16 1/2-13 screws that go through holes drilled in the 11" diameter flange of the window. An O-ring, which sits in a groove in the endcap, makes the high pressure seal between the Al window and the endcap. As explained in Section III.C.8, the surface of the window flange is bevelled to allow for the bulging of the endcap when TREAD is pressurized.

#### c) Endcap Feedthroughs

All communication between the inside and outside of the TREAD high pressure vessel is by way of specially designed feedthrough assemblies on the 2 1/2" endcaps. No holes were cut through the surface of the main cylinder. In each endcap, a total of 40 holes, ranging in diameter from 1 1/4" to 2 1/2", served to pass the scintillation counter light pipes, all electronic signals, high voltage, a thermometer, a pressure transducer, and hydrogen gas through the endcaps. Each feedthrough assembly is sealed against leakage of the high pressure hydrogen gas and is strong enough to withstand a 14 atm pressure differential from the inside during normal operation and a 1 atm pressure differential from the outside during evacuation of the vessel. Viton O-rings are used for all seals. In order that TREAD satisfy the safety requirements of the ASME Code for High Pressure Vessels, a sample

of each type of feedthrough assembly was shown to withstand a hydrostatic pressure five times the operating pressure in a small test chamber.

The light pipes for the pulse height counters and anticounters extend through 2" and 1 1/4" diameter holes at radii of 9 5/8" and 12 1/8", respectively, on the endcaps, as shown in Figure III.4. They were machined from pieces of solid 2 1/2" and 1 1/2" diameter lucite rods with thick "heads" for high pressure support. The light pipes were carefully polished to minimize light loss. The high pressure seals are made on the outside of the endcaps with stainless steel clamps that squeeze an O-ring against the light pipe and the endcap surface. The magnetic shields for the phototubes are attached to this clamp, as shown in Figure III.16. Inside the vessel, the light pipe "heads" are clamped against the endcaps to hold them in place when TREAD is evacuated. Figure III.19 is a computer-generated diagram of a pulse height counter light pipe with its O-ring clamp.

Special "electronic feedthrough plugs" were designed to pass the ~ 7 kV high voltage to the sense wires inside TREAD and to pass the sense wire signals to the preamplifiers outside TREAD. The plugs are also used to read out the currents drawn by the inner and outer field shaping cages for monitoring purposes. Each endcap has four electronic feedthrough plugs, and each plug has seven independent feedthrough spigots. A sample is shown in Figure III.20. Signal connections on both sides of the feedthrough are made with standard SHV high voltage connectors. The body of the plug provides the ground continuity, and a piece of center conductor from an RG59 cable carries the signal. The conductor passes from one connector to the other through a hole in the plug body and through a cup of epoxy which provides the high pressure seal around the conductor. Prototype feedthrough plugs were shown to withstand high voltage up to 10 kV before breaking down, so the plugs were considered reliable for use at the 6-7 kV required for TREAD sense wires.

At a radius between that of the pulse height counters and anticounters, each endcap has four 1 1/4" diameter holes for stainless steel "service plugs" which serve as feedthroughs for the far alpha source light pipes, a thermometer, a pressure transducer, the input and output gas lines, and the RG19 high voltage cable. The service plugs are all similarly designed: 1/4-20 screws compress an O-ring on the inside surface of the endcap to make the high pressure seal between the endcap and the plug, and each of the above items feeds through the body of one of the plugs. A blank plug is used in one of the holes. A description of the individual service plugs follows.

One of the service plugs on each endcap is used as a feedthrough for the far alpha source lightpipe. The alpha source assembly and the feedthrough for the lightpipe are shown in Figure III.21. The lightpipe is located between pulse height counters 31 and 32 on each endcap. (The numbering convention for the counters is shown in Figure V.3.) The 3/4" diameter lightpipe tapers to 11/16" at the feedthrough and rests in a tapered hole in the service plug. The lightpipe is thus supported against high pressure inside the vessel. Outside the endcap, a brass cap screws onto the service plug and compresses an O-ring to make the seal between the plug and the lightpipe. The frictional force applied through the compressed O-ring prevents the lightpipe from moving when the vessel is evacuated. The magnetic shield for the phototube and a bakelite liner are attached to the brass cap.

One service plug endcap feeds a resistance thermometer into the vessel to monitor the temperature of the hydrogen gas. The thermometer is manufactured by the Burns Engineering Co., Minnetonka, Minnesota and is accurate to 0.1%. A sensing element of platinum wire is housed in the tip of a 11.5" long sheath of 1/4" diameter Type 316 stainless steel which protrudes into the vessel. A calibrated Model 101 Digital Thermometer converts the resistance of the sensing element to temperature, and a BCD readout card transfers the temperature reading in units of °F to a CAMAC input register using 4 bits/digit. During data

taking, the temperature was read out and written to tape at the end of every accelerator spill.

One service plug on the upstream endcap is a feedthrough for the 1" diameter RG19 coaxial cable which carries -130 kV to the high voltage plates in the center of TREAD. A single 160 foot length of cable connects the Spellman -200 kV power supply to the upstream high voltage plate. As shown in Figure III.22, the cable's polyethylene insulator and copper center conductor pass through the service plug and extend to the upstream plate. There, the center conductor slides into a rounded aluminum socket and presses against a spring to insure contact. The electrical connection to the downstream plate is made through an aluminum spring clip. Outside the vessel, an O-ring is compressed between two steel collars to make the pressure seal between the insulator and the service plug. The cable's ground braid and outer insulating jacket are cut as shown in the figure. The ground connection is made through a brass pipe fitting which screws into the outermost steel collar. The threaded end of the pipe fitting is split; screwing it into the collar clamps the cable against movement. To provide additional mechanical support, aluminum strips were welded to the pipe fitting, and hose clamps press these strips tightly against the outer jacket. The high voltage cable can be extracted easily from the vessel by removing the screws that connect the two collars. That is, the pipe fitting and hose clamps remain in place.

The gas circulation and purification system is connected to TREAD through through two 1/2" stainless steel pipes which screw into service plugs. The input pipe delivers gas to a circular copper manifold which distributes the input gas evenly around the center of the upstream endcap. The manifold is made from a piece of 1/2" diameter copper tubing. Gas is exhausted from the downstream end.

The pressure transducer (Model 300D/TJE, manufactured by Sensotec, Inc., Columbus, Ohio), which monitors the gas pressure in TREAD and



activates input and exhaust valves, is screwed onto the outside of one of the service plugs. A hole through the center of the plug exposes the transducer to the gas in TREAD.

### III.C.7 Gas Circulation and Purification System

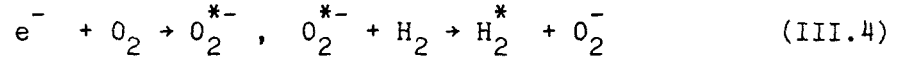
A schematic diagram of the gas system is shown in Figure III.23. The purification elements are catalytic converters followed by molecular sieves. The converters contain palladium pellets which catalyze the burning of hydrogen with oxygen to form water. Two such converters (Model D-200-1200, Engelhard Industries, Union, New Jersey) with a total of 5 lbs of Pd are used in parallel in order to facilitate gas flow. The molecular sieves adsorb the water formed in the catalytic converters and other impurities present in the gas. They are 4 A° sieves (Model 461, Matheson Gas Products, East Rutherford, New Jersey) containing a total volume of 0.6 ft<sup>3</sup> of sodium aluminosilicate. At a flow rate of 75 ft<sup>3</sup> (three TREAD volumes)/hr at 15 atm, the pressure drop across the purification elements is approximately 2 psi.

The pump, which must operate in hydrogen at pressures up to 300 psi, was designed and built at The Rockefeller University. The principle of the design is to house the bellows along with the driving motor inside a vessel which is maintained at the system pressure through a small orifice. Thus, the differential pressure across the bellows is small and a common, inexpensive pump (Model MB118, Metal Bellows Corp., Sharon, Mass.) can be used inside the pump vessel.

Typically, after evacuating, flushing with helium, and filling TREAD and the gas purification system with 0.99999 pure hydrogen, it takes about two hours for the TPC's to operate efficiently.

As noted previously, the wire pulse height attenuation as a function of drift time is characterized by a time constant of about

1.8 msec. Since the electron attachment to oxygen proceeds mainly through the reactions



the dependence of the attenuation time constant,  $\tau$ , on the oxygen impurity level,  $f_{O_2}$ , is given by

$$\tau^{-1} = k \cdot N_{H_2} \cdot N_{O_2} = k \cdot N_{H_2}^2 \cdot f_{O_2} \quad (III.5)$$

where  $N$  is the gas density. Using the measured value of the 3-body attachment coefficient for thermal electrons (Shimamori and Hatano, 1976)  $k = (4.8 \pm 0.3) \times 10^{-31} \text{ cm}^6 \text{ s}^{-1}$ , we estimate that the oxygen impurity level during our steady state operation is  $< 1$  part in  $10^8$ .

Figure III.24 shows the components of the gas system in more detail. The labelling numbers next to the valve and regulator symbols are referred to in a gas system operations manual. This manual is a guide to the various filling and evacuating procedures for the TREAD vessel.

### III.C.8 TREAD Safety

Our plan to integrate high pressure explosive gas, very high voltage, and thin windows in the TREAD apparatus stimulated concern at Fermilab about the safety of the system. An ad hoc safety committee consisting of physicists and engineers was established to review the proposed design of the various components of TREAD, work out operating

procedures, and generally oversee the development of TREAD into a safe system. The following is a list of the major safety requirements:

1. Every part of the TREAD apparatus which would come in contact with the high pressure hydrogen gas and hydrogen ions created by corona discharge was required to be made of a material immune to hydrogen embrittlement. In particular, the 304 stainless steel for the main cylinder, the A515 carbon steel for the endcaps, the beryllium for the entrance window, and the aluminum for the exit window are suitable materials for hydrogen containment.
2. TREAD, viewed as a high pressure system, was required to comply with the ASME (American Society of Mechanical Engineers) Code for High Pressure Vessels. The code defines the pressure testing procedures and minimum design safety factors that are required to establish a safe operating pressure for various vessel compositions and configurations. A "System Pressure" of 300 psi was established for the main TREAD vessel by hydrostatic testing to 450 psi ( $450 = 1.5 \times 300$ ). During this test, the beam-window holes in the endcaps were covered with thick plates, and the other endcap holes were plugged with lucite or stainless steel feedthroughs similar to those used in the experiment.
3. The feedthrough assemblies on the endcaps were considered structural components of the TREAD vessel. Since they are constructed from non-Code materials, a sample of each type of feedthrough had to be hydrostatically tested to 1500 psi ( $1500 = 5 \times 300$ ) for a period of 24 hours. A sample or a prototype of each of the following feedthrough assemblies was tested: pulse height counter light pipe,

anticounter lightpipe, alpha source light pipe, sense wire signal feedthrough plug, and 130 kV high voltage feedthrough.

4. The thin beam windows were given special attention. The 0.080" thick aluminum window was designed to withstand 300 psi with a safety factor of 9.3, and the 0.030" thick Be window has a safety factor of 8.4 . The safety committee required that each window be pressure tested both hydrostatically and mounted on TREAD in its final configuration. The hydrostatic test for the two aluminum windows (one spare was made) was at 510 psi; for Be windows, 375 psi. The mounting technique for each window was devised to decouple the window from stresses due to the bulging of the endcaps during pressurization. A helium pressure test with the windows in place on TREAD at the "System Pressure" of 300 psi established the "Maximum Allowable Working Pressure" of 240 psi for the experiment.
5. As part of the Be window mounting assembly, a check valve was developed to contain the explosion of rushing gas in the event of a window rupture at high pressure. This "flapper valve" is described below.
6. The TREAD electrical system was required to comply with the National Electric Code. This led to the development of the inerting hoods and the safety interlock system described below.
7. Each experimenter was required to become familiar with the gas system procedures - changing gas bottles, filling the vessel, evacuating, purging - before performing these tasks on his own.

8. In general, laboratory safety practices for hydrogen targets had to be observed.

- a) The Beryllium Window Mount and the Flapper Valve

The beryllium entrance window is considered the most fragile part of TREAD vessel due to its brittleness. Figure III.25 shows a cross section of the Be window mount and the flapper valve assembly. The beryllium entrance window is mounted on a thick flange (11"o.d.  $\times$  2.5" thick at the center) to minimize the stress on the window as the vessel endcaps bulge when TREAD is pressurized. Careful measurements at 15 atm showed that the endcaps bend by as much as 2.5 mrad with respect to the relaxed position. Like the endcaps themselves, the flange is made of A515 steel and serves as part of the field return for the solenoid around the vessel. An aluminum collar (2.5"i.d.  $\times$  3.5"o.d.  $\times$  1/4" thick), a softer material than the Be itself, presses the window against an O-ring in the thick flange to make the pressure seal. This prevents the beryllium itself from being crushed or damaged if the screws which make the pressure seal are overtightened.

Fermilab engineers developed the details of the "flapper valve" assembly. It is designed to close automatically if the Be window ruptures. The flapper valve screws onto threads on the flange tube which houses the aluminum collar. This tube is made of 1020 steel and helps shield the phototubes from the magnetic flux lines that come through the beam hole in the endcap. If the window bursts while TREAD is pressurized, the escaping gas rushes into the cylindrical flapper valve chamber. Some of the gas is directed through an upward slit toward the actuator which swivels clockwise and releases the flapper plate. The flapper plate then slams against the outer wall of the chamber and closes the beam hole, preventing an uncontrolled venting of the high pressure hydrogen. The flapper valve assembly is not strictly

leak tight, however, so the high pressure gas in the chamber will slowly leak out.

The flapper valve assembly was tested at Fermilab by mounting it on a 12" dia. x 36" long cylinder and replacing the Be window with rupture discs designed to burst at 152 psi or 250 psi. For each test, we measured the pressure at which the rupture occurred, the pressure drop associated with the valve closing, and the rate of pressure drop after the valve had closed. We concluded from these tests that, in the event of a window failure on TREAD, only 1% of the hydrogen gas would escape before the valve would close. Then, the rest of the hydrogen would vent to atmospheric pressure over a period of a few minutes. The performance of the flapper valve was never tested while mounted on TREAD; the beryllium window never ruptured.

#### b) Aluminum Exit Window and Mounting

To allow for the bulging of the downstream endcap during pressurization of TREAD, the surface of the aluminum window flange is bevelled at an angle (2.5 mrad) such that the flange and endcap surfaces are parallel where they interface, as shown in Figure III.18. Since the window must be mounted while the endcaps are in their relaxed position, the mounting screws are tightened with a torque wrench to a specified value so as not to over-stress the window.

An iron tube, 11" i.d. x 1/4" thick x 18" long, is mounted on the downstream endcap over the Al window to protect the window from accidental damage. The tube also serves to protect the surrounding phototubes from the magnetic field leaking through the central 8" endcap hole and the Al window.

c) Inerting Hoods

There was concern that a slow hydrogen leak could develop through one of the O-rings that seal the many feedthrough plugs and light pipes on the endcaps of the vessel. The leaking hydrogen, combined with the oxygen in the atmosphere, would create a flammable gas mixture in the vicinity of the phototubes and sense wire preamps and would violate the National Electric Code. To avoid this problem, two large hoods were constructed to enclose the electronics on each endcap in an environment of inert gas. Each hood is made of 1/16" aluminum and is attached to a 1/2" aluminum flange which is mounted on the endcap. Gas seals are made with RTV and refrigerator gasket material. 12" diameter mylar windows allow the photon beam to pass into the upstream hood and out of the downstream hood. The hoods are easily removed to permit access to the endcap electronics.

All electrical connections to the endcaps, as well as the high pressure gas lines, enter the hoods through holes in the hood flanges. O-ring clamps, similar in design to the light pipe clamps on the endcaps, seal the feedthroughs for the stainless steel gas lines. Seals for the RG19 high voltage cable, the RG58 signal cables, and the RG59 high voltage cables are made by passing them through holes in tapered rubber stoppers which are squeezed into tapered holes in the hood flanges.

Whenever hydrogen is in the TREAD vessel, the hoods are filled with nitrogen gas at a very low positive pressure. The nitrogen continuously flows through the two hoods in series at a rate of about 1 ft<sup>3</sup>/hr, and the output nitrogen flows through a hydrogen detector before being vented to the outside atmosphere. As indicated in the description of the interlock system below, the detection of hydrogen automatically causes the TREAD vessel to vent to atmospheric pressure and all electrical power to the vessel to be turned off. A Photohelic pressure transducer monitors the nitrogen pressure in the hoods. Loss of

nitrogen flow as indicated by the Photohelic automatically turns off all the vessel's electrical power, but the vessel does not vent.

At the top of each hood is a 12" diameter mylar rupture disc which separates the hood volume from a purge container above. The purge containers are 12" diameter pipes made of 1/32" aluminum sheet metal, and they lead to an aluminum plenum which sits on top of the gas circulation cart. The plenum is attached to a large exhaust pipe which, in turn, leads to an exhaust fan outside the TPL building. Each rupture disc is set to be pierced by an arrowhead point if the pressure in the hood rises 3/4 psi above atmospheric pressure. The gas in the hood would then be vented safely through its purge container and the plenum to the outside atmosphere.

The pressure in the large exhaust pipe is monitored by a pressure transducer. A pressure below 1 atm, indicating that the exhaust fan is pulling air through the plenum, is required for TREAD to be pressurized. At no time during the running or testing of the experiment did we detect a hydrogen leak or the bursting of an inerting hood rupture disc.

#### d) Other Safety Items

The lucite used for the lightpipe feedthroughs is not expected to retain its tensile strength at temperatures above 140°F. Should the magnet cause the vessel's temperature to rise above this value, the lightpipes could soften and rupture under high pressure. Hence, the Klixon Thermal Switches, which disable the magnet's power supply if the temperature of the magnet rises above 175°F, do not provide adequate protection. For this reason, two Honeywell adjustable thermal switches were introduced to vent the vessel to atmospheric pressure if the vessel's temperature exceeds 100°F. Each switch responds to a gas bulb thermometer which is in direct contact with one of the flanges of the main vessel.



In addition to the hydrogen detector in the plenum above the gas circulation system, another detector is located on the ceiling of the TPL building above TREAD.

e) Safety Interlock System

As mentioned throughout this section, potentially hazardous conditions in or around TREAD automatically trigger the return to a safer situation. The electronics and controls for the automatic responses are integrated into the "Safety Interlock System". Two modules, one near TREAD and one in the counting room, house the control switches and relays. The Safety Interlock System also contains the circuitry for remote manual control and automatic control of the solenoid valves which exhaust and fill TREAD during normal operation.

The following conditions trigger the automatic venting of TREAD and cause an alarm to be sent to Fermilab's fire and emergency system (the FIRUS system):

- 1.) Detection of hydrogen in either detector
- 2.) Thermometers on vessel flanges above the limit of 100°F
- 3.) Loss of air flow through the purge containers and the outside exhaust pipe
- 4.) Detection of fire or smoke in the TPL area

Conditions 1.) through 4.) also cause all electrical power to TREAD, both inside and outside the inerting hoods, to be turned off. This includes the power to the magnet coils. In addition, loss of nitrogen flow in the inerting hoods as indicated by the Photohelic turns off all electrical power, but the vessel does not vent.

### III.C.9 Front Anticounter and Multiplicity Counters

A large scintillation counter is attached to the front of the upstream inerting hood to serve as a veto counter for muons and other charged particles entering TREAD. The counter is  $1/4$ " thick  $\times$  21" wide  $\times$  24" high and is positioned to completely cover the drift regions of the TPC's and the pulse height and anticounter banks. A  $1\ 3/4$ " diameter hole in the front anticounter allows the photon beam to pass through. A 3" square piece of  $1/4$ " thick lead with a  $1\ 7/8$ " hole is mounted in front of the anticounter hole. Photons from synchrotron radiation or other upstream sources which hit this piece of lead will either be absorbed or produce  $e^+e^-$  pairs and trigger the anticounter.

The multiplicity counters are mounted, one behind the other, outside the downstream inerting hood, a distance of 64" from the center of TREAD. The scintillator in each counter measures  $10.5" \times 10.5" \times 1/8"$  thick. The counters are isolated optically from each other and viewed by separate CA 8575 phototubes. A simple calculation shows that the counters cover approximately 94% of the solid angle in the rest frame of a particle with  $2\text{ GeV}/c^2$  invariant mass created at the center of TREAD with  $100\text{ GeV}/c$  momentum.

### III.C.10 Material TREAD Presents to Beam

The presence of TREAD in the photon beam does not degrade the beam significantly. The beam passes through  $0.030"$  of beryllium, four Al foils, each about  $0.0005"$  thick,  $84"$  of 15 atm hydrogen gas,  $0.080"$  of aluminum at the exit window,  $1/4"$  of scintillator at the multiplicity counters, and two  $0.010"$  thick mylar windows on the inerting hoods. This represents a total of 4.5% of a radiation length, so 3.4% of the beam photons convert into  $e^+e^-$  pairs as they pass through TREAD. During the test run of the experiment in 1981, an independent experiment ran

downstream of the TREAD apparatus, and the beam for that experiment was not affected noticeably by TREAD.

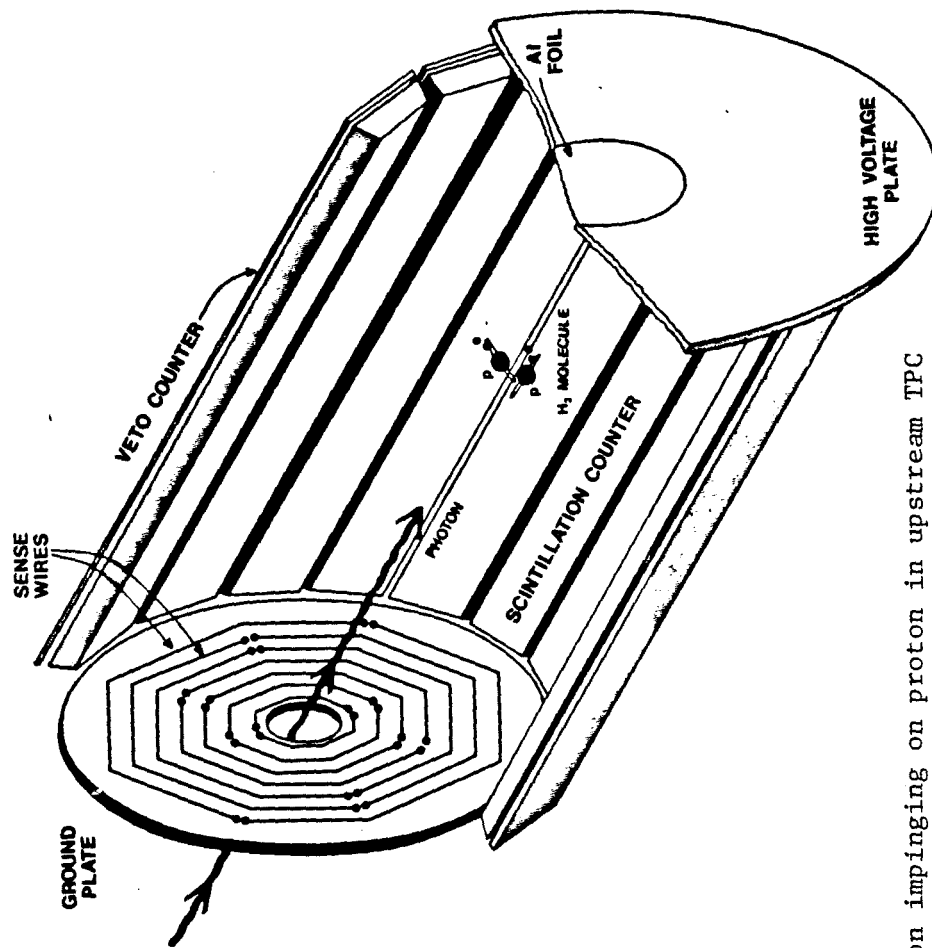


FIG. III.1 - Photon impinging on proton in upstream TPC

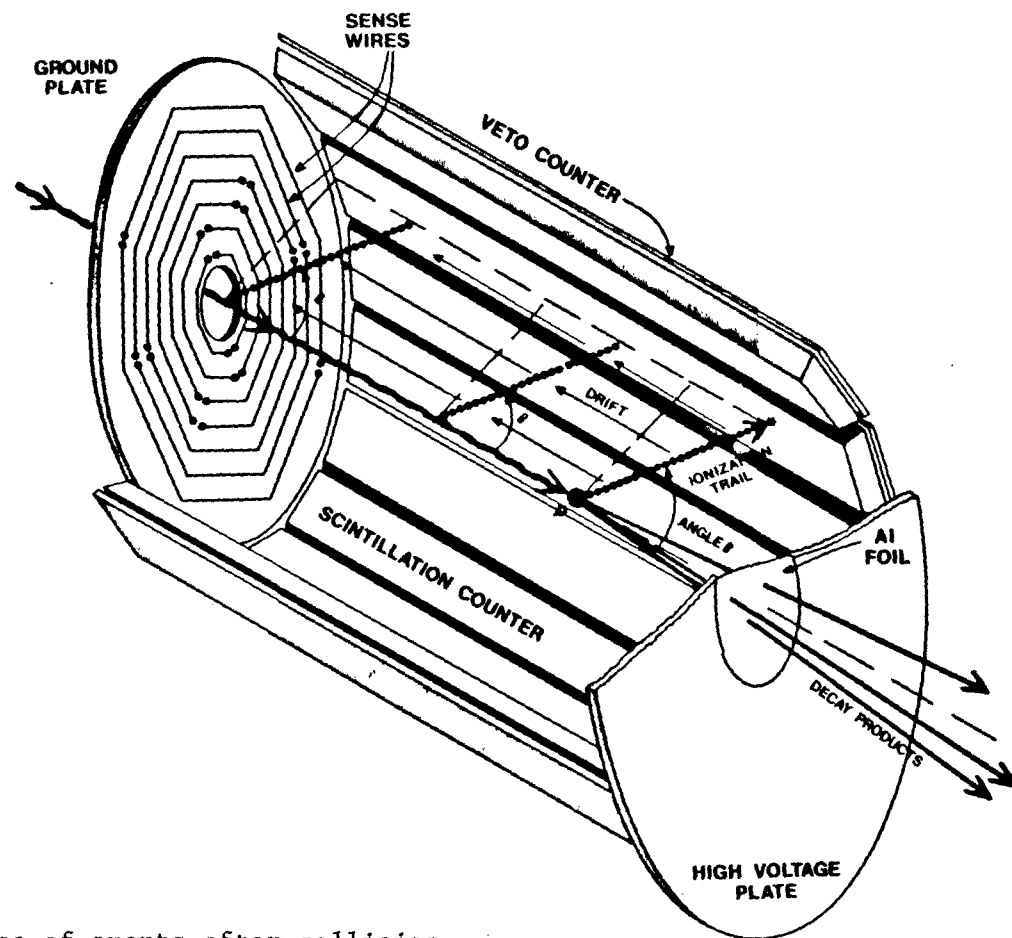
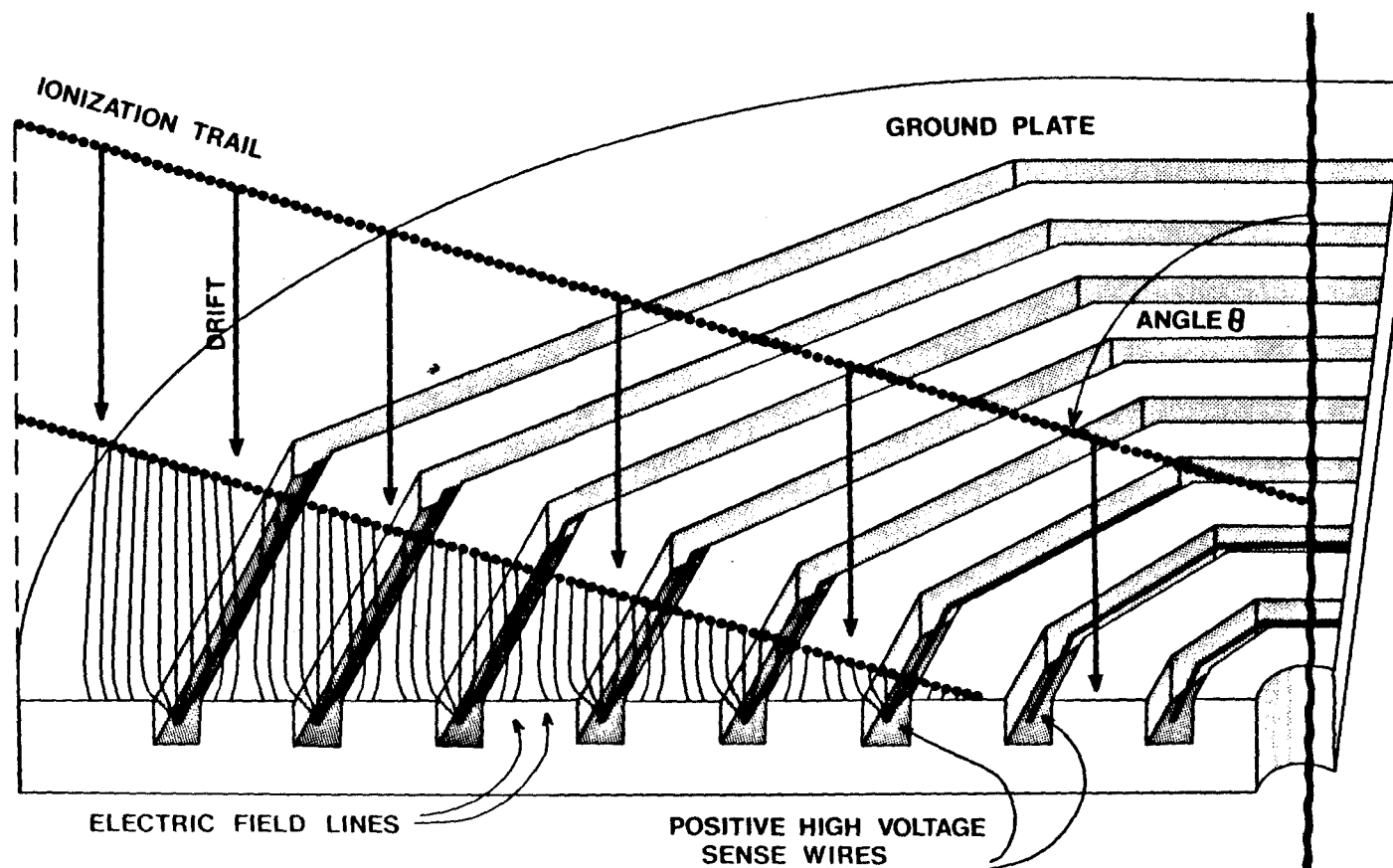


FIG. III.2 - Sequence of events after collision



-74-

FIG. III.3 - Ionization trail arriving at the sense wire plate

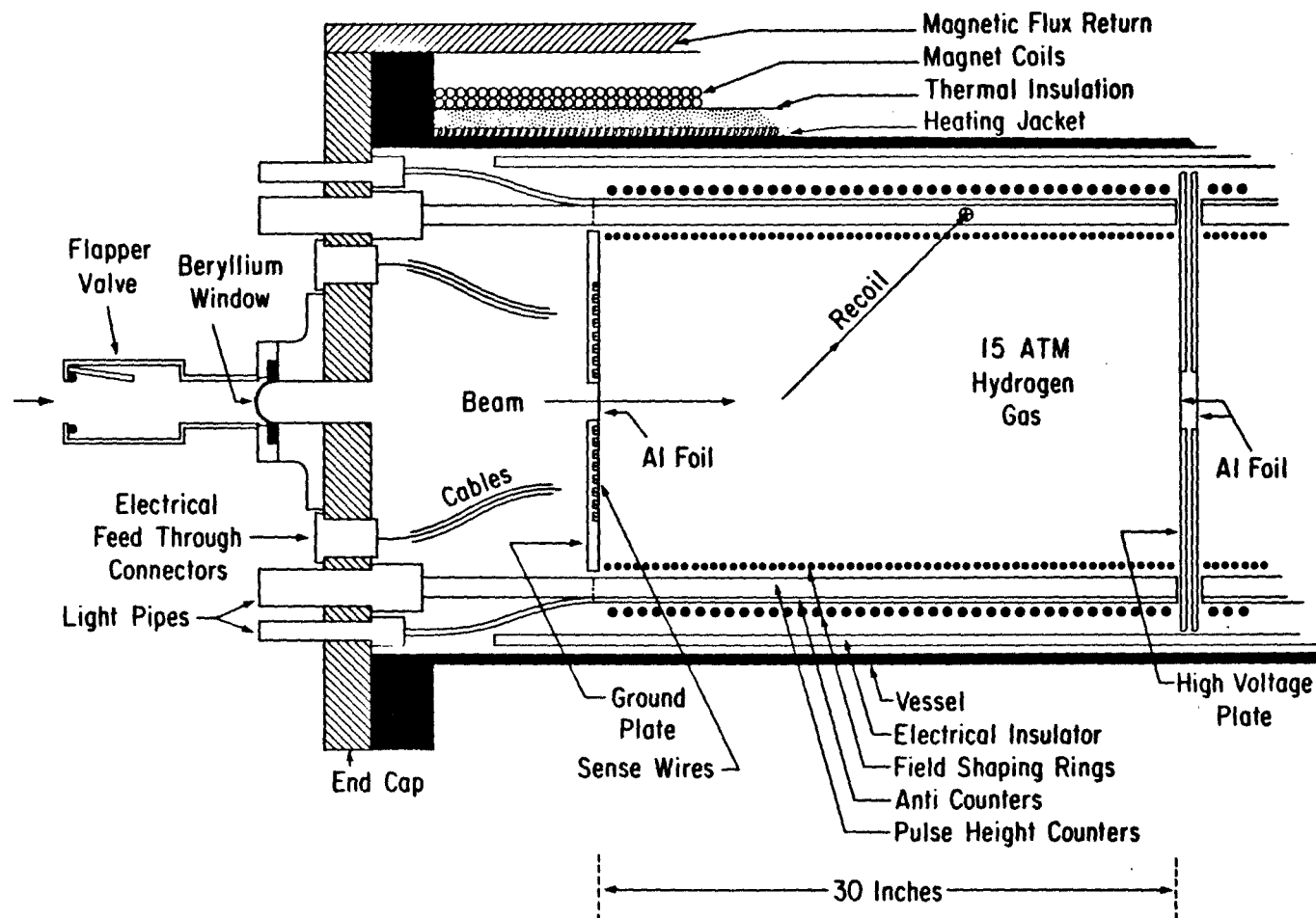


FIG. III.4 - TREAD schematic diagram -- side view

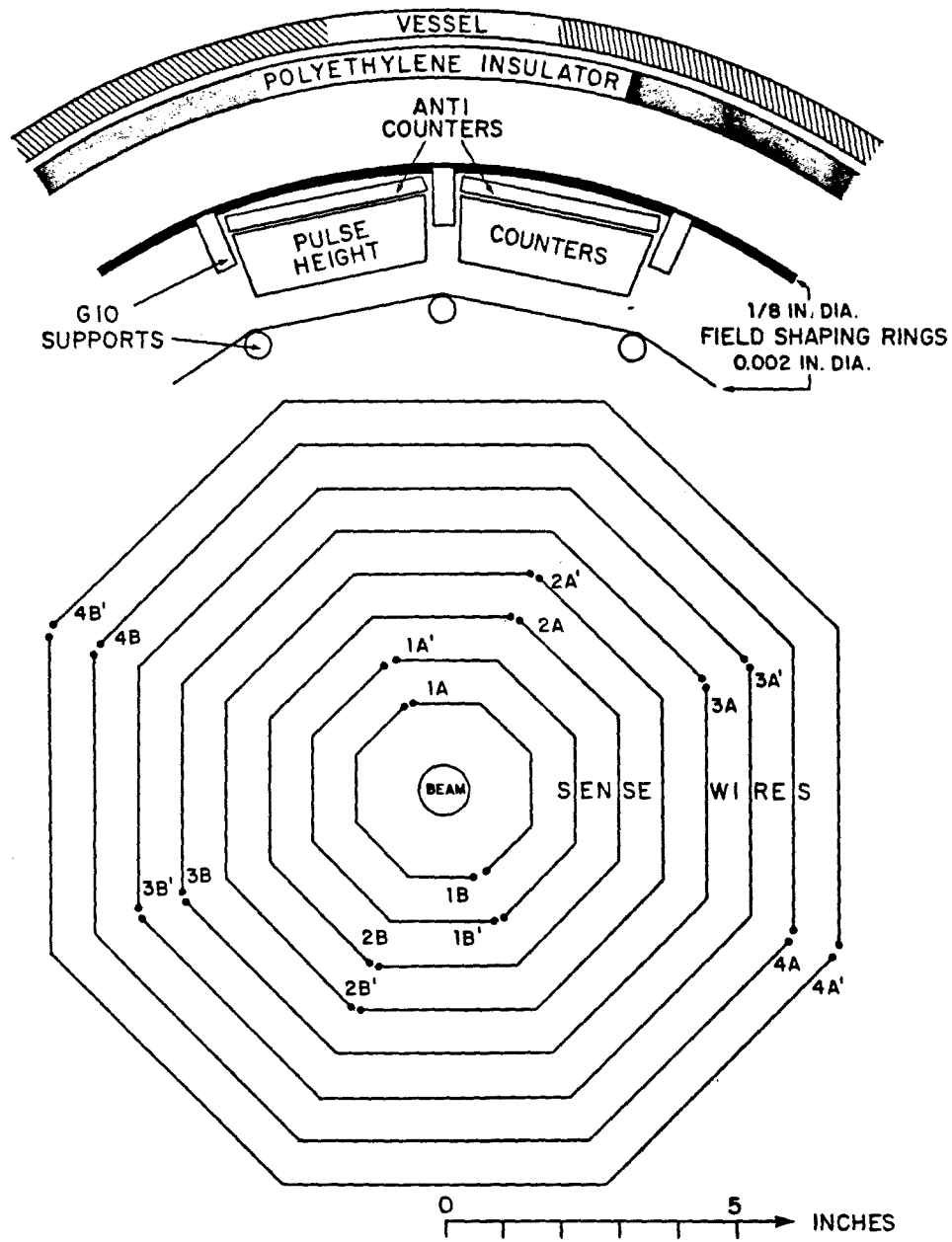


FIG. III.5 - TREAD schematic diagram -- end view



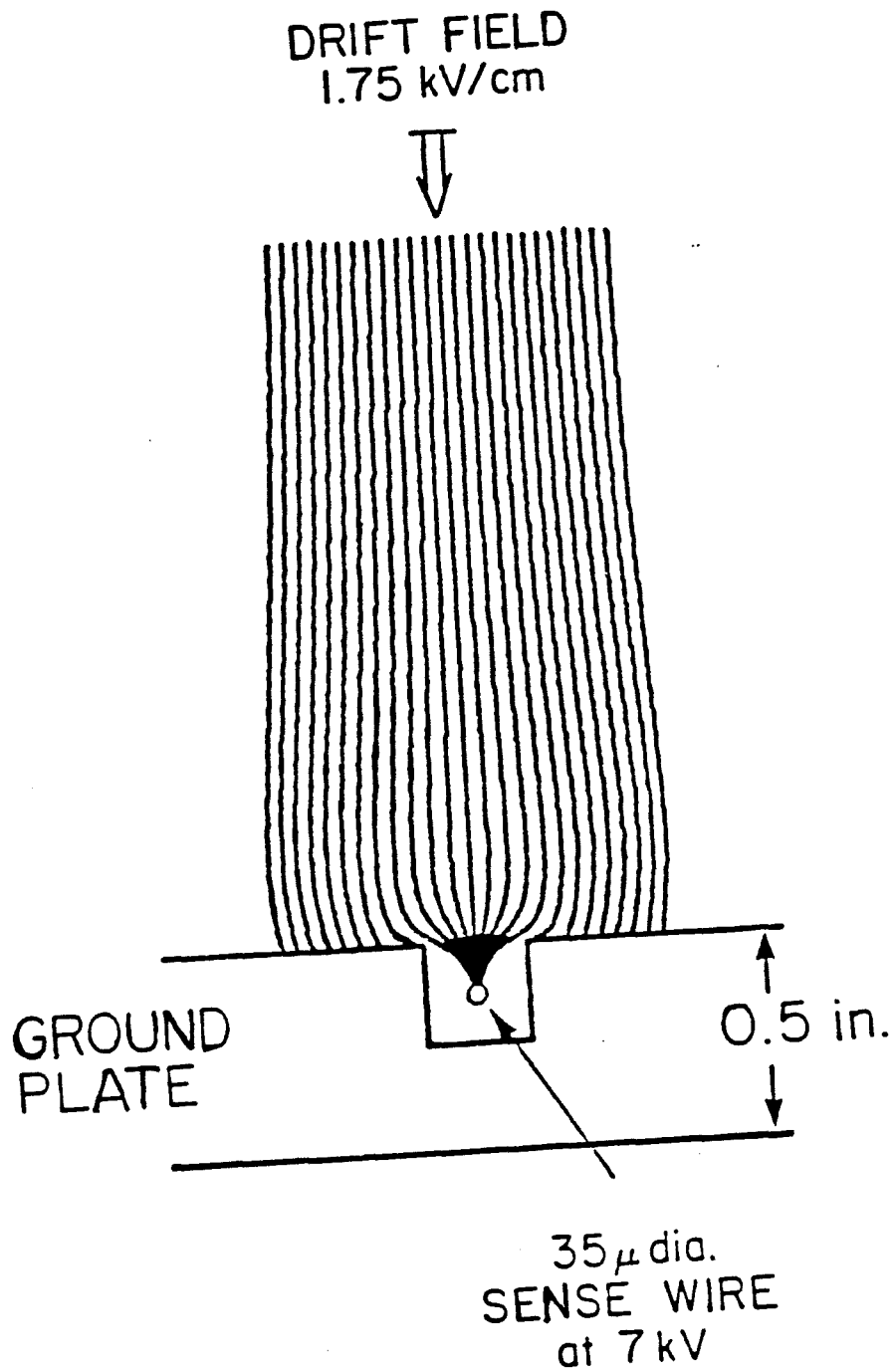


FIG. III.6 - The drift field in the vicinity of a sense wire

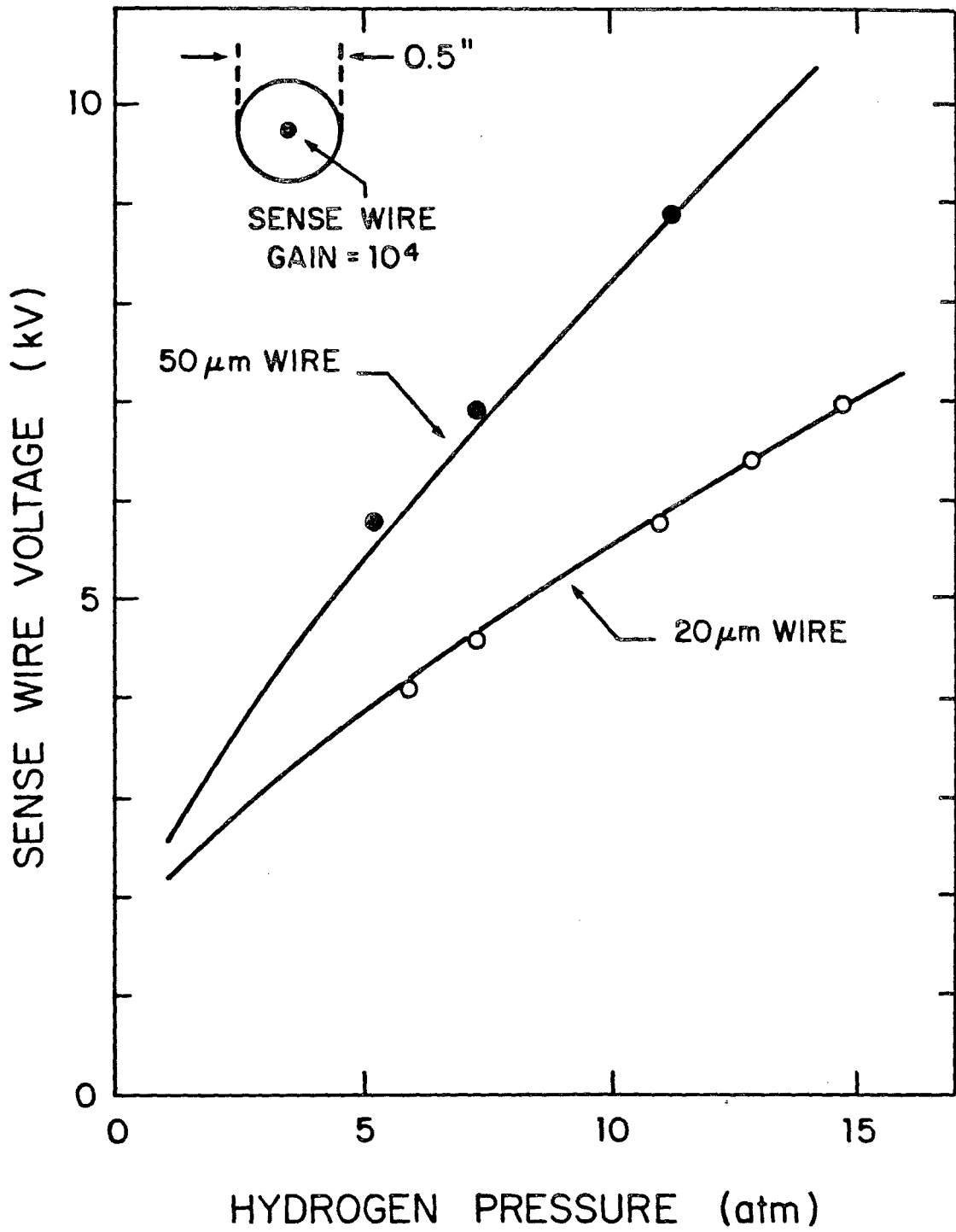


FIG. III.7 - Sense wire voltage vs. pressure at fixed gain

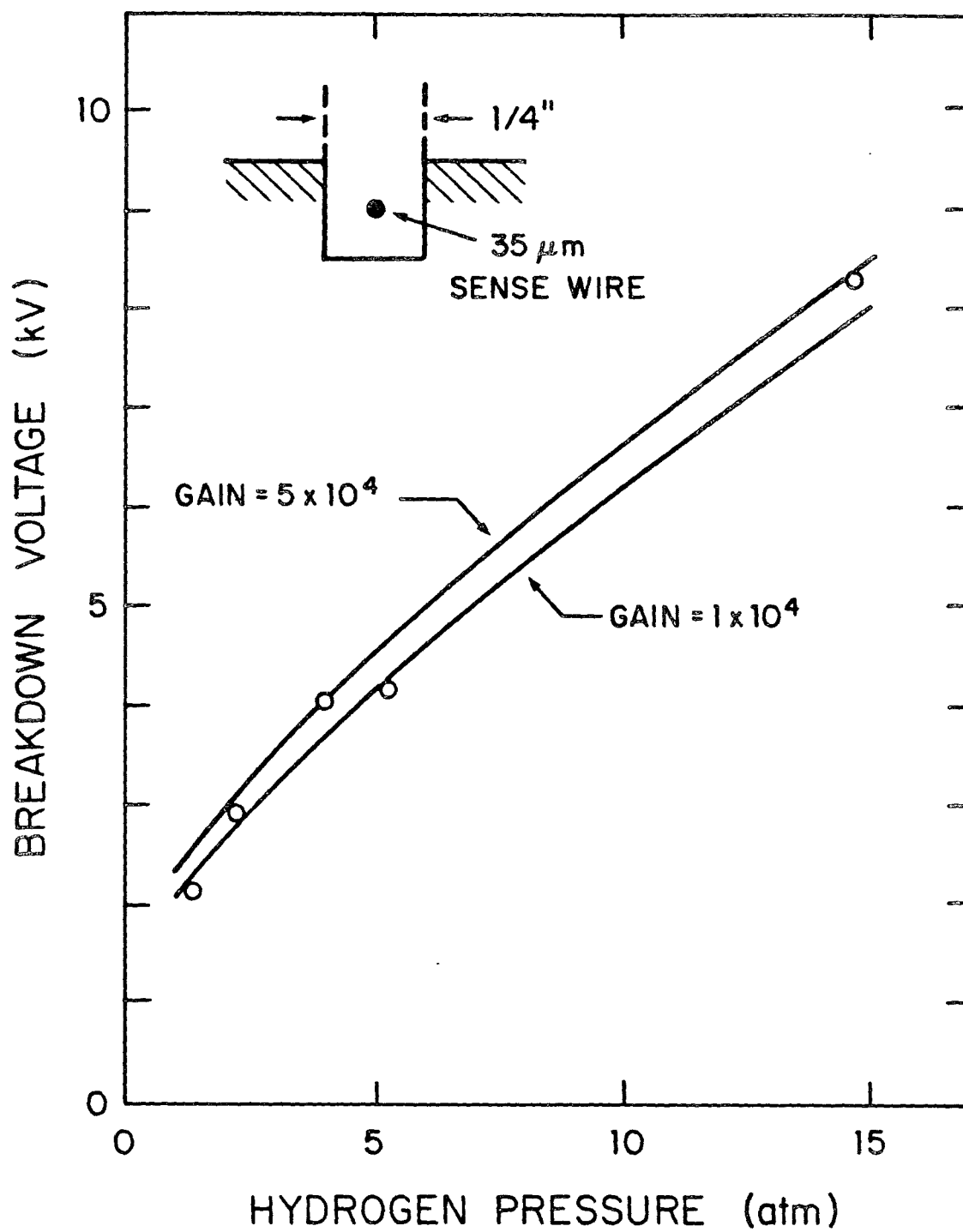


FIG. III.8 - Sense wire breakdown voltage vs. pressure

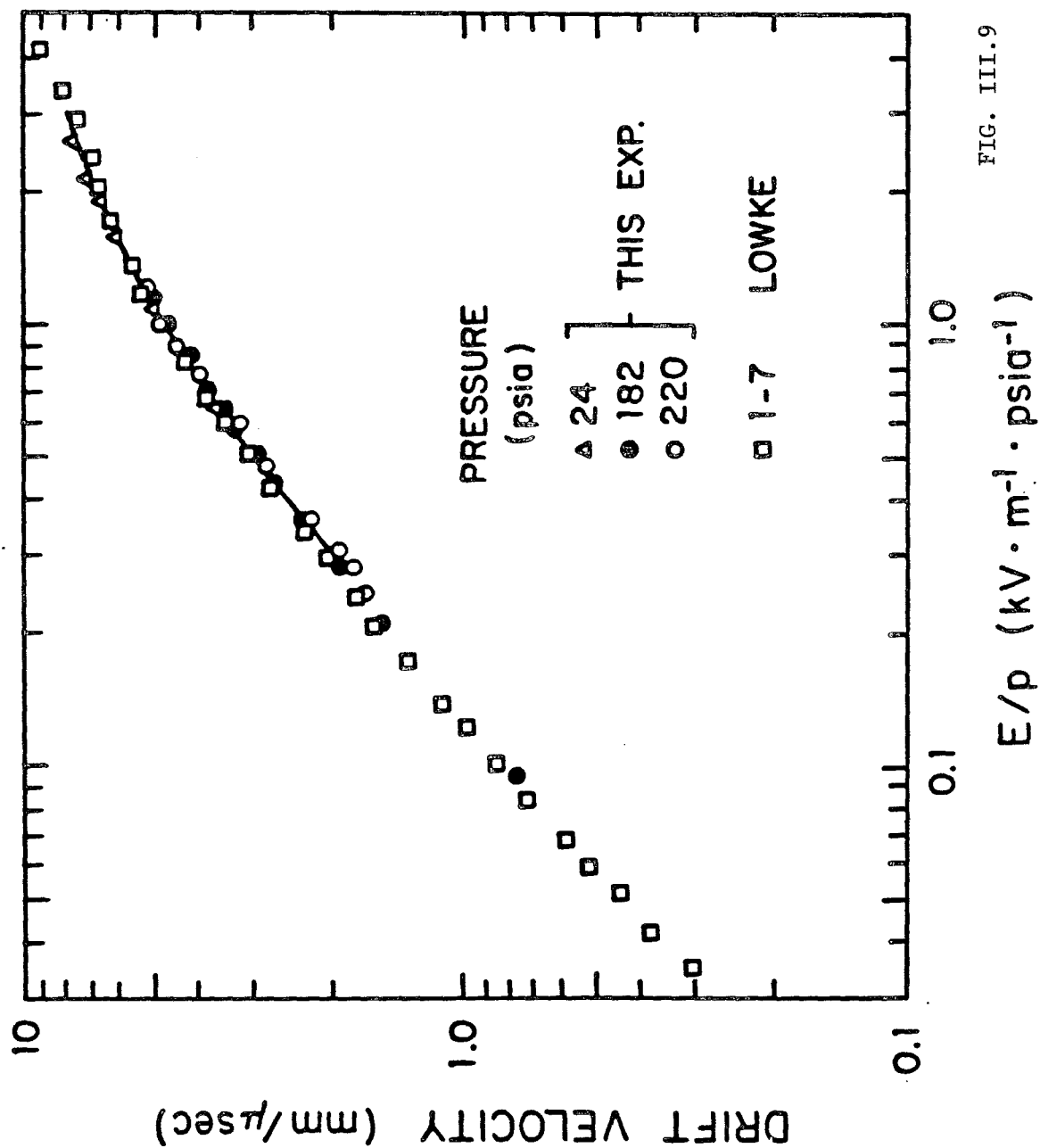


FIG. III.9

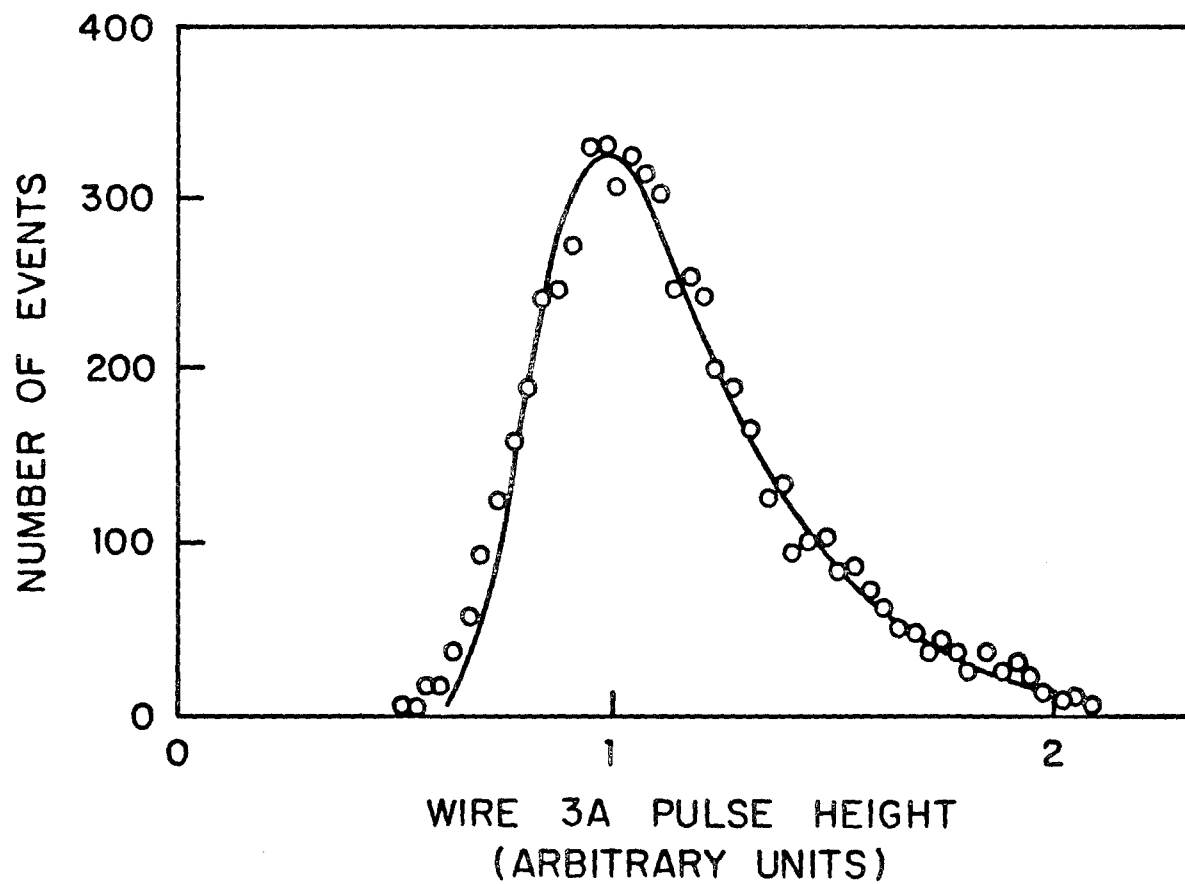


FIG. III.10 - Sense wire pulse height spectrum for cosmic ray tracks distributed through the entire drift space

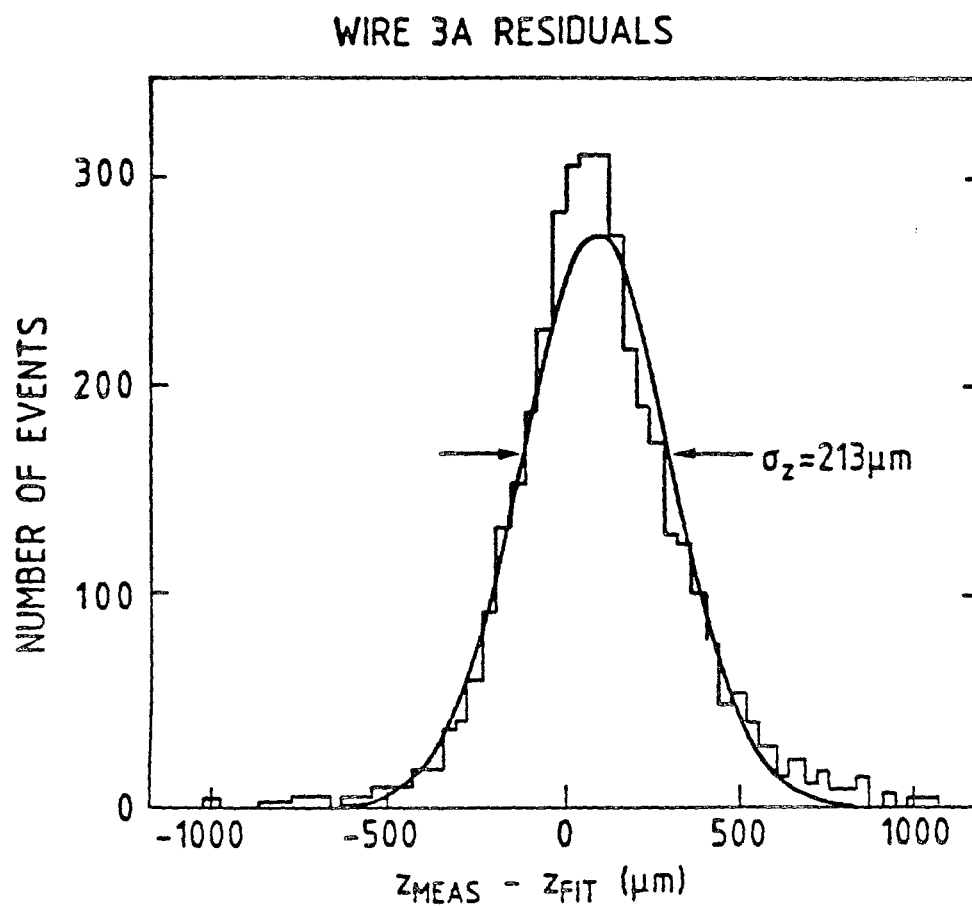


FIG. III.11 - Wire 3A (upstream) residuals from cosmic ray tracks distributed through the entire drift distance

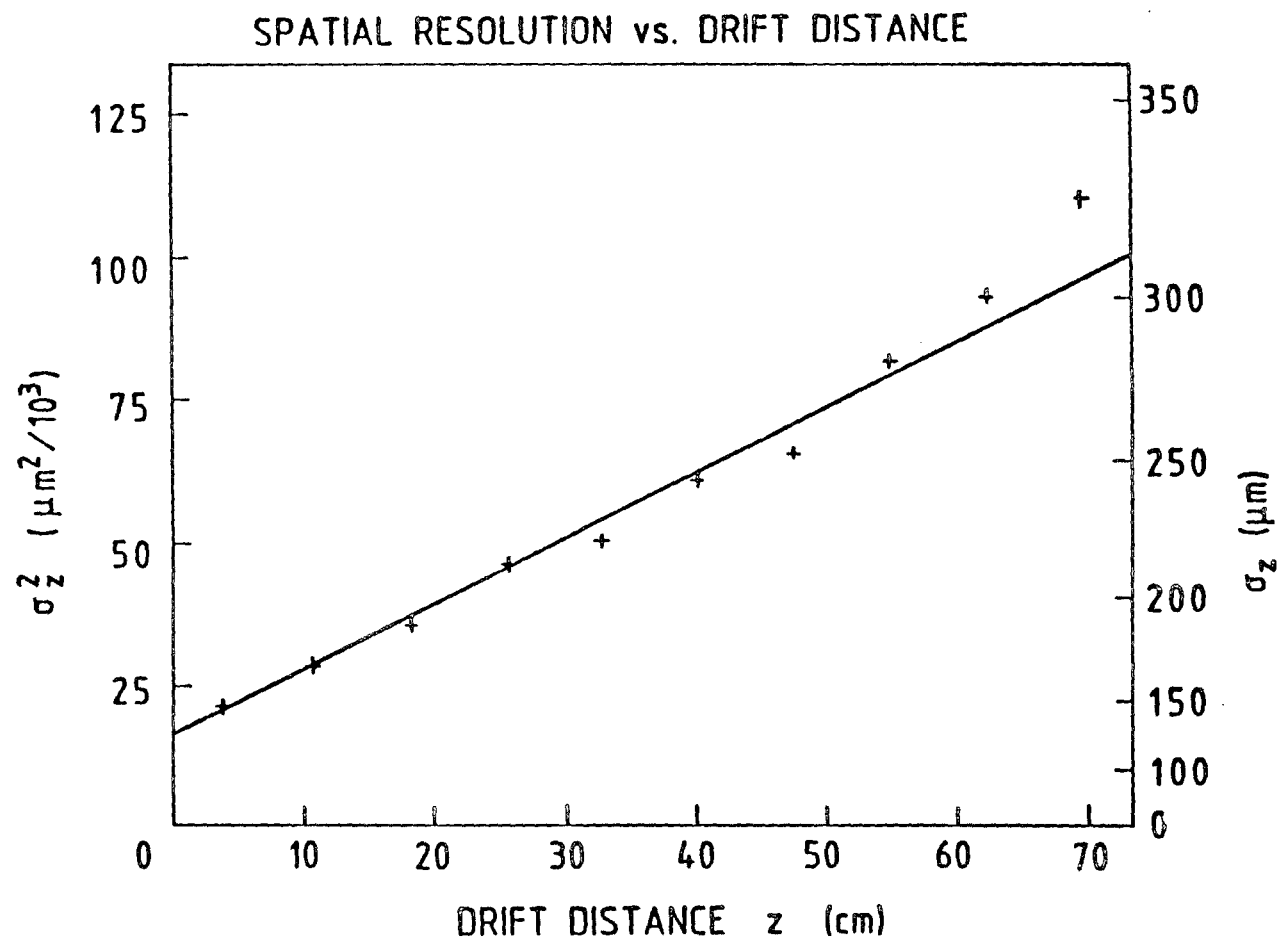


FIG. III.12

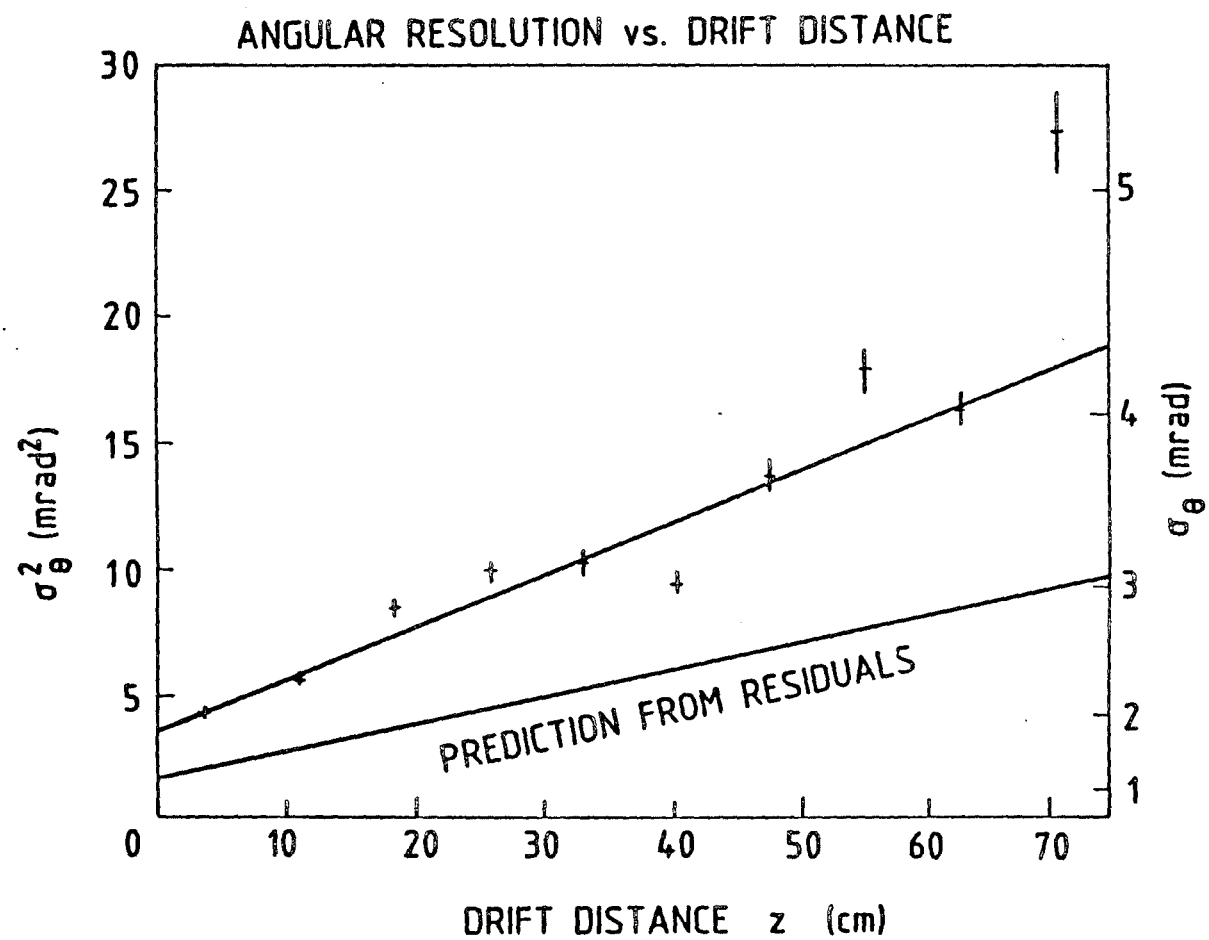


FIG. III.13



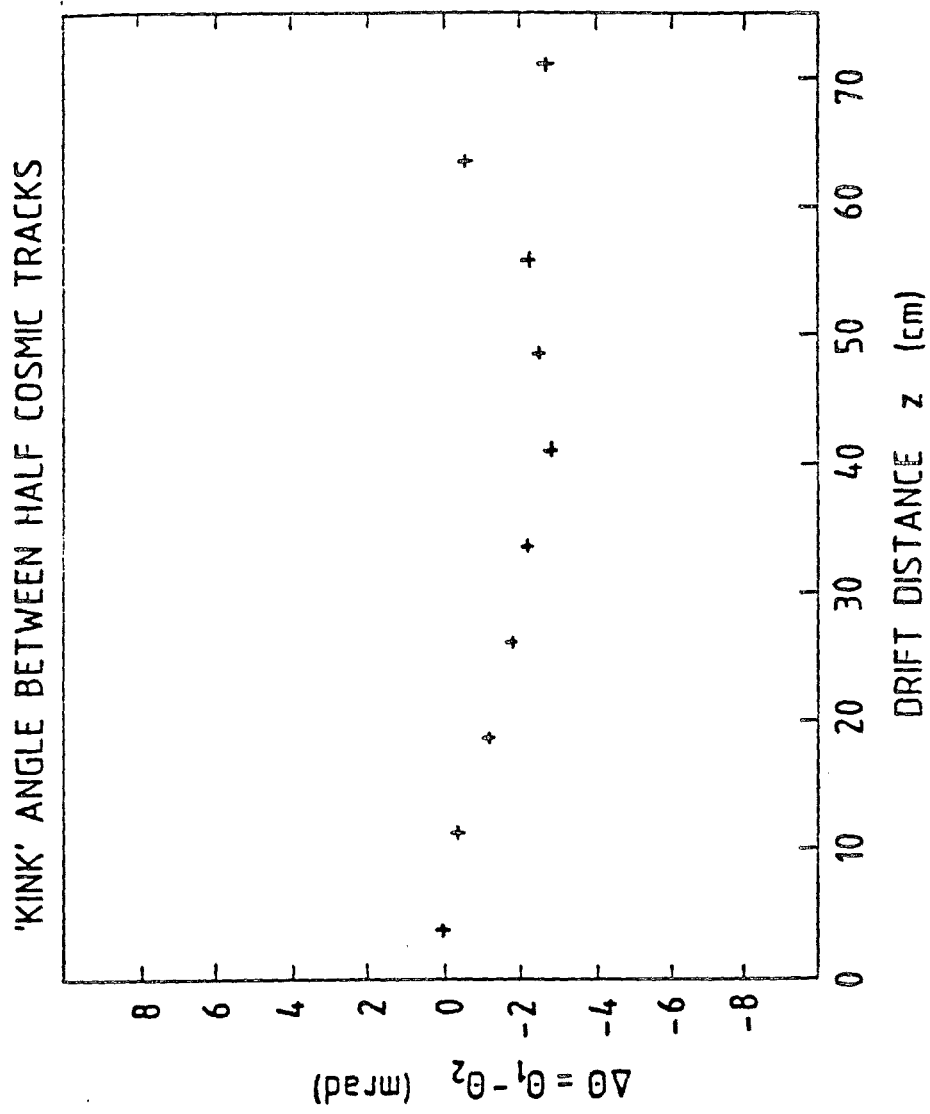


FIG. III.14

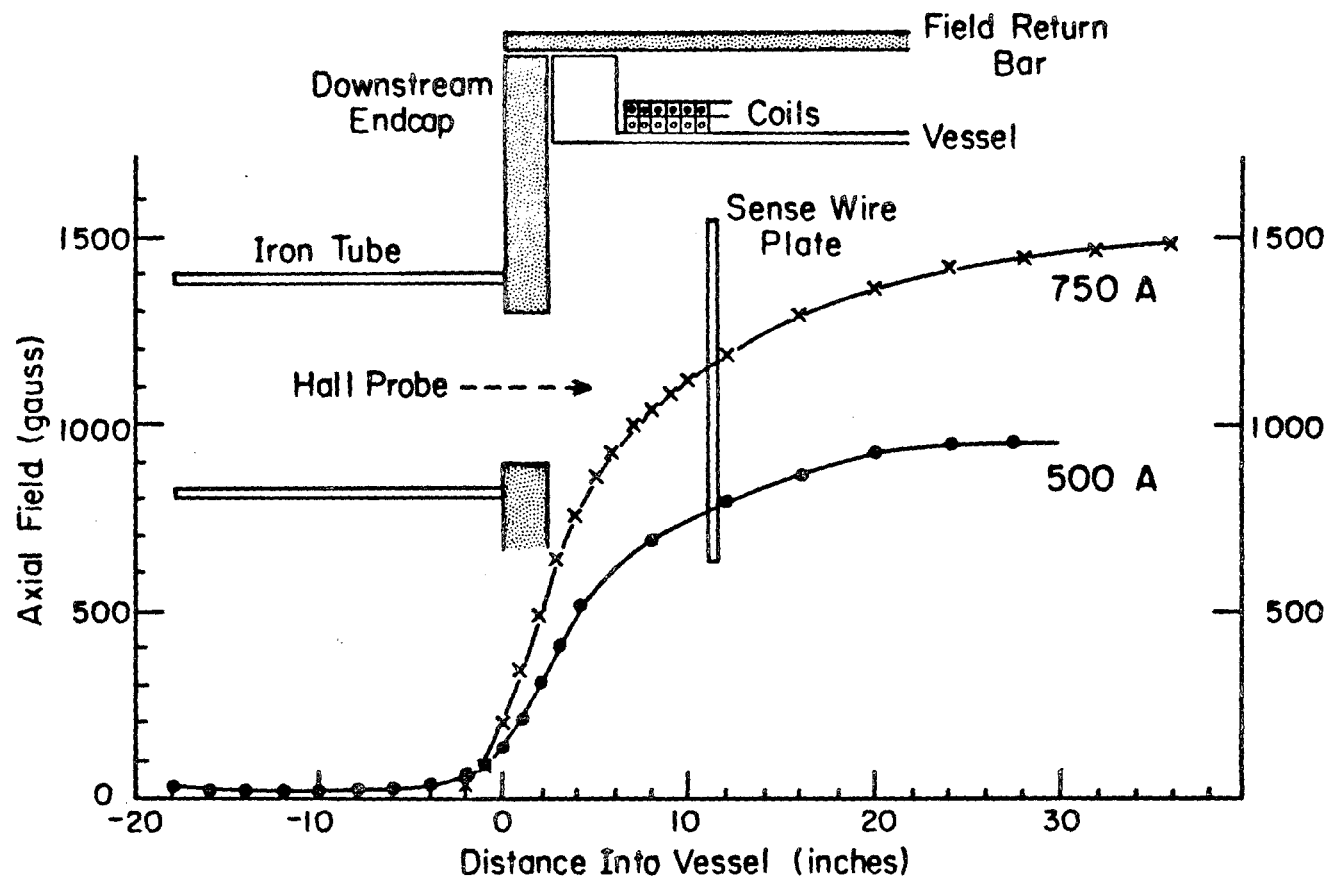


FIG. III.15 - Axial component of central field viewed along axis of TREAD

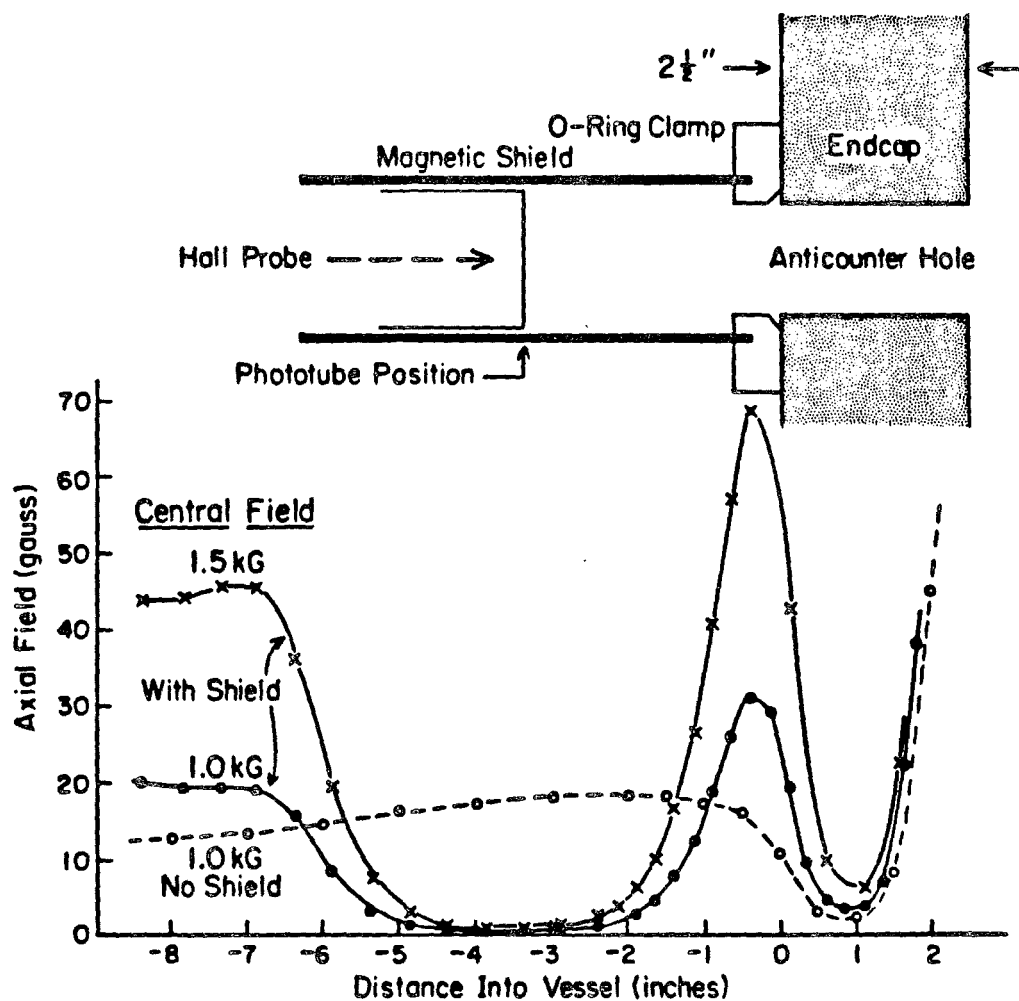


FIG. III.16 - Axial component of fringe field viewed at anticounter position

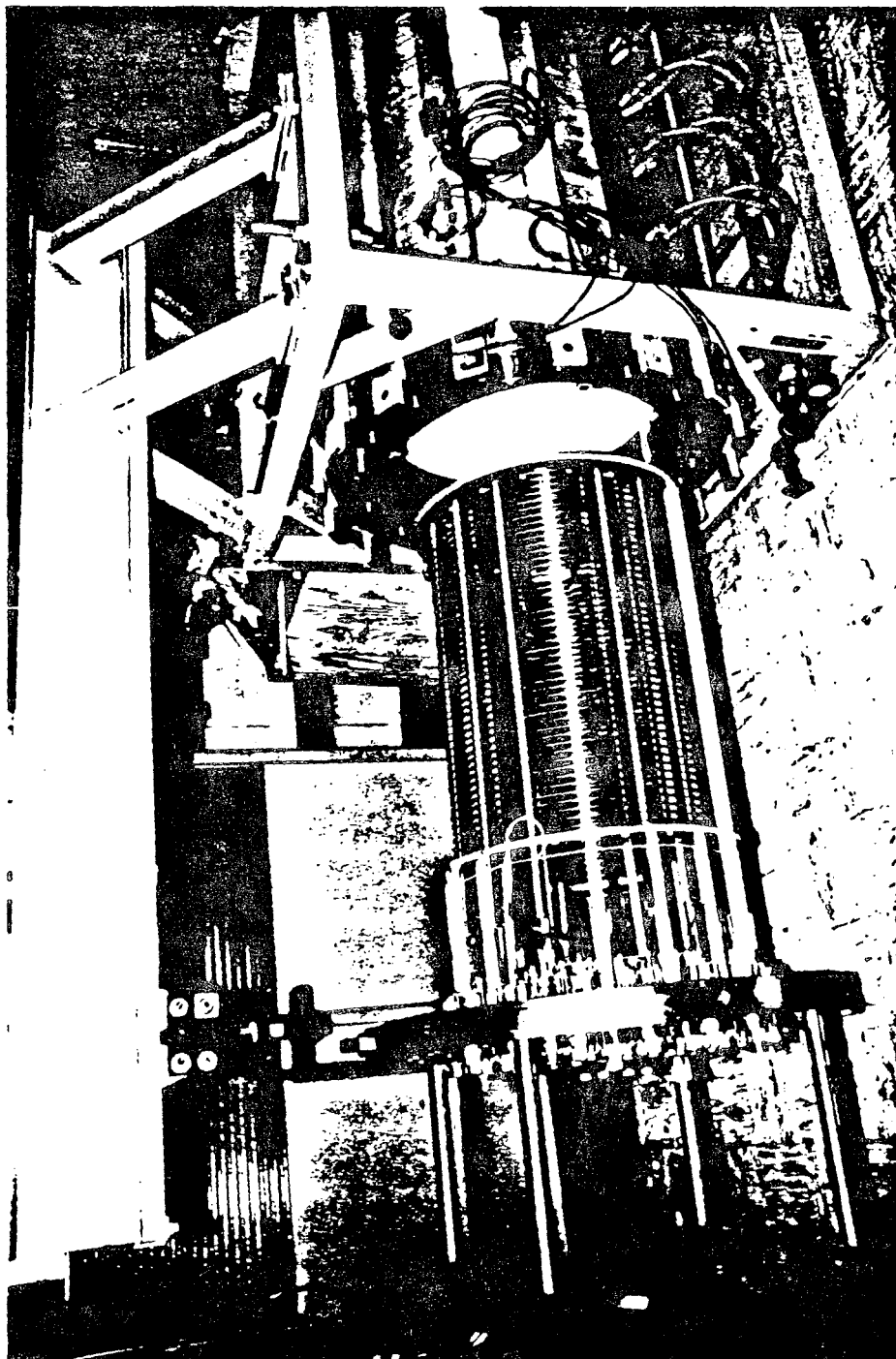
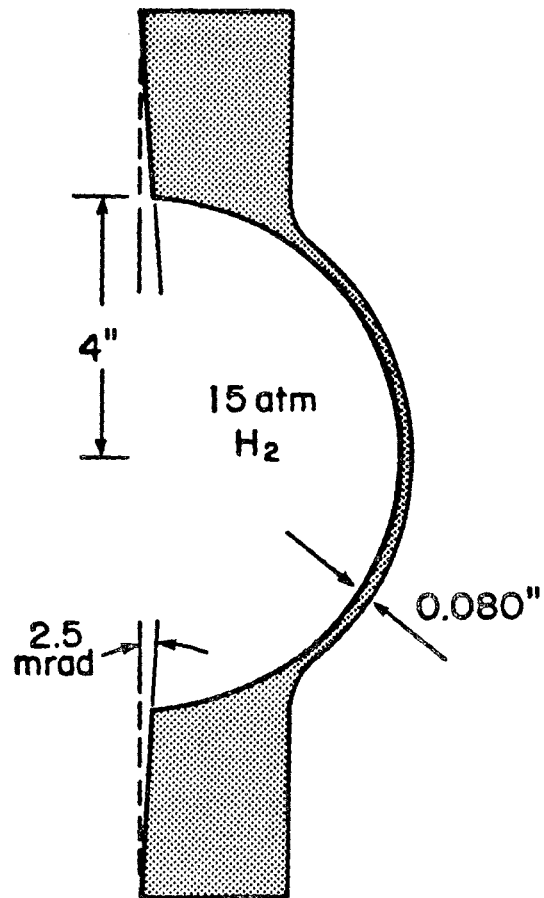


FIG. III.17 - Downstream endcap and TPC  
assembly extracted from TREAD



Aluminum Exit Window

FIG. III.18

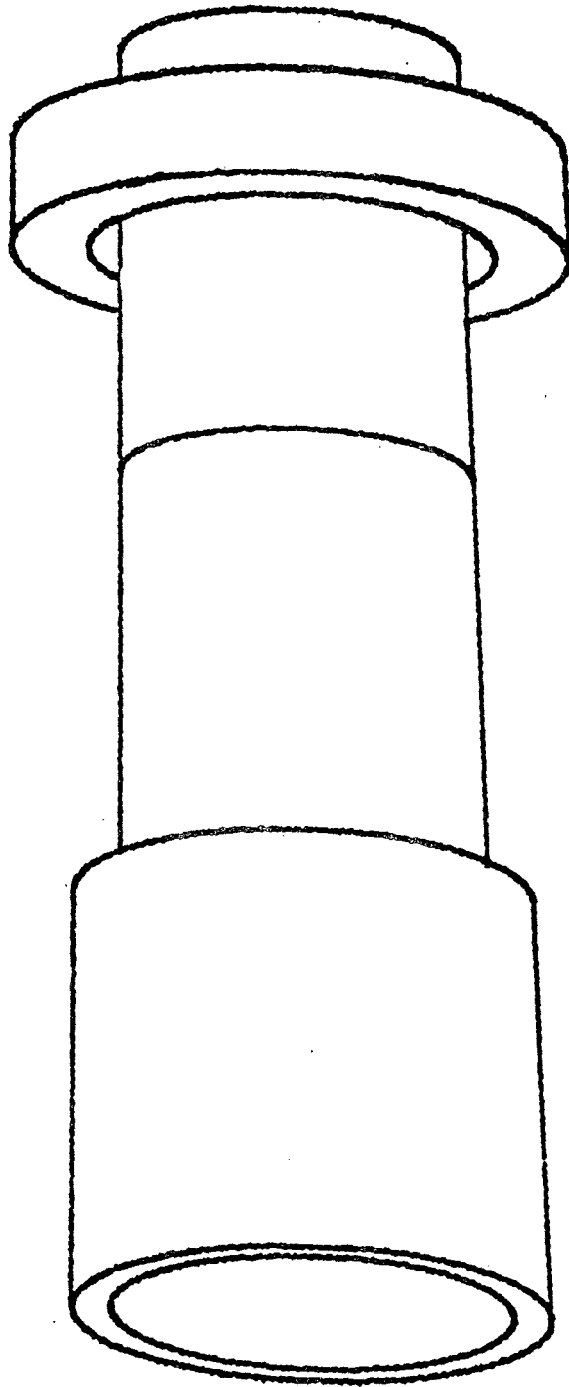


FIG. III.19 - Pulse height counter light  
pipe with O-ring clamp

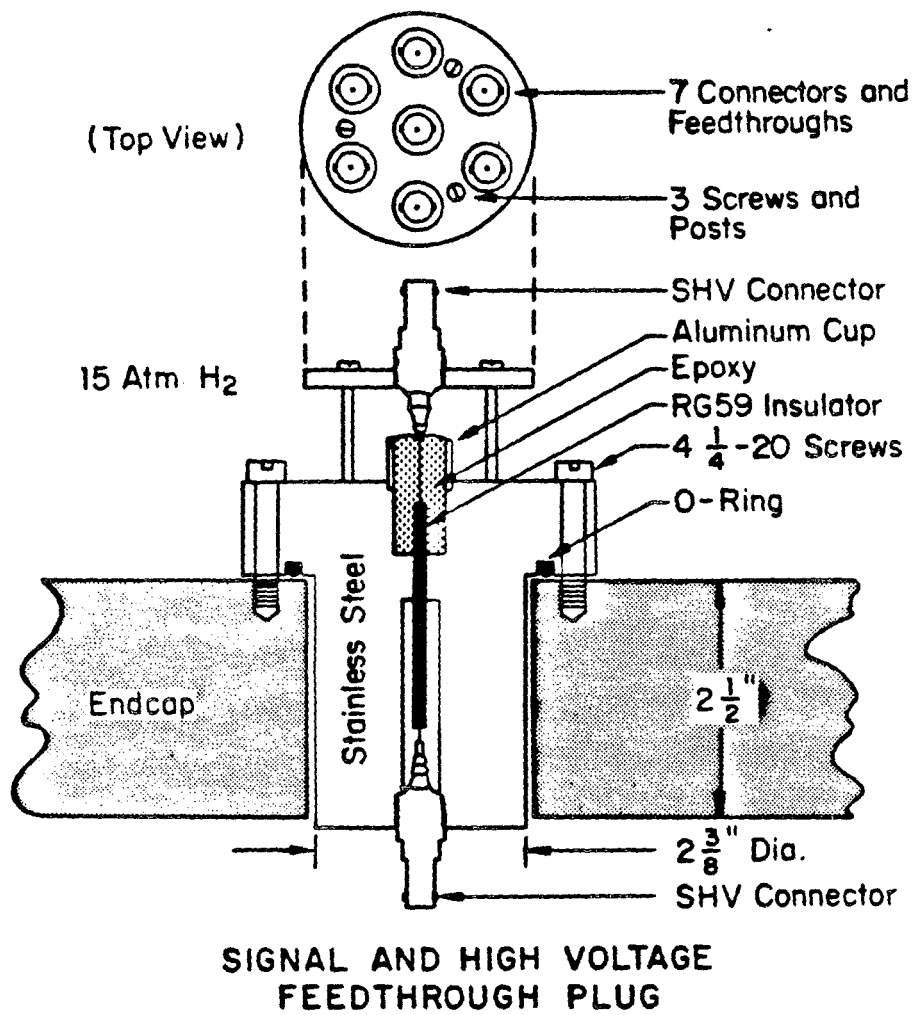
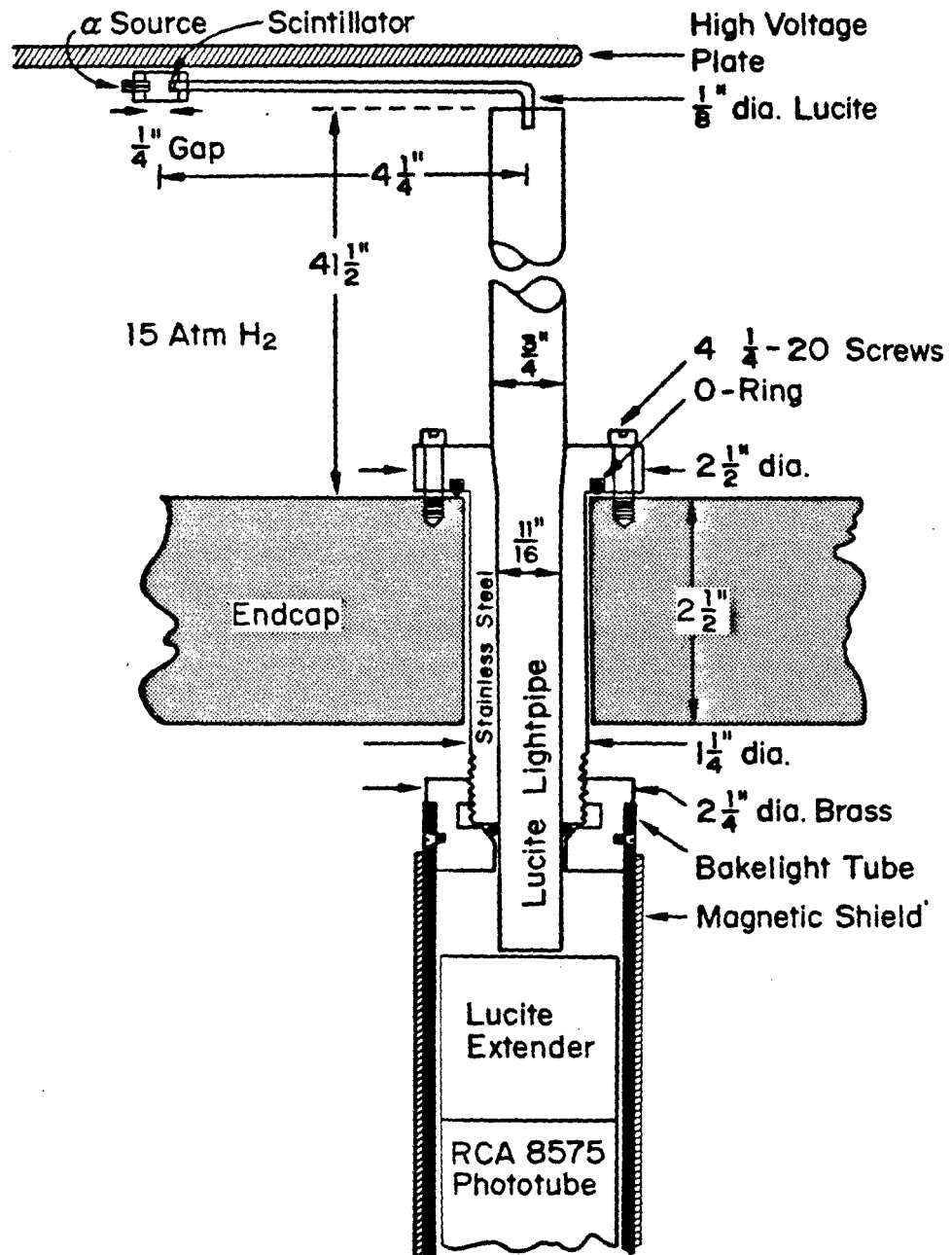


FIG. III.20



ALPHA SOURCE ASSEMBLY

FIG. III.21



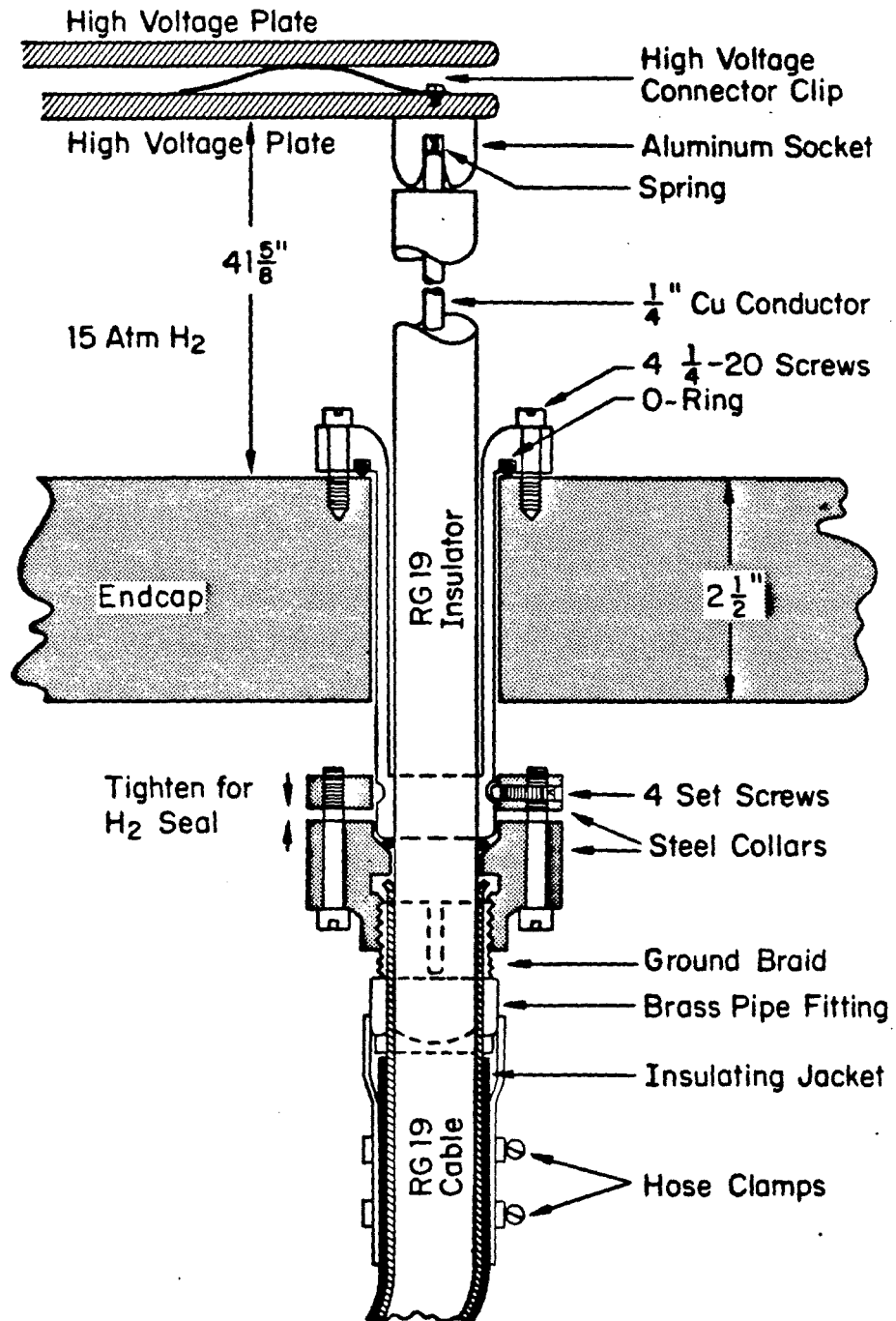


FIG. III.22 - -130 kV high voltage feedthrough

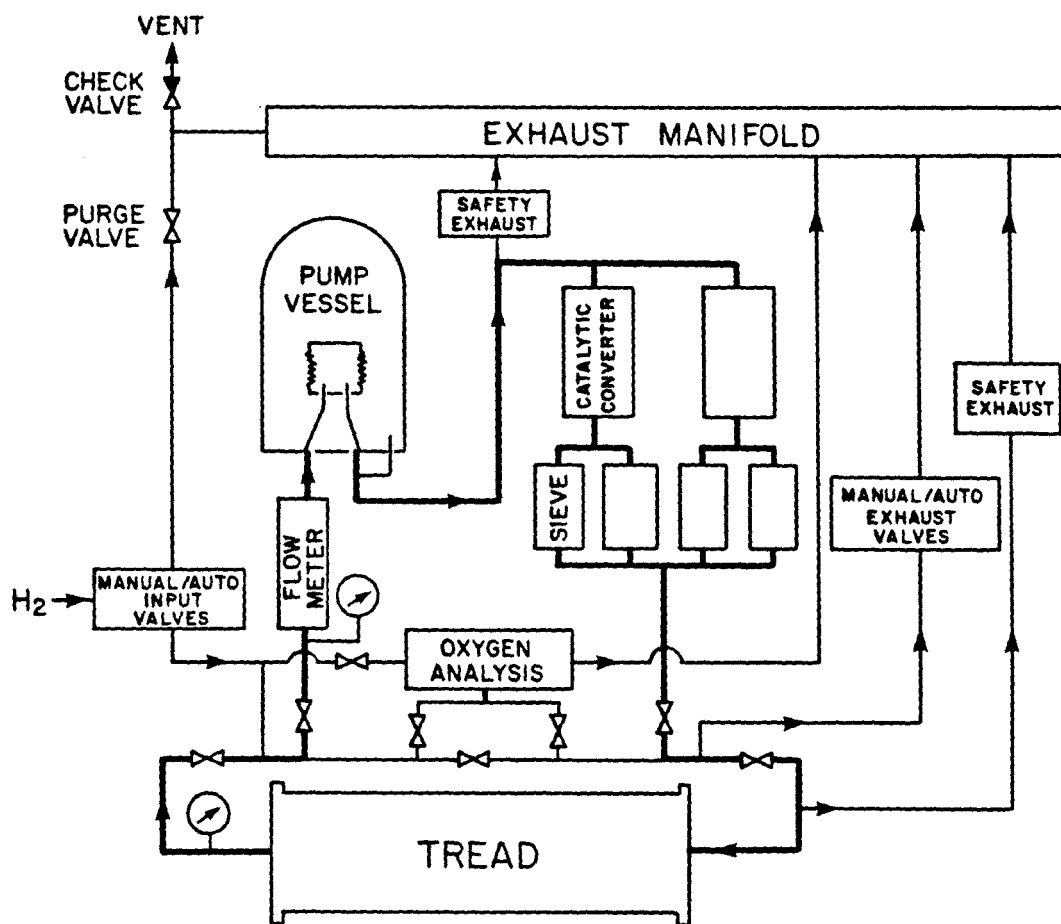


FIG. III.23 - Schematic diagram of the gas circulation and purification system

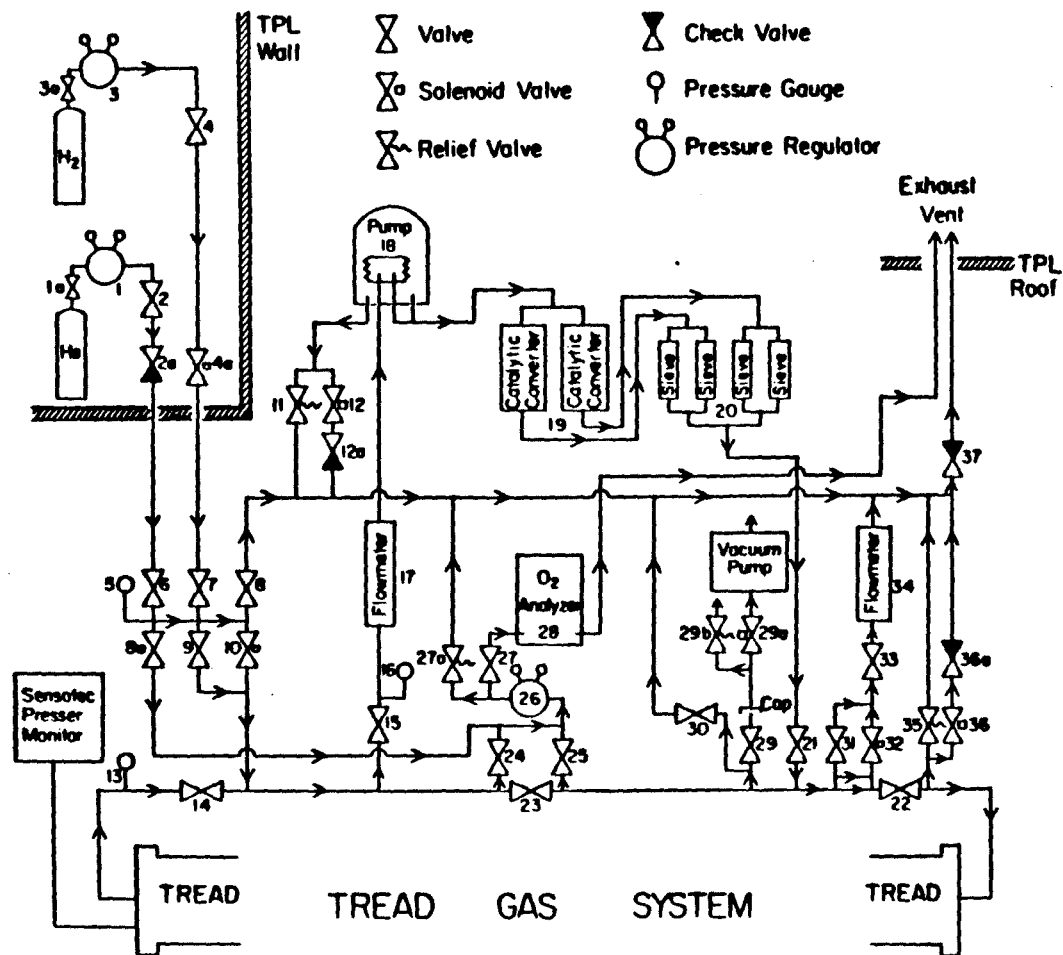


FIG. III.24

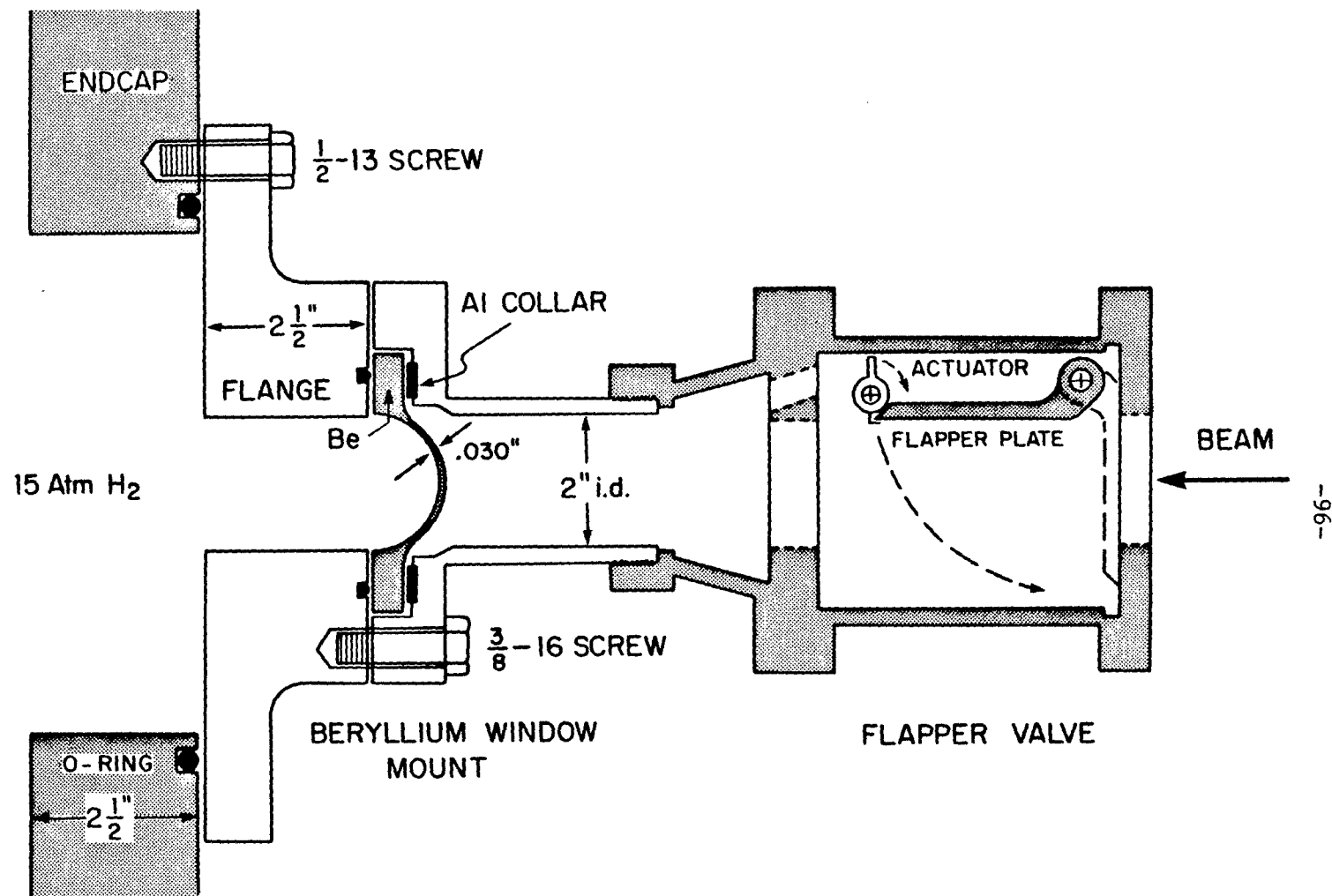


FIG. III.25

## CHAPTER IV. THE TAGGED PHOTON BEAM

As explained in Chapter II., the calculation of  $M_x^2$  using the Recoil Technique requires one to know the momentum,  $p_\gamma$ , of the incident photon. Fermilab's Tagged Photon Facility serves the dual purpose of providing the beam of incident bremsstrahlung photons and making the measurement of each photon's momentum. It was the responsibility of Fermilab's Proton Department to maintain the Tagged Photon Facility and oversee its proper use by experimenters.

The Tagged Photon Facility is located in the Proton-East experimental area. The main components of the facility are the electron beam, the tagging system, the forward electromagnetic detector (called the "C-counter"), and the tagging system electronics. A complete and detailed description of each of these components appears in the Ph.D. dissertation of John Cumalat (Cumalat,1977). The dissertation describes a measurement of the photon total cross section on protons in a liquid hydrogen target from 45 to 182 GeV/c. In this chapter, I present a brief description of the components of the Tagged Photon Facility, focussing on changes and improvements made since 1977. Then I explain the calibration procedure we use to convert the information from the tagging system to the quantity,  $p_\gamma$ , we need to calculate  $M_x^2$  for each recoil event.

### IV.A. THE ELECTRON BEAM

Figure IV.1 is a schematic diagram of the electron beam used to produce the bremsstrahlung photons which collide with protons in TREAD.

400 GeV primary protons from the accelerator are directed to the Proton-East area and strike the 40 cm long beryllium target, TEBY. Four dump magnets sweep charged secondary particles from forward neutral particles which are predominantly neutrons and gammas from neutral pion decay. 36% of the gammas produce  $e^+e^-$  pairs in a 1/8" Pb converter. Electrons from the  $e^+e^-$  pairs are then momentum-selected, focussed, and transported to the bremsstrahlung photon radiator 30 meters upstream of TREAD.

The electron beam was designed to have good momentum resolution, to have low pion yield relative to electrons, to cover a large energy range, and to have a small amount of beam halo. The first set of horizontal bending magnets provide the momentum dispersion and steer the beam away from the forward cone of muons produced by protons in the beam dump. Collimators define the momentum to  $\pm 2\%$  and reduce the pion contamination to about 1% at 100 GeV/c. The final beam line elements are bending magnets rather than focussing quadrupoles, so off-energy particles are swept out of the beam.

The "cleanness" of recoil events recorded by TREAD and the electronic dead time were greatly influenced by the electron beam halo and beam interactions upstream of the photon radiator. For this reason, special attention was paid to the electron beam tune and beam losses during data taking. Documented tuning procedures and guidance from Fermilab experts were available for experimenters. Remotely controlled Segmented Wire Ionization Chambers (SWIC's) could be inserted at various points along the beam's path to allow one to view horizontal and vertical beam profiles and make adjustments to appropriate magnet settings. Figures IV.2 through IV.5 show horizontal and vertical profiles at four different points in the beam line when the beam is tuned optimally at 137 GeV/c. A Polaroid camera was used to photograph the SWIC monitor which was located in the counting room. The dots on the profiles reflect the 1 mm wire spacing of the SWIC's.

The positions of the four SWIC's are indicated in Figure IV.1. Figure IV.2 shows the profiles of the primary proton beam upstream of the TEBY target. Figure IV.3 shows the electron beam after it has been dispersed horizontally for momentum selection; the horizontal dispersion can be seen in the bottom profile. Figure IV.4 shows the electron beam after collimation and horizontal focussing. Figure IV.5 shows the profiles of the photon beam just before it enters TREAD.

The cross sectional size of the photon beam entering TREAD is 2 cm horizontal  $\times$  1.2 cm vertical, with angular divergence of 0.44 mrad horizontal and 0.14 mrad vertical.

The photon data from March and April of 1982 was collected with the electron beam nominally tuned to 137 GeV/c. Studies were performed to determine the true electron momentum for a given nominal tune. This was done by calculating the field integrals in the bending magnets and measuring the deflection of electrons in the magnets with the SWIC's. The SWIC's were accurately surveyed before this procedure. The result was that the true electron momentum is 8% higher than the value of the nominal tune. Hence, tuning the beam at "137 GeV/c" yields a beam momentum of 148 GeV/c.

#### IV.B THE TAGGING SYSTEM AND THE C-COUNTER

Figure IV.6 is a schematic of the tagging system. The electrons pass through a tungsten radiator whose thickness corresponds to 20% of a radiation length. Bremsstrahlung photons are generated, to a good approximation, with the characteristic  $1/k$  energy spectrum. A tungsten radiator was chosen over copper to suppress low energy photons which initiate background interactions in TREAD. The three tagging magnets deflect recoil electrons into the tagging counters and noninteracting electrons into a beam dump made of tungsten, steel, and

concrete. A large vacuum vessel encloses the photons and recoil electrons to prevent interactions with air or windows.

A set of appropriately placed anticounters, A1-A11, serve to veto false tags in which there is no associated bremsstrahlung photon (trident events) or in which the recoil electron energy is incorrectly measured (due to knock-on electrons produced by the recoil in the radiator). Two other anticounters, Dump1 and Dump2, are located at the electron dump to veto events with very low energy bremsstrahlung photons or with two or more electrons arriving at the same time. The muon counters between the concrete shielding blocks had been used as anticounters by previous experiments, but these counters cover an area much larger than the cross section of TREAD. Instead, a smaller "front anticounter", described in Section III.C.9, was mounted on the front of TREAD to veto muons.

Figure IV.7 shows the 13 tagging counters, L1 to L13, used to measure the energy of recoil electrons. The active area of these counters allows photons to be tagged in the energy range  $0.45E_e < E_\gamma < 0.93E_e$ . L1 and L2 are composed of 40 alternating layers of 1/4" lucite and 1/4" lead. L1 is used as an anticounter in order to enhance the high energy end of the  $1/k$  bremsstrahlung spectrum. Tagging counters L9-L13 are lead glass shower counters.

Prior to our data-taking period beginning in January, 1982, tagging counters L3-L8 were also lead glass shower counters. But high rates in these counters caused radiation darkening and required them to be cleared periodically with ultraviolet light. To eliminate this inconvenience, the L3-L8 lead glass blocks were replaced by lead-lucite sandwich counters. Like counters L1 and L2, each counter consists of 40 alternating layers of 1/4" lucite and 1/4" lead. The active lucite cross section of each counter is 2 1/2" horizontal  $\times$  5" high. The 20 lead pieces are continuous horizontally across the six sandwiches, so their dimensions are 15"  $\times$  5"  $\times$  1/4". Because of an error in



installation, the most upstream layer of each stack is lucite, so the counters are only 19 radiation lengths deep. Light pipes fan the 20 lucite layers of each counter to a single photomultiplier tube.

In front of the tagging counters is an overlapping "picket fence" hodoscope of scintillation counters, H1-H13. These scintillators define the vertical acceptance of the tagging shower counters. Combinations of counter coincidences in this array define 33 tagging channels across the face of the shower counter bank. The overlap region between two scintillators is centered on one of the shower counters and defines a region in that counter from which very little energy from an electron-initiated shower is lost. The hodoscope signals are used in combination with the tagging counter signals for triggering and for the conversion of the tagging system information to photon energy.

The electronics and triggering system for the Tagging System is independent of the electronics for TREAD. A "good tag" signal is produced by the tagging system if a match-up between the hodoscopes and the tagging shower counters occurs without an in-time signal from one of the anticounters. This signal is referred to as  $\text{TAG} \cdot \bar{\text{A}}$  in the description of the trigger for a proton recoil in TREAD, as described in Chapter V.

Ionization generated in TREAD by the interactions of beam halo, low energy bremsstrahlung, synchrotron radiation, and muons caused high singles rates on the sense wires and presented a significant background problem. We made special efforts to reduce beam halo and provide a clean photon beam by surrounding the beam pipe just upstream of TREAD with lead bricks, placing lead "donut" collimators in the beam pipe, and stuffing lead wool in cracks around the pipe.

The forward electromagnetic detector, called the C-counter, is a total absorption lead-scintillator sandwich counter designed to measure the energy of electromagnetic showers. It is 2.5" wide  $\times$  5" high and is

located about 16 meters downstream of the tagging counters, centered on the photon beam.

#### IV.C. TAGGING SYSTEM CALIBRATION

The momentum of a recoil electron can be measured from its deflection in the tagging magnets, from the pulse height of the shower it generates in the tagging counters, or from a combination of the two. We rely on the magnetic approach. This makes the algorithm for determining the incident photon energy immune to the gain variations of the tagging counters. In particular, the lead glass counters, L9-L13, have unstable gains and poor resolution due to prolonged exposure to radiation.

Each of the 33 tagging bins, which are defined by the hodoscope/tagging counter match-ups, corresponds to a certain fraction of the original electron beam momentum. The correspondence between tagging bin and recoil electron energy is established with two different calibration runs. First, with the photon radiator out and the tagging magnets off, the 148 GeV/c electrons deposit all of their energy in the C-counter, yielding a full-energy C-counter pulse height. Then, a "Tag Only" calibration run is taken with the radiator in and the tagging magnets on. Bremsstrahlung photons (which do not interact in TREAD) deposit their energy in the C-counter while the recoil electrons are deflected into the various tagging bins. C-counter pulse height distributions are collected for each of the 33 tagging bins, and peaks of these distributions are scaled to the full-energy peak to determine the energy assigned to the corresponding tagging bin.

The energy calibration for the tagging bins assumes the linearity of the C-counter. The linearity of the C-counter was checked by running electrons of several different energies into the counter. In addition, during calibration runs with 148 GeV/c electrons, a peak corresponding

to 296 GeV/c was obtained from events with two electrons in the same rf bucket.

The energy of an incident bremsstrahlung photon is essentially the difference between the electron beam energy and the final-state electron energy measured by the tagging system. For some events, however, an electron produces more than one bremsstrahlung photon in the radiator; one interacts in TREAD and the others deposit their energy in the C-counter. For this reason, the energy of interacting photons is determined from

$$E_{\gamma} = E_e - E' - E_c \quad (\text{IV.1})$$

where  $E_e$  is the electron beam energy,  $E'$  is the energy recorded by the tagging system, and  $E_c$  is the energy in the C-counter. Figure IV.8 shows a typical photon spectrum which results from the "137 GeV/c" electron beam.

We estimate  $\pm 2\%$  resolution in the determination of  $E_{\gamma}$  for  $E_{\gamma}$  above about 75 GeV. The energy resolution of the C-counter is not as good as that of the tagging system, and the tagging system resolution and efficiency deteriorates for photons below 75 GeV. For these reasons, the energy resolution for photons below 75 GeV is estimated to be a factor of 2 to 4 worse than for those above 75 GeV.

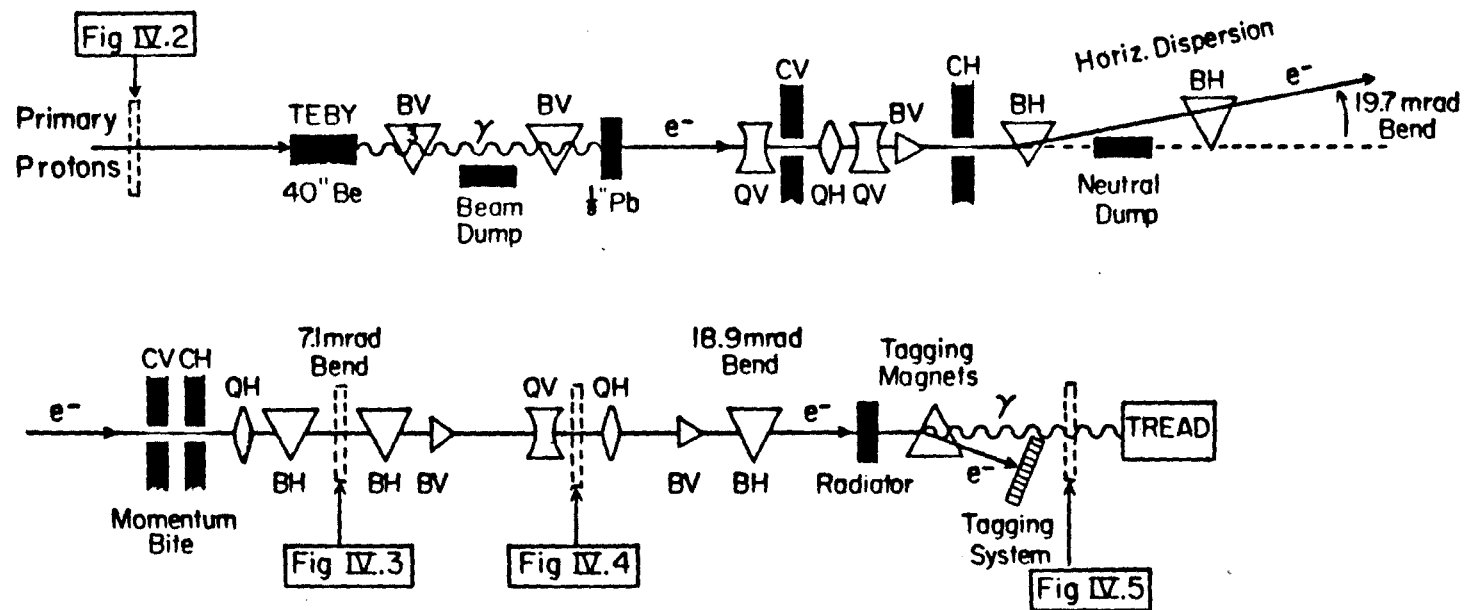
#### IV.D. THE PION BEAM

To form a negative pion beam, the 1/8" electron radiator in the neutral beam was replaced with 4" of lead. This represents 0.6 nuclear interaction lengths and 18 radiation lengths. The added thickness suppresses high energy electrons and allows neutrons in the beam to produce pions. The pion beam requires the downstream photon radiator to be out. The radiator can be removed by remote control from the counting room.

#### IV.E. RUNNING CONDITIONS

During the March-April 1982 data taking, the photon beam contained about  $1 \times 10^6$  tagged photons per pulse in the energy range  $70 < E_\gamma < 140$  GeV. The pion data were collected with a pion flux of about  $5 \times 10^4$  per pulse. This pion intensity was chosen so that the on-spill sense wire current in each TPC (about 20 nAmps) would be the same for photon and pion running. The pulse repetition period of the accelerator was about 10 seconds and the spill time was about one second.

Bending Dipoles	Focussing Quads	Collimators	
BH	QH	CH	Horizontal
BV	QV	CV	Vertical



## ELECTRON BEAM LINE SCHEMATIC

FIG. IV. 1



FIG. IV.4 - Electron beam profile after horizontal focussing

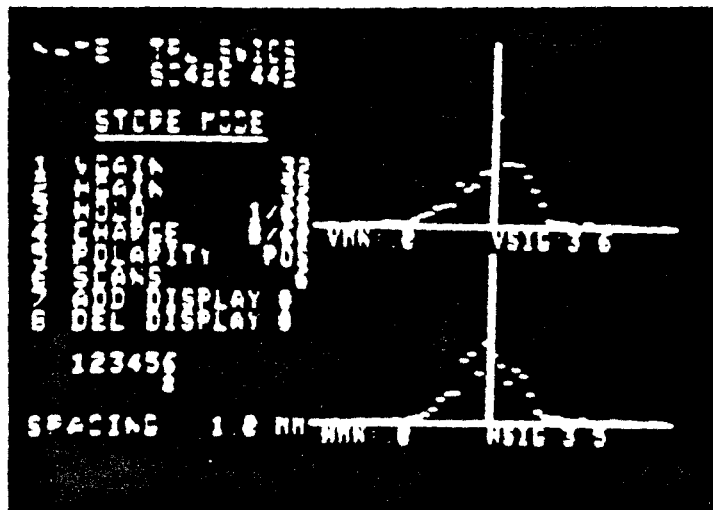
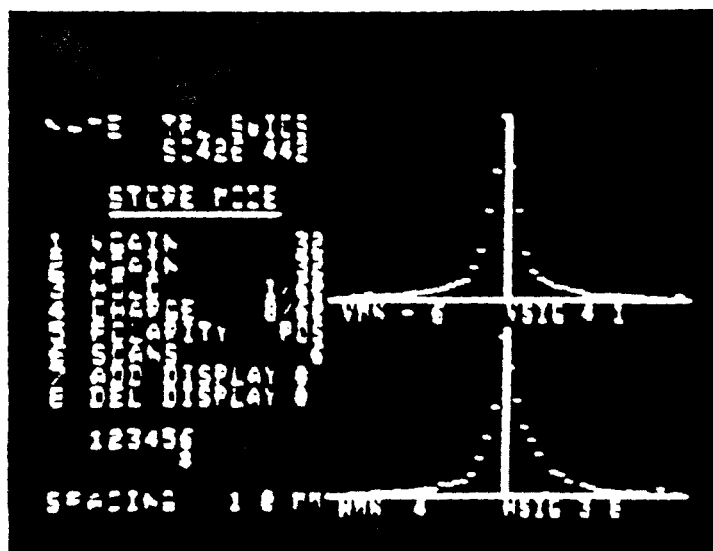


FIG. IV.5 - Photon beam profile just upstream of TREAD



## Tagging System Schematic

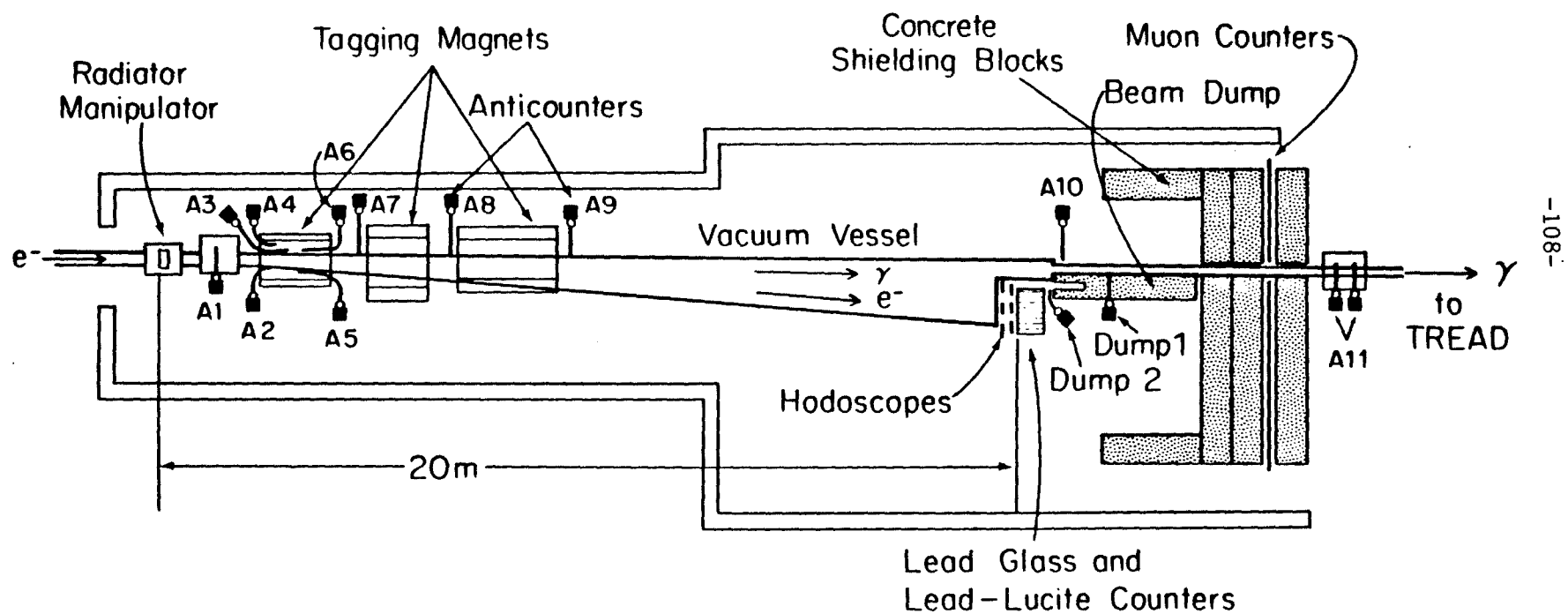


FIG. IV.6



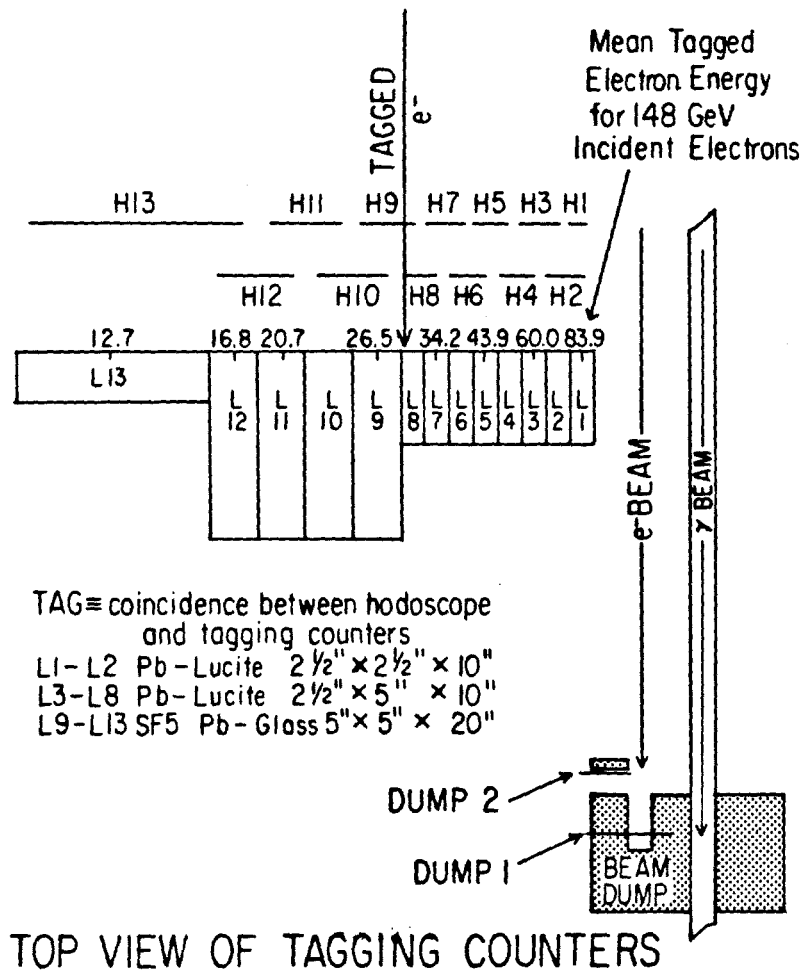


FIG. IV.7

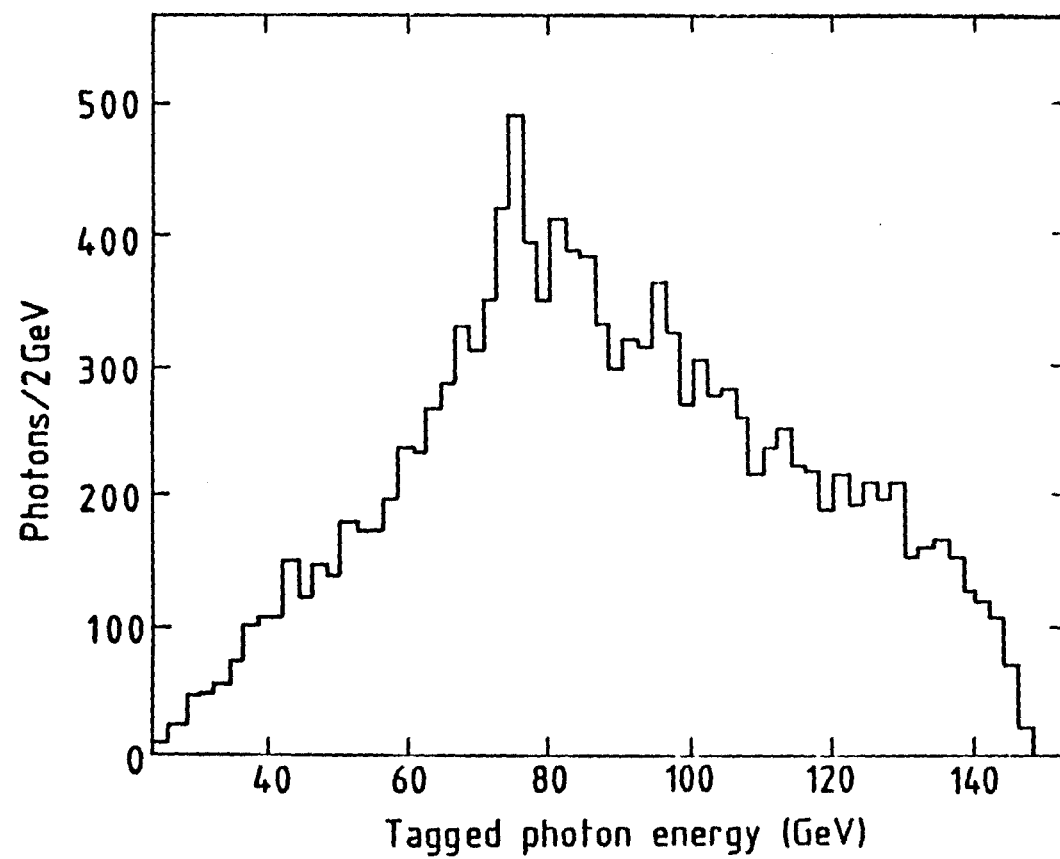


FIG. IV.8 - Tagged photon energy spectrum

## CHAPTER V. DATA ACQUISITION

It is the job of the data acquisition system to decide when a candidate for a diffractive photon dissociation event has occurred and to record the associated information from TREAD and the Tagging System. The data acquisition system serves the auxiliary purpose of regularly recording the various parameters for calibrating and monitoring TREAD. This chapter describes the trigger logic for photon dissociation events, the data acquisition hardware, and the trigger logic for pion runs and the various calibration runs taken throughout the experiment. The chapter will close with a summary of the data collected during 1982.

### V.A. PHOTON TRIGGER LOGIC

Figure V.1 is a schematic diagram of the ingredients in the data acquisition process for photon-initiated recoil events. Simply stated, analog output signals (some of them amplified) from TREAD's pulse height counters, sense wires, and front anticounter are discriminated, and the resulting logic ("yes"/"no") pulses, along with logic pulses from the Tagging System, pass through coincidence and anticoincidence circuits to form signals ("triggers") which initiate the retrieval of digitized information and the writing of an event to tape. A candidate for a recoil event is required to pass two successive trigger levels: a "fast" trigger, indicating that a photon-initiated recoil proton has deposited energy in a pulse height counter, followed by a "slow" trigger, indicating that the sense wires have detected the ionization track of the recoil.

Specifically, the fast trigger is defined by the expression

$$\text{FAST TRIGGER} = (\text{TAG} * \overline{\text{A}}) * \overline{(\text{C} > 40 \text{ GeV})} * \text{P}_i * \overline{\text{FA}}$$

where the stars indicate logical "AND".  $(\text{TAG} * \overline{\text{A}})$  is the "good tag" signal from the Tagging System described in Chapter IV, and  $\text{P}_i$  is a signal from any of the 32 pulse height counters.  $\overline{\text{FA}}$  represents the front anticounter in anticoincidence; the length of the front anti veto gate is 1  $\mu\text{sec}$ .  $\overline{(\text{C} > 40 \text{ GeV})}$  indicates that fast triggers are inhibited when the C counter registers electromagnetic energy greater than 40 GeV. The latter requirement helps to eliminate background events in which the  $\text{P}_i$  signal is not associated with an interacting photon and double bremsstrahlung events in which two photons are created in the radiator. The 1/4" anticounters which surround the pulse height counters inside TREAD are not used in the fast trigger; events in which the recoil punches through a pulse height counter are rejected during offline analysis. The timing of the fast trigger coincidence is determined by a narrow  $(\text{TAG} * \overline{\text{A}})$  pulse. The fast trigger decision occurs within about 100 nsec of the arrival of the constituent analog signals. At this time, appropriately delayed pulse heights and arrival times of the signals from the pulse height counters, anticounters, multiplicity counters, and Tagging System Pb-glass blocks are digitized and stored for later retrieval in CAMAC analog-to-digital converters (ADC's) and time-to-digital converters (TDC's).

Further fast triggers are then "gated off" for 200  $\mu\text{sec}$  to allow the recoil's ionization trail to drift to the upstream or downstream sense wire plate. As explained in Chapter III, the segmenting of the octagonal sense wires into halves partitions the TPC's into 8 azimuthal sectors with two counters each. The pulse height counter that initiates a fast trigger determines which (upstream/downstream) half of TREAD contains the track and which combination of eight wire-halves should

detect the track. During the 200  $\mu$ sec Sense Wire Enable Latch (SWEL), one of two "Hardware Track Finders", designed and constructed at Rockefeller University, searches for pulse patterns from the eight sense wire halves which correspond to the sector of the fast trigger. A slow trigger occurs when the arrival times of the signals from a minimum of four of the appropriate sense wire halves are within 35  $\mu$ sec of each other. During the SWEL, the arrival times (measured with respect to the fast trigger) of up to 8 hits on each wire are digitized and stored using a TDC/clock system, also built at Rockefeller University, and CAMAC scalars. However, the pulse height for only one hit is digitized for each wire for a given event. The pulse height selected for digitization is the largest of those received from a given wire up to the time of the slow trigger.

When an event satisfies both trigger requirements, an interrupt signal is sent to the PDP 11/55 computer which supervises the data acquisition. An online experiment-control program, Fermilab MULTI, reads the contents of the CAMAC system and transfers the information for that event to a buffer in the computer's memory. Each event record is an array of 304 16-bit words. When five events accumulate in the buffer, they are written to tape at 1600 bpi (bits per inch).

MULTI can accept different types of triggers with event records in different formats according to "Trigger Type Gates" sent to the computer, as shown in Figure V.1. For example, a beam gate enables the photon triggers just described during the  $\sim 1$  second accelerator spill. After each acceleration cycle, an End of Spill (EOS) record is written to tape. The EOS record contains the temperature and pressure of the gas in TREAD and many quantities scaled during the spill, including the photon beam intensity, singles rates in the counters and wires, and trigger rates. Triggers for pion runs and calibration runs will be described below.

MULTI can perform online arithmetic computations on the entries in incoming event arrays selected according to various criteria. Histograms and correlation plots of computation results can be accumulated and displayed on a graphics terminal for monitoring. Graphical representation of events can also be displayed. Figure V.2 is an online "picture" of an event in the downstream TPC "frozen" at the time of the fast trigger. The high voltage plate and two counters are outlined, and the arrow gives the photon beam direction. Each star represents a hit recorded on a sense wire half during the SWEL, and the wire halves (A or B) corresponding to the two counter sectors are indicated. A track finding routine selects approximately colinear points, performs a least-squares fit to a straight line, and a line is drawn to mark the recoil proton's path. Events which satisfy the trigger requirements range from very clean (only one hit on each of the eight appropriate wire halves) to very dirty (eight hits on each wire half with no recoil track found among the hits).

Figure V.3 is an event picture similar to the TPC cross section, Figure III.5. The counter which initiated the fast trigger is marked, and the wire hits of a recoil track found by the track finder are shown. The small circles on the sense wire corners indicate where they are broken into halves.

#### V.B. SOME HARDWARE DETAILS

The photomultipliers for all of the scintillation counters are RCA 8575 tubes with bases electrically isolated from TREAD and each other. In the counting room, the analog signals from the pulse height counters and anticounters are resistively split; half of each signal is connected to an ADC, half is amplified  $\times 10$  and used in the fast logic. The fast logic consists of NIM-standard amplifiers, discriminators, coincidence units, fan-ins, fan-outs, and gate generators made by Lecroy Research Systems or EG&G Ortec. The counter pulse heights are digitized by a

Lecroy 2280 System which employs three Model 2285 ADC modules. Each module has 24 twelve-bit (4095 counts) charge-integrating ADC channels with 10 counts/pC gain. A processor module fans out a single enabling gate to all ADC channels at the time of the fast trigger. Two different gate widths, 1  $\mu$ sec and 440 nsec, were used during the experiment. A long gate is required in order to integrate the NaI calibration pulses whose decay times are 300-400 nsec.

The arrival times of appropriately delayed pulse height counter logic pulses are digitized by CAMAC Model 2228A 11-bit TDC's set for 50 psec/count resolution. The fast trigger serves as the start signal for the TDC's.

Each TPC sense wire is coupled to its high voltage and a signal preamplifier through a preamplifier box mounted just outside TREAD, inside an inerting hood. The high voltage on each sense wire can be adjusted independently. The coupling to the preamplifier is through a high voltage blocking capacitor which is encapsulated in epoxy to prevent electrical discharges and breakdown. The preamplifiers, designed around an op-amp/driver hybrid integrated circuit (Model TRA510, manufactured by Lecroy), have 35 nsec rise time, 2.5  $\mu$ sec decay time and 1 V/pC gain. These characteristics are well suited to the slow drift times and low sense wire gain in hydrogen. In the counting room, the preamp signals are amplified further using  $\times 10$  linear amplifiers and are fanned out to discriminators for drift time measurements and the slow trigger, and to analog circuits for measurements of pulse height ( $dE/dx$ ). Since we are only interested in recoil protons with  $dE/dx$  six to ten times that of minimum ionizing particles, the sense wire gain and the discriminator thresholds are set to make the wires inefficient for minimum ionizing tracks. With a gain of about 150, only  $> 5$  times minimum ionizing tracks trigger the discriminators.

As shown in Figure V.2, it is often the case that several hits not associated with the recoil track appear on the sense wires during the

SWEL. In order to maximize multihit capability while minimizing the expenditure on electronics, multiplexing circuits are used in the sense wire logic system to digitize only the information from the wires associated with the sector of the fast trigger. If the fast trigger is in the upstream (downstream) half of TREAD, the TDC system digitizes the hit times only for the 16 wire-halves on the upstream (downstream) sense wire plate. The TDC system works as follows: At the time of the fast trigger, the pulse train from a 50 Mhz clock is fanned out to the inputs of eight CAMAC scaler channels for a given wire-half. As the hits are received on the wire, the pulse train into successive channels is stopped. Independent of the time a given slow trigger is satisfied, the TDC's count for the full duration of SWEL. If a wire registers fewer than eight hits during SWEL, the "unused" hits appear as the number of counts which corresponds to the length of SWEL. The 50 Mhz clock yields a 20 nsec least count resolution.

The pulse height measurements proceed as follows: At the time of the fast trigger, the analog signals from the outer six sense wire halves in the trigger sector are multiplexed to six peak-detect/sample-and-hold circuits. These circuits are designed from operational amplifiers with a high gain-bandwidth product (80 Mhz) in order to respond uniformly to signals with the wide range of rise times we observe from tracks of different drift times, angles, and  $dE/dx$ . The peak detectors hold the value of the largest pulse height they receive. At the time of the slow trigger, the values are digitized by an Ortec AD811 12-bit ADC, and they are written to tape at the end of the SWEL.

#### V.C. OTHER TRIGGERS

The trigger sequence for pion-initiated dissociation events is the same for photon-initiated events with the exception that, in the fast trigger, the signals from the Tagging System and the C-counter are replaced by a "beam" signal from the upstream-most multiplicity counter.



Triggers for calibration data fall into two categories: off-spill triggers, which are accepted during the ~10 seconds between beam spills, and on-spill triggers for dedicated calibration runs.

During both photon and pion running, off-spill triggers were accepted to record NaI calibration signals from the pulse height counters and "far" alpha source drift times for drift velocity monitoring. Similar to the recoil triggers, each of the off-spill triggers has a "fast" followed by a "slow" requirement. The fast part of a NaI trigger is a discriminated signal from any one of the 32 pulse height counters; for the alpha source trigger, it is a signal from the ZnS scintillator piece. The slow part of each trigger capitalizes on the long decay times of the NaI and ZnS analog pulses to differentiate the desired signals from other signals (phototube noise and, in the case of NaI, cosmic rays) in the counters. Integrating amplifiers give output pulse heights proportional to the total charge in the NaI and ZnS analog pulses, and discriminators in the slow logic screen against unwanted background triggers.

Four types of dedicated calibration runs were taken:

1.) Longitudinal muon runs for counter calibration

The trigger for these runs consists of the front anticounter in coincidence with coincident signals from any upstream-downstream counter pair. There is no slow logic requirement. During these runs, the analog signals from the pulse height counters into the ADC's are attenuated by 6 db (a factor of 2) to accomodate the large pulse heights.

2.) "Tag only" runs for Tagging System calibration

The  $(TAG \cdot \bar{A})$  signal described in Chapter IV serves as the trigger.

### 3.) Electron beam runs

Electron beam runs are used to calibrate the multiplicity counters and the C-counter. The electron beam travels into the TPL when the photon radiator is out and the tagging magnets are off. The trigger for an electron run is a signal from one of the multiplicity counters.

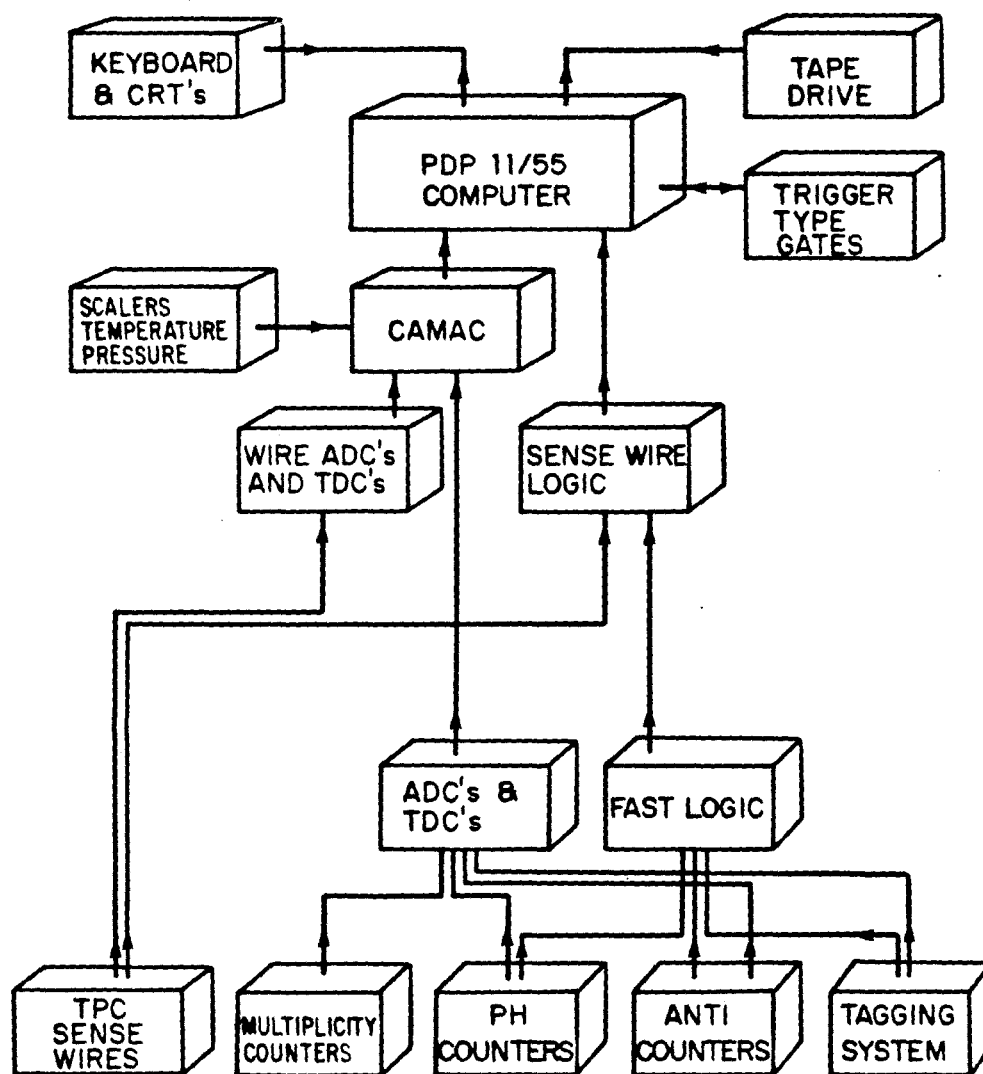
### 4.) Cosmic ray runs

Cosmic ray runs have a fast and a slow trigger. The fast trigger consists of coincident signals from diametrically opposed pulse height counters, and the slow trigger uses the normal wire coincidence slow logic. These runs are used to study light attenuation in the pulse height counters and anticounters and beam-off spatial resolution, as described in Chapter III.B.3.

## V.D. SUMMARY OF MARCH-APRIL 1982 DATA

The results presented in this dissertation are derived from photon and pion data collected during March and April of 1982. 150 photon tapes and 13 pion tapes were written. Each 2400 foot tape contains approximately 50,000 recoil triggers.

About  $7 \times 10^6$  photon and  $7 \times 10^5 \pi^-$  events were recorded. Of these,  $9.9 \times 10^4$  photon and  $4.6 \times 10^4$  pion events contained "clean" recoil tracks with at least six out of the eight appropriate sense wire halves firing. The final event selection described in Chapter VI.J resulted in 9,000 photon and 9,200  $\pi^-$  events for physics analysis.



## DATA AQUISITION SYSTEM

FIG. V.1

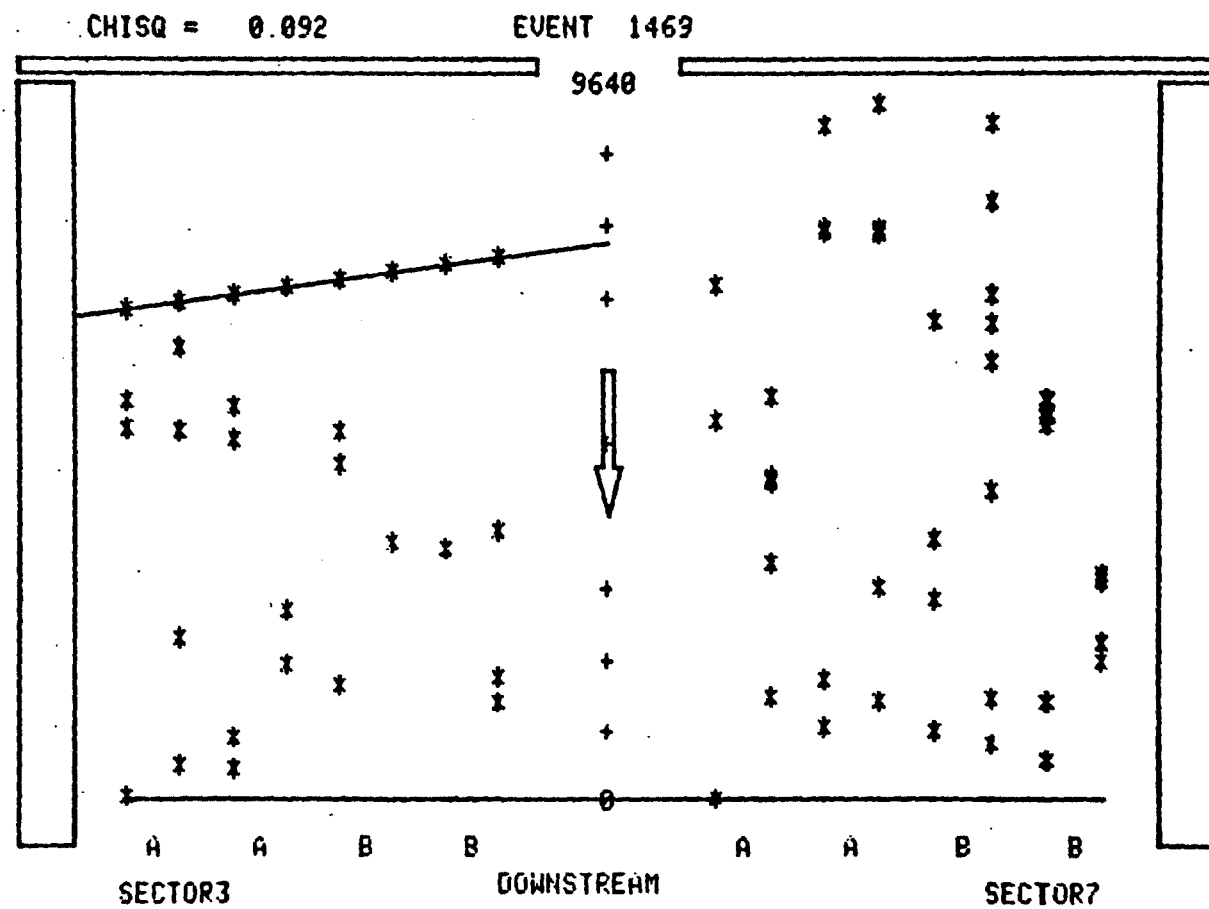


FIG. V.2 - Online event picture of wire hits (side view)

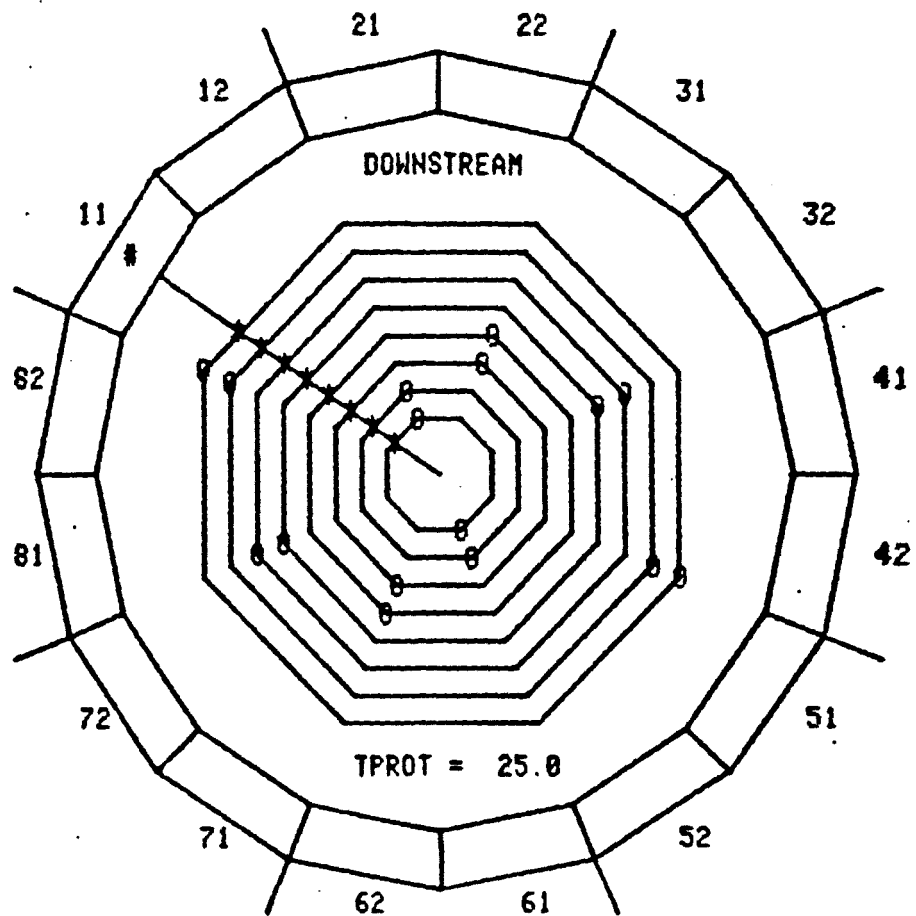


FIG. V.3 - Online event picture (end view)

## CHAPTER VI. DATA ANALYSIS

### VI.A. OVERVIEW

This chapter describes the analysis of incident-photon data (beam energy range 70-140 GeV) and incident-pion data (beam momentum 100 GeV/c) collected during March and April of 1982. The photon data presented here represents just over half of the photon data accumulated in 1982. The pion data represents our total sample. The main computer at Fermilab was used to analyze the counter calibration runs and to produce condensed tapes from the original data tapes. The rest of the analysis was performed on the VAX 11/780 in the Cool-Goulianos Lab at Rockefeller University.

For each set of data, there are two main analysis goals. The first goal is to select as many good proton recoil events as possible from the pool of events which satisfied the particular trigger requirements and were written to tape. The second goal is to convert the recorded information from TREAD and, in the case of the photon data, the Tagging System to the four physical quantities of interest: the recoil kinetic energy,  $T$ , the polar angle,  $\theta$ , the charged multiplicity of the "missing mass" decay products, and the momentum of the incident particle. The procedure for determining the incident photon momentum from the Tagging System is described in Chapter IV. For the pion data, the incident momentum is determined by the beam tune.

The event selection is based on the appearance of a single recoil particle which can be identified as a proton. The determination of the four physical quantities is based on the calibration of the detection

systems which measure these quantities. Indeed, the selection and calibration procedures are coupled in many ways.

The pion data proves to be useful for two reasons. First, since the kinematic regions in  $s$ ,  $t$ , and  $M_x^2/s$  covered by the data from TREAD are very similar to those covered by the 100 GeV/c pion data from E-396, the results of the two experiments can be checked against each other. Second, the ~6000 elastic scattering events in the pion data sample provide a cross calibration between the  $T$  and  $\theta$  measurements in TREAD. This is due to the fact that for elastic scattering the momentum transfer,  $t$ , uniquely determines the polar angle of the recoil proton.

We regard the pion elastic events to be a reference data sample for fine-tuning the calibrations of the  $T$  and  $\theta$  measurements. The pion data was collected over a period of two days in April 1982; the photon data was collected over a period of six weeks. Hence, the pion data is subject to fewer long-term systematic shifts in calibration than the photon data. The photon and pion data were collected under the same physical conditions, i.e., the intensity of the pion beam was adjusted to yield singles rates in the sense wires and counters which were close to those observed during the photon running. We assume that those aspects of the calibrations which are determined by the pion elastic events can be applied to the photon data as well.

The data analysis proceeds through stages of increasing refinement. First-round algorithms and routines are introduced to convert:

- 1.) counter pulse heights to recoil kinetic energies
- 2.) sense wire times to recoil polar angles
- 3.) sense wire pulse heights to recoil ionization energy losses
- and 4.) multiplicity counter pulse heights to final state charged multiplicities.

These four analysis topics are discussed separately in Sections VI.B, VI.C, VI.D, and VI.F, respectively. The anticounters must be calibrated to determine whether a given recoil proton indeed stops in one of the pulse height counters. The anticounter calibration is discussed in Section VI.E. In addition, a small number of background events are rejected with a recoil time-of-flight cut. The conversion of arrival times of counter signals to recoil times-of-flight is discussed in Section VI.G.

Guided by the above calibrations, a set of minimum requirements, or Essential Cuts, are established to select events containing a "clean" recoil particle. Following the Essential Cuts, an anticounter cut and a cut on the quantity  $T \cdot dE/dx$ , i.e. recoil mass, yield a first-round sample of pion and photon events for which the recoil particle is identified as a proton stopping in a pulse height counter. These cuts are described in Section VI.H.

Two refinements then lead to the selection of the final data sample. First, pion elastic events from the first-round sample are used to fine-tune the  $T$  and  $\theta$  calibrations. Pion elastic events are characterized by a charged multiplicity of one and a missing mass equal to the pion mass. Dividing the pion elastic events according to which of the 32 counter/wire combinations detected the recoil for a given event, small adjustments to the  $T$  and  $\theta$  calibrations are made for each combination. That is, the fine tuning of the  $T$  and  $\theta$  calibrations is done counter-by-counter. The cross calibration of  $T$  and  $\theta$  using pion elastic events is described in Section VI.I. Second, as described in Section VI.J, improved  $t$ -dependent recoil mass cuts are introduced which are based on a "truncated mean" algorithm. The final data sample comes from applying the  $T$  and  $\theta$  adjustments and the new recoil mass cuts to those events which survive the Essential Cuts.

Small corrections for geometric acceptance and nuclear interactions in the pulse height counters are applied to the data.



These corrections are described in Section VI.K. A detailed discussion of the measured missing mass resolution for pion elastic events and  $\rho^0$  photoproduction events follows in Section VI.L.

## VI.B. CALIBRATION OF PULSE HEIGHT COUNTERS

### VI.B.1 Conversion of Pulse Height to Kinetic Energy

A recoil proton loses energy by ionization as it travels through the hydrogen gas on the way to a scintillation counter, then loses the rest of its energy in the scintillator. The goal of the calibration procedure for the pulse height counters is to convert the measured pulse height for a given recoil event to the energy loss of the stopping proton in the scintillator. The measured pulse height, which is recorded as a certain number of ADC counts above a pedestal, varies with the amount of light produced by the proton, the attenuation of the light in the scintillator, the gain and linearity of the phototube, and the linearity of the ADC system. The energy loss in the scintillator is then added to the energy loss in the gas to yield the recoil proton's total kinetic energy.

The measured pulse height is first corrected for light attenuation using the z position of the hit in the counter as measured by the TPC in TREAD. As explained in Section VI.B.2, attenuation coefficients for each counter were determined using cosmic ray data. An average attenuation of 26% was measured for signals travelling the full length of a 30" counter.

The first-order algorithm for converting attenuation-corrected pulse height to an energy loss in the scintillator is derived according to a method developed for Experiment 396 (Cool et al., 1981b) in which

1" thick scintillation counters measured the kinetic energy of stopping recoil protons. The starting point is a formula (Craun and Smith, 1970) which successfully describes light production in many organic scintillators :

$$\frac{dL}{dE} = \frac{C}{1 + k_B dE/dx} \quad (VI.1)$$

Here,  $dL$  is the quantity of fluorescence light generated when a charged particle with energy  $E$  loses a quantity of energy  $dE$  through ionization along a path increment  $dx$  within the scintillator,  $C$  is a constant independent of  $E$  and charged particle type, and  $k_B$  is an efficiency parameter which depends on scintillator type and even the particular scintillator batch. The appearance of the  $dE/dx$  term in the denominator reflects the fact that minimum ionizing particles generate more light per unit energy loss than do, say, protons with kinetic energy in the MeV range whose  $dE/dx$  is much larger. That is, the saturation of the light production from a stopping proton is due to the high ionization density along the proton's path in the scintillator.

Equation (VI.1) leads to a function  $E(L)$ , which translates the pulse height,  $L$ , of a stopping proton to its energy loss,  $E$ , in the scintillator in the following manner:

The calibration constant,  $C$ , is periodically determined from pulse heights of beam-associated, minimum-ionizing muons passing longitudinally through the counters. Because  $dE/dx$  is small for these "straight-through" muons, the saturation term in (VI.1) can be neglected. The energy deposited by the muons in 30" of scintillator is calculated (Crispin and Hayman, 1964 and Sternheimer, 1967) to be 155.6 MeV. At the beginning of each data-taking period, the photomultiplier voltages were adjusted so that the center of the muon peak for each counter, having been attenuated by 6 db (a factor of 2), would fall

about 2000 ADC counts above pedestal. Using these numbers as upper limits of integration, Equation (VI.1) can be integrated to yield

$$C = \frac{2 \times 2000 \text{ ADC counts}}{155.6 \text{ MeV}} \quad (\text{VI.2})$$

Assuming the phototube-to-ADC systems respond to light linearly, this establishes a minimum-ionizing energy loss scale for the ADC channel of each counter. Details of the analysis of the muon calibration runs are given in Section VI.B.3.

The saturation term in (VI.1) is non-negligible for recoil protons. An expression

$$\frac{dE}{dx} = \frac{269.15}{E^{0.785}} \quad (\text{VI.3})$$

is obtained by an eye-ball fit to tabulated data (Janni, 1966) of  $E$  (in MeV) vs.  $dE/dx$  (in MeV/gm/cm<sup>2</sup>) for 2-50 Mev protons in scintillator similar to NE110. If the constant,  $k_B$ , were known for our particular scintillator batch, one could integrate Equation (VI.1) to obtain the function  $L(E)$ :

$$L(E) = C \int_0^E \frac{dE'}{1 + k_B \frac{269.15}{E'^{0.785}}} = C I(E) \quad (\text{VI.4})$$

and invert it to obtain  $E(L')$ , where  $L' = L/C$  has units of "light-equivalent" minimum-ionizing energy. Published values for  $k_B$  range from 0.002 to 0.016 gm·cm<sup>-2</sup>·MeV<sup>-1</sup>. We therefore found it necessary to evaluate  $k_B$  from our pion data in an early stage of the analysis. The

value of  $k_B=0.0115$  was determined by requiring that the resulting function  $E(L')$  lead to a missing mass distribution for elastic events centered on the mass of the pion.

To facilitate the inversion to  $E(L')$ , the integral,  $I(E)$ , in formula (VI.4) can be cast in a more convenient form. For a given value of  $k_B$ , an array of  $E$  and  $I(E)$  values were generated by numerical integration, and the resulting points were fit to the function

$$E(L') = a (L'/15)^{b + c \ln (L'/15)} \quad (VI.5)$$

using the least-squares method with free parameters  $a$ ,  $b$ , and  $c$ . With the above value for  $k_B$ , we obtained  $a=21.86$ ,  $b=0.8213$ , and  $c=0.26$ . Equation (VI.5) served as the first-order algorithm to convert recoil pulse height to energy loss in the scintillator in the data analysis described below.

A formula to add the proton's energy loss in the hydrogen gas to Equation (VI.5) is obtained as follows: The Sternheimer formula (Sternheimer, 1966) allows one to calculate the range,  $R$  (in  $\text{gm}/\text{cm}^2$ ), of a proton with kinetic energy,  $T$  (in MeV), in hydrogen. The results for  $2 < T < 50$  are well described by a power law

$$R = \alpha T^\beta \quad (VI.6)$$

with  $\alpha = 0.00045$  and  $\beta = 1.95$ . Considering the range,  $R$ , to consist of the distance,  $l$ , travelled in the gas ( $22.9 \text{ cm}/\cos\theta$ ) plus the distance travelled in the scintillator, where we know the energy loss is  $E(L')$ , we obtain

$$T = (l\rho/\alpha + E(L')^\beta)^{\frac{1}{\beta}} \quad (VI.7)$$

where  $\rho$  is the density of 15 atm of hydrogen.

The linearity of the phototube-to-ADC systems was checked for several counters. The Lecroy 2285A ADC specifications quote a typical integral linearity of  $\pm 0.1\%$ . By examining the ratio of pulse heights from the NaI calibration sources and longitudinal muons at different phototube high voltages, we determined that the phototubes and bases are linear to about 4% over a dynamic range large compared to the range of pulse heights from recoil protons which stop in the scintillators.

#### VI.B.2 Light Attenuation in Pulse Height Counters

NE110 scintillator is advertised as having an attenuation length of 400 cm. We measured the light attenuation of each of the 32 pulse height counters by studying the counter pulse height produced by cosmic rays as a function of  $z$ , the distance the light must travel before reaching the end of the scintillator and the light pipe. The fast trigger for a cosmic ray run is a cosmic ray passing through two diagonally opposite counters; the TPC then measures the  $z$  position and angle of the track. Histograms of (pulse height - pedestal)  $\times \cos\theta$  were collected in eight  $z$  bins for all counters.  $\theta = 0$ , here, corresponds to tracks perpendicular to the axis of TREAD, so the  $\cos\theta$  term above normalizes the pulse heights of angled tracks, whose path lengths in the counters are longer, to pulse heights of  $0^\circ$  tracks.

Figure VI.1 shows a typical pulse height spectrum. The position of the peak was determined by a least-squares fit to a Landau shape plus a linear polynomial, and the result is superposed on the figure. The specifics of fitting to a Landau shape are discussed in another context in the next section. The error in the peak determination was taken to be the sum in quadrature of the error of the peak parameter computed by the fitting routine, and the pedestal error. This gives a typical error in peak determination of 1.5%. Figure VI.2 shows the variation of the peak with  $z$  position, measured in cm, in a counter with worse-than-average attenuation.  $z=0$  corresponds to the scintillator-light pipe

interface at the phototube end of the counter. Two fits to the eight  $z$  points are shown. One is a simple exponential in  $z$ , and the other allows for a quadratic term in the exponent. The latter is clearly superior, so two attenuation parameters,  $a$  and  $b$ , are used for correcting measured recoil pulse heights for each counter, according to the formula

$$PH(\text{true}) = PH(\text{measured}) \times \frac{A}{\exp(a \cdot (z-35) + b \cdot (z-35)^2)} \quad (\text{VI.8})$$

where  $A$ , a normalization constant, is the value of the denominator for a given counter at  $z=0$ . The mean value of the parameter,  $a$ , for the 32 pulse height counters is  $a = 0.00481 \text{ cm}^{-1}$  or  $1/(208 \text{ cm})$  and the standard deviation is 0.00117. The mean value obtained for  $b$  is  $b = 0.0000547$  with a standard deviation of 0.0000223. The average attenuation from the last  $z$  bin (75 cm) to the first  $z$  bin (5 cm) is  $25.6 \pm 5.0 \%$ .

The variation in the measured attenuation properties for the 32 counters can also be expressed in terms of the average attenuation factor for a signal generated by a minimum ionizing muon passing through the entire counter length. The attenuation correction for such a signal involves the integral of the attenuation function over the length of the counter. The average factor used to correct such longitudinal muon signals is  $1.256 \pm 0.8$ , i.e. the mean attenuation is  $20.4 \pm 6.4 \%$ .

### VI.B.3 Calibration Using Longitudinal Muons

During the experiment, regular muon calibration runs were taken to establish the calibration constants for the pulse height counters. The trigger for these runs is described in Section V.3.

The pulse height spectrum from a calibration run in April '83 for Counter 82U is shown in Figure VI.3 in units of ADC counts. Each histogram bin is 25 ADC counts wide. The histogram was prepared by requiring in software that Counter 82U and its partner in the trigger, Counter 82D, each had the largest pulse height in the corresponding half of TREAD. This helped to eliminate from the histogram events in which a muon did not traverse the full length of each counter pair, and helped to make the Landau-distributed straight-through peak stand prominently above a flat background. The large number of pedestal and low-pulse-height events have been suppressed from the figure.

The 5-parameter fit used to determine the counter's calibration constant for this run is shown in the figure. The observed spectrum is assumed to consist of a main straight-through peak and a background distribution; the peak, the background, and the resultant are shown separately. The reference (Sauli, 1977) gives an analytic expression for energy loss in thin media which closely approximates observed Landau shapes. Three parameters specify the straight-through peak as a function of the abscissa,  $x$  :

$$\text{PEAK}(x) = A_1 \cdot e^{-\frac{1}{2}(\lambda + e^{-\lambda})} \quad (\text{VI.9})$$

where

$$\lambda = \frac{x - A_2}{A_2 \cdot A_3} \quad (\text{VI.10})$$

$A_1$  corresponds to the peak height,  $A_2$ , the "center", is the most probable energy loss, and  $A_3$  is the fractional width of the distribution.

The background, which exists only for pulse heights below the main peak, is assumed to arise from events in which the muon did not pass through the entire length of the counter. For each  $x < A_2$ , the background function should contain contributions from Landau distributions with centers ranging from zero to  $A_2$ . Hence, the background, as a function of  $x$ , is an integral over Landau distributions whose fractional widths are assumed to be the same as that of the main peak. Two additional parameters allow the height of each background Landau distribution to vary linearly with the value,  $z$ , of its center:

$$\text{BACKGROUND}(x) = \int_1^{A_2} \frac{dz}{A_2 - 1} (A_4 + A_5 \cdot z) e^{-\frac{1}{2} (\lambda' + e^{-\lambda'})} \quad (\text{VI.11})$$

where

$$\lambda' = \frac{x - z}{z \cdot A_3} \quad (\text{VI.12})$$

A lower limit of 1 is used in the background integral instead of 0 to avoid a singularity in the exponential part of the integrand at the lower limit.

The function  $\text{PEAK}(x) + \text{BACKGROUND}(x)$  is fit to the data points using the least-squares routine, CURFIT. The  $A_2$  value found by the fitting routine is corrected for light attenuation in the scintillator and used to calculate the calibration constant,  $C$ , for a given counter



according to Equation (VI.2). The constants from 15 calibration runs during March and April, 1982, were tabulated and used in the offline analysis of the photon and pion recoil data. The calibration constants for most of the 32 counters reflect gain shifts less than 2% over the six week period with run-to-run variations less than about 1%. For a given recoil event, an interpolating algorithm selects a value for the calibration constant between the tabulated values for the two calibration runs which sandwich the event in time.

Four factors contribute to the uncertainty in the determination of the longitudinal muon calibration constants. First, the statistical uncertainty in the determination of the center,  $A_2$ , by CURFIT is on average 0.3% (sigma), or about 6 ADC counts out of 2000. Second, the ADC pedestal distributions have a standard deviation of about 4 counts, comparable to the fitting uncertainty.

There are two systematic uncertainties: the uncertainty in  $A_2$  due to the background shape used in the fit and the uncertainty caused by gain shifts and the interpolating algorithm. Two alternative, and simpler, background shapes were tried for several counters, and the average change induced in the resulting  $A_2$  values was less than 0.5%. I estimate the uncertainty due to interpolation to be about 0.5%. These factors contribute to an overall uncertainty of less than 1% in the determination of the calibration constants.

#### VI.B.4 Calibration Using NaI Light Pulsers

The Americium-doped NaI pulsers on the ends of the counters serve as a secondary calibration in that they are only used to check the muon calibration information. Figure VI.4 shows the Gaussian + linear polynomial fit to the NaI pulse height distribution for Counter 72D accumulated over a period of about ten hours. A pedestal of 417 counts has not been subtracted from this figure. Cosmic ray signals appear to

the left of the NaI peak, although they have been suppressed from the histogram by requiring that no other counter have a pulse height above pedestal. The uncertainty of 2 counts in the center of the NaI peak reflects the fit uncertainty and the pedestal width.

Figure VI.5 compares the behavior of the NaI peaks, the muon calibration constants, and their ratio as a function of time, or run number, for a counter whose gain drifted upward by about 8% during March-April. The quantities plotted are taken relative to the average of the quantity in the plot. The error bars on the NaI points are from the fits to the peaks; no errors are shown for the muon calibration constants, although a 0.5% uncertainty is used when calculating the ratios. Generally, the NaI peaks and muon calibration constants track together over time. The NaI points for a typical counter show an RMS deviation of 0.009 about their average value. Dividing by the muon calibration reduces this to 0.007. This suggests that the stability of the counters is better than 0.7%.

#### VI.C. DETERMINATION OF THE RECOIL POLAR ANGLE

As suggested by the "event picture", Figure V.2, the measurement of a recoil proton's polar angle requires not only a Track Fitting routine but also a Track Finding routine to determine which points constitute the recoil track among the wire hits recorded for the event. Calibration of the drift velocity allows the fit parameters to the wire times to be converted to polar angle and z position of the track in TREAD.

##### VI.C.1 Track Finding

The Track Finding routine does pattern recognition to find tracks. Physics analysis was performed on events for which only a

single track could be found. The minimum requirements for a good track are

- 1.) Each unprimed/primed (see Figure III.5) wire pair in the trigger sector has at least one hit, not necessarily in the track found by the algorithm. This corresponds to the trigger condition.
- 2.) At least 3 wire pairs are included in the track.
- 3.) At least 4 wires are included in the track.

The track-finding algorithm searches the wire-hit array for approximately collinear points which constitute a track within some angular tolerance. Beginning at the outside of the chamber (i.e., with wire pairs 4 and 3) and working inwards, the program calculates an angle based on two points. If the angle is within a preset tolerance, the program extrapolates a straight line and looks for additional points within a preset "road width" about the nominal track. If it finds new points, it updates the angle using the points farthest apart before extrapolating further. In practice, the program goes on to the next wire pair as soon as it has found any acceptable point in the wire pair under consideration. If, after looking at all wire pairs, condition (2) above has been satisfied, the program looks for additional points on the remaining wires. It then checks condition (3). All possible 3-pair combinations are tried. During the analysis, the angular tolerance used by the Track Finding routine was  $\pm 400$  counts/wire spacing, or about  $\pm 57^\circ$ , and a road width of  $\pm 100$  counts, or 0.8 cm.

#### VI.C.2 Track Fitting

The routine used to fit the acceptable points found by the Track Finder is POLFIT. This routine does a least-squares fit to a polynomial of any degree with explicitly defined errors for each point. The errors

are provided in the form of the resolution for each wire. The resolutions were obtained by an iterative procedure in which fits were performed on a large sample of events and (fit-measured) residuals were histogrammed and fit with Gaussian shapes. The resulting means and sigmas were used as the zero-time offsets and resolutions in the following iteration. The final widths were the values that produced the same result in the next iteration. Offsets and individual wire resolutions were derived for cosmic ray data, pion data, and photon data. Each of the 32 counters had eight wire offsets associated with it. Most of the analysis used offsets and wire resolutions derived from pion data.

As soon as a track has been found, POLFIT is called to give a preliminary fit. Before giving a final result, the program tries to obtain the best fit possible consistent with the track finding criteria. To this end, it checks to see if other hits on a given wire yield a better fit than the hit originally found, eliminates hits if they distort the fit, and selects the best fit combination if more than one is found.

The chosen points are fit to the straight line

$$t = P_1 + P_2 \cdot x \quad (\text{VI.13})$$

where  $t$  has units of TDC counts,  $x$  is measured in units of the 0.75" space between the wires, and  $P_1$  and  $P_2$  are fit parameters.

### VI.C.3 Calibration of Drift Velocity

The drift velocity of electrons in the drift space, measured in two independent ways, is used to convert the parameters,  $P_1$  and  $P_2$ , to the  $z$  position of the interaction point in the chamber and the polar angle of the track according to

$$z = P_1 \cdot \frac{z(HV)}{t_{\max}} \quad (VI.14)$$

and

$$\tan\theta = P_2 \cdot \frac{z(HV)}{t_{\max} \cdot \text{wire spacing}} \quad (VI.15)$$

where  $z(HV) = 76.2$  cm is the distance to the high voltage plate from the sense wire plate at  $z = 0$ ,  $t_{\max}$  is the drift time from the high voltage plate, the wire spacing =  $3/4'' = 1.91$  cm, and  $\theta = 0^\circ$  is perpendicular to the beam direction. The accuracy with which we need to know the drift velocity, or  $t_{\max}$ , varies with the recoil angle. In the absence of other effects, a  $\pm 2.5$  mrad angular uncertainty arises from a  $\pm 3\%$  uncertainty in drift velocity at  $5^\circ$  or a  $\pm 0.5\%$  uncertainty at  $45^\circ$ .

The two independent monitors of the drift velocity over time revealed that the constant, average value of  $t_{\max} = 9655$  TDC counts was sufficiently accurate for use throughout the analysis. For alpha source drift times (collected after each beam spill) were histogrammed and fit on a run-to-run basis and were compared to the drift velocity calculated according to Equation (III.3) using recorded values for the gas temperature and pressure, assuming a constant electric field. During March-April, the distribution of  $t_{\max}$  values from the fits to the alpha source times shows an rms deviation of 0.4% about the value 9655. The angular uncertainty introduced by using this average value in (VI.15) is small compared to other contributions to the overall angular resolution. We demonstrated that the calculated values of the velocity from Equation (III.3) follow the fluctuations in the alpha source times, so some of the 0.4% variation could be corrected for.

#### VI.D dE/dx CALIBRATION

As explained in Chapter II, measurements of  $dE/dx$  from sense wire pulse heights are combined with measurements of kinetic energy,  $T$ , in the scintillators to identify recoil particles as protons and eliminate background events. For a given recoil track, the recorded wire pulse heights, in units of ADC counts, are multiplied by a normalization factor, and averaged, to yield a value of  $dE/dx$  in arbitrary units. The normalization factors were determined as follows: For each wire, a histogram of the product,  $T \cdot (\text{wire pulse height})$ , was accumulated for pion events with a good recoil track. Such a histogram contains a peak which corresponds to protons and many background events, mostly at smaller values. The normalization constants were adjusted so that the proton peaks were individually centered on the same value, which was defined to be the proton mass,  $1 \text{ GeV}/c^2$ .

As discussed in Section VI.J, histograms of  $T \cdot dE/dx$  provide the basis for final event selection. The determination of the mass of the recoil proton from  $T$  and  $dE/dx$  is limited by the  $dE/dx$  resolution which is about  $\pm 30\%$  per wire. Six wire pulse heights are recorded for each track. Using the average of six wires as  $dE/dx$  results in  $\sigma(dE/dx)$  of about 13.5%. More specifically, the widths of the  $dE/dx$  distributions grow with  $T$  (or  $t$ ), starting at 11% near  $|t| = 0.02(\text{GeV}/c)^2$  and ending at 16% near  $|t| = 0.1(\text{GeV}/c)^2$ . The increase in  $dE/dx$  widths is due to the decrease in primary ionization as  $|t|$  increases. When the truncated mean algorithm, described in Section VI.J, is used for  $dE/dx$ , the widths grow from 10% at low  $|t|$  to 12.5% at high  $|t|$ .

A couple of comments about the  $dE/dx$  measurements are in order. First, the 13.5% measurement resolution makes us insensitive to the changing  $dE/dx$  as the proton loses energy (a few MeV) along its path across the sense wire region. Second, the procedure for recording the wire pulse heights causes a small fraction of good proton recoil events to be discarded in the analysis. The wire pulse heights are digitized

at the time of the coincidence in the Hardware Track Finder, which may occur before the real track arrives at the sense wire plate due to accidental wire hits. In this case, a  $T \cdot dE/dx$  value will be calculated which is unrelated to the track found by the analysis routine, and the event will be rejected with a recoil mass cut.

#### VI.E. ANTICOUNTER CALIBRATION

The anticounters were not used as veto counters during data acquisition. Rather, anticounter cuts were applied to the data during off-line event selection. In principle, a nonzero anticounter signal in time with the pulse height (PH) counter signal for an event with a good track indicates that the recoil particle punched through the PH to the anticounter. However, it was discovered that any light generated in a PH counter produces a small signal in the corresponding anticounter. This is due to a small amount of light which is transmitted between the two exposed (yet polished) lucite light guides and also feeds through the thin bakelite sheet which optically separates the two scintillators but is not totally opaque. In fact, the light which feeds from PH counters to anticounters in longitudinal muon runs is used to normalize the 32 anticounter cuts relative to each other. The idea of off-line anticounter cuts is to reject events with an anticounter signal large enough to represent a punch-through recoil, but to retain events with an anticounter signal smaller than that due to the light feedthrough of the highest energy (~59 MeV) proton which stops in the PH counter.

The pulse height from light which feeds into a given anticounter when a muon passes longitudinally through the corresponding PH counter was determined from anticounter pulse height spectra in muon calibration runs. These spectra are approximately symmetric distributions whose centers vary by up to 50% due to variations in anticounter phototube gains and physical differences in the light feedthrough paths. The values, representing the light feedthrough from 156.6 MeV (see Section

VI.B.1) minimum ionizing energy deposition in the PH counters, are approximately equal to the anticounter pulse heights from minimum ionizing cosmic rays passing through the  $1/4$ " thickness of the anticounters themselves. A recoil event was rejected if the pulse height in the corresponding anticounter, after correcting for light attenuation in the scintillator, was greater than 1.5 times the muon feedthrough value. Indeed, the cut value is safely above the expected feedthrough from the highest energy stopping proton. Furthermore, it was shown that most actual punch-through recoils give anticounter pulse heights from three to five times minimum ionizing, making the cut effective for rejection of these events. We estimate that  $<1\%$  of the actual punch-through events are not rejected by the anticounter cut.

The light attenuation along the length of the 30" anticounters was studied using cosmic rays in the same manner described in Section VI.B.2 for the pulse height counters. The anticounters have a greater attenuation than the PH counters. The average attenuation for light originating at the middle of an anticounter is 35%. There are large anticounter-to-anticounter variations and a few counters show 70% attenuation. This is compared to an average of about 20% from the centers of the PH counters.

#### VI.F. MULTIPLICITY COUNTER CALIBRATION

The charged multiplicity of the events was determined from the pulse height in the multiplicity counters. The counters were calibrated with single electrons ( $n = 1$ ) and electron pairs ( $n = 2$ ). Clean electron pair spectra were obtained during tagging system calibration runs ("Tag Only" runs) from photons producing pairs in the beam windows. A multiplicative normalization constant was introduced for each counter and the peaks of the  $n = 1$  and  $n = 2$  distributions established a multiplicity scale.



For each recoil event, the larger of the two normalized pulse heights of the two counters was discarded. This reduced the Landau tail, enabling the remaining pulse height to be a more direct representation of the charged multiplicity. Pulse height spectra for events in the region  $4 < M_X^2 < 10 \text{ (GeV/c)}^2$  from  $\pi^- p \rightarrow Xp$  and  $\gamma p \rightarrow Xp$  are shown in Figure VI.6. The two spectra contain an equal number of events. It is clear that for both  $\pi^- p$  and  $\gamma p$  the tails of the spectra from different multiplicities overlap.

Taking into account the fact that charge conservation restricts the photon and  $\pi^-$  charged multiplicities to even and odd numbers respectively, the two spectra look identical. This is consistent with the universality of charged multiplicity distributions observed in hadron induced reactions (Goulianos et al., 1982). More quantitatively, it was found previously (Cool et al., 1982 and Goulianos et al., 1982) that the charged multiplicity distribution of the "decay" products of a hadronic mass  $M$  has a mean value  $n_0 = 2M^{\frac{1}{2}}$  ( $M$  in GeV) and is represented well by a Gaussian function with a width  $D = n_0/2$ . The normalized probability distribution of the charged multiplicity  $n$  is thus given by

$$P_n = \frac{2}{\sqrt{2\pi} D} \exp \left[ - (n - n_0)^2 / 2D^2 \right] \quad (\text{VI.16})$$

$$n_0 = 2M^{\frac{1}{2}} \quad (M \text{ in GeV})$$

$$D = n_0/2$$

Anticipating our result that in the region  $4 < M_X^2 < 10 \text{ GeV}^2$  the diffractive cross sections for  $\pi^-(\gamma) + p \rightarrow X + p$  vary as  $1/M_X^2$ , and using this information in conjunction with the above multiplicity law, we have calculated the curves which are superimposed on the data in Figure VI.6.

#### VI.G. RECOIL TIME-OF-FLIGHT CALIBRATION

To eliminate background events, the measured arrival time of the signal in the pulse height counter is compared with the expected arrival time as calculated from the energy and track fitting results. The measured arrival time, in units of TDC counts, is converted to nanoseconds (50 picoseconds/count), and a correction is applied for time-slewing. The expected arrival time is the sum of the times for the photon to reach the interaction point, the recoil to reach the counter, and the light in the counter to reach the phototube. The (expected TOF - measured TOF) distributions for otherwise good recoil tracks are approximately Gaussian with rms widths of about 1.5 nanoseconds. These distributions are centered on zero with additive constants that vary from counter to counter by a few nanoseconds.

#### VI.H. ESSENTIAL CUTS FOR FIRST ROUND EVENT SELECTION

With the above algorithms in hand, offline event selection could proceed. Events from the original photon and pion tapes which passed two loose cuts were selected and written to "condensed" tapes. First, the product of  $T$  and  $dE/dx$ , calculated using the average of all six wire pulse heights, was required to be above a minimum value. 28% of the original photon events and 62% of the original pion events survived this cut. Second, an event was only saved if the track finder found at least one 4-point track. Only 7.2% of the original photon events (1 out of 14) and 22% of the original pion events (1 out of 5) satisfied both cuts. The rejected events were mostly due to accidental coincidences of Compton electrons in the chamber with beam associated pulses in the counters. The following is a breakdown of the remaining photon events according to number of points found in the (first) track:

Points Found in Track

4	60%
5	21%
6	9%
7	6%
8	4%

"Clean" recoil events were then required to satisfy the following set of Essential Cuts:

1. Only one PH counter fired its discriminator at the time of the fast trigger.
2. Only one track was found by the Track Finder.
3. The number of hits found by the Track Finder was six, seven, or eight.
4. Fiducial cut: the z position of the interaction point as determined by the Track Fitting routine was not closer than 2.5 cm to the sense wire plate or the high voltage plate.
5. Time-of-flight cut: the measured TOF was within 4 nanoseconds of the predicted TOF.
6. t cut: the calculated t was in the range  $0.02 < |t| < 0.1 \text{ (GeV/c)}^2$ .
7. For the photon data, the tagging system information was clean; in particular, only the lead-glass blocks associated with the electron shower had a large pulse height.

The t cut insured that the measured T's were insulated from the upper and lower limits set by the pulse height counters. The TOF cut primarily insured that the proton did not recoil from a photon in a different rf bucket than the photon measured by the tagging system.

Figure VI.7 shows a scatter plot of the recoil kinetic energy against  $dE/dx$  for photon data that survive the Essential Cuts. The prominent band represents recoil protons and illustrates the inverse proportionality of  $T = \frac{1}{2} M_p v^2$  and  $dE/dx$  for protons in the MeV range. The horizontal band is composed of two main background components. The first consists of  $>59$  MeV protons which have penetrated into an anticounter, producing a small amount of  $dE/dx$  in the chamber yet depositing less than their total energy in the PH counter. The second component consists of recoil protons whose  $dE/dx$  has been mismeasured in the manner described in Section VI.D.

Figure VI.8 is a histogram of the product  $T \cdot dE/dx$  for events in Figure VI.7 showing the proton peak on the right and background events on the left. As mentioned previously, the position of the proton peak is normalized to unity so that the abscissa represents  $M(\text{recoil})/M(\text{proton})$ . The effect of the anticounter cut described in Section VI.E is shown in the figure. The remaining background events are primarily those with mismeasured  $dE/dx$ . A simple cut  $0.7 < T \cdot dE/dx < 1.4$  on a similar plot from the pion data yielded the first round sample of events used for  $T$  and  $\theta$  cross calibration which is described next.

## VI.1. CROSS CALIBRATION OF T AND $\theta$ ALGORITHMS USING PION ELASTIC EVENTS

Pion elastic events were selected with two additional cuts: a missing mass cut  $-1.2 < M_x^2 < 1.2 \text{ (GeV/c}^2\text{)}^2$  around the elastic peak (see Figure VII.4 for a pion missing mass distribution) and a multiplicity cut  $0.5 < n < 1.5$  for a single final state particle. A small admixture of inelastic events is included in this sample. The polar angle and kinetic energy of elastic events are related through

$$\sin \theta = \sqrt{T/2M_p} \quad (\text{VI.17})$$

where, here  $\theta = 0^\circ$  is taken to be perpendicular to the beam direction. the aim of the cross calibration was to adjust the algorithms for determining T and  $\theta$ , described in Sections VI.B and VI.C, for each counter so that Equation (VI.17) is satisfied throughout the  $|t|$  range of the experiment. This is equivalent to insuring that the missing mass distributions for the elastic events are properly centered on the pion mass.

Limited statistics for each of 32 counters permitted a further subdivision only into low  $|t|$ ,  $0.02 < |t| < 0.06 \text{ (GeV/c}^2\text{)}$ , and high  $|t|$ ,  $0.06 < |t| < 0.01 \text{ (GeV/c}^2\text{)}$ , bins. The flexibility for decoupling low and high  $|t|$  adjustments comes from the fact that the T algorithm, Equation (VI.7), has two terms: the range term  $\ell\rho/\alpha$  which dominates at low  $|t|$  when little energy is deposited in the pulse height counter, and the counter term  $E(L')$  which dominates at high  $|t|$ . Two iterations of low  $|t|$  and high  $|t|$  adjustments resulted in (1.) a range term 10% lower than expected from Equation (VI.6), (2.) counter-by-counter polar angle offsets, typically  $(\pm)2$  mrad with a maximum of  $(\pm)4$  mrad, and (3.) counter-by-counter scale factors to the  $E(L')$  term, with a typical value of 1.1, positive only. Tables of constants incorporating the adjustments were used throughout further analysis of pion and photon data.

Equation (VI.17) for elastic events and an iterative cross calibration procedure could be used to map the track distortions in the TPC's in a manner similar to that described for cosmic rays in Chapter III.B.3. Among other benefits, the resulting improvement in angular resolution and missing mass resolution would aid a search for resonance structures in the high mass continua for both pion and photon dissociation. The mapping would require sufficient pion statistics to divide the elastic events according to pulse height counter and in many bins in  $z$  and  $|t|$ ; a data sample at least 20 times as large as our existing sample is needed. Some members of the group have considered a second generation, higher statistics pion run for this purpose.

#### VI.J. FINAL EVENT SELECTION

It was discovered that when using the average of six normalized wire pulse heights to calculate  $dE/dx$  the  $T \cdot dE/dx$  distributions change from symmetric at low  $|t|$  to Landau at high  $|t|$  where fewer primary ions are produced. The Landau tail can be reduced by discarding the largest two pulse heights and taking the average of the remaining four. The effect of using this "truncated mean" algorithm to calculate  $dE/dx$  is shown in Figure VI.9. In the top part,  $dE/dx$  is a six-wire average and the fit represents a Landau distribution. In the bottom part,  $dE/dx$  is a truncated four-wire average and the fit is a Gaussian. The truncated mean algorithm was used in the final event selection for both the pion and photon data.

The widths of the truncated distributions increase with  $|t|$ , as mentioned in Section VI.D, from 10% at low  $|t|$  to 12.5% at high  $|t|$ , and there is some counter-to-counter variation. The final recoil mass cuts retain events within  $-2\sigma$  and  $+2.5\sigma$  from  $M(\text{recoil})/M(\text{proton}) = 1$ , but the  $\sigma$ 's vary continuously with  $|t|$  as determined by the fits to the individual counter distributions. The background contamination in the number of good events selected is estimated to be  $\leq 2\%$ .

#### VI.K. CORRECTIONS

The largest correction to the data is due to the geometric acceptance of the apparatus. The acceptance is a simple analytic function of  $\theta$ , the recoil polar angle. The acceptance for a given  $\theta$  is proportional to the available target length which increases with increasing  $\theta$ , as can be seen in Figure III.4. The available target length varies according to  $L(\theta) = L - R \cot \theta$  where  $L$  is the length of a TPC section and  $R$  is the radius to the pulse height counters. The acceptance is therefore  $L(\theta)/L = 1 - 0.3 \cot \theta$ . For our range of polar angles,  $45^\circ < \theta < 90^\circ$ , the acceptance varies from 78% to 100%. The geometric acceptance correction applied to the pion elastic  $t$  distribution lowers the apparent slope by about  $\frac{1}{2}$  unit.

The data also have to be corrected for  $t$ -dependent nuclear interactions of the recoil protons in the scintillator (Gottschalk and Kannenberg, 1971). A small fraction (<2%) of recoil protons lose energy through nuclear interactions and generate less light in the scintillator than those which lose all their energy through ionization. Such events appear to have a lower  $|t|$  and a higher missing mass than the true values. The correction for nuclear interactions applied to the pion elastic  $t$  distribution, which includes compensation for events gained or lost from mass cuts around the elastic peak, lowers the apparent slope by about  $\frac{1}{4}$  unit.

#### VI.L. MASS RESOLUTION

The missing mass resolution was studied for elastic events in the pion data and for  $\rho^0$  events in the photon data. As explained in Chapter II, missing mass is calculated from the kinetic energy and polar angle of the recoil proton and from the incident beam energy, so the missing mass resolution has contributions from the uncertainties in these quantities. The object of the study was to determine whether the

measured mass resolution and its  $t$  dependence could be understood in terms of our best estimates for the resolutions in  $T$ ,  $\theta$ , and  $p_\pi$  or  $p_\gamma$ .

Pion elastic events are produced by definition at a unique missing mass, and the width of the missing mass elastic peak is due solely to the measurement uncertainties in  $T$  and  $\theta$ . On the other hand, the  $\rho^0$  meson has a natural width in  $M^2$  of about  $0.118 \text{ GeV}^2$  (from PPDB, 1982), and in addition our measured width has a small contribution from  $p_\gamma$ . I discuss the pion elastic resolution first.

#### VI.L.1. Pion Elastic Mass Resolution

As shown in Figure VI.12 the measured mass resolution for pion elastic events grows from  $0.23 \text{ GeV}^2$  at low  $|t|$  to  $0.36 \text{ GeV}^2$  at high  $|t|$ . The data points represent the widths of Gaussian fits to the elastic peaks in five  $|t|$  bins. We do not separate directly the contributions from  $T$  (or  $t$ ) and  $\theta$  using the data themselves, but rather we estimate the contributions by the following arguments.

Our experience from the hadron experiment E-396 suggests the resolution in our determination of  $t$  is  $\sigma_t = 0.002 (\text{GeV}/c)^2$  which is equivalent to  $\sigma_T = 1 \text{ MeV}$  (Cool et al., 1981b). The two experiments measured recoil protons in the same kinetic energy range by stopping them in scintillation counters, and the calibration procedures were the same.

An estimation of the angular resolution for recoil protons is more difficult. For this discussion, it is useful to imagine the recoil track as two segments, one extending from the interaction point to the radius of the first sense wire, and the other extending over the sense wire region. Then the angular resolution has independent contributions from (A.) multiple Coulomb scattering (MCS) of the proton in the first segment, (B.) MCS combined with the spatial resolution in the TPC in the second segment, and (C.) track distortions in the chamber. The three



contributions are added in quadrature to give the estimate for total angular uncertainty. Some information about track distortions can be obtained from the cosmic ray studies described in Chapter III.B.3. However, the cosmic rays do not experience significant MCS passing through the chamber gas, so MCS must be treated as a separate problem for the recoil protons.

The effect of the MCS for (A.) is that the proton enters the sense wire region with a direction altered from the true polar angle at the interaction point. Through the 1.5" distance to the first sense wire, the protons in our energy range suffer angular deflections according to a roughly Gaussian probability distribution whose width varies as  $1/|t|$  (Scott, 1963). The contribution (A.) to the angular resolution is indicated as "MCS before wires" in Figure VI.11 which shows the separate contributions to  $\sigma_\theta$  versus  $|t|$ .

Contribution (B.) was studied through Monte Carlo simulation of multiply-scattered tracks across the sense wire region. The program starts with a proton crossing the first sense wire at  $90^\circ$ . At each successive wire radius a change  $\Delta z$  in the proton's  $z$  position and a change  $\Delta\theta$  in the flight direction are randomly chosen according to Gaussian probability distributions whose widths are coupled and vary, as before, as  $1/|t|$ . When straight lines are fit to a large sample of eight point tracks generated in this manner, the distribution of angles is a Gaussian centered on  $90^\circ$ . The widths of these "MCS only" angular distributions are shown as a function of  $|t|$  in Figure VI.10.

In practice, however, the sense wires record eight spatial points from multiply-scattered tracks via the drift times of electron clusters, and there is an uncertainty in each measurement which corresponds to the spatial resolution. The measured spatial resolution for pion elastic tracks increases from  $150\text{ }\mu\text{m}$  to  $250\text{ }\mu\text{m}$  over our  $|t|$  range. The measured spatial resolution was incorporated into the Monte Carlo simulation by further varying the  $z$  coordinates of the multiply-scattered tracks

before fitting with straight lines. The resulting angular resolution is shown as "MCS + measured residuals" in Figure VI.10. The figure shows that, for contribution (B.) to the total angular resolution, MCS dominates at low  $|t|$  and spatial resolution dominates at high  $|t|$ . Contribution (B.) is also shown in Figure VI.11.

The recoil data themselves do not provide sufficient information to study contribution (C.), i.e., distortions of the tracks as they drift to the sense wire plate. This is possible with cosmic ray data, as described in detail in Chapter III.B.3, as one can compare measured angular resolution with that predicted from measured spatial resolution. The cosmic ray events were accumulated in special runs with conditions different than recoil runs--higher sense wire voltage and no beam in the TPC's--so the results do not necessarily apply. However, some "beam-on" cosmic rays were included among the recoil triggers and a small amount of cosmic ray data was accumulated at a lower sense wire voltage. A detailed study was not possible. But it appeared that track distortions are more severe under these circumstances. The value 4.9 mrad is consistent with these measurements and was chosen to represent contribution (C.) in Figure VI.11. The sum in quadrature of contributions (A.), (B.), and (C.) yields  $\sigma_\theta$  of about 5.5 mrad throughout the  $|t|$  range.

Figure VI.12 shows the contributions to  $\Delta M_x^2$  versus  $|t|$  for elastic events using  $\sigma_t = 0.002 \text{ (GeV/c)}^2$  and  $\sigma_\theta$  from Figure VI.11. The sum in quadrature yields a curve which closely matches the measured mass resolution. The agreement supports the estimate of 4.9 mrad for the contribution to the angular resolution from track distortions. In an effort to better understand the distortions, studies were performed which demonstrated that the measured mass resolution and its variation with  $|t|$  do not depend on integrated beam intensity in a spill, the instantaneous intensity as measured by the number of spurious wire hits in the chamber, or the number of spurious wire hits close in time to the hits which constitute the recoil track.

## VI.L.2. $\rho^0$ Mass Resolution

A plot similar to Figure VI.12 was prepared to compare the measured mass resolution for photoproduction of  $\rho^0$  mesons ( $M_X^2 = 0.6 \text{ GeV}^2$ ) to the resolution expected from the various contributions, but it is not included here. The  $\rho^0 \rightarrow \pi^+\pi^-$  events were chosen from the photon missing mass distributions by requiring a charged multiplicity  $n = 2$  and a missing mass in the range  $-0.6 < M_X^2 < 1.8 \text{ GeV}^2$ . Gaussian fits to the  $\rho^0$  peaks in five  $|t|$  bins have rms widths which increase from  $0.3 \text{ GeV}^2$  at low  $|t|$  to  $0.48 \text{ GeV}^2$  at high  $|t|$ . Four known contributions to the resolution are the following: the contribution from  $\Delta t$  using  $\sigma_t = 0.002 (\text{GeV}/c)^2$ , the contribution from  $\Delta\theta$  using  $\sigma_\theta$  as in Figure VI.11, the contribution from  $\Delta p_\gamma$  using a photon energy resolution of 2%, and the contribution from the natural width of the  $\rho^0$ . The sum in quadrature of these contributions yields an expected mass resolution which is approximately 15% smaller than the measured resolution for the  $\rho^0$ . Due to the fact that the photon data was accumulated over a long period of time compared to the pion data, the discrepancy presumably derives from systematic shifts in calibration.

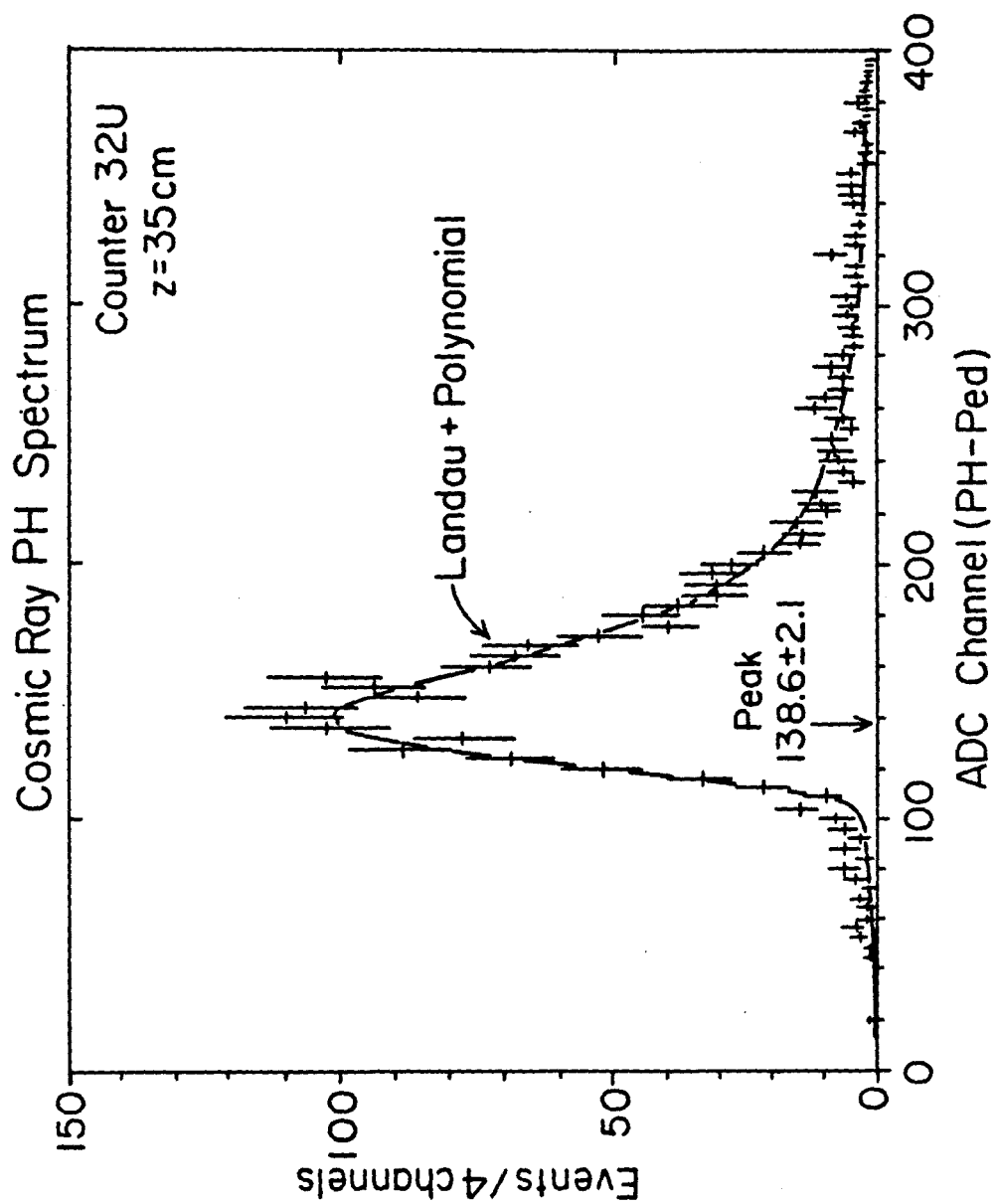


FIG. VI.1

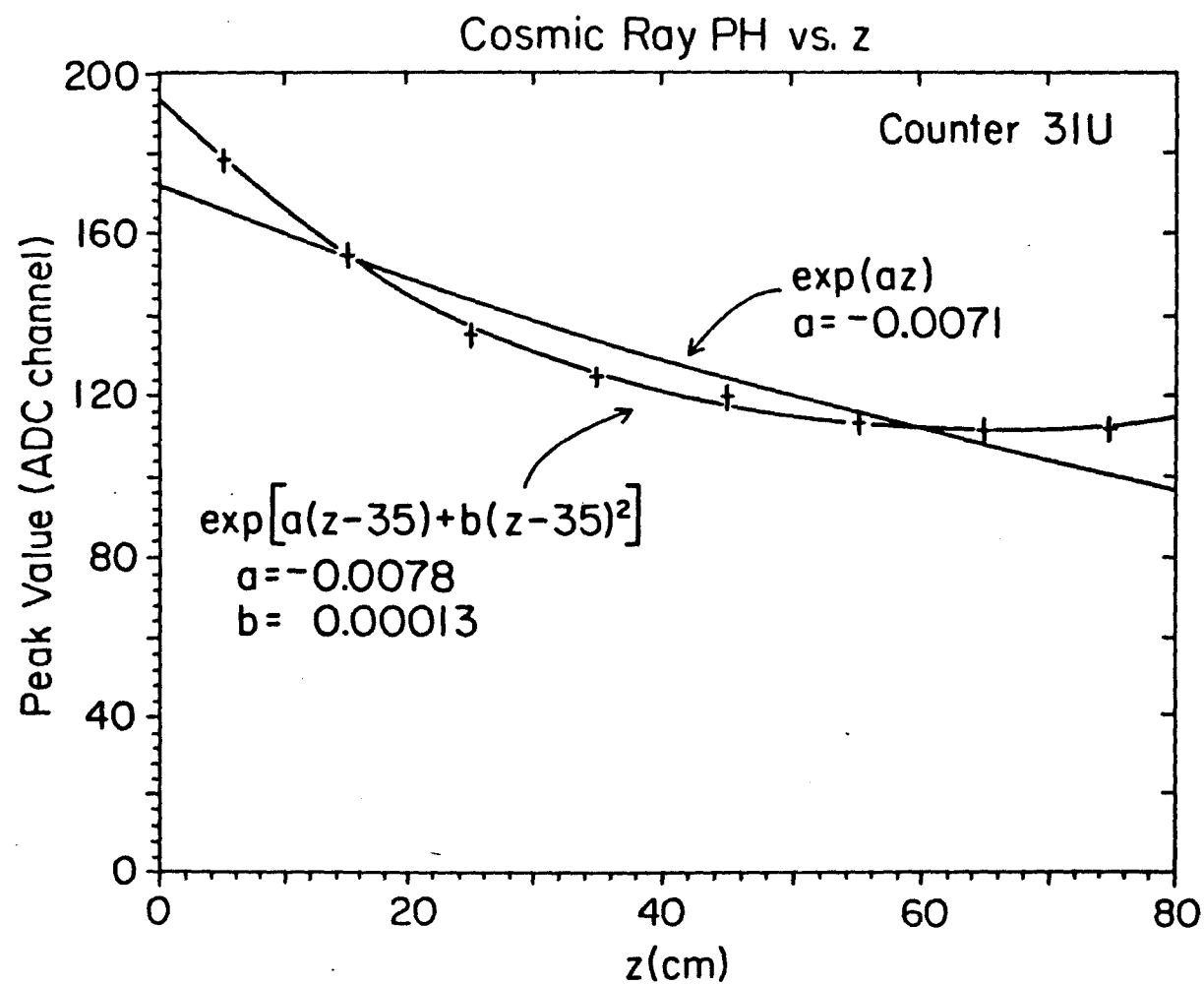


FIG. VI.2 - Light attenuation in pulse height counter

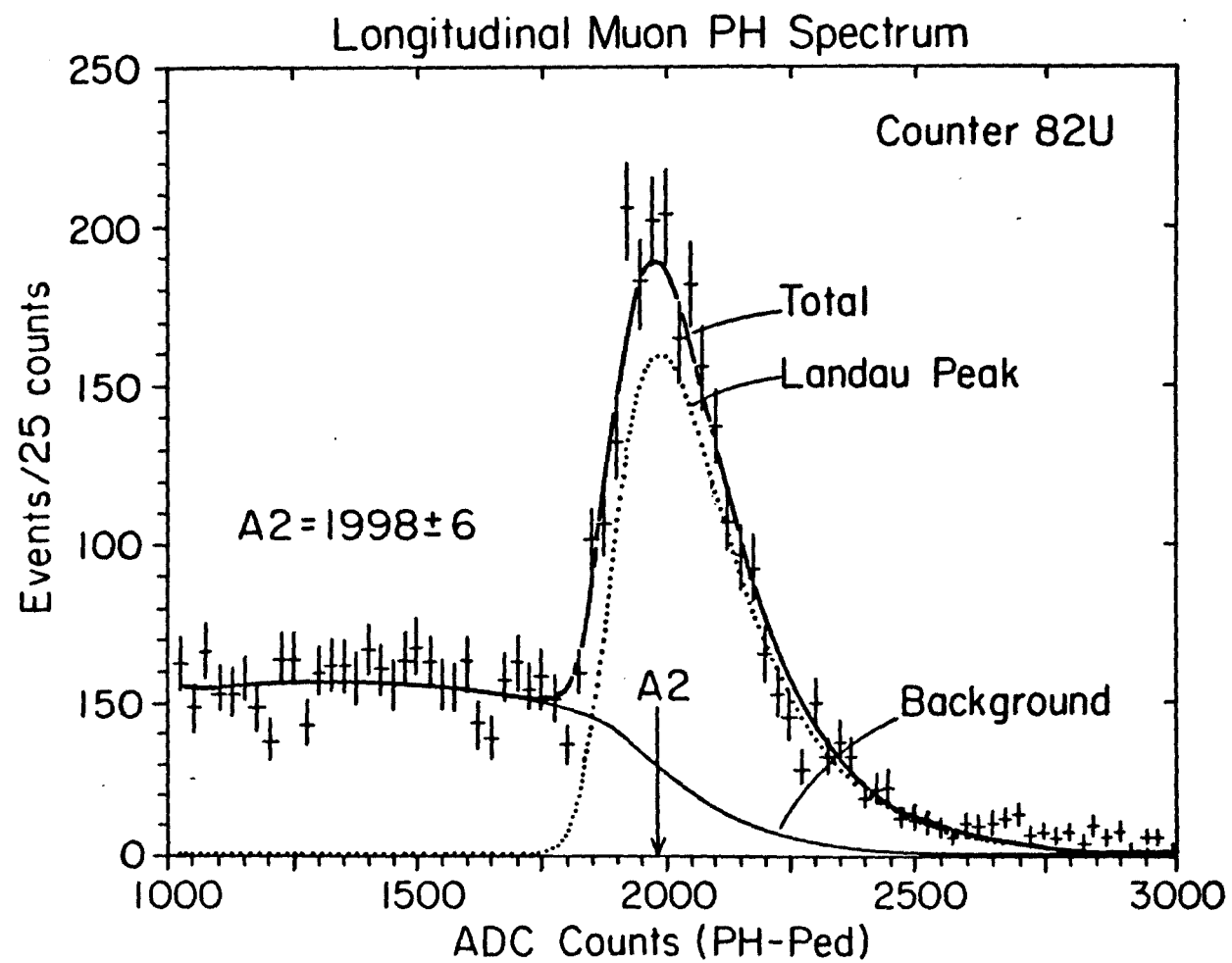


FIG. VI.3

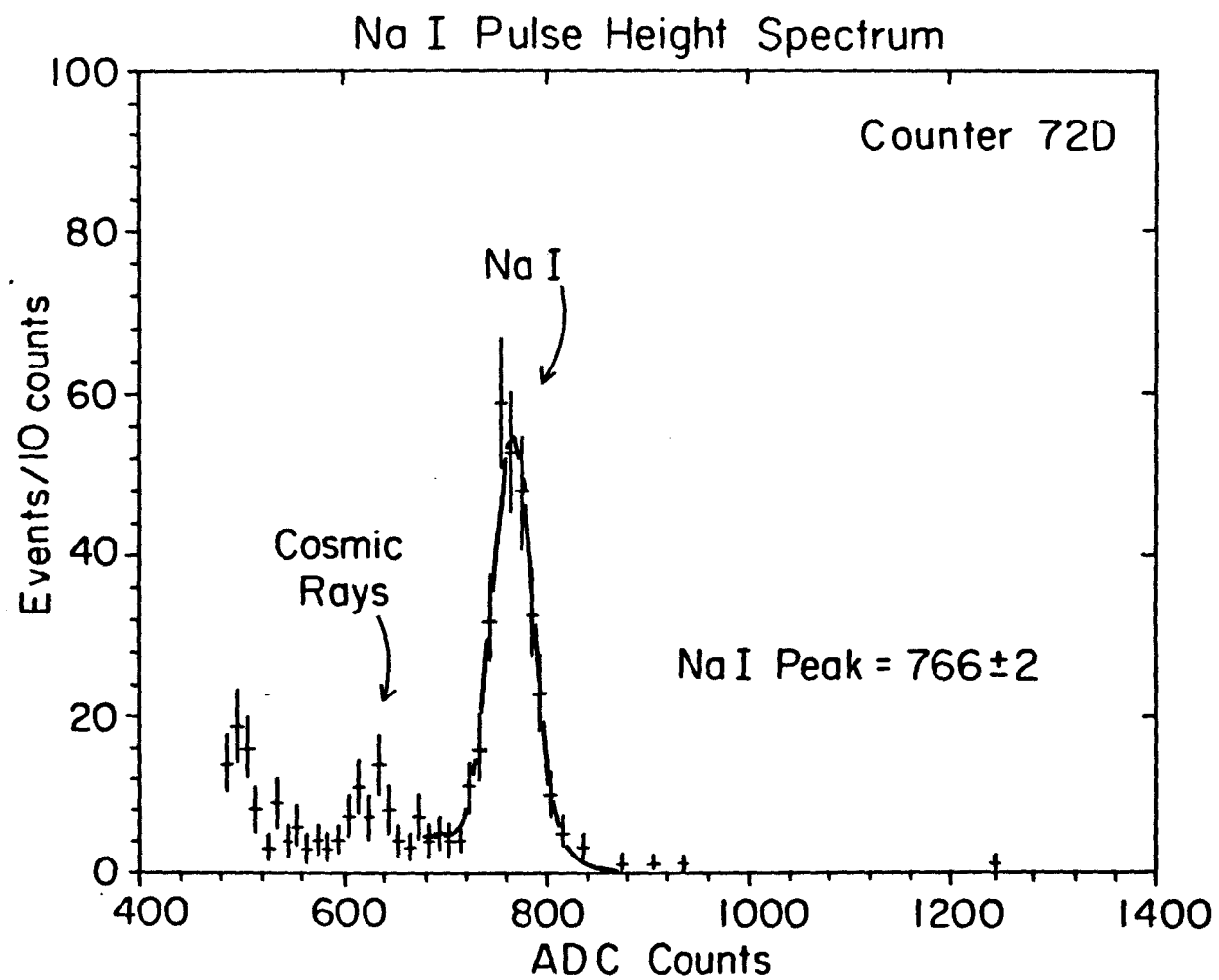


FIG. VI.4

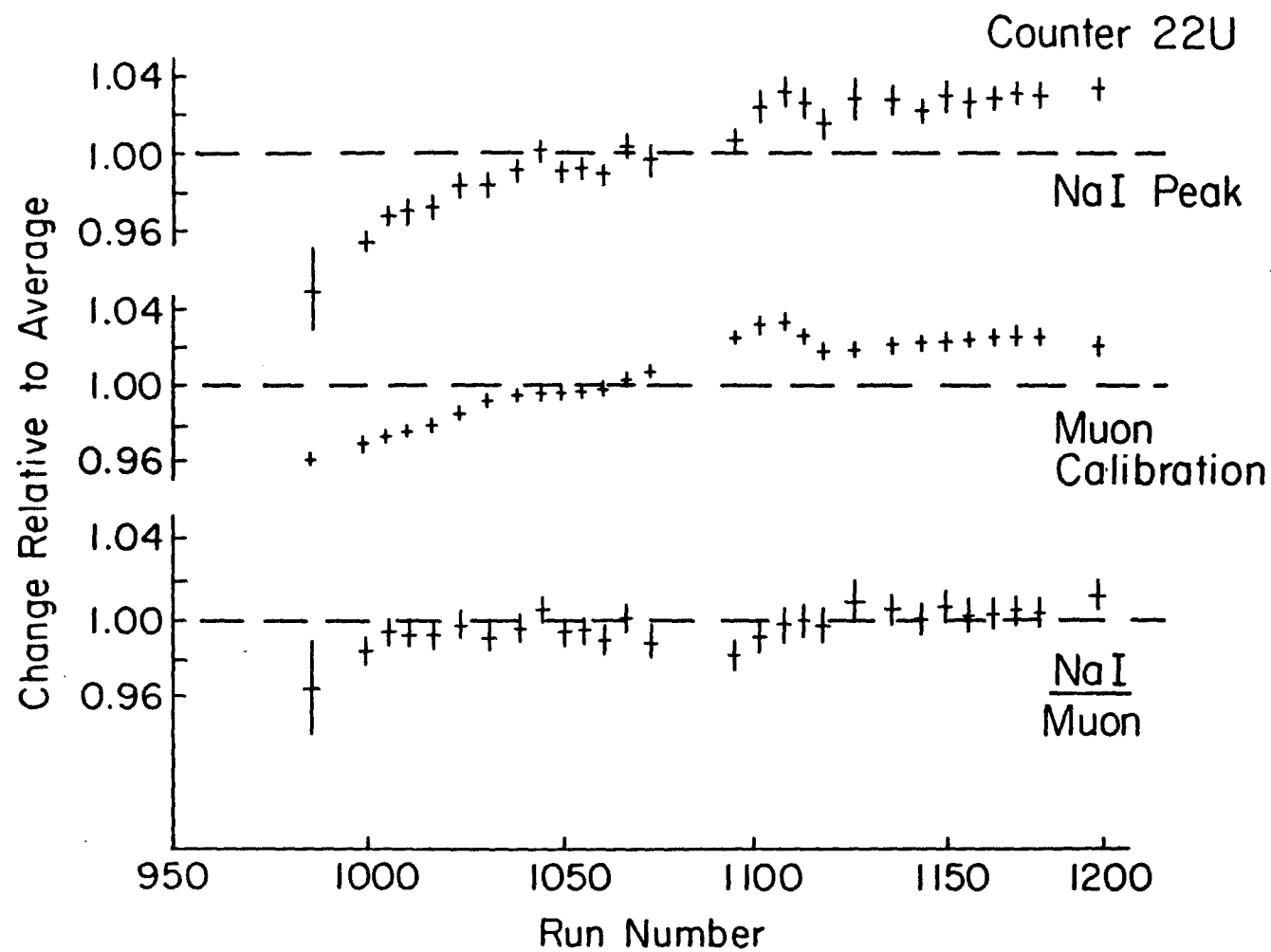


FIG. VI.5 - Tracking of NaI calibration with longitudinal muons



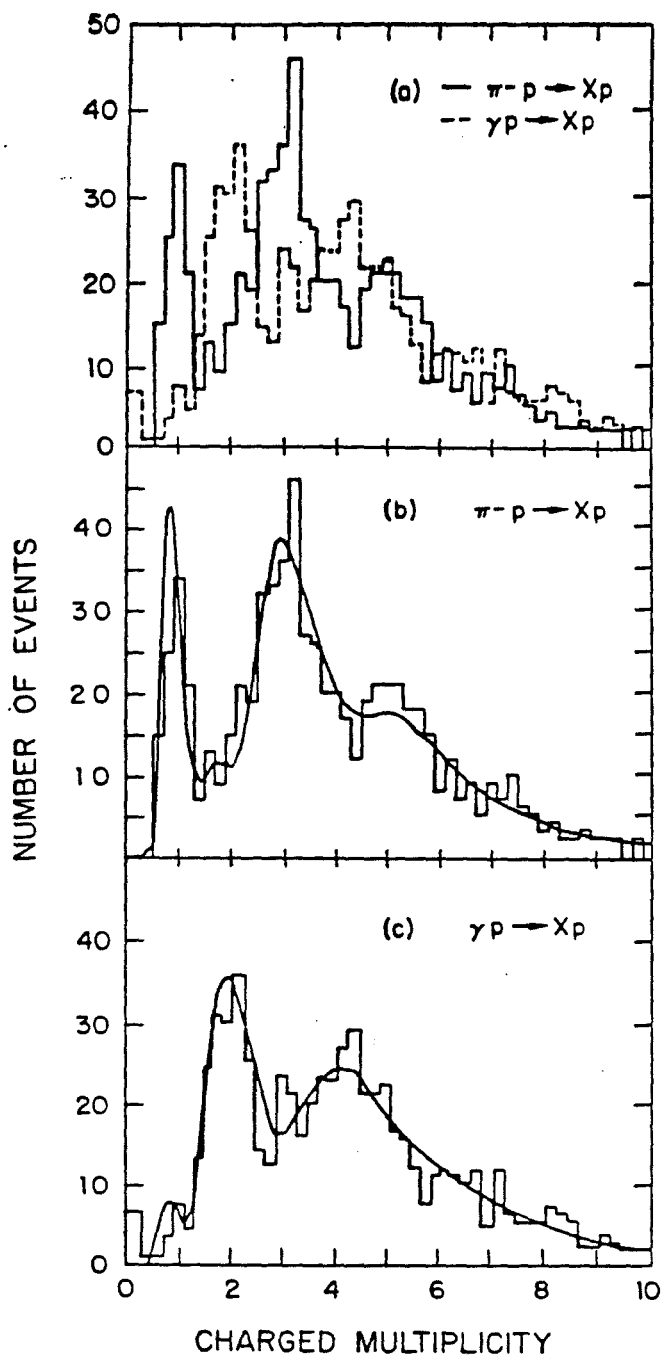


FIG. VI.6 - Charged particle multiplicity of the diffractive state X for  $\pi^- (\gamma) + p \rightarrow X + p$  in the mass range  $4 < M_X^2 < 10 \text{ GeV}^2$

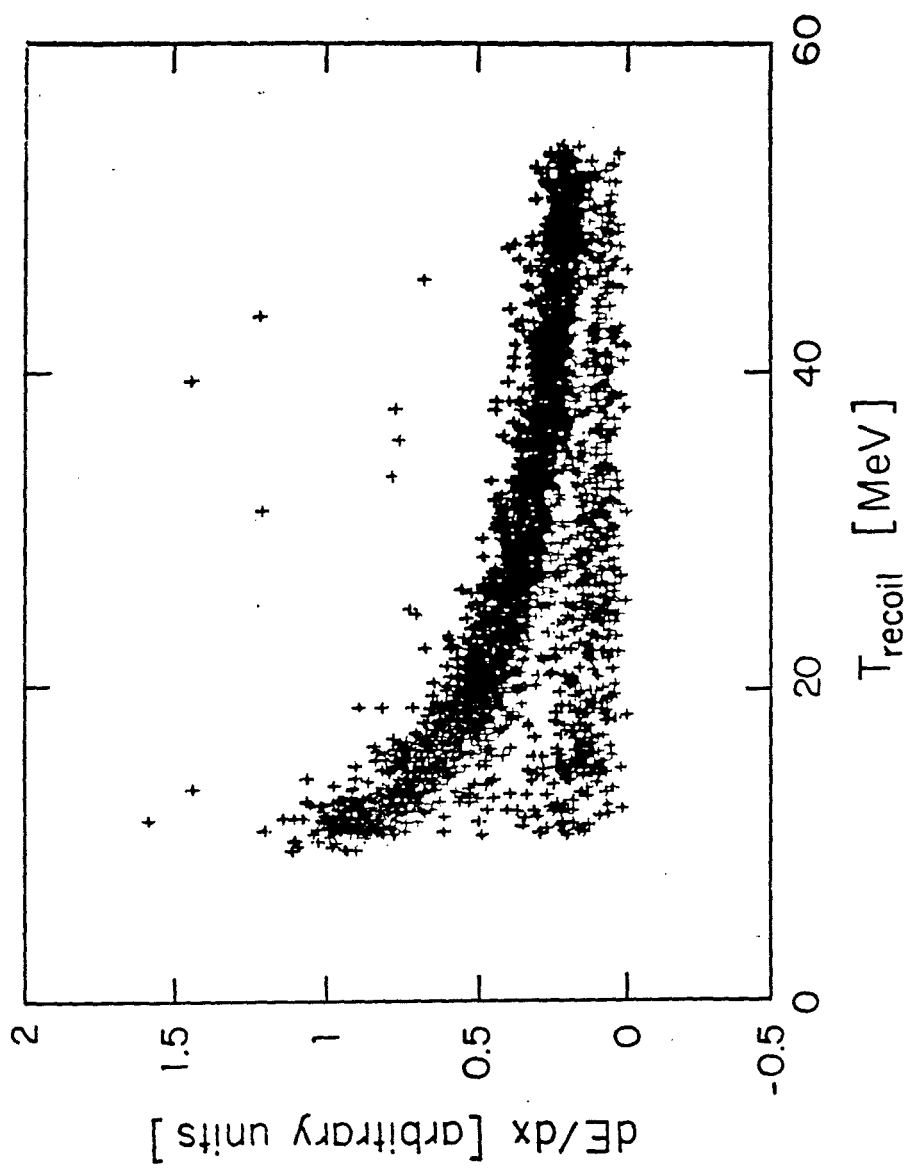


FIG. VI.7

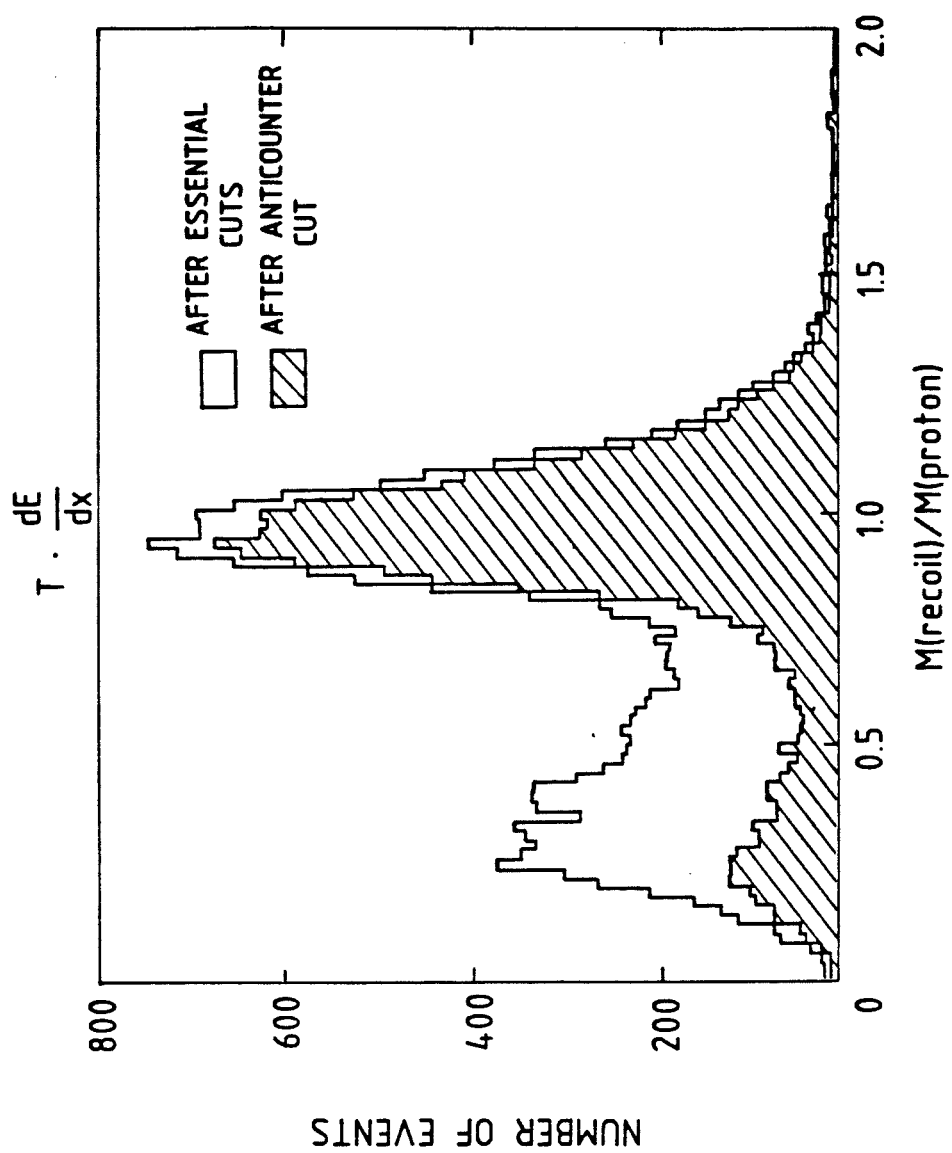


FIG. VI.8

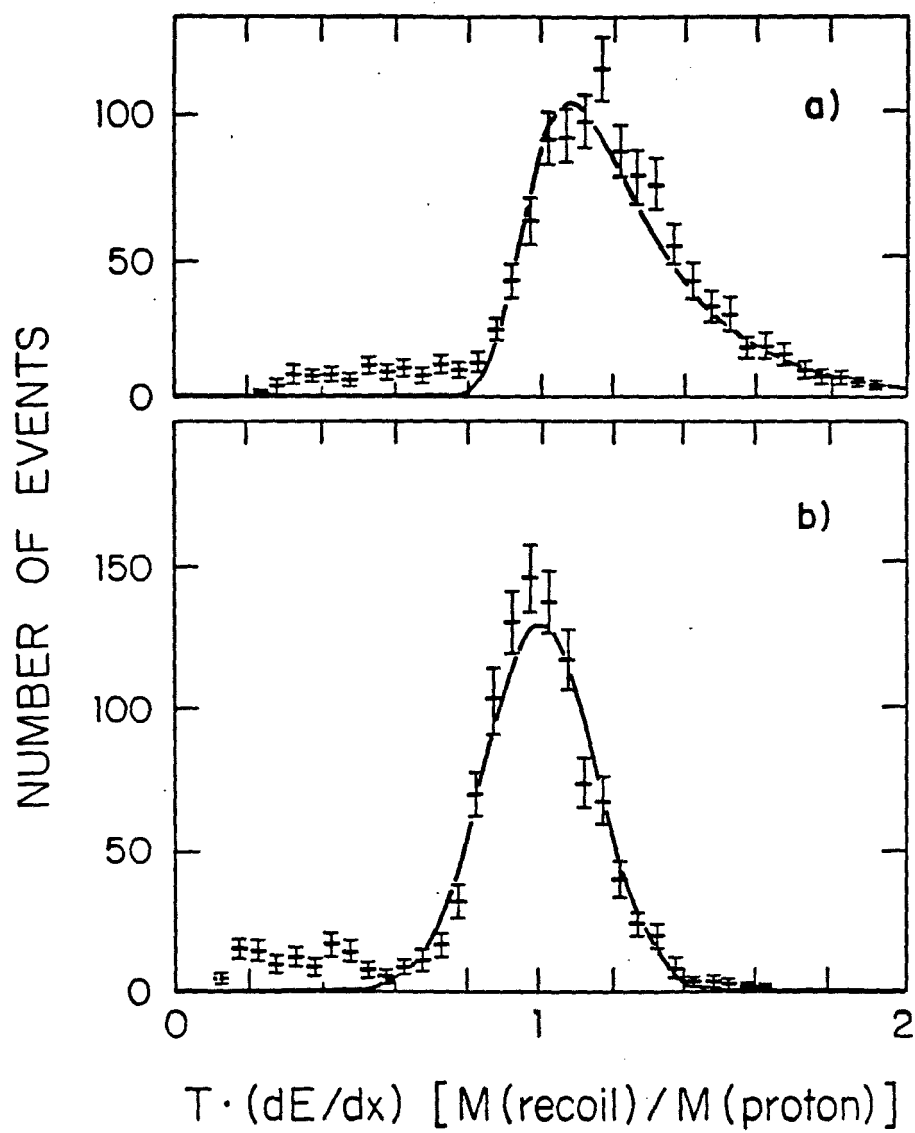


FIG. VI.9 - The effect of the truncated mean algorithm for  $dE/dx$  on the product  $T \cdot dE/dx$

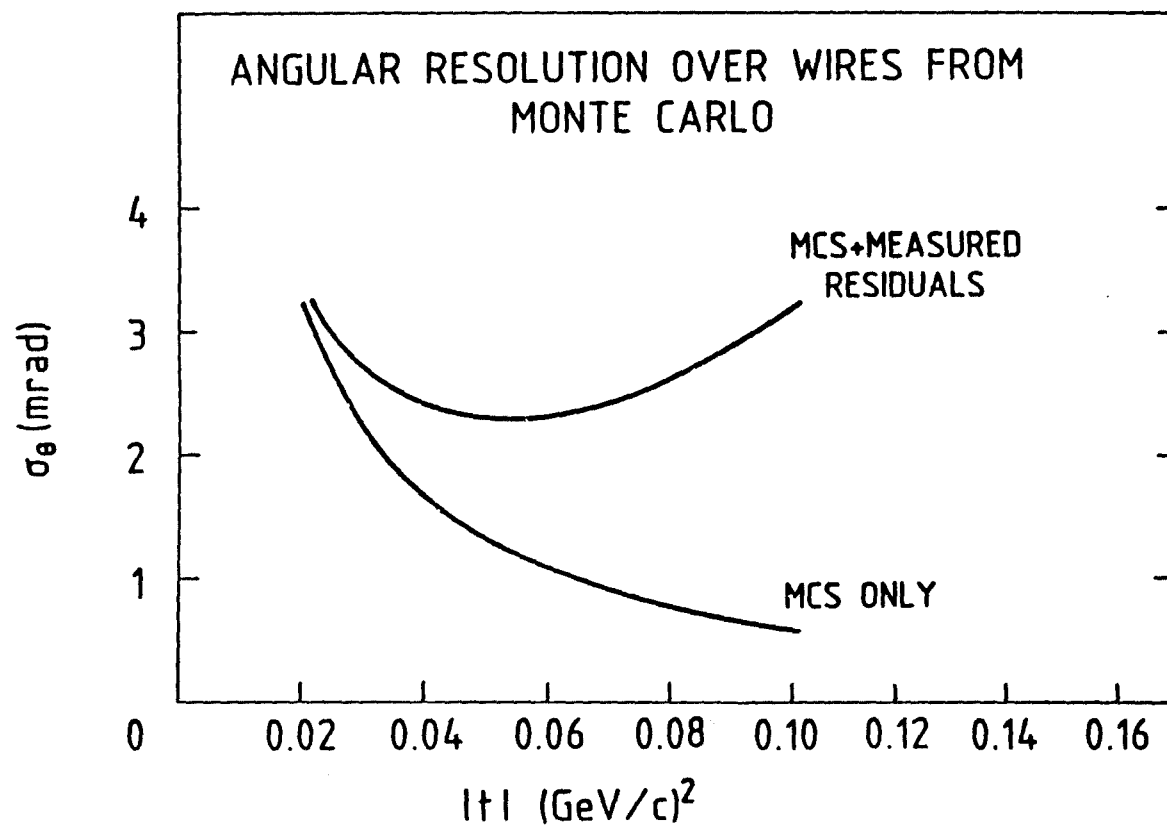


FIG. VI.10

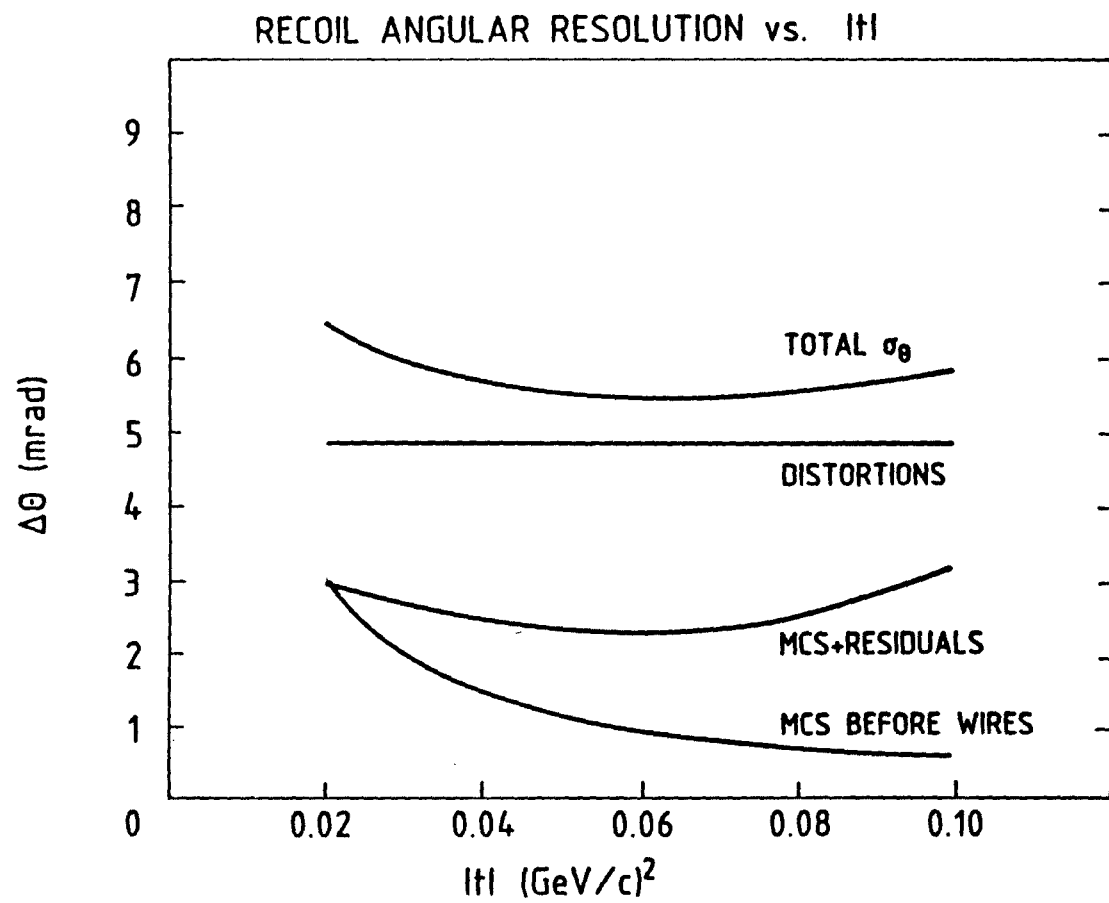


FIG. VI.11 - Contributions to the angular resolution versus  $|t|$

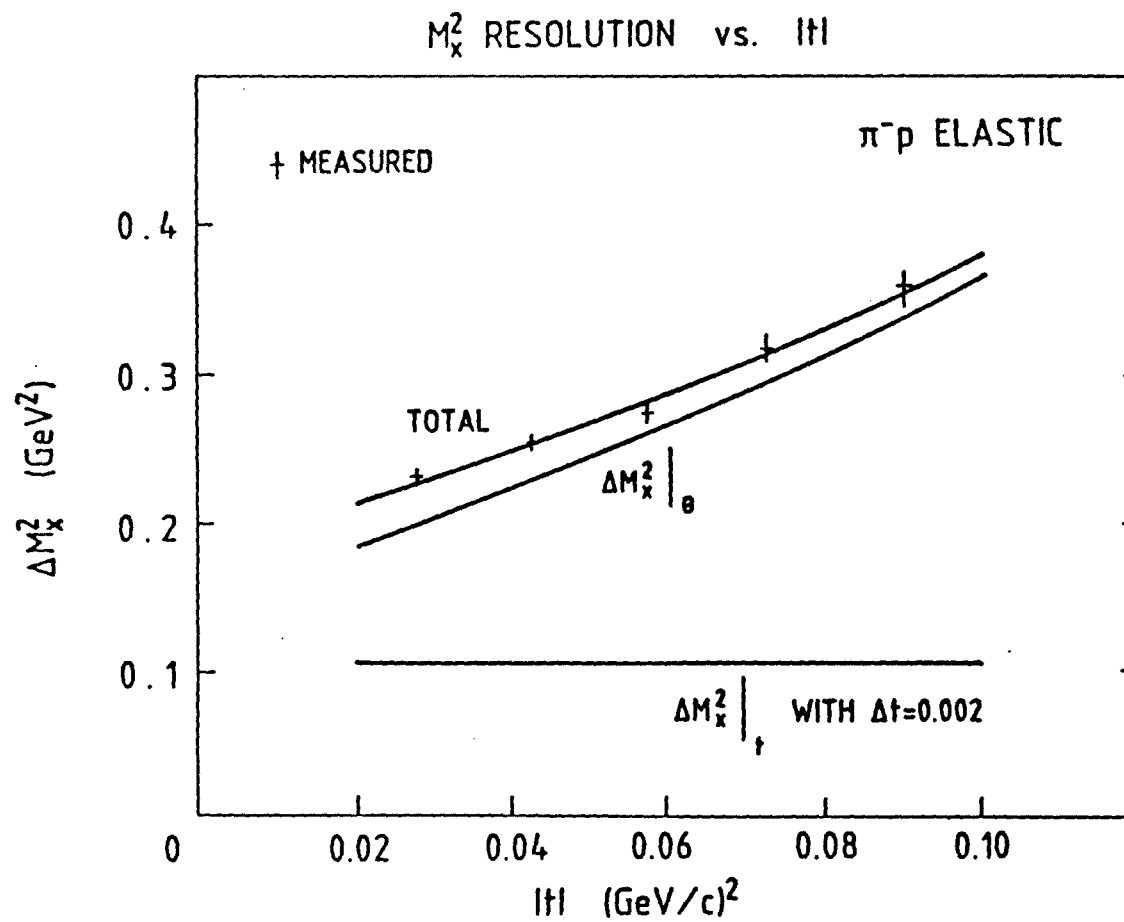


FIG. VI.12 - Measured and predicted  $M_x^2$  resolution for  $\pi^-p$  elastic events

## CHAPTER VII. RESULTS

The events which appear in the following plots were recorded during March-April, 1982, and satisfy the event selection criteria described in Chapter VI.

### VII.A. THE MASS DISTRIBUTIONS

Figure VII.1 shows the missing mass distribution for photon diffraction dissociation. All events with  $t$  and  $p_\gamma$  in the range  $0.02 < |t| < 0.1 \text{ (GeV/c)}^2$  and  $70 < p_\gamma < 140 \text{ GeV/c}$  are included. We observe a continuous spectrum of excited states with a prominent peak at the mass  $M_x^2 = 0.6 \text{ (GeV/c)}^2$  of the  $\rho^0$  meson. Figure VII.2 shows the same events plotted on a logarithmic scale. The solid line is a least-squares fit to the function  $C/M_x^2$  for the high mass region  $4 < M_x^2 < 10 \text{ (GeV/c)}^2$ . Since the average  $p_\gamma$  is about 100 GeV/c, this mass region corresponds to values of  $(1-x) < 0.05$  for which, according to the parameterization of Equation (I.6), non-diffractive contributions are negligible. As shown in Figure VII.3, however, our missing mass distribution extends to higher values of  $M_x^2$ .

For comparison with the photon mass distribution, Figure VII.4 shows the missing mass distribution for 100 GeV/c incident pions. The pion events span the same range in  $|t|$  as the photon events. The peak, centered on  $M_x^2 = M_\pi^2$ , corresponds to elastic scattering, and the high mass continuum falls as  $1/M_x^2$ .



## VII.B. THE $t$ DISTRIBUTIONS

Within any given small range in  $M_x^2$ , the events from the above missing mass distributions exhibit exponential  $t$  dependence. The  $t$  distributions for photon dissociation are shown in Figure VII.5 in two regions of  $M_x^2$ . The top points represent  $\rho^0 \rightarrow \pi^+ \pi^-$  events as defined by  $-0.6 < M_x^2 < 1.8 \text{ (GeV/c}^2\text{)}^2$  and charged multiplicity  $n = 2$ . The bottom set of high mass points,  $3.6 < M_x^2 < 6.0 \text{ (GeV/c}^2\text{)}^2$ , includes all multiplicities. The plotted  $t$  distributions include  $t$ -dependent corrections for geometric acceptance in TREAD and nuclear interactions in the pulse height counters. Fits to the simple exponential form  $e^{bt}$  are shown.

Figure VII.6 shows the slope parameter  $b$  as a function of  $M_x^2$  for both the photon and pion data. The pion elastic scattering slope and the high mass diffractive slopes are in good agreement with the values of  $8.92 \pm 0.31$  and  $4.3 \pm 0.7 \text{ (GeV/c)}^{-2}$  measured in the hadron experiment (Cool et al., 1981a and 1981b) described in Chapter II. This figure illustrates the overall correspondence between photon and pion diffraction dissociation. In particular, the slope parameters become roughly independent of  $M_x^2$  for high masses, reaching a value about half that for elastic  $\pi^- p$  or  $\rho^0 p$  scattering.

Small differences are apparent as well. First, the slope parameter for rho production is about one unit higher than for pion elastic scattering. Second, the A1 region near  $M_x^2 \approx 0.8 \text{ (GeV/c}^2\text{)}^2$  in the pion data has a very steep slope. The slope  $15.8 \pm 2.8$  shown in Figure VII.6 was obtained for events of charged multiplicity  $\geq 3$  ( $A1 \rightarrow \pi^+ \pi^- \pi^-$ ) in order to exclude events from the nearby elastic peak. The large slope in this low mass inelastic region is essential for satisfying the FMSR at small values of  $|t|$ . As discussed in Chapter I, as  $|t| \rightarrow 0$  in Equation (I.9) the elastic contribution vanishes; however, due to the large value of the slope of the low mass inelastic region, the relative contribution of this region increases at small  $|t|$  and the

FMSR is satisfied. Our data are not accurate enough to provide a stringent test of the FMSR as a function of  $t$ . Such a test was performed (Akimov et al., 1976) for  $pp \rightarrow Xp$ ; it was found that the slope parameter of the low mass region was indeed high and its magnitude was exactly right to satisfy the FMSR.

In the photon data, no such increase in slope appears for events just to the right of the  $\rho^0$ , even for high multiplicity events. It would appear, then, that the  $\rho'(1600)$ , which decays predominantly to four pions, does not correspond to the  $A_1$  enhancement in the pion data. Following the above argument, we would not expect the FMSR to be satisfied at small  $|t|$ . However, data from experiments at lower energies indicate that the slope in the mass region  $M_x^2 < M_\rho^2$  is higher than the slope of the  $\rho^0$ , as shown in Figure VII.7 (from Bauer et al., 1978). Our experimental resolution does not permit us to observe directly this increase of slope at low masses, but indirect evidence is provided by the fact that our measured slope of the  $\rho^0$  is larger than that of pion elastic scattering. Thus, the low mass "tail" of the  $\rho^0$  in  $\gamma p \rightarrow Xp$  may play the role of the  $A_1$  enhancement in pion dissociation.

Further discussion of the FMSR for the photon data follows in Section VII.D.

### VII.C. THE FACTORIZATION RULE

A pictorial representation of the factorization test is given in Figures VII.8a and b. Figure VII.8a shows our measured pion and photon mass distributions scaled to the corresponding total cross sections. Scaling the high mass continuum to the total cross section requires absolute normalization. Since we did not measure accurately the integrated luminosity for either data sample, we scale the continuum distributions to our extracted number of pion elastic events or rho events, and use previously measured cross sections for these exclusive

channels to scale to the total cross sections (see Appendix for details and references). The figure shows that the scaled, high mass photon cross section overlaps the scaled pion cross section. This in itself can be taken as a positive test of the Factorization Rule in view of the fact that the photon total cross section is about 200 times smaller than the pion total cross section.

As discussed in Chapter I.C, the Factorization Rule is expressed in Regge formalism in terms of the parameter  $(1-x) = (M_x^2 - M_0^2)/s$  where  $M_0$  is the mass of the incident hadron. According to the simple VDM, photon dissociation proceeds via an intermediate vector meson  $\rho^0$ ,  $\omega$ , or  $\phi$ . Since the  $\rho^0$  dominates, we will consider only the effect of the  $\rho^0$  in this discussion. If the photon indeed fluctuates into a  $\rho^0$  before participating in the diffraction dissociation interaction with the proton, the mass of the incident particle in the photon case should be  $M_\rho^2 = 0.6 \text{ (GeV/c}^2\text{)}^2$ , instead of a zero. In order to compare the photon data with the pion data under the VDM, Figure VII.8b shows the scaled mass distributions plotted against  $M_x^2 - M_0^2$ , where  $M_0 = M_\pi$ ,  $M_\rho$  for the pion and photon data, respectively. Except for the difference in the widths of the elastic peak and the rho peak, which is partly due to the natural width of the  $\rho^0$  and partly due to the slightly different resolutions of the two sets of data, the two spectra look identical. The high mass parts of the two distributions again overlap, so the Factorization Rule appears to hold in the VDM view of photon diffraction dissociation.

Turning the argument around, one could assume that factorization holds for the photon data and try to deduce the best value of the mass of the incident VDM "hadron", i.e., the average mass of the photon at the time of its hadronic interaction with the proton. For the pictorial representation of Figure VII.8, this involves translating the photon mass distribution left or right until the best overlap of the two high mass continua is achieved. But comparing parts a.) and b.) of the figure, factorization does not favor a particular value of  $M_0^2$  in the

range from zero to  $M_\rho^2$ . The same statement is true when a quantitative factorization test is performed by fitting the measured  $\pi^-$  and  $\gamma$  high mass cross sections with the functional form for  $d^2\sigma/dt dx$  given in Equation (I.6). The quantitative factorization test is presented in the Appendix. The main limitation arises from the uncertainty in extracting the number of pion elastic or rho events from the continuous missing mass distributions. However, applying the FMSR to the photon data leads to a better determination of the  $M_0^2$  value appropriate for photon dissociation.

#### VII.D. THE FINITE MASS SUM RULE

As explained in Chapter I.C, when applying the FMSR to experimental data which contains overlapping elastic and inelastic events, Equation (I.9) can be written as

$$R = \frac{\int_0^{v_0} v \frac{d^2\sigma}{dt dv} dv}{\int_0^{v_0} v \left( \frac{d^2\sigma}{dt dv} \right)_{\text{fit at large } v} dv} = 1 \quad (\text{VII.1})$$

where the lower limit of integration in the numerator has been omitted but it is understood that one must sum over all events below  $v_0$ , including the elastic events that appear at negative values of  $v_0$  because of resolution smearing. Figures VII.9a and VII.9b show  $v(d^2\sigma/dt dv)$  for our pion and photon data plotted against  $v = M_X^2 - M_\pi^2, \gamma + |t|$ . For  $v > 4 \text{ GeV}^2$ , our data for both reactions are flat, reflecting the  $1/M_X^2$  behavior of the high mass cross sections and hence triple-Pomeron dominance. The  $A_1(M_X^2=1.63)$  and  $\rho'(M_X^2=2.56)$  peaks are clearly visible in the pion and photon data, respectively. Applying the FMSR with  $v_0 = 4 \text{ GeV}^2$ , we find  $R_\pi = 1.10 \pm 0.05$  and

$R_\gamma = 1.43 \pm 0.04$ . This straightforward application of the FMSR fails for the photon data.

In the spirit of our application of the Factorization Rule, we treat  $M_O^2$  as a free parameter and demand the validity of the FMSR for the photon data, i.e.,  $R_\gamma = 1$  in Equation (VII.1). We find  $M_O^2 = 0.46 \pm 0.02 \text{ GeV}^2$ . The important point is that this number lies between zero and the square of the  $\rho^0$  mass. Our interpretation is that the value  $M_O^2 = 0.46 \text{ GeV}^2$  arises from the averaging of two independent channels through which the photon participates in diffraction dissociation. The first is the standard VDM channel for which the incident mass is  $M_O^2 = M_\rho^2 = 0.6 \text{ GeV}^2$ . The second is a "direct" channel for which  $M_O^2 = M_\gamma^2 = 0$ . The term "direct" here refers to a strong interaction of the photon that does not proceed via an intermediate vector meson. Weighting each channel according to the probability  $P_{\gamma,\rho}$  for finding the photon in the corresponding state at the time of the interaction,  $M_O^2$  is given by

$$M_O^2 = \frac{P_\gamma \sigma_\gamma^D M_\gamma^2 + P_\rho \sigma_\rho M_\rho^2}{P_\gamma \sigma_\gamma^D + P_\rho \sigma_\rho} = \frac{P_\rho \sigma_\rho M_\rho^2}{\sigma_\gamma^T} \quad (\text{VII.2})$$

where  $\sigma_\gamma^D$  is the "direct"  $\gamma$  total cross section. We then find  $P_\rho \sigma_\rho / \sigma_\gamma^T = M_O^2 / M_\rho^2 = (0.46 \pm 0.02) / 0.6 = 0.78 \pm 0.035$  and consequently

$$\sigma_\gamma^D = (0.22 \pm 0.035) \sigma_\gamma^T \quad (\text{VII.3})$$

i.e., the direct hadronic photon cross section is  $22.0 \pm 3.5\%$  of the total. Recalling the discussion of the VDM in Chapter I, this value is in agreement with results on shadowing of photon total cross sections in

nuclei and with the fact that the simple VDM accounts for only ~80% of measured photon total cross sections at high energies.

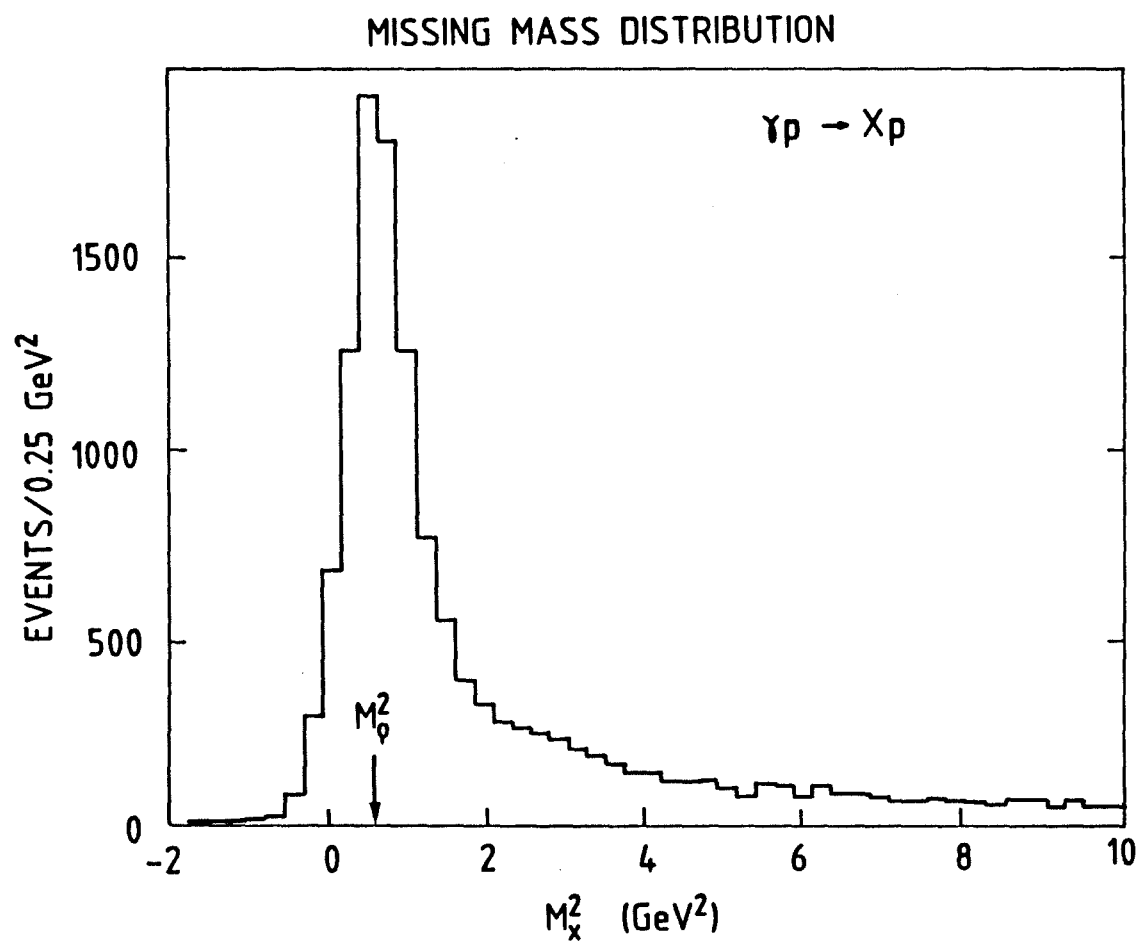


FIG.VII.1 - Missing mass distribution for  $\gamma p \rightarrow X p$  with  $70 < p_\gamma < 140$  GeV/c

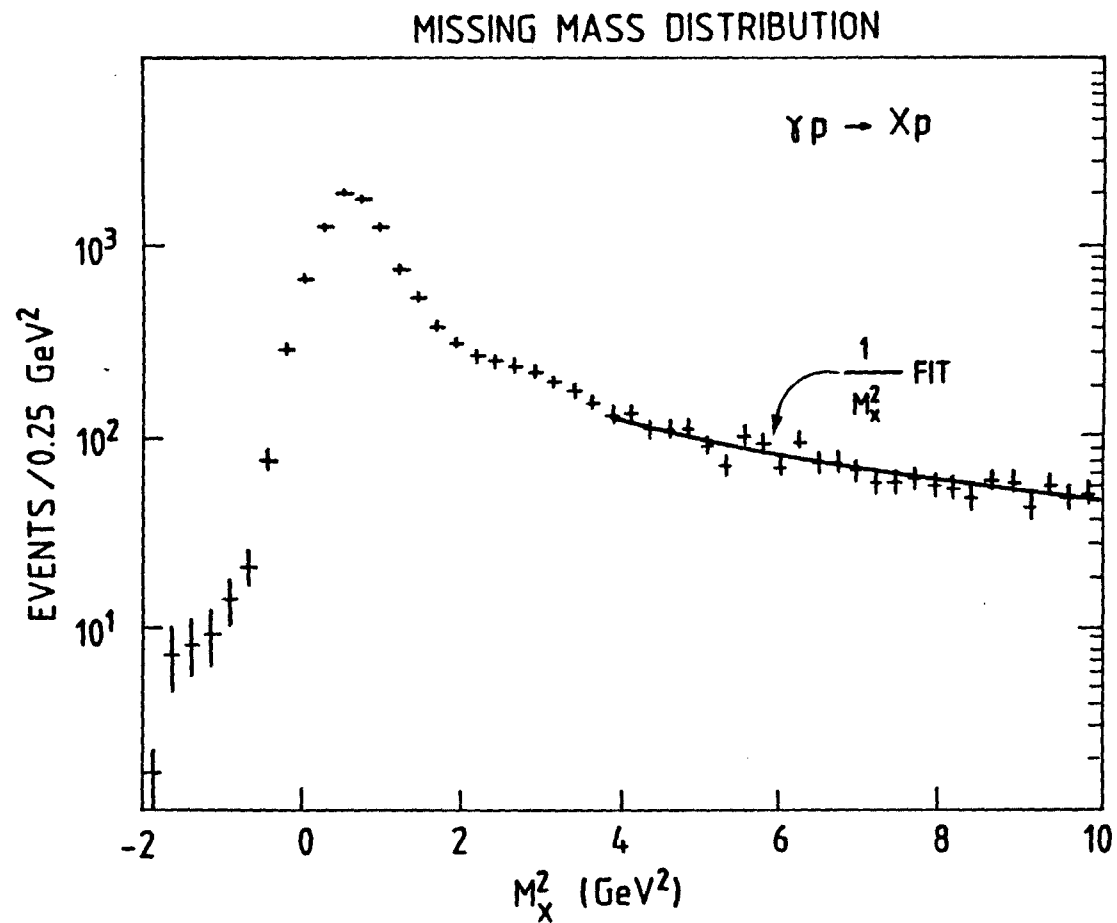


FIG. VII.2 - Missing mass distribution for  $\gamma p \rightarrow X p$   
with  $1/M_X^2$  fit in high mass region



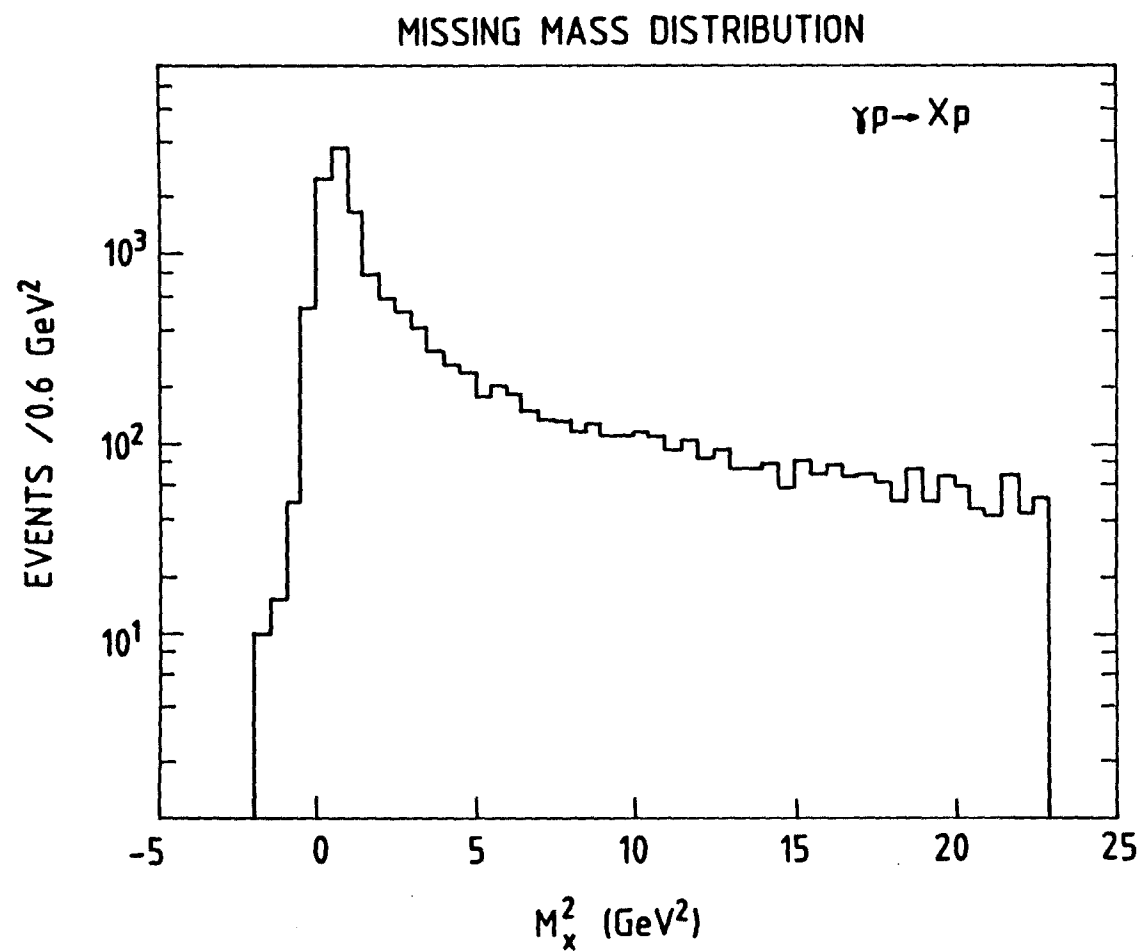


FIG. VII.3 - Missing mass distribution for  $\gamma p \rightarrow X p$  showing higher masses

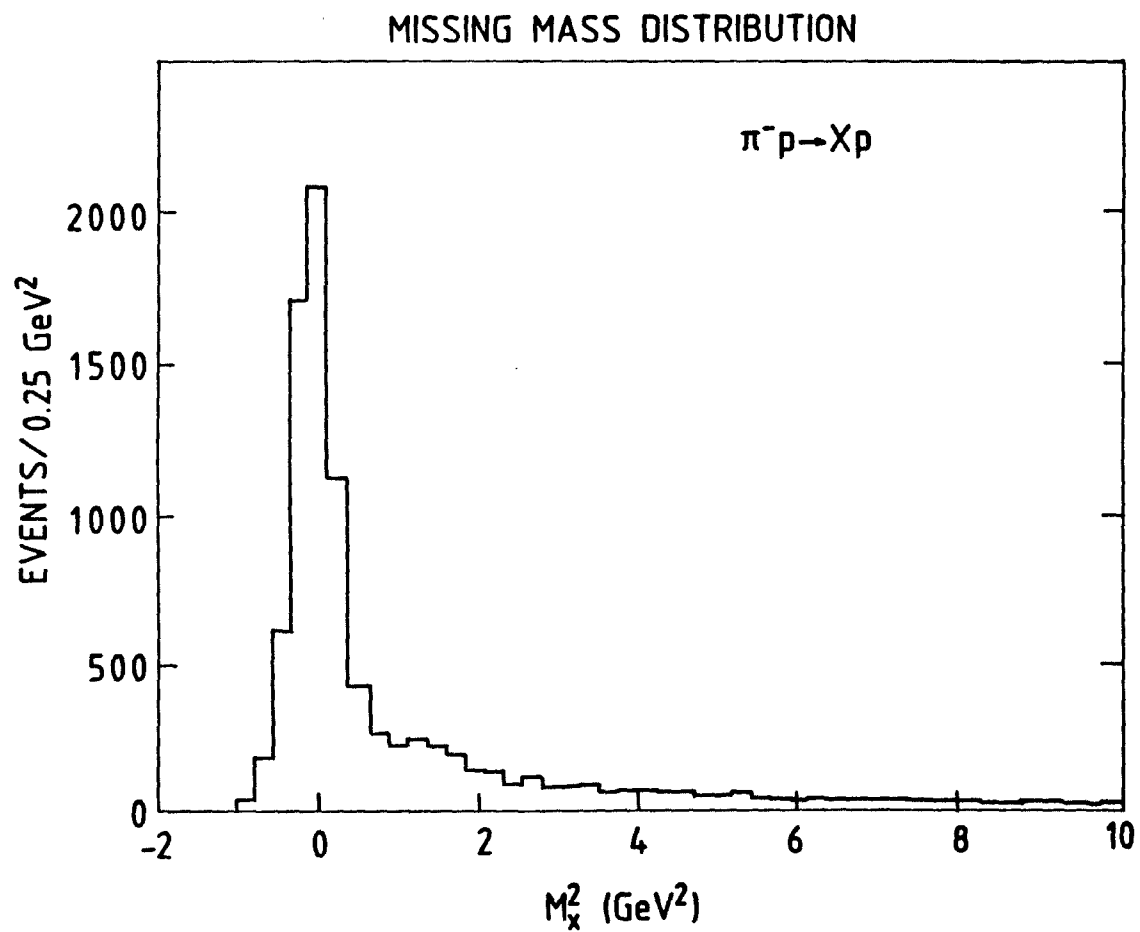


FIG. VII.4 - Missing mass distribution for  $\pi^-p \rightarrow Xp$   
with 100 GeV/c incident pions

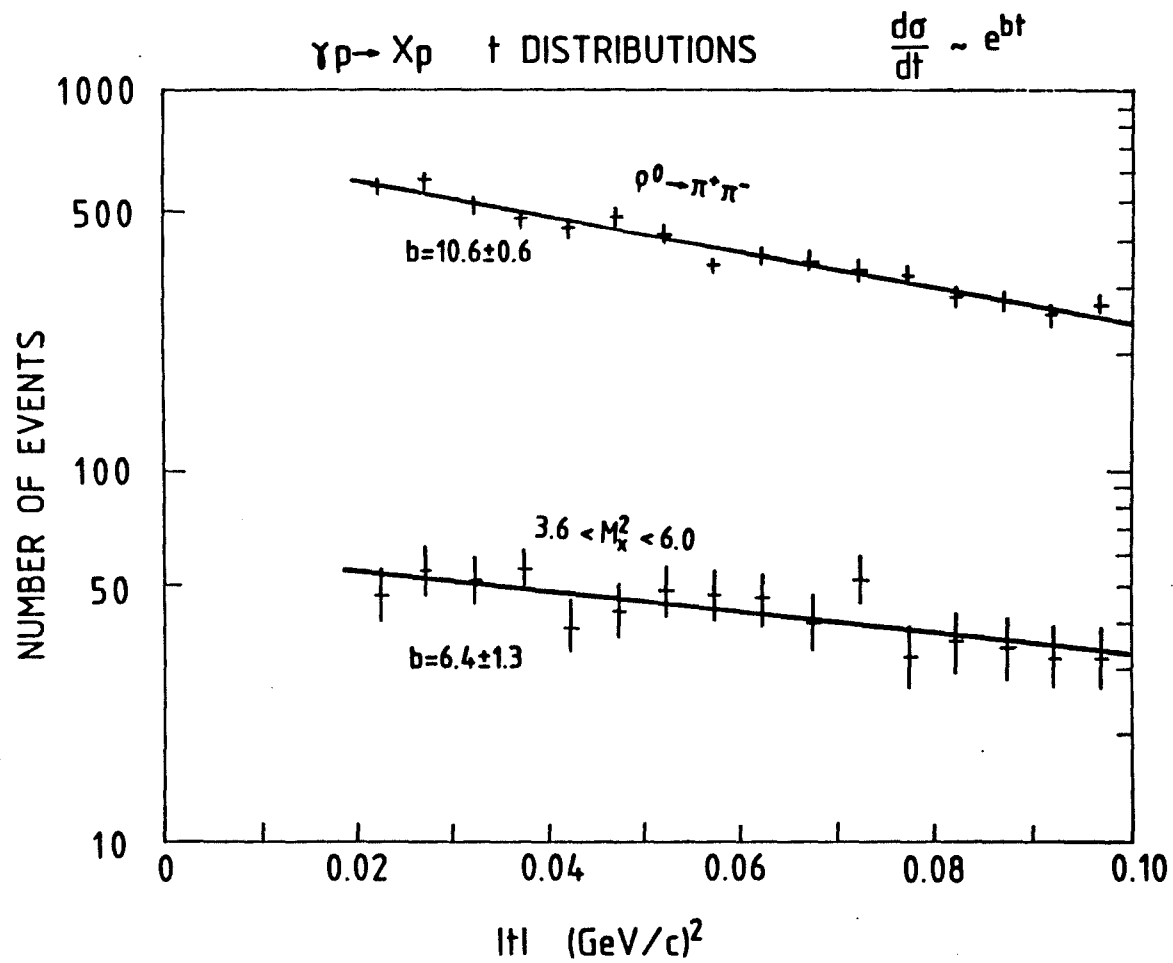


FIG. VII.5 - The  $t$  distributions for  $\rho^0$  events and high mass events

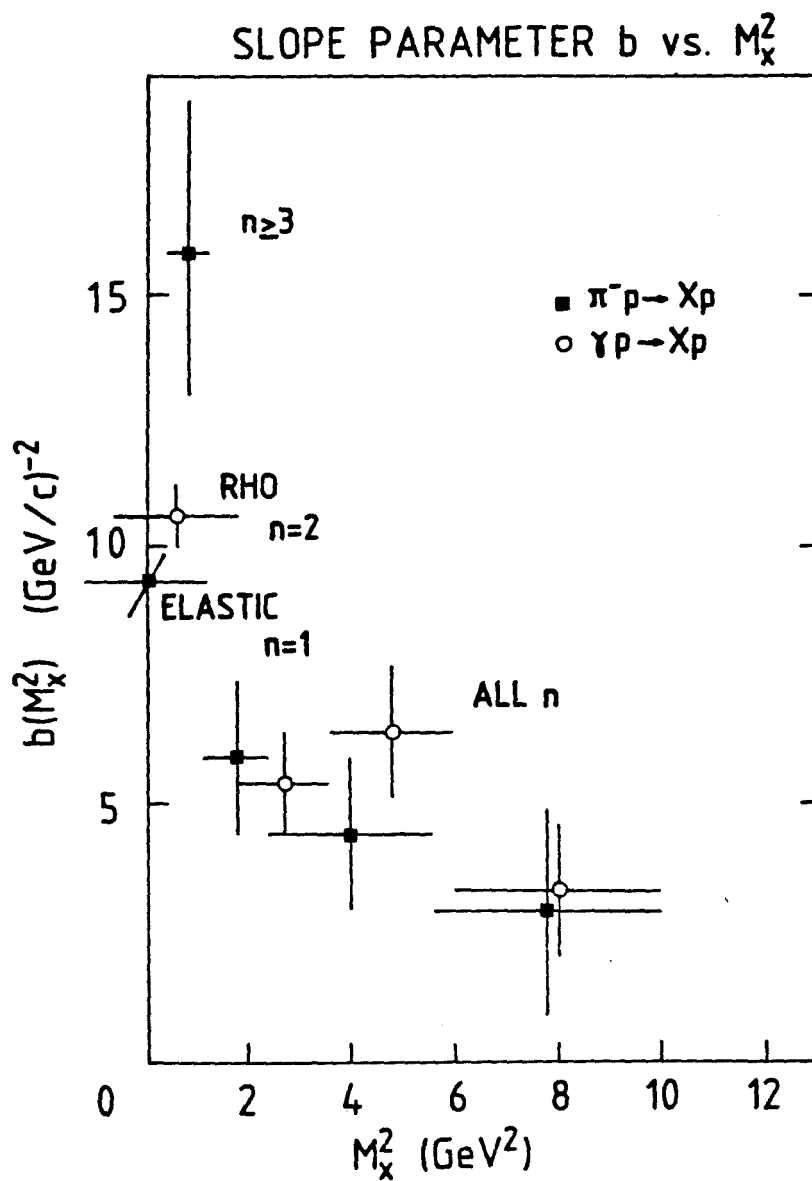


FIG. VII.6 - The slope parameter  $b$  versus  $M_x^2$  for  $\gamma p \rightarrow Xp$  and  $\pi^- p \rightarrow Xp$

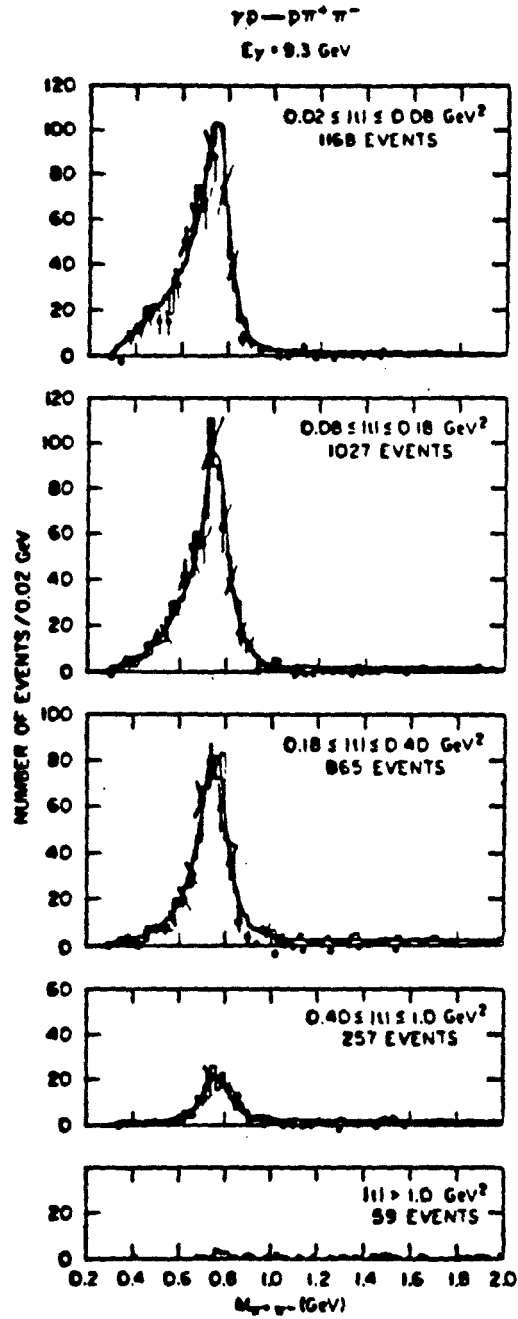


FIG. VII.7 - Distributions of the  $\pi^+ \pi^-$  mass for different  $t$  intervals in  $\gamma p \rightarrow p \pi^+ \pi^-$  at 9.3 GeV

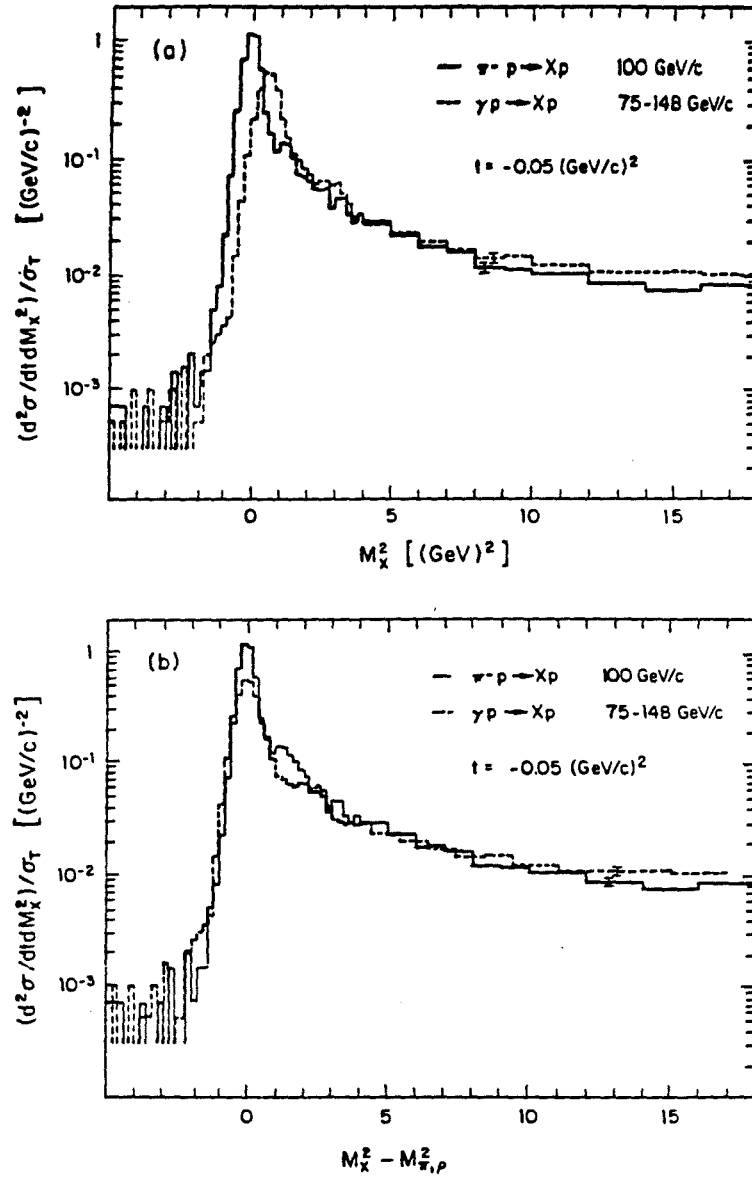


FIG. VII.8 - Factorization of differential to total cross sections. Distributions plotted (a) vs.  $M_X^2$ , (b) vs.  $M_X^2 - M_{\pi,\rho}^2$

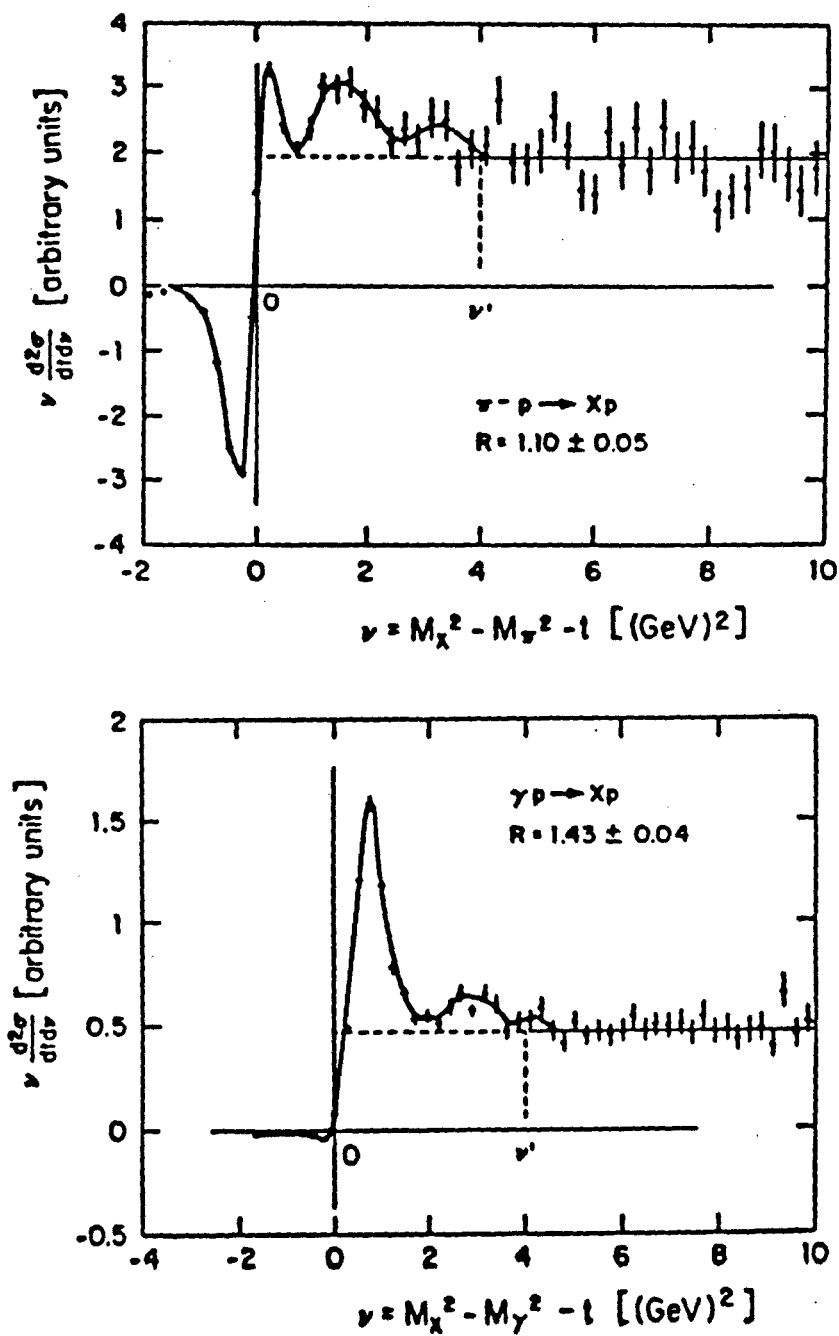


FIG. VII.9 - Test of the FMSR for  
 (a) pions with  $M_o^2 = M_\pi^2$   
 (b) photons with  $M_o^2 = M_\gamma^2 = 0$

## CHAPTER VIII. APPENDIX: CROSS SECTIONS AND RESULTS FOR PUBLICATION

The results of the experiment were submitted for publication to The Physical Review after Chapters I through VII of this thesis were prepared. For completeness, I present those final results here. This chapter contains a detailed description of the procedure for extracting the number of pion elastic events and rho events from the continuous missing mass distributions. Absolute differential cross sections for diffraction dissociation are then obtained by normalizing the inelastic distributions to known cross sections for the elastic processes. The extracted pion elastic events and rho events are also used in a treatment of the FMSR different than that presented in Chapter VII. This treatment yields a "direct" hadronic cross section for the photon about the same as that given in Chapter VII, but the estimated uncertainty in the value is greater here.

### VIII.A. EXTRACTION OF ELASTIC EVENTS

Figure VIII.1 shows a mass distribution for photon data. Because of the finite resolution in the measurement of  $M_x^2$ , there is significant overlap between the "elastic"  $\rho$  peak and the inelastic events. Since the shape of the inelastic mass distribution is not known a priori, the extrapolation of the high mass data into the region under the "elastic" peak cannot be carried out directly. Instead, we use a procedure based on the charged multiplicity of the events (Figure VI.6) and the multiplicity distributions described previously (Equation VI.16).

For the photon data, only even multiplicities are allowed, and therefore a cut requiring  $1.5 < n < 2.5$  rejects efficiently events with charged multiplicity  $n \neq 2$ . The events retained within the cut are



mostly due to  $\rho^0 \rightarrow \pi^+\pi^-$ , but they also include the  $n = 2$  component of the dissociation of higher diffractive masses. However, because of the Landau tail in the pulse height distributions, this cut rejects some events with charged multiplicity of 2. These events may be regained statistically by normalizing the peak of the  $n = 2$  distribution to the  $\rho$  peak in the uncut data. Figure VIII.1a shows the  $n = 2$  spectrum obtained in this manner. Subtracting this spectrum from the overall mass distribution yields the  $n \neq 2$  inelastic spectrum, also shown in Figure VIII.1a. We now use the multiplicity law, Equation (VI.16), to correct the inelastic spectrum for the missing  $n = 2$  multiplicities. The result is shown in Figure VIII.1b along with its complement to the overall distribution which now represents the "elastic"  $\rho$  signal. This procedure was applied at each  $t$  bin. The same method, but with a multiplicity cut around  $n = 1$  instead of  $n = 2$ , was used to extract the elastic events from the pion data.

#### VIII.B. NORMALIZATION

In principle the normalization of the data could be determined from the event rates. However, uncertainties in beam intensity, triggering efficiency, dead time, solid angle, and event reconstruction losses limited the accuracy of such a determination to ~30%. For this reason, the data were normalized through the elastic events. In the pion case, the elastic data were fitted to the function  $d\sigma/dt = A \exp(bt)$  and the constant  $A$  was scaled to the optical point,  $d\sigma/dt(t=0) = \sigma_T^2(1+\rho^2)/16\pi$ , where  $\sigma_T$  is the total cross section and  $\rho$  is the ratio of the real to the imaginary part of the forward scattering amplitude. We set  $\rho = 0$ , which leads to an uncertainty in  $A$  of < 1%, and used the value of 24.0 mb for the total cross section at 100 GeV/c (Carroll et al., 1979). In the photon case, the normalization was obtained by scaling the number of our "elastic" events to the normalized photoproduction cross sections of (Callahan et al.), taking into account the small admixture of  $\omega$  and  $\phi$  events under the peak. The

net correction to the normalization arising from the non-resonant Drell-Söding term, discussed in Section VIII.C, is negligible when averaged over our  $t$  range. Our estimated normalization accuracy is  $\pm 10\%$  for the pion data and  $\pm 13\%$  for the photon data.

#### VIII.C. ELASTIC CROSS SECTIONS

The elastic cross sections for  $\pi^- p \rightarrow \pi^- p$  and  $\gamma p \rightarrow p p$  are given in Table VIII.1. The data were fitted to the form

$$\frac{d\sigma}{dt} = A e^{bt} \quad (\text{VIII.1})$$

and normalized by adjusting the parameter  $A$  as explained in Section VIII.B. Figure VIII.2 shows some  $t$  distributions. Slope parameter values are plotted in Figure VIII.3. The photon elastic data contain about 6%  $\omega$  and 4%  $\phi$  signal. The effect of this contamination on the  $p$  slope is insignificant. However, the normalization of the inelastic data, as mentioned previously, was corrected accordingly. The pion slope of  $9.9 \pm 1.0 \text{ (GeV/c)}^{-2}$  agrees, within errors, with the value of  $8.92 \pm 0.31 \text{ (GeV/c)}^{-2}$  obtained in the Fermilab experiment E-396 (Cool et al., 1981b). The  $p$  slope is about one unit larger than that of  $\pi^-$ . This difference can be understood in terms of the Drell and Söding mechanism which produces a non-resonant background in the vicinity of the  $p$  peak (Drell, 1960 and Söding, 1966). The mass resolution of our experiment does not permit a direct determination of this background. However, a calculation using the fit parameters of (Callahan et al.) shows that the net result of this  $t$  dependent effect is to increase the slope parameter by about one unit. Correcting for this effect changes the value of the  $p$  photoproduction slope from  $10.6 \pm 1.0$  to  $9.6 \pm 1.0 \text{ (GeV/c)}^{-2}$ . The corrected value is then identical, within errors, to our  $\pi^-$  elastic scattering slope,  $9.9 \pm 1.0 \text{ (GeV/c)}^{-2}$ , in agreement with the prediction of the VDM.

#### VIII.D. INELASTIC CROSS SECTIONS

The inelastic cross sections for  $\pi^-(Y) + p \rightarrow X + p$  as a function of  $M_X^2$  and  $1-x = (M_X^2 - M_0^2)/s$ , where  $x$  is the Feynman variable and  $M_0$  is the mass of the incident particle, are given in Tables VIII.2 and VIII.3, respectively. For each  $M_X^2$  or  $1-x$  bin, all data in the region  $0.02 < |t| < 0.1 \text{ (GeV/c)}^2$  were used to calculate the value at  $t = -0.05 \text{ (GeV/c)}^2$  for which the cross sections are presented. For a given  $s$ , there is, of course, a one to one correspondence between  $1-x$  and  $M_X^2$ . However, in the case of the photon data a given  $1-x$  value corresponds to different  $M_X^2$  values depending on the energy of the photon within the energy bin. For this reason the data are given both in the  $M_X^2$  and the  $1-x$  representations. Since the extraction of elastic events, as discussed in Section VIII.A, can only be done in the  $M_X^2$  representation, the cross sections  $d\sigma/dx$  in Table VIII.3 are presented only for values of  $1-x$  corresponding to  $M_X^2 \geq 3 \text{ GeV}^2$  (for the lowest value of the energy in the energy bin). On the other hand, since our efficiency deteriorates for  $(1-x) > 0.1$ , the upper value of  $M_X^2$  in Table VIII.2 corresponds to  $1-x \sim 0.1$ .

The  $t$  distributions for various  $M_X^2$  intervals are given in Table VIII.1. Figure VIII.3 shows the slope parameter  $b$  of the  $t$  distributions as a function of  $M_X^2$ . For  $M_X^2 > 4 \text{ GeV}^2$ , the inelastic slopes are about one half of the elastic slopes and appear to be independent of  $M_X^2$ . With the exception of a small difference in the elastic slopes, which was explained above in terms of the Drell-Söding mechanism, the photon and pion slopes are the same, as expected by VDM.

The distributions in  $1-x$  are particularly significant for diffractive processes. Table VIII.3 and Figure VIII.4 present  $1-x$  distributions for pion and photon data and fits to the form

$$\frac{d^2\sigma}{dt dx} = \left[ \frac{A}{1-x} + B(1-x) \right] e^{b(t + 0.05)} \quad (\text{VIII.2})$$

This fit is inspired by the triple-Regge model. The form of the A term is predicted by the triple-Pomeron amplitude. In hadron dissociation, this term was found to scale to the total cross section of the dissociating hadron, as predicted by factorization. The B term, on the other hand, does not scale and, moreover, it was found to vary significantly from experiment to experiment. This term is presumed to arise from non-diffractive processes. The events from such processes are likely to have more large angle tracks emanating from the target in addition to the recoil proton and therefore are detected with different efficiency by different experiments. This experiment suppresses events with more than one large-angle track, which are the events that contribute to B. Since the efficiency of our apparatus for minimum ionizing tracks was set purposefully low to reduce accidentals (our fastest recoil protons were six times minimum ionizing), it is impossible to calculate our bias against events of the B type. We therefore attribute no physical significance to the B terms presented in Table VIII.3 other than that the photon data appear to have a larger B term than the pion data. The value of  $A/\sigma_T$  of the pion data is in agreement with the value  $0.113 \pm 0.003 \text{ (GeV/c)}^{-2}$  found in a previous experiment (Cool et al., 1981a).

The  $1/(1-x)$  behavior of Equation (I.8) and the scaling of the diffractive to the total cross section, both predicted in the Regge model, have been found to hold for  $\pi^\pm$ ,  $K^\pm$ , and  $p^\pm$  hadrons dissociating on protons (Cool et al., 1981a). Since Equation (VIII.2) fits the photon data satisfactorily, triple-Pomeron behavior is now also established for photons. The values of the  $A/\sigma_T$  terms of our pion and 75-148 GeV photon data are, respectively,  $0.122 \pm 0.006$  and  $0.118 \pm 0.006$ . Thus, within the relative normalization uncertainty of  $\pm 16\%$ , factorization is satisfied. These results indicate that the photon indeed behaves like a hadron despite the fact that its hadronic

cross section is about 200 times smaller than that of the pion. In the VDM, it would be more appropriate to use  $M_0 = M_\rho$  in Equation (I.4) which defines the variable  $1-x$ . Such a choice would change the value of  $A/\sigma_T$  of the photon data from  $0.122 \pm 0.006$  to  $0.110 \pm 0.005$ . Within errors, this last value is still in agreement with the value of the pion data. The test of factorization in our data cannot discriminate between the photon as an ordinary hadron and the prediction of the VDM.

The test of the finite mass sum rule (FMSR), Equation (I.9), is shown in Figure VIII.5. The term  $|t| \cdot (d\sigma_{el}/dt)$  is simply a  $\delta$ -function at  $v = |t|$ . However, for presentation purposes, it is plotted as an area whose abscissa extends over a finite region of  $v$ . The value of  $v_0$  was taken to be  $4 \text{ (GeV)}^2$ , safely above the "resonance region". The data for  $v$  larger than  $v_0$  were fitted by using Equation (VIII.2). The reader is reminded that the cross-symmetric variable  $v$  is given by

$$v = M_x^2 - M_0^2 - t = (1-x) s - t \quad (\text{VIII.3})$$

The FMSR is tested by comparing the left-hand to the right-hand side of Equation (I.9). Numerically, we evaluate the quantity

$$R = \frac{|t| \frac{d\sigma_{el}}{dt} + \int_0^4 v \frac{d^2\sigma}{dt dv} dv}{\int_0^4 v \left[ \frac{d^2\sigma}{dt dv} \right]_{\text{fit for } v > 4} dv} \quad (\text{VIII.4})$$

A deviation of  $R$  from unity indicates violation of the FMSR. The sensitivity of the test increases as the value of the upper limit of integration,  $v_0$ , decreases. However,  $v_0$  should not be allowed to fall into the low mass resonance region. Our choice of  $v_0 = 4 \text{ GeV}^2$  satisfies these criteria.

Figure VIII.5a shows the pion data. We find  $R_\pi = 1.10 \pm 0.06$ . The photon data, for the energy bin 75-148 GeV, are shown in Figures VIII.5b and VIII.5c. In Figure VIII.5b we consider the photon to be the incident "hadron". Therefore, we set  $M_0 = 0$  in Equation (VIII.3), yielding  $v = M_x^2 - t$ , and find  $R_\gamma = 1.48 \pm 0.07$ . Clearly, in this straightforward application, the FMSR fails for the photon data. In Figure VIII.5c, the incident (dissociating) hadron is considered to be the  $\rho$ -meson and therefore  $M_0$  is set equal to the mass of the  $\rho$  yielding  $R_\rho = 0.87 \pm 0.06$ . This value is in better agreement with unity than the value of  $R_\gamma$ . Thus our results favor the VDM.

Actually, the value of  $R_\rho$  appears to be somewhat smaller than unity. Within the VDM, this could be caused by a "direct" dissociation of the incident photon, where the term "direct" means an interaction that does not proceed via an intermediate vector meson. Such an interaction has been proposed in order to explain the shadowing effects of photons incident on nuclear targets (Bauer et al., 1978). The "direct" interaction would produce an inelastic spectrum  $v (d^2\sigma/dt dv)$  in Figure VIII.5b which would be fairly flat in  $v$ , similar to the pion inelastic spectrum of Figure VIII.5a. Compton scattering, the elastic peak from such a "direct" interaction, was eliminated in our trigger. Assuming no interference between the "direct" and VDM amplitudes, the ratio of the "direct" to the VDM dissociation cross sections may be determined by subtracting a constant term from the cross sections in Figure VIII.5b and demanding that the remaining cross sections satisfy the FMSR according to the VDM. Following such a procedure, this ratio is found to be  $0.33 \pm 0.16$ . Assuming now that the "direct" and VDM diffractive cross sections scale to the corresponding total cross

sections, our result may be interpreted as representing a measurement of the "direct" hadronic cross section of the photon. In terms of the total cross section,  $\sigma_Y^T$ , the "direct" cross section is thus given by

$$\sigma_Y^D = (0.25 \pm 0.12) \sigma_Y^T \quad (\text{VIII.5})$$

This value is consistent with the fact that the simple VDM accounts for only ~80% of the total photon cross section. Furthermore, since the "direct" cross section is not expected to exhibit shadowing effects in nuclei, our result is also consistent with experiments on nuclear shadowing which indicate that ~20% of the photon cross section is not shadowed.

#### VIII.E. RESONANCE STRUCTURES

As seen in Figure VIII.5, both the pion and the photon cross sections exhibit resonance-like behavior in the region of  $M_X^2 < 4 \text{ GeV}^2$ . In the pion case, enhancements can be seen in the vicinity of the  $A_1(1270)$  and the  $A_3(1680)$ , while in the photon case only one enhancement is visible, in addition to the  $\rho$ , corresponding to the  $\rho'(1600)$ .

In order to extract the masses, widths and cross sections of these enhancements, it is necessary to know the shape of the background under the peaks. Figure VIII.6 shows the inelastic ( $\rho$  removed) cross sections  $M_X^2 (d^2\sigma/dtdM_X^2)/\sigma_T$  at  $t = -0.05 (\text{GeV}/c)^2$ . This figure differs from Figure VIII.5 in that  $M_X^2$  is used instead of  $\nu$ , resulting in very similar background shapes for the pion and photon data. In particular, the rise of the pion cross section from threshold is identical to that of the photon cross section, assuming that the interacting photon has the mass of the  $\rho$  as expected by the simple VDM. The shoulder to the left of the prominent peak in the photon case indicates that the extrapolation of the high mass data fit into the low mass region is a good representation of the background down to

$M_x^2 \approx 1.5 \text{ GeV}^2$ . A similar extrapolation in the pion data should then represent the background correctly down to  $M_x^2 \approx 1.5 - M_\rho^2 = 0.9 \text{ GeV}^2$ . Therefore, the pion and photon data were fitted in the mass regions 1.0-3.6 and 2.2-3.6  $\text{GeV}^2$ , respectively, using as background the extrapolations of the corresponding high mass fits. Since the widths of the peaks are comparable to the  $M_x^2$  experimental resolution of  $\pm 0.3 \text{ GeV}^2$ , Gaussian functions were used to fit the data. The solid curves in Figure VIII.6 show the best fits obtained in this manner, multiplied by  $M_x^2$ . The parameters of the fits are given in Table VIII.4. The last two rows in the Table present the  $b$  slopes and the total cross sections integrated over  $t$ , obtained by assuming the form  $d\sigma/dt = Ae^{bt}$ . The slopes were taken from Table VIII.1. For the  $A_1$ , we use the slope of  $13.7 \pm 2.0 (\text{GeV}/c)^{-2}$ , which was obtained from events of charged multiplicity  $n_c \neq 1$ , mainly  $n_c = 3$ . For the  $A_2$  and  $\rho'$ , the slopes are the averages over the mass regions 1-5 and 2-5  $(\text{GeV})^2$ , respectively.

The masses of our enhancements are consistent with their nominal values, although our  $\rho'$  mass seems to be somewhat high. The widths, after unfolding the experimental resolution, are in the range of 300-400 MeV, in agreement with values measured previously in  $\pi^-p$  (Antipov et al., 1973) and  $\gamma p$  (Aston et al., 1981) diffractive interactions. Finally, our measured inclusive cross sections are in the range expected from these previous measurements which were made in exclusive channels. In particular, the production cross section of the  $\rho'(1600)$  by 40 GeV photons, followed by its decay into its (dominant) channel of  $\rho^0 \pi^+ \pi^-$ , was measured to be (Aston et al, 1981)  $0.54 \pm 0.17 \text{ } \mu\text{b}$ . Considering the uncertainty in the branching ratio and the errors in the cross section measurements, our value of  $0.66 \pm 0.13 \text{ } \mu\text{b}$  is not inconsistent with the above measurement. Although the accuracy of the data does not permit more definite quantitative conclusions to be drawn, the agreement with previous measurements is found to be satisfactory.



#### VIII.F. CONCLUSION

The differential cross section for diffractive photon dissociation on hydrogen,  $\gamma p \rightarrow Xp$ , is dominated by a  $\rho$  peak and a high mass continuum. The  $\rho$  peak is exponential in  $t$  and has a slope parameter approximately equal to that of  $\pi^-p$  elastic scattering. The high mass data are also exponential in  $t$  and have slope parameter values close to those of  $\pi^-p \rightarrow Xp$ . The  $M_x^2$  distribution, plotted against  $M_x^2 - M_\rho^2$  and scaled to the total cross section, is very similar to that of  $\pi^-$  dissociation. At high masses, it has a dominant  $1/M_x^2$  behavior, indicating a large triple-Pomeron presence in the diffractive amplitude. The scaling of the photon and pion data to their corresponding total cross sections establishes factorization at the level of  $\pm 16\%$ , limited by the uncertainty in the normalization of the data. Finally, the finite mass sum rule fails in a straight-forward application, but is approximately satisfied if the "incident hadron" is considered to be the  $\rho$  meson. These results confirm the validity of the simple VDM according to which the dissociation proceeds through an intermediate  $\rho$  meson.

There may be, however, a small discrepancy from the predictions of the VDM. Namely, the FMSR does not appear to be satisfied completely with the  $\rho$  as the only "incident hadron". If it is assumed that this discrepancy is caused by a certain probability that the photon dissociates "directly" (not via a  $\rho$  meson) into hadrons, and the ratio of "direct" to VDM cross sections is adjusted to satisfy the FMSR, this ratio is found to be  $0.33 \pm 0.16$ . The further assumption that the diffractive cross sections scale to the corresponding total cross sections yields the result that the "direct" hadronic cross section of the photon is  $25 \pm 12\%$  of the total. This number agrees with experiments on shadowing of photon cross sections on nuclei and with the fact that the simple VDM accounts for only  $\sim 80\%$  of the photon total cross section.

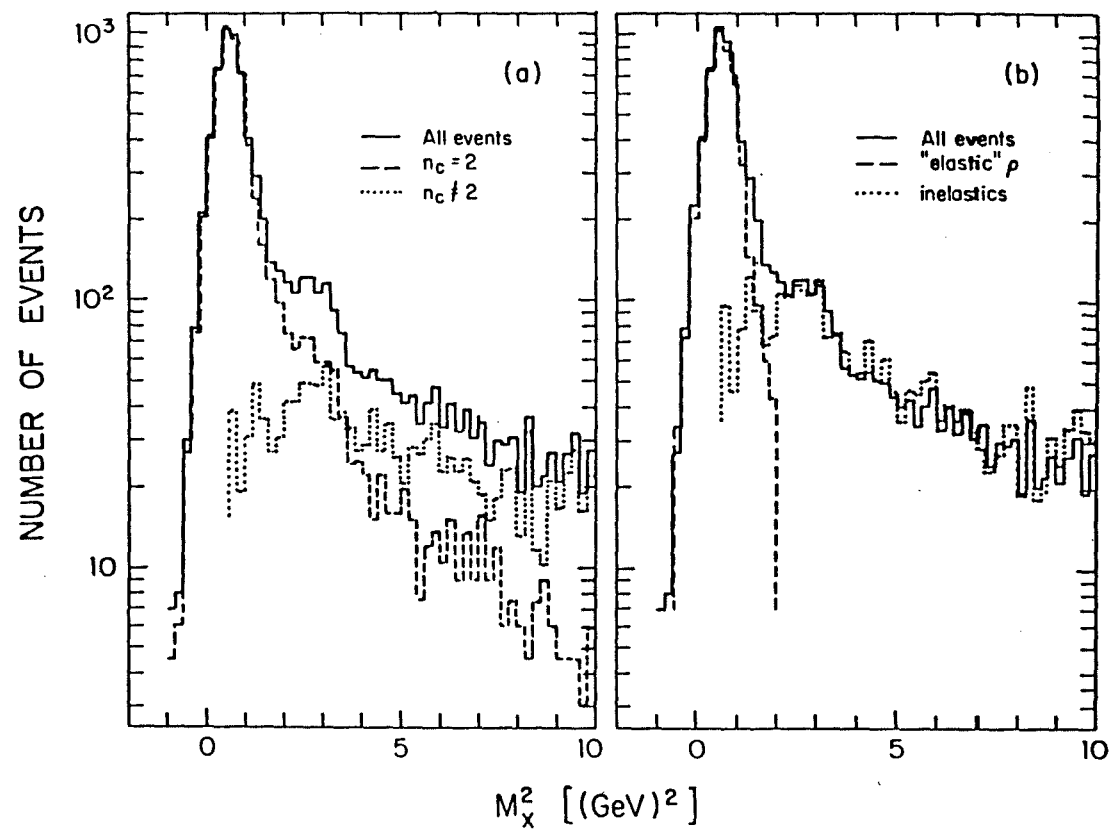


FIG. VIII.1 - Photon missing mass distributions with "elastic"  $\rho$  and inelastic contributions shown

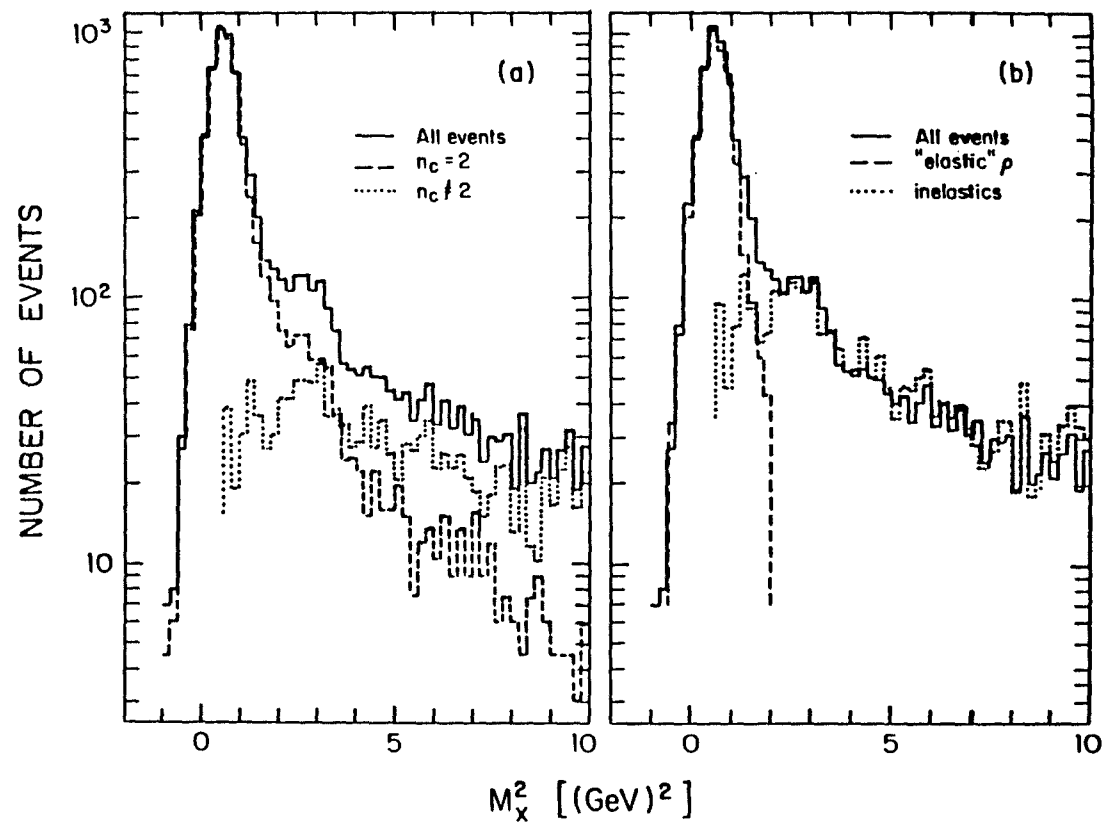


FIG. VIII.1 - Photon missing mass distributions with "elastic"  $\rho$  and inelastic contributions shown

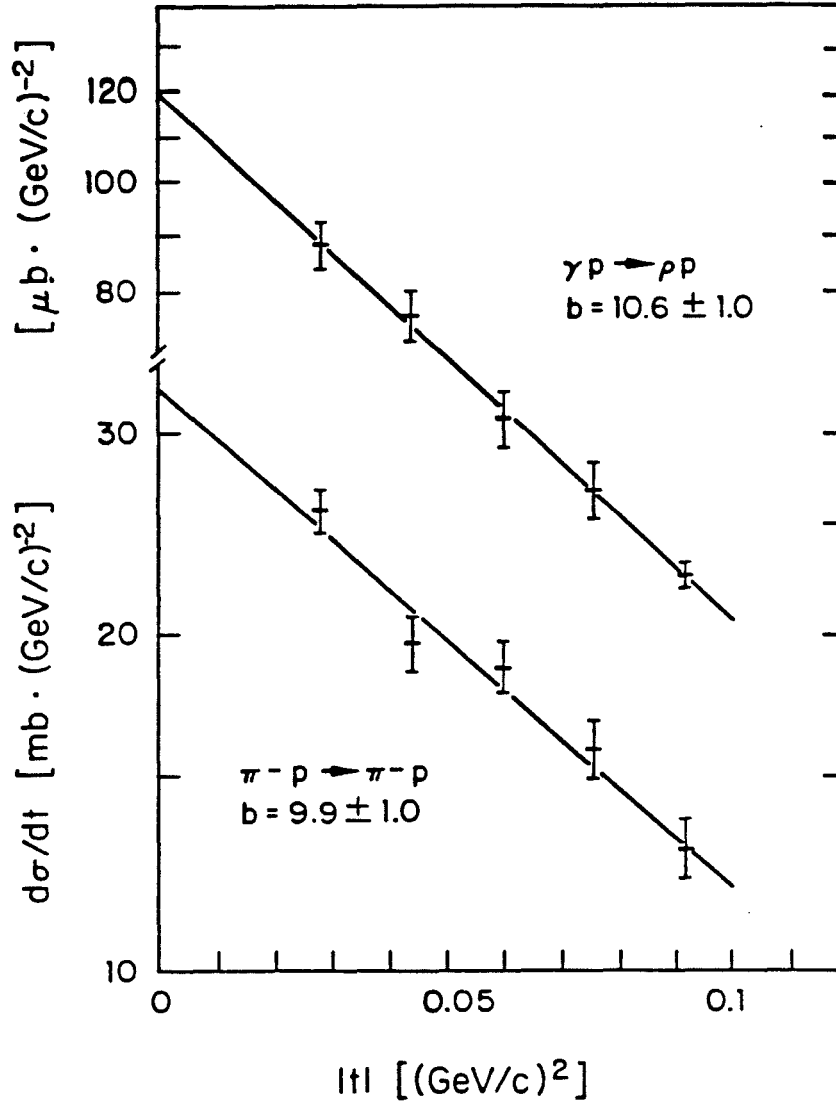


FIG. VIII.2 - Elastic differential cross sections as a function of  $t$ . The lines represent fits to the form  $d\sigma/dt = A e^{bt}$

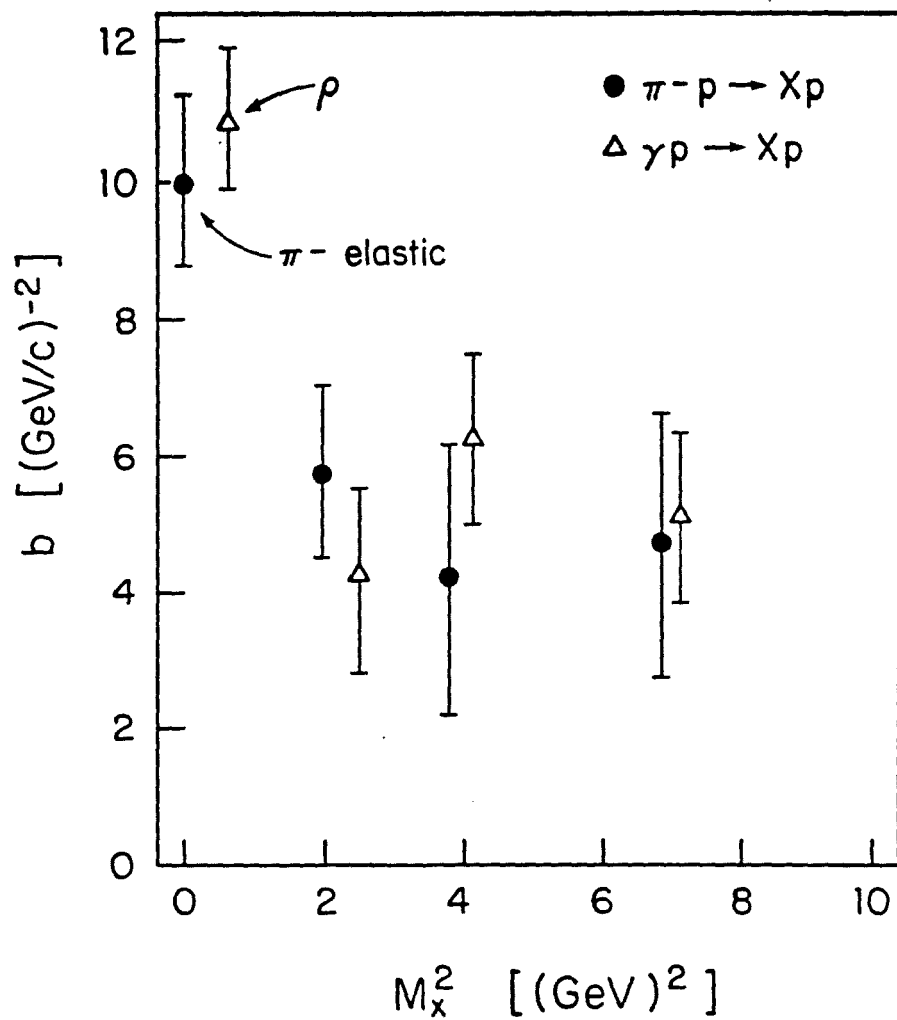


FIG. VIII.3 - The slope parameter  $b$  as a function of  $M_X^2$  for  $\pi^- p$  and  $\gamma p$

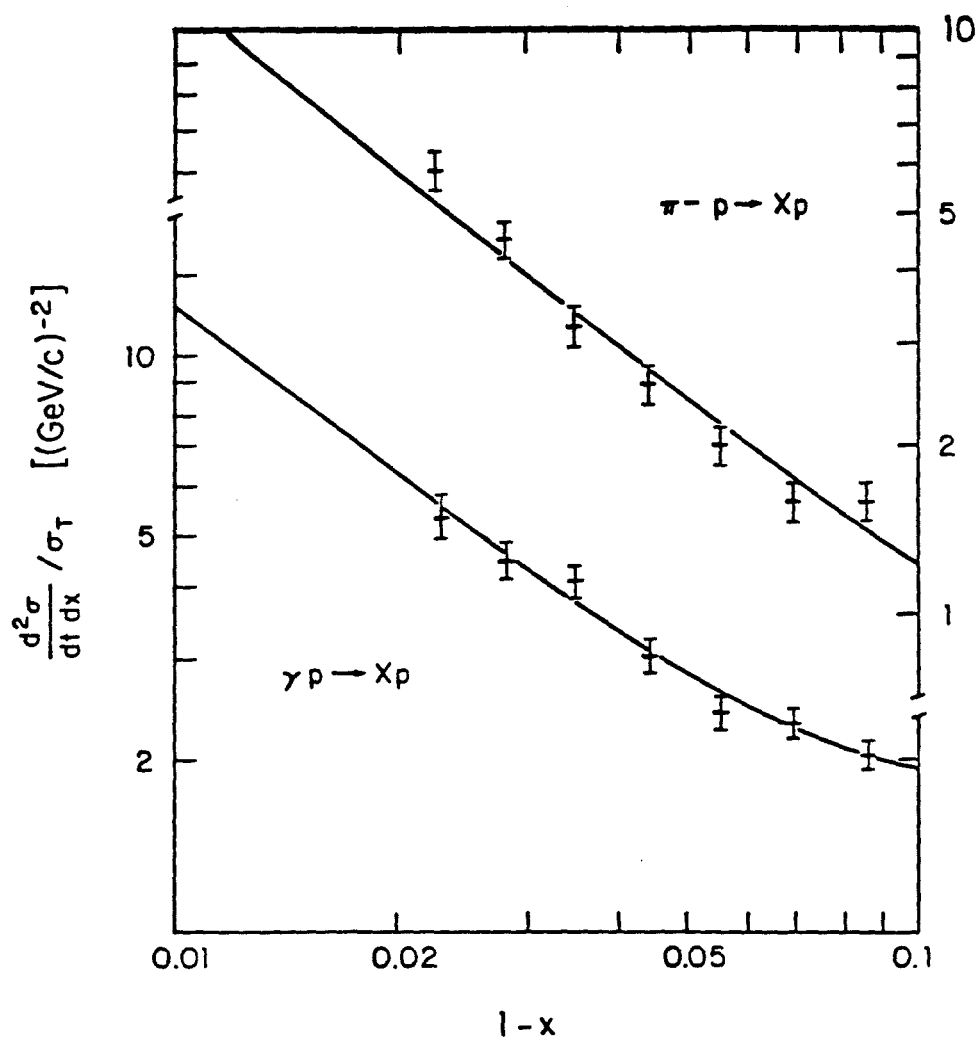


FIG. VIII.4 -  $(1-x)$  distributions of pion and photon differential cross sections. Curves are fits to  $d\sigma/dx = A/(1-x) + B(1-x)$

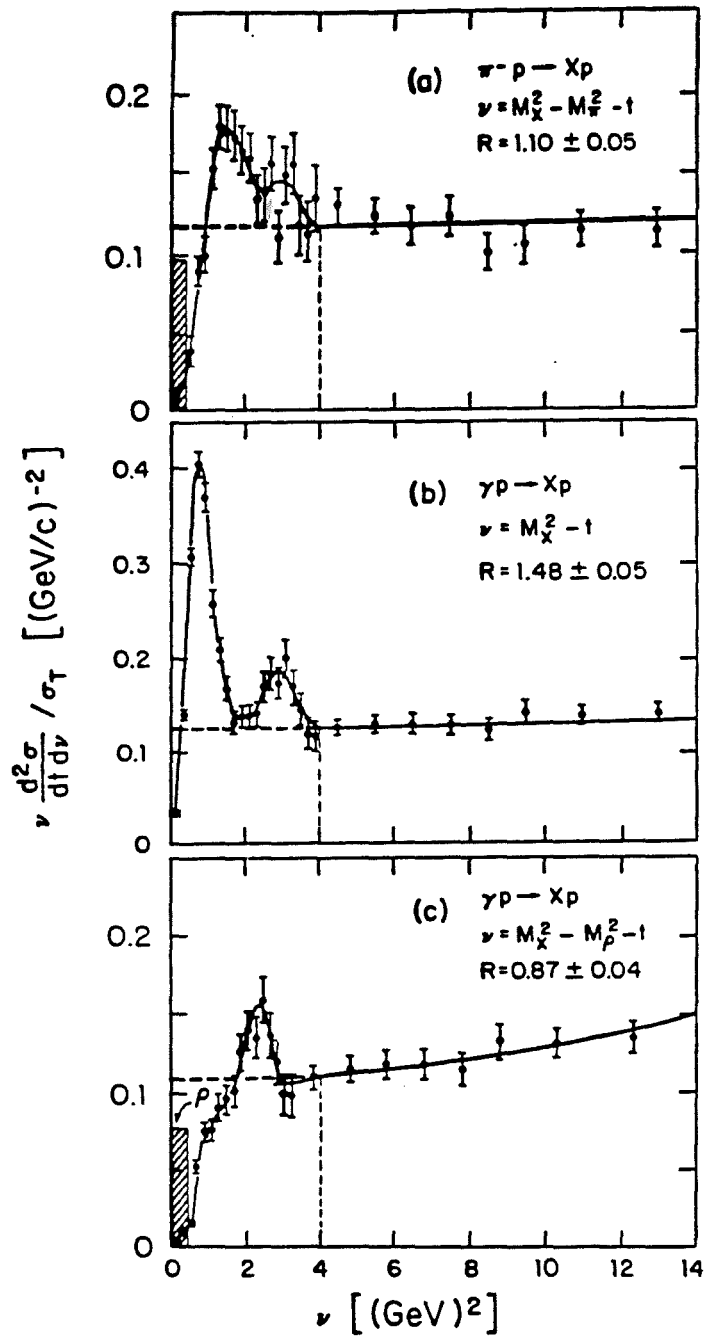


FIG. VIII.5 - Test of the FMSR for

- (a) pions with  $M_O^2 = M_\pi^2$
- (b) photons with  $M_O^2 = 0$  and
- (c) photons with  $M_O^2 = M_\rho^2$

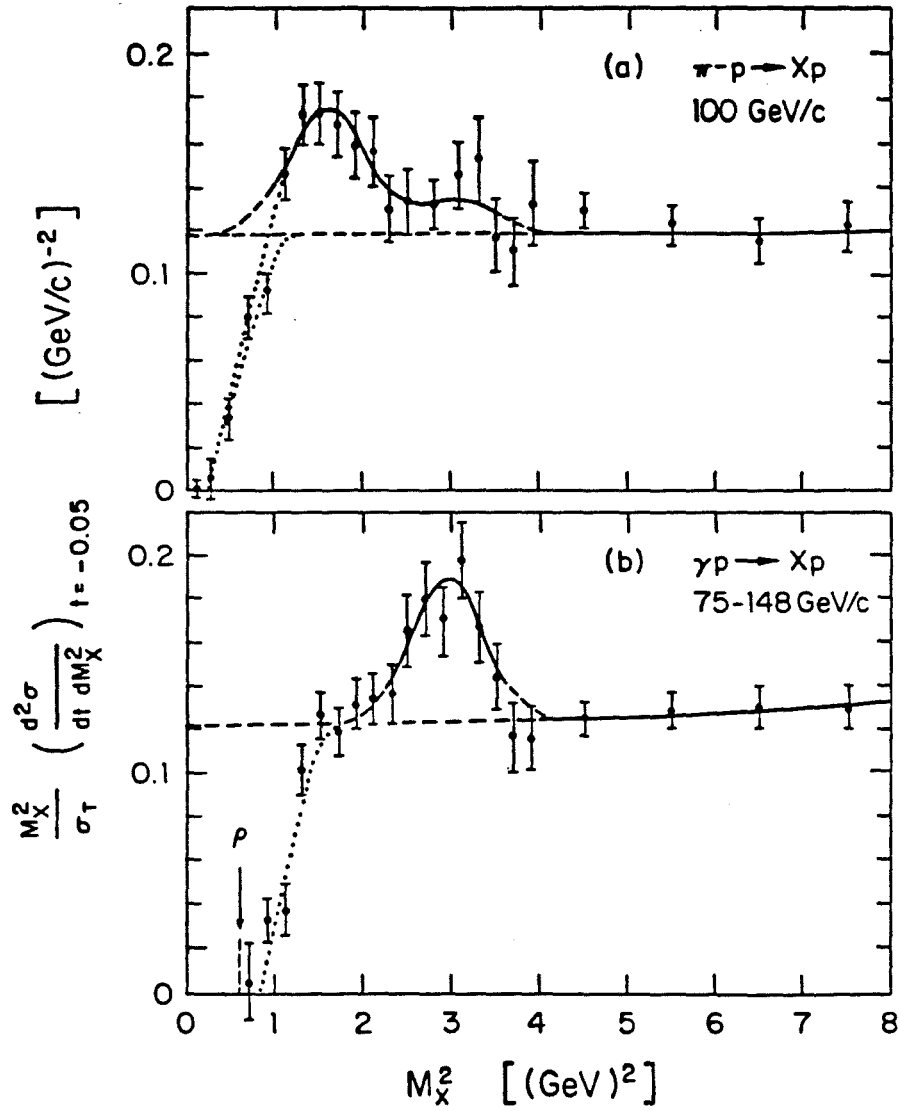


FIG. VIII.6 - Resonance structures

(a)  $A_1$  and  $A_2$  for the pion, and

(b)  $\rho^1$  for the photon

Solid curves are fits, broken  
ones are by-eye extrapolations



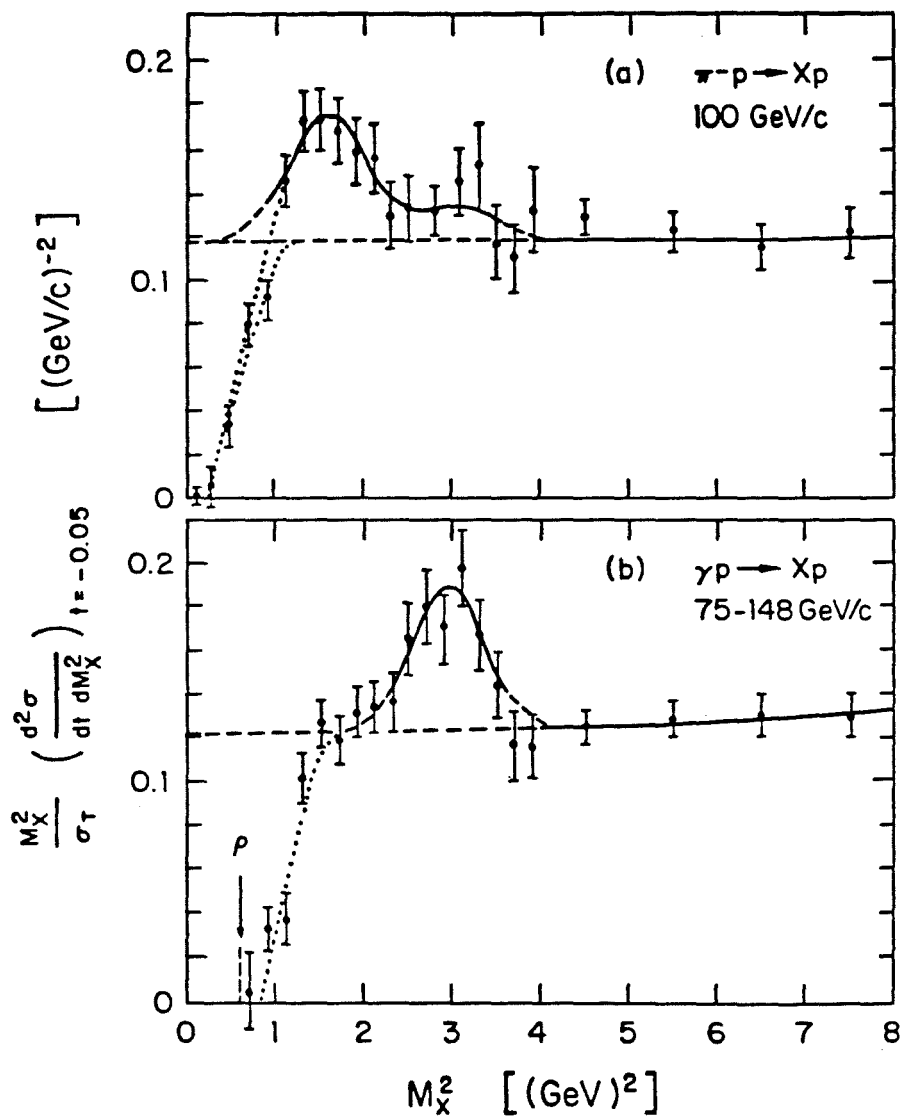


FIG. VIII.6 - Resonance structures

(a)  $A_1$  and  $A_3$  for the pion, and

(b)  $\rho'$  for the photon

Solid curves are fits, broken  
ones are by-eye extrapolations

TABLE I. Differential cross sections  $do/dt$  and fits to the form  $Ae^{bt}$

$\pi^- + p \rightarrow X + p$ at 100 GeV/c						
[mb·(GeV/c) <sup>-2</sup> ]						
t value (GeV/c) <sup>2</sup> \ M <sub>x</sub> <sup>2</sup> (GeV) <sup>2</sup>	Elastic	0.6-1.6*	1.0-3.0	3.0-5.0	5.0-9.0	
0.020-0.036	25.6±1.1		5.17±0.29	1.87±0.17	1.82±0.17	
0.036-0.052	19.6±1.1		4.16±0.26	1.69±0.16	1.68±0.16	
0.052-0.068	18.7±0.9		3.54±0.24	1.34±0.15	1.76±0.17	
0.068-0.084	15.8±0.9		3.75±0.24	1.50±0.15	1.33±0.15	
0.084-0.100	12.9±0.8		3.53±0.24	1.42±0.15	1.41±0.15	
A mb (GeV/c) <sup>-2</sup>	32.73		5.59±0.45	2.01±0.25	2.09±0.26	
b (GeV/c) <sup>-2</sup>	9.9±1.0	13.7±2.0	5.8 ±1.3	4.2 ±2.0	4.7 ±2.0	
$\chi^2/DF$ (3DF)	1.32	1.10	2.27	0.93	0.67	

$\gamma + p \rightarrow X + p$ at 75-148 GeV/c						
[μb·(GeV/c) <sup>-2</sup> ]						
t value (GeV/c) <sup>2</sup> \ M <sub>x</sub> <sup>2</sup> (GeV) <sup>2</sup>	p-peak	1.2-2.0*	2.0-3.0	3.0-5.0	5.0-9.0	
0.020-0.036	88.0±4.1		8.57±0.74	9.92±0.80	11.50±0.86	
0.036-0.052	76.1±3.8		9.47±0.78	9.92±0.80	10.24±0.81	
0.052-0.068	61.4±3.4		8.37±0.73	10.5±0.82	8.50±0.74	
0.068-0.084	53.3±3.2		7.80±0.71	8.37±0.73	8.18±0.73	
0.084-0.100	45.0±1.1		6.18±0.63	7.15±0.68	9.92±0.80	
A μb(GeV/c) <sup>-2</sup>	119.1		10.8±1.1	12.1±1.2	11.9 ±1.2	
b (GeV/c) <sup>-2</sup>	10.6±1.0	3.7±1.7	4.2±1.4	6.3 ±1.3	5.1±1.3	
$\chi^2/DF$ (3DF)	0.13	0.11	1.23	1.33	2.00	

\*Includes only events with charged multiplicity  $n_c \geq 1$  for  $\pi^-$  and  $n_c \geq 2$  for  $\gamma$

TABLE VIII.1

TABLE II-A. Inelastic differential cross sections  $d^2\sigma/dt dM_x^2$  at  $t = -0.05 \text{ (GeV/c)}^2$  for  $\pi^- p \rightarrow Xp$  at 100 GeV/c and  $\gamma p \rightarrow Xp$  from 75 to 148 GeV/c [in  $\text{mb (GeV/c)}^{-2} \text{ (GeV)}^{-2}$  and  $\mu\text{b (GeV/c)}^{-2} \text{ (GeV)}^{-2}$ , respectively]. The  $\pi^- p$  elastic and  $p$  signals were subtracted from the data as described in the text.

$M_x^2$ (GeV) <sup>2</sup>	Beam Particle and Momentum (GeV/c)			
	$\pi^- (100)$	$\gamma (75-100)$	$\gamma (100-148)$	$\gamma (75-148)$
0.0-0.2	0.23 ± 0.99			
0.2-0.4	0.38 ± 0.74			
0.4-0.6	1.59 ± 0.47			
0.6-0.8	2.75 ± 0.32	2.42 ± 4.40	0.00 ± 3.60	0.97 ± 2.82
0.8-1.0	2.45 ± 0.25	6.61 ± 2.57	1.97 ± 2.21	4.23 ± 1.68
1.0-1.2	3.18 ± 0.26	6.05 ± 1.92	2.39 ± 1.71	3.92 ± 1.28
1.2-1.4	3.20 ± 0.24	9.65 ± 1.53	8.71 ± 1.49	8.96 ± 1.07
1.4-1.6	2.77 ± 0.24	10.05 ± 1.27	9.58 ± 1.25	9.73 ± 0.89
1.6-1.8	2.38 ± 0.21	8.42 ± 1.09	7.75 ± 1.02	8.06 ± 0.74
1.8-2.0	2.01 ± 0.19	7.98 ± 1.04	8.09 ± 1.00	8.03 ± 0.72
2.0-2.2	1.79 ± 0.18	7.10 ± 0.98	7.64 ± 0.97	7.37 ± 0.69
2.2-2.4	1.36 ± 0.16	7.12 ± 0.98	6.71 ± 0.90	6.89 ± 0.66
2.4-2.6	1.29 ± 0.15	7.80 ± 1.02	7.57 ± 0.96	7.67 ± 0.70
2.6-2.8	1.36 ± 0.16	8.35 ± 1.06	7.10 ± 0.93	7.68 ± 0.70
2.8-3.0	0.90 ± 0.13	5.66 ± 0.87	7.84 ± 0.98	6.79 ± 0.66
3.0-3.2	1.13 ± 0.14	8.64 ± 1.08	6.26 ± 0.87	7.38 ± 0.69
3.2-3.4	1.12 ± 0.14	6.22 ± 0.92	5.53 ± 0.82	5.85 ± 0.61
3.4-3.6	0.80 ± 0.12	4.33 ± 0.77	5.17 ± 0.80	4.76 ± 0.55
3.6-3.8	0.72 ± 0.11	4.21 ± 0.76	3.21 ± 0.63	3.67 ± 0.49
3.8-4.0	0.82 ± 0.12	3.53 ± 0.69	3.33 ± 0.64	3.42 ± 0.47
4.0-5.0	0.69 ± 0.05	3.44 ± 0.31	3.05 ± 0.27	3.23 ± 0.20
5.0-6.0	0.54 ± 0.04	2.94 ± 0.28	2.50 ± 0.25	2.70 ± 0.19
6.0-7.0	0.425 ± 0.040	2.58 ± 0.27	2.06 ± 0.23	2.30 ± 0.17
7.0-8.0	0.391 ± 0.038	1.87 ± 0.23	2.08 ± 0.23	1.98 ± 0.16
8.0-9.0	0.282 ± 0.033	1.89 ± 0.23	1.48 ± 0.19	1.67 ± 0.15
9.0-10.0	0.269 ± 0.032	1.90 ± 0.23	1.55 ± 0.20	1.71 ± 0.15
10.0-12.0	0.251 ± 0.022	1.76 ± 0.16	1.22 ± 0.13	1.47 ± 0.10
12.0-14.0	0.211 ± 0.020	1.27 ± 0.14	1.26 ± 0.13	1.27 ± 0.09
14.0-16.0	0.184 ± 0.019	1.31 ± 0.14	1.22 ± 0.13	1.26 ± 0.09
16.0-18.0	0.206 ± 0.021	1.30 ± 0.14	1.11 ± 0.12	1.20 ± 0.09

TABLE VIII.2a

TABLE II-B. Differential cross sections as in Table II-A including the  $\pi^-p$  elastic and  $\rho$  signals. The data beyond  $M_x^2 = 2 \text{ GeV}^2$  are not shown here as they are identical to those in Table II-A. The cross sections extend to negative values of  $M_x^2$  due to the finite resolution of the experiment.

$M_x^2$ (GeV) <sup>2</sup>	Beam Particle and Momentum (GeV/c)			
	$\pi^-$ (100)	$\gamma$ (75-100)	$\gamma$ (100-148)	$\gamma$ (75-148)
-5.0-(-4.8)	0.017 ± 0.017	0	0.12 ± 0.12	0.06 ± 0.06
-4.8-(-4.6)	0.017 ± 0.017	0	0	0
-4.6-(-4.4)	0.017 ± 0.017	0.13 ± 0.13	0	0.06 ± 0.06
-4.4-(-4.2)	0	0	0	0
-4.2-(-4.0)	0	0	0.24 ± 0.16	0.12 ± 0.09
-4.0-(-3.8)	0	0	0	0
-3.8-(-3.6)	0.017 ± 0.017	0	0	0
-3.6-(-3.4)	0	0.13 ± 0.13	0.12 ± 0.12	0.12 ± 0.09
-3.4-(-3.2)	0.000 ± 0.017	0	0	0
-3.2-(-3.0)	0.017 ± 0.017	0	0.12 ± 0.12	0.06 ± 0.06
-3.0-(-2.8)	0	0.13 ± 0.13	0	0.06 ± 0.06
-2.8-(-2.6)	0.035 ± 0.025	0.13 ± 0.13	0.12 ± 0.12	0.12 ± 0.09
-2.6-(-2.4)	0	0	0	0
-2.4-(-2.2)	0	0.13 ± 0.13	0.24 ± 0.16	0.18 ± 0.11
-2.2-(-2.0)	0.052 ± 0.030	0	0	0
-2.0-(-1.8)	0.017 ± 0.017	0	0.12 ± 0.12	0.06 ± 0.06
-1.8-(-1.6)	0.035 ± 0.025	0.13 ± 0.13	0	0.06 ± 0.06
-1.6-(-1.4)	0.035 ± 0.025	0.26 ± 0.18	0.24 ± 0.16	0.24 ± 0.12
-1.4-(-1.2)	0.122 ± 0.046	0.13 ± 0.13	0.48 ± 0.24	0.30 ± 0.14
-1.2-(-1.0)	0.192 ± 0.058	0.39 ± 0.23	0.36 ± 0.21	0.36 ± 0.15
-1.0-(-0.8)	0.54 ± 0.10	0.26 ± 0.19	0.60 ± 0.27	0.44 ± 0.17
-0.8-(-0.6)	1.77 ± 0.18	0.13 ± 0.13	0.84 ± 0.32	0.50 ± 0.18
-0.6-(-0.4)	6.28 ± 0.33	0.66 ± 0.29	2.63 ± 0.56	1.69 ± 0.33
-0.4-(-0.2)	17.0 ± 0.55	3.82 ± 0.71	6.00 ± 0.85	4.95 ± 0.56
-0.2-0.0	28.5 ± 0.71	11.09 ± 1.21	14.04 ± 1.30	12.61 ± 0.89
0.0-0.2	26.8 ± 0.69	26.05 ± 1.86	25.23 ± 1.74	25.57 ± 1.27
0.2-0.4	14.0 ± 0.50	48.33 ± 2.53	44.15 ± 2.30	46.05 ± 1.70
0.4-0.6	6.04 ± 0.33	72.14 ± 3.09	57.95 ± 2.64	64.57 ± 2.02
0.6-0.8	4.05 ± 0.27	72.37 ± 3.10	53.32 ± 2.54	62.26 ± 1.98
0.8-1.0	2.92 ± 0.23	49.74 ± 2.57	40.56 ± 2.21	44.85 ± 1.68
1.0-1.2	3.37 ± 0.25	27.83 ± 1.92	24.19 ± 1.71	25.87 ± 1.28
1.2-1.4	3.32 ± 0.24	17.60 ± 1.53	18.29 ± 1.49	17.93 ± 1.07
1.4-1.6	2.81 ± 0.24	12.15 ± 1.27	12.86 ± 1.25	12.50 ± 0.89
1.6-1.8	2.42 ± 0.21	8.83 ± 1.09	8.63 ± 1.02	8.70 ± 0.74
1.8-2.0	2.03 ± 0.19	8.04 ± 1.04	8.27 ± 1.00	8.14 ± 0.72

TABLE VIII.2b

TABLE III.

Cross Sections  $\frac{d^2\sigma}{dt dx} / \sigma_T$   $[(\text{GeV}/c)^{-2}]$  for  $\pi^-(\gamma)+p \rightarrow X+p$  at  $t = -0.05 (\text{GeV}/c)^2$   
and fits to the form  $d^2\sigma/dt dx = [A/(1-x) + B(1-x)] e^{b(t + 0.05)}$

Beam Particle	$\pi^-$	$\gamma$	$\gamma$	$\gamma$
Beam Momentum (GeV/c)	100	75-100	100-148	75-148
$\sigma_T$	24.0 mb	115.9 $\mu\text{b}$	114.9 $\mu\text{b}$	115.3 $\mu\text{b}$
$A/\sigma_T (\text{GeV}/c)^{-2}$	$0.118 \pm 0.006$	$0.130 \pm 0.009$	$0.111 \pm 0.007$	$0.122 \pm 0.006$
$B/\sigma_T (\text{GeV}/c)^2$	$0.6 \pm 1.6$	$7.0 \pm 2.4$	$8.0 \pm 2.6$	$7.2 \pm 1.7$
$\chi^2 / \text{DF} (4\text{DF})$	1.86	1.02	0.38	1.00
Range of (1-x) $\times 10^2$	Cross sections			
2.0-2.5	$5.93 \pm 0.42$	$5.89 \pm 0.53$	$4.92 \pm 0.46$	$5.37 \pm 0.39$
2.5-3.1	$4.56 \pm 0.34$	$4.63 \pm 0.43$	$4.24 \pm 0.39$	$4.42 \pm 0.29$
3.1-3.9	$3.23 \pm 0.25$	$4.42 \pm 0.37$	$3.76 \pm 0.32$	$4.07 \pm 0.24$
3.9-4.9	$2.56 \pm 0.20$	$3.37 \pm 0.29$	$2.73 \pm 0.25$	$3.03 \pm 0.19$
4.9-6.1	$2.01 \pm 0.16$	$2.43 \pm 0.23$	$2.41 \pm 0.21$	$2.42 \pm 0.15$
6.1-7.7	$1.60 \pm 0.13$	$2.39 \pm 0.20$	$2.27 \pm 0.18$	$2.32 \pm 0.13$
7.7-9.6	$1.60 \pm 0.12$	$2.17 \pm 0.18$	$1.94 \pm 0.16$	$2.05 \pm 0.12$

TABLE VIII.3

TABLE IV. Parameters of resonance structures obtained by fits to the pion ( $A_1$  and  $A_2$ ) and photon ( $\rho'$ ) data.

Parameter	Resonance Structure	$A_1(1270)$	$A_2(1680)$	$\rho'(1600)$
$M^2$	$[(\text{GeV})^2]$	$1.44 \pm 0.13$	$2.96 \pm 0.34$	$2.88 \pm 0.09$
$a_{M^2}$	$[(\text{GeV})^2]$	$0.46 \pm 0.17$	$0.46 \pm 0.34$	$0.42 \pm 0.10$
$M$	$[\text{MeV}]$	$1200 \pm 54$	$1720 \pm 99$	$1697 \pm 27$
$\frac{d\sigma}{dt}(t=-0.05)$	$\left[\frac{\mu\text{b}}{(\text{GeV})^2}\right]$	$1060 \pm 248$	$146 \pm 84$	$2.65 \pm 0.39$
$b$	$[(\text{GeV}/c)^{-2}]$	$13.7 \pm 2.0$	$5.0 \pm 1.2$	$5.3 \pm 1.0$
$a_T$	$[\mu\text{b}]$	$153 \pm 37$	$38 \pm 23$	$0.66 \pm 0.13$

TABLE VIII.4

# REFERENCES

1. (Genz and Schmidt, 1973) H. Genz and W. Schmidt, Nucl. Phys. B59, 629 (1973)
2. (Bauer et al., 1978) T. Bauer, R. Spital, D. Yennie, F. Pipkin, "The Hadronic Properties of the Photon in High-Energy Interactions", Rev. Mod. Phys. 50 (1978) (References within this review article are relevant for the photon experiments and VDM formalism mentioned in this section.)
3. (Bartenev et al., 1973a) V. Bartenev et al., Phys. Rev. Lett. 31, 1088 (1973)
4. (Bartenev et al., 1973b) V. Bartenev et al., Phys. Rev. Lett. 31, 1367 (1973)
5. (Bartenev et al., 1974) V. Bartenev et al., Physics Lett. 51B, 299 (1974)
6. (Akimov et al., 1975a) Y. Akimov et al., Phys. Rev. Lett. 35, 763 (1975)
7. (Akimov et al., 1975b) Y. Akimov et al., Phys. Rev. Lett. 35, 766 (1975)
8. (Akimov et al., 1975c) Y. Akimov et al., Phys. Rev. D12, 3399 (1975)
9. (Akimov et al., 1976) Y. Akimov et al., Phys. Rev. D14, 3148 (1976)
10. (Cool et al., 1981a) R.L. Cool et al., Phys. Rev. Lett. 47, 701 (1981)
11. (Cool et al., 1981b) R.L. Cool et al., Phys. Rev. D24, 2821 (1981)
12. (Cool et al., 1982) R.L. Cool et al., Phys. Rev. Lett. 48, 1451 (1982)
13. (Goulianos et al., 1982) K. Goulianos et al., Phys. Rev. Lett. 48, 1454 (1982)
14. (Alberi and Goggi, 1981) G. Alberi and G. Goggi, Physics Reports 74 (1981)
15. (Breakstone et al., 1981) A.M. Breakstone et al., Phys. Rev. Lett. 47, 1778 (1981)

16. (Cool et al., 1980) R.L. Cool et al., "Diffractive Hadron Dissociation at 100 and 200 GeV" (Submitted to the XXth Intl. Conf. on High Energy Physics, Madison, Wisconsin-July 1980) Rockefeller University Report No. DOE/EY/2232A-89
17. (Ekelof, 1976) T. Ekelof, "Low-Energy Recoil Measurements in High-Energy Physics", CERN 76-23, 20 December 1976
18. (Auger et al., 1976) J.P. Auger et al., "Proton - He Elastic Scattering at Intermediate Energies", Nuclear Physics A262, 372-388 (1976)
19. (Sliwa, 1983) K. Sliwa, Fermilab, Personal Communication
20. (Chapin et al., 1982) T. Chapin et al., NIM 197, 305 (1982)
21. (Townsend, 1902) J.S. Townsend, Phil. Mag. 3, 557 (1982)
22. (Rose, 1956) D.J. Rose, Phys. Rev. 104, 273 (1956)
23. (Lowke, 1963) J.J. Lowke, Aust. J. Phys. 16, 115 (1963)
24. (Huxley and Crompton, 1974) L.G.H. Huxley and R.W. Crompton, The Diffusion and Drift of Electrons in Gases, J. Wiley, New York, 1974, pp. 358-364
25. (Wagner et al., 1967) E.B. Wagner, F.J. Davis and G.S. Hurst, J. Chem. Phys. 47 (1967); see also (Huxley and Crompton, 1974) pp.615-624
26. (Shimamori and Hatano, 1976) H. Shimamori and Y. Hatano, Chem. Phys. Lett. 38, 242 (1978)
27. (Cumalat, 1977) J. Cumalat, "Measurements of the Photon Total Cross Section on Protons from 45 GeV to 182 GeV", Ph.D. Thesis, University of California, Santa Barbara, September 1977
28. (Craun and Smith, 1970) R.L. Craun and D.L. Smith, NIM 80, 239 (1970)
29. (Crispin and Hayman, 1964) A. Crispin and P.J. Hayman, "Ionization Loss of Muons in a Plastic Scintillator", Proc. Phys. Soc. 83, 1051 (1964)
30. (Sternheimer, 1967) R.M. Sternheimer, Phys. Rev. 164, 349 (1967)
31. (Janni, 1966) Joseph F. Janni, USAF Technical Report AFWL-TR-65-150
32. (Sternheimer, 1966) R.M. Sternheimer, Phys. Rev. 145, 247 (1966)



33. (Sauli, 1977) F. Sauli, "Principles of Operation of Multiwire Proportional and Drift Chambers", CERN 77-09, 3 May 1977, p. 7
34. (Gottschalk and Kannenberg, 1971) B. Gottschalk and S.L. Kannenberg, NIM 97, 291 (1971)
35. (PPDB, 1982) Particle Properties Data Booklet, April 1982, from Physics Letters 111B (1982)
36. (Scott, 1963) W.T. Scott, Rev. Mod. Phys. 35, 231 (1963)
37. (Carroll et al., 1979) S. Carroll et al., Phys. Lett. 80B, 423 (1979)
38. (Callahan et al.) P. Callahan et al., submitted to Phys. Rev. Letters
39. (Drell, 1960) S.D. Drell, Phys. Rev. Lett. 5, 278 (1960)
40. (Söding, 1966) P. Söding, Phys. Lett. 19, 702 (1966)
41. (Antipov et al., 1973) Y.M. Antipov et al., Nucl. Phys. B63, 153 (1973); also C. Daum et al., Phys. Lett. 89B, 281 (1980); *ibid.* 89B, 285 (1980)
42. (Aston et al., 1981) D. Aston et al., Nucl. Phys. B189, 15 (1981)